Proceedings of the

12th "Patras" Workshop on Axions, WIMPs and WISPs, PATRAS 2016

June 20-24, 2016
Jeju Island, South Korea

Impressum

Proceedings of the 12th Patras Workshop on Axions, WIMPs and WISPs (PATRAS 2016)

June 20-24, 2016, Jeju Island, South Korea

Organizing Committee

Yannis K. Semertzidis (Chair, CAPP/IBS & KAIST)
Vassilis Anastassopoulos (University of Patras)
Laura Baudis (University of Zurich)
Joerg Jaeckel (University of Heidelberg)
Axel Lindner (DESY)
Andreas Ringwald (DESY)
Marc Schumann (AEC Ben)
Konstantin Zioutas (University of Patras & CERN)

Local Organizing Committee

Yannis K. Semertzidis (Chair)
Woohyun Chung
Yeaji Jang
Sookyung Jung
YoungIm Kim
ByeongRok Ko
Soohyung Lee
Yujung Lee
Ka Young Oh
Eleni Petrakou
SungWoo Youn

Preface

The 12th Patras workshop on Axions, WIMPs and WISPs took place in the beautiful resort Jeju Island of South Korea from June 20th to 24th, 2016. It was the first time this conference moved to Asia without the best direct access from most international airports. Nonetheless we broke again a record in the number of registered participants, toping 130 of them from Korea and all around the world. The increased number of active participants is a testament to the vitality of the field, one that is growing in numbers but also in scope of research goals. The workshop presentations covered a wide range of activities, both in theory and experiments with several new ideas that have a great promise. From the level of the talks one can safely conclude that the progress in the field of dark matter is destined to reach major breakthroughs in the coming years. During the workshop the weather was mostly decent allowing occasional visits to the nearby beautiful sandy beaches, great walking expeditions to the volcanic island gorgeous scenery, but also providing the unique experience of whole-day torrential rain! The food combined Korean and Western cuisine for all tastes.

This workshop continues a rich and successful series, reviewing recent theoretical advances, laboratory experiments, as well as astrophysical and cosmological results in the fields of axions, WIMPs and WISPs. The program was complemented with a reach poster session on a large variety of subjects and a Patras Poster Prize was also awarded as was done the previous year in Spain. The committee for the Patras Poster Prize 2016 was composed by Axel Lindner (chair), Paola Arias and Chanda Prescod-Weinstein. The committee evaluated formal and scientific contents of the posters as well as the oral presentations of the participants. Due to the high quality of the posters, the committee agreed to award a first prize (300 €) and two second prizes (150 €each). The winner of the Patras Poster Prize 2016 (first place) was Samantha M. Lewis (University of California), for her excellent presentation "Microwave resonators R&D in support of the ADMXHF/Extreme Axion Experiment". The winners of the second places of the Patras Poster Prize 2016 were Younggeun Kim (KAIST, and IBS/CAPP) for his presentation "3He gas handling system and RF discharge for optical pumping" and YoungIm Kim (IBS/CAPP) for her presentation "Design and performance of a signal processing system for CULTASK experiment". Reading the present proceedings one cannot help notice the high quality of the contributions, that the field is picking up momentum and with so many new ideas and efforts the competition is indeed increasing. It is clear that the field is healthy and it is a great time to be involved in this line of research. Enjoy!

Acknowledgements

Contents

Chapter 1

Contributed Talks

SM*A*S*H

Andreas Ringwald,

Deutsches Elektronen-Synchrotron (DESY), Hamburg, Germany

We present a minimal model for particle physics and cosmology. The Standard Model (SM) particle content is extended by three right-handed SM-singlet neutrinos N_i and a vector-like quark Q, all of them being charged under a global lepton number and Peccei-Quinn (PQ) $U(1)$ symmetry which is spontaneously broken by the vacuum expectation value $v_\sigma \sim 10^{11}$ GeV of a SM-singlet complex scalar field σ. Five fundamental problems – neutrino oscillations, baryogenesis, dark matter, inflation, strong CP problem – are solved at one stroke in this model, dubbed "SM*A*S*H" (Standard Model*Axion*Seesaw*Higgs portal inflation). It can be probed decisively by upcoming cosmic microwave background and axion dark matter experiments.

1 The quest for a minimal model of particle cosmology

The discovery of the Higgs boson has marked the completion of the SM particle content. However, observations in particle physics, astrophysics, and cosmology point to the existence of particles and interactions beyond the SM. In fact, the SM lacks an explanation of *i)* neutrino oscillations, *ii)* the baryon asymmetry of the Universe, *iii)* dark matter, *iv)* inflation, and *v)* the non-observation of strong CP violation.

Remarkably, problems *1)-3)* are solved in the Neutrino Minimal SM (νMSM) [1, 2]: a minimal extension of the SM by three right-handed singlet neutrinos N_i, having Dirac masses $m_D = Fv/\sqrt{2}$ arising from Yukawa couplings F with the Higgs (H) and lepton (L_i) doublets, as well as explicit Majorana masses M,

$$\mathcal{L} \supset -\left[F_{ij}L_i\epsilon H N_j + \frac{1}{2}M_{ij}N_i N_j\right], \tag{1}$$

where we have exploited a Weyl spinor notation. In the seesaw limit, $M \gg m_D$, the neutrino mass spectrum splits into a light set given by the eigenvalues $m_1 < m_2 < m_3$ of the matrix $m_\nu = -m_D M^{-1} m_D^T$, with the eigenstates corresponding mainly to mixings of the active left-handed neutrinos ν_α, and a heavy set given by the eigenvalues $M_1 < M_2 < M_3$ of the matrix M, with the eigenstates corresponding to mixings of the sterile right-handed neutrinos N_i. Problem *1)* is thus solved by the usual seesaw type-I mechanism. Intriguingly, problems *2)* and *3)* can be solved simultaneously if $M_1 \sim$ keV and $M_2 \sim M_3 \sim$ GeV. In fact, in this case $N_{2,3}$ create flavored lepton asymmetries from CP-violating oscillations in the early Universe which are crucial for the generation of the baryon asymmetry of the Universe via flavored leptogenesis and of the lightest sterile neutrino N_1 – the dark matter candidate of the νMSM – by the MSW effect. Moreover, it was argued in Ref. [3] that also problem *4)* can be solved in the νMSM by allowing

a non-minimal coupling of the Higgs field to the Ricci scalar, $S \supset -\int d^4x \sqrt{-g}\, \xi_H\, H^\dagger H R$, which promotes the Higgs field to an inflaton candidate.

However, the success of the νMSM as a minimal model of particle cosmology is threatened by several facts. First of all, recent findings in astrophysics have seriously constrained the parameter space for N_1 as a dark matter candidate [4, 5]. Secondly, the large value of the non-minimal coupling $\xi_H \sim 10^5 \sqrt{\lambda_H}$, where λ_H is the Higgs self-coupling, required to fit the amplitude of the scalar perturbations inferred from the cosmic microwave background (CMB) temperature fluctuations, imply that perturbative unitarity breaks down at the scale $M_P/\xi_H \sim 10^{14}$ GeV, well below the scale of inflation, $M_P/\sqrt{\xi_H} \sim 10^{16}$ GeV, making the inflationary predictions unreliable [6, 7]. Thirdly, Higgs inflation cannot be realised at all if the Higgs quartic coupling λ_H runs negative at large (Planckian) field values due to the corrections from top quark loops. Although, given the current experimental uncertainties, a definite conclusion cannot yet be drawn, see e.g. [8, 9], the presently favoured central values of the strong gauge coupling and the Higgs and top quark masses imply that λ_H becomes negative at a field value corresponding to an energy scale $\Lambda_I \sim 10^{11}$ GeV, much lower than what is required for Higgs inflation, and is thus inconsistent with it.

These three obstacles of the νMSM are circumvented in SMASH - an extension of the SM which features the Axion, the type-I Seesaw and Higgs portal inflation [10, 11] - as we will review in these proceedings.

2 The SMASH model

The SM particle content is extended not only by three right-handed singlet neutrinos N_i, but also by a vector-like color-triplet quark Q, as in the KSVZ [12, 13] model. The SM quarks and leptons as well as the N_i and Q are assumed to be charged under a global lepton number and PQ $U(1)$ symmetry [14] which is spontaneously broken by the vacuum expectation value $v_\sigma \sim 10^{11}$ GeV of a SM-singlet complex scalar field σ. The most general scalar potential reads

$$V(H, \sigma) = \lambda_H \left(H^\dagger H - \frac{v^2}{2} \right)^2 + \lambda_\sigma \left(|\sigma|^2 - \frac{v_\sigma^2}{2} \right)^2 + 2\lambda_{H\sigma} \left(H^\dagger H - \frac{v^2}{2} \right) \left(|\sigma|^2 - \frac{v_\sigma^2}{2} \right),$$

while the most general Yukawa couplings of the new fields are given by

$$\mathcal{L} \supset -\left[F_{ij} L_i \epsilon H N_j + \frac{1}{2} Y_{ij} \sigma N_i N_j + y\, \tilde{Q} \sigma Q + y_{Q_{d_i}} \sigma Q d_i + h.c. \right].$$

After $U(1)$ symmetry breaking the sterile neutrinos N_i, the particle excitation ρ of the modulus of the σ field, and the exotic quark Q get large masses $\propto v_\sigma \gg v = 246$ GeV: $M_{ij} = \frac{Y_{ij}}{\sqrt{2}} v_\sigma + \mathcal{O}\left(\frac{v}{v_\sigma} \right)$, $m_\rho = \sqrt{2\lambda_\sigma}\, v_\sigma + \mathcal{O}\left(\frac{v}{v_\sigma} \right)$, and $m_Q = \frac{y}{\sqrt{2}} v_\sigma + \mathcal{O}\left(\frac{v}{v_\sigma} \right)$. Therefore, as far as physics around the electroweak scale or below is concerned, these heavy particles can be integrated out (unless one considers tiny Yukawa and self couplings). The corresponding low-energy Lagrangian of SMASH is identical to that of the SM, augmented by seesaw-generated neutrino masses, $m_\nu = 0.04\,\text{eV} \left(\frac{10^{11}\,\text{GeV}}{v_\sigma} \right) \left(\frac{-F\, Y^{-1}\, F^T}{10^{-4}} \right)$, and mixing (thus solving problem 1)), plus one new particle: the particle excitation A of the angular degree of freedom of the complex σ field – the Nambu-Goldstone boson of the spontaneous symmetry breaking of the $U(1)$, which is dubbed "axion" in the literature dealing with the PQ solution of the strong CP
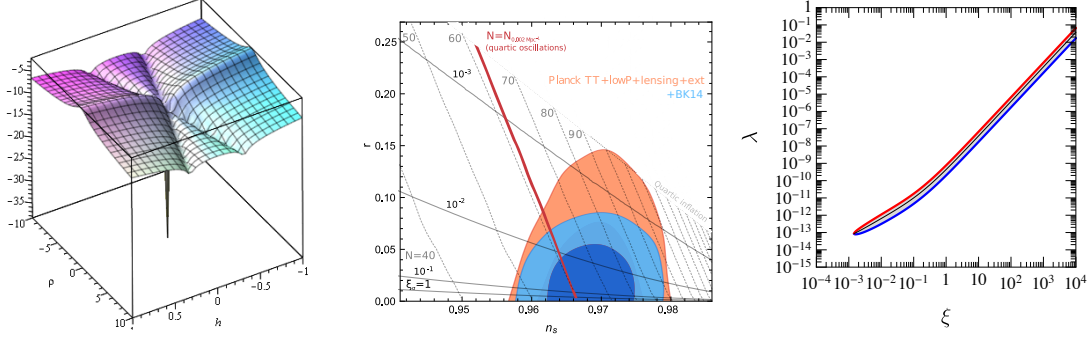
Figure 1: Left: Decadic log of the SMASH scalar potential in the Einstein frame, as a function of h and ρ, all in units of M_P, for $\kappa_H < 0$, $\kappa_\sigma < 0$, supporting mixed Higgs-Hidden-Scalar Inflation along one of the valleys. Middle: Bounds on r vs. n_s [18], compared to the predictions from (H)HSI in SMASH for fixed values of the non-minimal coupling ξ_σ and the number of e-folds N, respectively. Right: Required self-coupling versus non-minimal coupling to reproduce CMB results on inflation. All figures from [11].

problem [15, 16] and "majoron" in the literature dealing with the spontaneous breaking of a global lepton symmetry. Integrating out the exotic quark induces an anomalous coupling of the axion field to the topological charge density in QCD, $\mathcal{L} \supset -\frac{\alpha_s}{8\pi} \frac{A}{f_A} G^c_{\mu\nu} \tilde{G}^{c,\mu\nu}$, promoting the axion field to a dynamical theta parameter, $\theta(x) = A(x)/f_A$, which relaxes to zero in the vacuum, $\langle\theta\rangle = 0$, thereby solving problem 5). While the strong CP problem is solved for any value of the axion decay constant $f_A = v_\sigma$, the dark matter will be comprised by axions only if f_A is around 10^{11} GeV, as we will see later. In this case, the axion mass is predicted to be around $m_A = 57.0(7) \left(\frac{10^{11}\text{GeV}}{f_A}\right) \mu\text{eV}$ [15, 17].

3 Inflation

The non-minimal couplings in SMASH, $S \supset -\int d^4x \sqrt{-g} \left[\xi_H H^\dagger H + \xi_\sigma \sigma^* \sigma\right] R$, stretch the scalar potential in the Einstein frame, which makes it convex and asymptotically flat at large field values. Depending on the signs of the parameters $\kappa_H \equiv \lambda_{H\sigma}\xi_H - \lambda_H\xi_\sigma$ and $\kappa_\sigma \equiv \lambda_{H\sigma}\xi_\sigma - \lambda_\sigma\xi_H$, it can support Higgs Inflation (HI), Hidden Scalar Inflation (HSI), or even mixed Higgs-Hidden Scalar Inflation (HHSI) (cf. Fig. 1 (left)). For $\xi \simeq 10^5\sqrt{\lambda} \gtrsim 10^{-3}$, where

$$\xi \equiv \begin{cases} \xi_H, & \text{for HI,} \\ \xi_\sigma, & \text{for HSI,} \\ \xi_\sigma, & \text{for HHSI,} \end{cases} \qquad \lambda \equiv \begin{cases} \lambda_H, & \text{for HI,} \\ \lambda_\sigma, & \text{for HSI,} \\ \lambda_\sigma\left(1 - \frac{\lambda^2_{H\sigma}}{\lambda_\sigma\lambda_H}\right), & \text{for HHSI,} \end{cases} \tag{2}$$

the predicted values of the CMB observables such as the amplitude of scalar perturbations A_s, the spectral index n_s, and the tensor-to-scalar ratio r are in perfect consistency with the current observations, see Fig. 1 (middle). Importantly, for (H)HSI, the effective self-coupling λ is a free parameter and therefore can be chosen small, $\lambda \sim 10^{-10}$, such that the required non-minimal coupling to fit the amplitude of primordial scalar perturbations is of order unity,
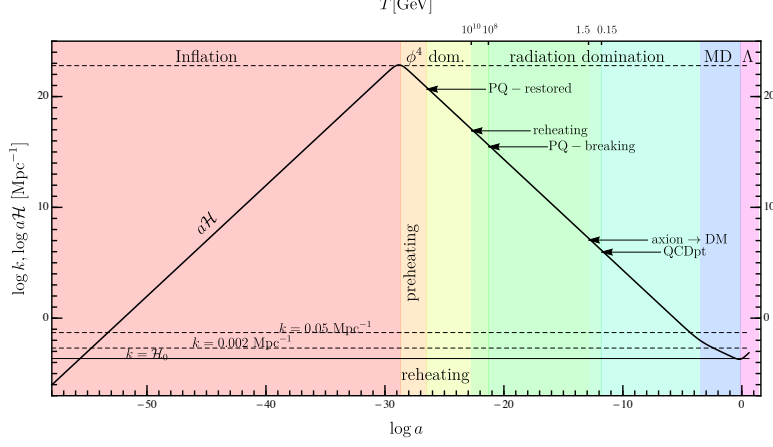
Figure 2: The history of the Universe in SMASH HHSI, emphasising the transition from inflation to radiation-domination-like Universe expansion $a\mathcal{H} \propto 1/a$ before standard matter and cosmological constant domination epochs [11].

$\xi_\sigma \sim 1$, cf. Fig. 1 (right). In this region of parameter space, the perturbative predictivity of SMASH is guaranteed and superior to HI, which necessarily operates at large ξ_H, since λ_H is not small. Remarkably, the requirement of predictive inflation, free of unitarity problems, demands $r \gtrsim 0.01$, which will be probed by CMB experiments such as LiteBIRD and PRISM.

4   Stability

Self-consistency of inflation in SMASH requires a positive scalar potential all the way up to the Planck scale. Importantly, the Higgs portal term $\propto \lambda_{H\sigma}$ in the scalar potential helps to ensure absolute stability in the Higgs direction via the threshold stabilisation mechanism pointed out in [19, 20]. We have found that stability can be achieved if the threshold parameter $\delta = \lambda_{H\sigma}^2/\lambda_\sigma$ is between 10^{-3} and 10^{-1}. Instabilities could also originate in the σ direction, due to quantum corrections from the right-handed neutrinos N_i and the exotic quark Q. Stability in the σ direction then restricts their Yukawas to $\sum Y_{ii}^4 + 6y^4 \lesssim 16\pi^2\lambda_\sigma/\log\left(30M_P/\sqrt{2\lambda_\sigma}v_\sigma\right)$.

5   Reheating

Both in (H)HSI, slow-roll inflation ends at a value of $\rho \sim \mathcal{O}(M_P)$, where the effect of $\xi_\sigma \sim 1$ is negligible and the inflaton starts to undergo Hubble-damped oscillations in a quartic potential, with the Universe expanding as in a radiation-dominated era, which lasts until reheating, cf. Fig. 2. After the latter, radiation domination continues, though driven by a bath of relativistic particles. This fixes the thick red line in Fig. 1 (middle) as the prediction for r, n_s and N in SMASH. The fluctuations of σ grow fast due to parametric resonance while the inflaton background oscillates in its quartic potential, leading to a rapid restoration of the PQ symmetry after about 14 oscillations. The following reheating stage differs considerably for HSI and HHSI.

In the former, the large induced particle masses quench inflaton decays or annihilations into SM particles, resulting in a low reheating temperature, $T_R \sim 10^7$ GeV, such that the produced relativistic axions are never thermalized. Correspondingly, HSI predicts a significant amount of cosmic axion background radiation (CAB): an increase $\Delta N_\nu^{\rm eff} = \mathcal{O}(1)$ of the effective number of relativistic neutrino species beyond the SM value $N_\nu^{\rm eff}({\rm SM}) = 3.046$ [21]. This disvafors HSI, since the current results from CMB and baryon acoustic oscillations yield $N_\nu^{\rm eff} = 3.04 \pm 0.18$ at 68% CL and thus do not allow an additional contribution of order one [18]. For this reason, inflation in SMASH must be of HHSI type and therefore the inflaton contains a (small) Higgs component. The latter allows for efficient reheating of the Universe by the production of SM gauge bosons. The reheating temperature in this case is predicted to be around $T_R \sim 10^{10}$ GeV. Such temperature ensures a thermal restoration of the PQ symmetry for the relevant region of parameter space, since the critical temperature T_c of the PQ phase transition goes as $T_c/v_\sigma \simeq 2\sqrt{6\lambda_\sigma}/\sqrt{8(\lambda_\sigma + \lambda_{H\sigma}) + \sum_i Y_{ii}^2 + 6y^2}$. A thermal background of axions is produced at this stage which later decouples and results in a moderate CAB corresponding to $\triangle N_\nu^{\rm eff} \simeq 0.03$, a prediction which may be checked in a future CMB polarisation experiment.

6   Dark Matter

Dark matter is produced in SMASH by the re-alignment mechanism [22, 23, 24] and the decay of topological defects (axion strings and domain walls) [25]. In order to account for all of the cold dark matter in the Universe, the PQ symmetry breaking scale is predicted to be in the range 3×10^{10} GeV $\lesssim f_A \lesssim 1.2 \times 10^{11}$ GeV, corresponding to an axion mass in the range $50\,\mu$eV $\lesssim m_A \lesssim 200\,\mu$eV [11, 17]. Here, the uncertainty originates mainly from the difficulty in predicting the relative importance of the two main production mechanisms of axionic dark matter, i.e. re-alignment and topological defect decay. Fortunately, the axion dark matter mass window will be probed in the upcoming decade by axion dark matter direct detection experiments such as CULTASK, MADMAX, and ORPHEUS.

7   Baryogenesis

The origin of the baryon asymmetry of the Universe is explained in SMASH by thermal leptogenesis [26]. In HHSI, after reheating and thermal PQ restoration, the RH neutrinos become massive and at least the lightest RH neutrino N_1 will retain an equilibrium abundance. However the stability bound on $M_1 \lesssim 10^8\,(\lambda/10^{-10})^{1/4}(v_\sigma/10^{11}{\rm GeV})$ GeV, for a hierarchical N_i spectrum ($M_3 = M_2 = 3M_1$), is just borderline compatible with vanilla leptogenesis from the decays of N_1, which demands $M_1 \gtrsim 5 \times 10^8$ GeV [27, 28]. Nevertheless, leptogenesis can occur with a mild resonant enhancement [29] for a less hierarchical RH neutrino spectrum, which relaxes the stability bound and ensures that all the RH neutrinos remain in equilibrium after the phase transition.

8   Acknowledgments

References

[1] T. Asaka, S. Blanchet and M. Shaposhnikov, "The nuMSM, dark matter and neutrino masses," Phys. Lett. B **631** (2005) 151 [hep-ph/0503065].

[2] T. Asaka and M. Shaposhnikov, "The nuMSM, dark matter and baryon asymmetry of the universe," Phys. Lett. B **620** (2005) 17 [hep-ph/0505013].

[3] F. L. Bezrukov and M. Shaposhnikov, "The Standard Model Higgs boson as the inflaton," Phys. Lett. B **659** (2008) 703 [arXiv:0710.3755 [hep-th]].

[4] A. Schneider, "Astrophysical constraints on resonantly produced sterile neutrino dark matter," JCAP **1604** (2016) no.04, 059 [arXiv:1601.07553 [astro-ph.CO]].

[5] K. Perez, K. C. Y. Ng, J. F. Beacom, C. Hersh, S. Horiuchi and R. Krivonos, "(Almost) Closing the Sterile Neutrino Dark Matter Window with NuSTAR," arXiv:1609.00667 [astro-ph.HE].

[6] J. L. F. Barbon and J. R. Espinosa, "On the Naturalness of Higgs Inflation," Phys. Rev. D **79** (2009) 081302 [arXiv:0903.0355 [hep-ph]].

[7] C. P. Burgess, H. M. Lee and M. Trott, "Power-counting and the Validity of the Classical Approximation During Inflation," JHEP **0909** (2009) 103 [arXiv:0902.4465 [hep-ph]].

[8] D. Buttazzo, G. Degrassi, P. P. Giardino, G. F. Giudice, F. Sala, A. Salvio and A. Strumia, "Investigating the near-criticality of the Higgs boson," JHEP **1312** (2013) 089 [arXiv:1307.3536 [hep-ph]].

[9] A. V. Bednyakov *et al.*, "Stability of the Electroweak Vacuum: Gauge Independence and Advanced Precision," Phys. Rev. Lett. **115** (2015) 20, 201802 [arXiv:1507.08833 [hep-ph]].

[10] G. Ballesteros, J. Redondo, A. Ringwald and C. Tamarit, "Unifying inflation with the axion, dark matter, baryogenesis and the seesaw mechanism," arXiv:1608.05414 [hep-ph].

[11] G. Ballesteros *et al.*, "Standard Model-Axion-Seesaw-Higgs Portal Inflation. Five problems of particle physics and cosmology solved in one stroke," arXiv:1610.01639 [hep-ph].

[12] J. E. Kim, "Weak Interaction Singlet and Strong CP Invariance," Phys. Rev. Lett. **43** (1979) 103.

[13] M. A. Shifman, A. I. Vainshtein and V. I. Zakharov, "Can Confinement Ensure Natural CP Invariance of Strong Interactions?," Nucl. Phys. B **166** (1980) 493.

[14] R. D. Peccei and H. R. Quinn, "CP Conservation in the Presence of Instantons," Phys. Rev. Lett. **38** (1977) 1440.

[15] S. Weinberg, "A New Light Boson?," Phys. Rev. Lett. **40** (1978) 223.

[16] F. Wilczek, "Problem of Strong p and t Invariance in the Presence of Instantons," Phys. Rev. Lett. **40** (1978) 279.

[17] S. Borsanyi *et al.*, "Lattice QCD for Cosmology," arXiv:1606.07494 [hep-lat].

[18] P. A. R. Ade *et al.* [Planck Collaboration], "Planck 2015 results. XIII. Cosmological parameters," arXiv:1502.01589 [astro-ph.CO].

[19] O. Lebedev, "On Stability of the Electroweak Vacuum and the Higgs Portal," Eur. Phys. J. C **72** (2012) 2058 [arXiv:1203.0156 [hep-ph]].

[20] J. Elias-Miro, J. R. Espinosa, G. F. Giudice, H. M. Lee and A. Strumia, "Stabilization of the Electroweak Vacuum by a Scalar Threshold Effect," JHEP **1206** (2012) 031 [arXiv:1203.0237 [hep-ph]].

[21] G. Mangano, G. Miele, S. Pastor and M. Peloso, "A Precision calculation of the effective number of cosmological neutrinos," Phys. Lett. B **534** (2002) 8 [astro-ph/0111408].

[22] J. Preskill, M. B. Wise and F. Wilczek, "Cosmology of the Invisible Axion," Phys. Lett. B **120** (1983) 127.

[23] L. F. Abbott and P. Sikivie, "A Cosmological Bound on the Invisible Axion," Phys. Lett. B **120** (1983) 133.

[24] M. Dine and W. Fischler, "The Not So Harmless Axion," Phys. Lett. B **120** (1983) 137.

[25] M. Kawasaki, K. Saikawa and T. Sekiguchi, "Axion dark matter from topological defects," Phys. Rev. D **91** (2015) 6, 065014 [arXiv:1412.0789 [hep-ph]].

[26] M. Fukugita and T. Yanagida, "Baryogenesis Without Grand Unification," Phys. Lett. B **174** (1986) 45.

[27] G. F. Giudice, A. Notari, M. Raidal, A. Riotto and A. Strumia, "Towards a complete theory of thermal leptogenesis in the SM and MSSM," Nucl. Phys. B **685** (2004) 89 [hep-ph/0310123].

[28] W. Buchmuller *et al.*, "Leptogenesis for pedestrians," Annals Phys. **315** (2005) 305 [hep-ph/0401240].

[29] A. Pilaftsis and T. E. J. Underwood, "Resonant leptogenesis," Nucl. Phys. B **692** (2004) 303.

The Local Dark Matter Distribution from Hydrodynamic Simulations

Nassim Bozorgnia[1,*], Francesca Calore[2], Matthieu Schaller[3], Mark Lovell[4], Gianfranco Bertone[1], Carlos S. Frenk[3], Robert A. Crain[5], Julio F. Navarro[6,7], Joop Schaye[8] and Tom Theuns[3]

[1]GRAPPA, University of Amsterdam, Science Park 904, 1090 GL Amsterdam, Netherlands
[2] LAPTh, Université Savoie Mont Blanc & CNRS, 9 Chemin de Bellevue, B.P.110 Annecy-le-Vieux, F-74941, France
[3] Institute for Computational Cosmology, Durham University, South Road, Durham DH1 3LE, UK
[4] Max-Planck-Institut für Astronomie, Königstuhl 17, D-69117 Heidelberg, Germany
[5] Astrophysics Research Institute, Liverpool John Moores University, 146 Brownlow Hill, Liverpool L3 5RF, UK
[6] Department of Physics & Astronomy, University of Victoria, Victoria, BC, V8P 5C2, Canada
[7] Senior CIfAR Fellow
[8] Leiden Observatory, Leiden University, PO Box 9513, NL-2300 RA Leiden, Netherlands
[*] presenting author

We investigate the predictions of the EAGLE and APOSTLE hydrodynamic simulations for dark matter direct detection searches. We extract the dark matter density and velocity distribution at the Solar position for a set of simulated galaxies which satisfy Milky Way observational constraints, and use them to analyze current direct detection data. We find that the local dark matter density of the Milky Way-like galaxies fall in the range of $0.41 - 0.73$ GeV/cm^3, and their dark matter velocity distributions fit well a Maxwellian distribution with peak speed in the range of $223 - 289$ km/s.

1   Introduction

The uncertainties in the dark matter (DM) distribution in our Galaxy leads to large uncertainties in the interpretation of results from direct DM experiments. Direct DM searches aim at measuring the small recoil energy of a target nucleus in the detector after the collision with a DM particle arriving from the Milky Way (MW) halo. The DM density and velocity distribution in the Solar neighborhood are key astrophysical inputs in the calculation of direct detection event rates.

In the Standard Halo Model (SHM), which is the most commonly adopted halo model in the analysis of direct detection data, the DM halo is spherical and isothermal with an isotropic Maxwell-Botzmann velocity distribution. The fiducial value of the local DM density is 0.3 GeV/cm^3, and the peak speed of the local velocity distribution is assumed to be equal to the local circular speed of 220 or 230 km/s. Since many of the assumptions of the SHM are not valid, in this work which is based on [1], we extract the local DM distribution of MW-like
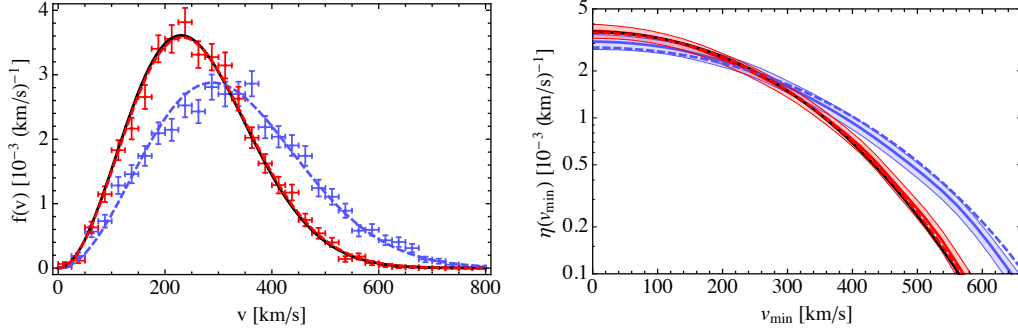
Figure 1: Left: DM speed distributions (mean and 1σ Poisson errors) in the Galactic rest frame for two MW-like haloes with speed distributions closest to (red) and farthest from (blue) the SHM Maxwellian (solid black line). Right: Time averaged halo integrals as a function of $v_{\min}$ for the same two galaxies shown in the left panel, obtained from the mean velocity distributions (solid colour lines) and the velocity distributions at $\pm 1\sigma$ from the mean (shaded bands). In the left and right panels, the best fit Maxwellian speed distributions and their corresponding halo integrals are shown by dashed lines with matching colours for each galaxy, respectively.

galaxies from the EAGLE [2, 3] and APOSTLE [4, 5] high resolution hydrodynamic simulations which include both DM and baryons, and study their implications for DM direct detection. From the full set of galaxies in the simulations, we select 14 MW-like galaxies using a set of criteria based on the observed MW kinematical data.

2 Dark matter density and velocity distribution

The event rate in direct detection experiments depends on the local DM density, ρ_χ, and the DM velocity distribution in the detector rest frame, $f_{\det}(\mathbf{v}, t)$. For the case of spin-independent elastic scattering, the differential event rate can be written as,

$$\frac{dR}{dE_R} = \frac{\rho_\chi A^2 \sigma_{\mathrm{SI}}}{2 m_\chi \mu_{\chi p}^2} F^2(E_R) \eta(v_{\min}, t),$$

where E_R is the recoil energy of the nucleus with mass number A after the scattering with a DM particle with mass m_χ, σ_{SI} is the spin-independent DM-nucleon scattering cross section, $\mu_{\chi p}$ is the reduced mass of the DM–nucleon system, and $F(E_R)$ is a form factor. The minimum speed required for the DM particle to deposit a recoil energy E_R in the detector is $v_{\min} = \sqrt{m_A E_R / (2\mu_{\chi A}^2)}$, where m_A is the nucleus mass, and $\mu_{\chi A}$ is the reduced mass of the DM and nucleus. $\eta(v_{\min}, t)$ is the *halo integral*, which together with ρ_χ contain the astrophysics dependence of the recoil rate,

$$\eta(v_{\min}, t) \equiv \int_{v > v_{\mathrm{mim}}} d^3 v \frac{f_{\det}(\mathbf{v}, t)}{v}.$$

To determine the DM density and velocity distribution of the simulated MW-like galaxies at the Solar position, we consider a torus aligned with the stellar disc, with a galactocentric
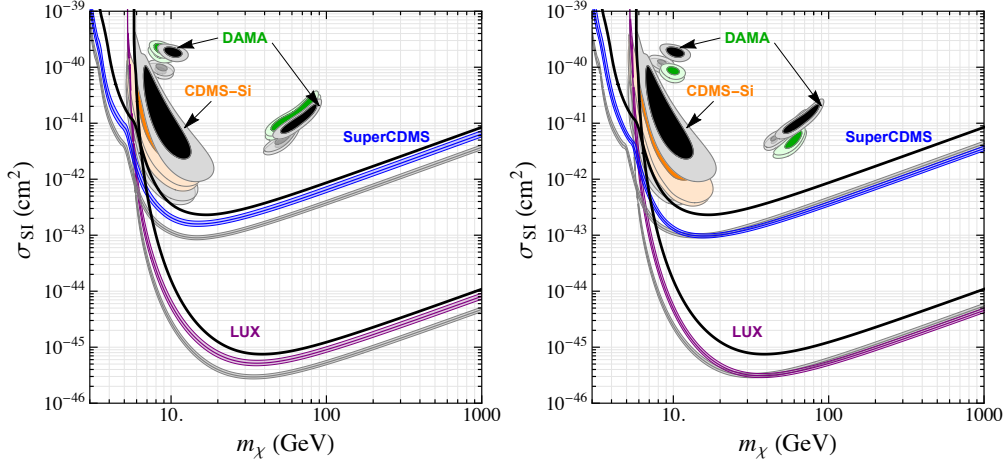
Figure 2: The DAMA (at 90% CL and 3σ) and CDMS-Si (at 68% and 90% CL) preferred regions, and the LUX and SuperCDMS (at 90% CL) exclusion limits in the $m_\chi - \sigma_{\rm SI}$ plane for two MW-like galaxies with smallest (shown in colour) and largest (shown in gray) local DM density (left panel), and two galaxies with speed distributions closest to (shown in colour) and farthest from (shown in gray) the SHM Maxwellian (right panel). For each galaxy, the shaded exclusion band and the two adjacent allowed regions of the same colour are obtained from the upper and lower 1σ limits of the halo integral. The black exclusion limits and allowed regions correspond to the SHM Maxwellian.

radius in the range of $7 - 9$ kpc, and a height of $|z| < 1$ kpc with respect to the galactic plane. For the 14 simulated MW-like galaxies, we find the average DM density in the torus is in the range of $0.41 - 0.73$ GeV/cm^3.

The local DM speed distribution in the Galactic rest frame is shown in the left panel of Fig. 1 for two MW-like galaxies with speed distributions closest to and farthest from the SHM Maxwellian (with a peak speed of 230 km/s). We fit a Maxwellian speed distribution with a free peak speed (shown in dashed) to the DM speed distributions of the simulated galaxies, and find the best fit peak speed in the range of $223 - 289$ km/s. The right panel of Fig. 1 shows the time-averaged halo integrals for the same MW-like galaxies shown in the left panel. The halo integrals obtained from the best fit Maxwellian speed distributions fall within the 1σ uncertainty band of the halo integrals of the simulated MW-like galaxies.

3 Implications for dark matter direct detection

To perform an analysis of direct detection data, we use the local DM density and velocity distribution of our selected MW-like galaxies. We investigate how the exclusion limits set by the LUX [6] and SuperCDMS [7] experiments, and the preferred regions set by the DAMA [8] and CDMS-Si [9] experiments vary in the DM mass and spin-independent cross section plane. The left panel of Fig. 2 shows the exclusion limits and allowed regions for the four direct detection experiments obtained using the DM distribution of two MW-like galaxies with the

smallest and largest local DM density. To show the effect of the velocity distribution on the preferred regions and exclusion limits, in the right panel of Fig. 2, we show the results for the two haloes with velocity distribution closest to and farthest from the SHM Maxwellian. The shaded exclusion bands and the two adjacent preferred regions of the same colour are obtained from the upper and lower 1σ uncertainty limits of the halo integral. The exclusion limits and allowed regions shown in black are obtained assuming a local DM density of 0.3 GeV/cm^3, and the SHM Maxwellian velocity distribution with peak speed of 230 km/s.

As can be seen from Fig. 2, the largest shift in the exclusion limits and preferred regions for the simulated MW-like galaxies compared to the SHM is due to the variation of the local DM densities of the simulated MW-like galaxies. The effect of the velocity distribution is only important at lower DM masses, where the experiments probe larger $v_{\min}$ values, and are therefore sensitive to the high velocity tail of the DM velocity distribution.

4   Acknowledgments

References

[1] N. Bozorgnia *et al.*, "Simulated Milky Way analogues: implications for dark matter direct searches," JCAP **05**, 024 (2016) [arXiv:1601.04707 [astro-ph.CO]].

[2] J. Joop *et al.*, "The EAGLE project: simulating the evolution and assembly of galaxies and their environments," Mon. Not. Roy. Astron. Soc. **446**, 521 (2015) [arXiv:1407.7040 [astro-ph.GA]].

[3] R. A. Crain *et al.*, "The EAGLE simulations of galaxy formation: calibration of subgrid physics and model variations," Mon. Not. Roy. Astron. Soc. **450**, no. 2, 1937 (2015) [arXiv:1501.01311 [astro-ph.GA]].

[4] T. Sawala *et al.*, "The APOSTLE simulations: solutions to the Local Group's cosmic puzzles," Mon. Not. Roy. Astron. Soc. **457**, no. 2, 1931 (2016) [arXiv:1511.01098 [astro-ph.GA]].

[5] A. Fattahi *et al.*, "The APOSTLE project: Local Group kinematic mass constraints and simulation candidate selection," Mon. Not. Roy. Astron. Soc. **457**, no. 1, 844 (2016) [arXiv:1507.03643 [astro-ph.GA]].

[6] D. S. Akerib *et al.* (LUX Collaboration), "First results from the LUX dark matter experiment at the Sanford Underground Research Facility," Phys. Rev. Lett. **112**, 091303 (2014) [arXiv:1310.8214 [astro-ph.CO]].

[7] R. Agnese *et al.* (SuperCDMS Collaboration), "Search for Low-Mass WIMPs with SuperCDMS," Phys. Rev. Lett. **112**, 241302 (2014) [arXiv:1402.7137].

[8] R. Bernabei, *et al.*, "Final model independent result of DAMA/LIBRA-phase1," Eur. Phys. J. **C73**, 2648 (2013) [arXiv:1308.5109].

[9] R. Agnese *et al.* (CDMS Collaboration), "Silicon Detector Dark Matter Results from the Final Exposure of CDMS II," Phys. Rev. Lett. **111**, 251301 (2013) [arXiv:1304.4279].

Light Dark Matter Search with AURIGA

Antonio Branca[1], on behalf of the AURIGA Collaboration

[1]INFN, Sezione di Padova, Via Marzolo 8, I-35131 Padova, Italy;

We present a search for a new scalar particle, called moduli, performed using the cryogenic resonant-mass gravitational wave detector AURIGA. This scalar may give a significant contribution to the Dark Matter (DM) in our Universe. DM clusters under the galaxies gravitational effect, forming the so called galactic halo. The interaction of ordinary matter with a DM halo composed by moduli causes the oscillation of solids with a frequency equal to the mass of the DM particle. In particular, the putative signal would appear as a narrow peak ($\triangle f \sim 1\,\mathrm{mHz}$) in the sensitive band of AURIGA, some $100\,\mathrm{Hz}$ at about $1\,\mathrm{kHz}$. We used high quality data, selected out of an acquisition of years of continuous running. The search sets upper limits at $95\%\,C.L.$ on the moduli coupling to matter $d_i \lesssim 10^{-5}$ around moduli masses $m_\Phi = 3.6 \cdot 10^{-12}\,\mathrm{eV}$.

1 Light Dark Matter and matter effects

Scalar fields, Φ, often arise in theories like the String Theory (known as moduli), with mass values, m_Φ, depending on the assumed model. They are good Dark Matter (DM) candidates, within the contest of the standard DM model with an energy density of $\rho_{DM} = 0.3\,\mathrm{GeV/cm^3}$, if they are heavier than $m_\Phi \simeq 10^{-22}\,\mathrm{eV}$. Moreover, this scalar field can be described with a classical wave if it is lighter than $m_\Phi \simeq 0.1\,\mathrm{eV}$ [1]:

$$\Phi(\mathbf{x}, t) = \Phi_0 cos(m_\Phi t - m_\Phi \mathbf{v} \cdot \mathbf{x}) + O(\mathbf{v}^2) \tag{1}$$

Moduli interact with ordinary matter, in particular with electrons and electromagnetic field:

$$\mathcal{L} \supset \sqrt{4\pi \mathrm{G_N}}\,\Phi \left[d_{m_e} m_e \bar{e} e - \frac{d_e}{4} F_{\mu\nu} F^{\mu\nu} \right] \tag{2}$$

where G_N is the Newton's constant, d_{m_e} and d_e are the dimensionless coupling to the electron and electromagnetic field, respectively (expressed as a fraction of the gravitational strength). As shown by eq. 2, the effect of moduli can be absorbed by the fine structure constant, α, and electron mass, m_e, in such a way that:

$$\alpha(\mathbf{x}, t) = \alpha \left(1 + d_e \sqrt{4\pi G_N} \Phi(\mathbf{x}, t) \right) \tag{3}$$

$$m_e(\mathbf{x}, t) = m_e \left(1 + d_{m_e} \sqrt{4\pi G_N} \Phi(\mathbf{x}, t) \right) \tag{4}$$

taking into account eq. 1, relations 3 and 4 imply an oscillation of the fine structure constant and of the electron mass around their nominal values. As a consequence, also the atom's size,

$a_0 \sim 1/\alpha m_e$, oscillate, with a deformation with respect the nominal value (strain) given by:

$$h \equiv \frac{\delta a_0}{a_0} = - \left(d_e + d_{m_e} \right) \sqrt{4\pi G_N} \, \Phi(\mathbf{x}, t) \tag{5}$$

This effect of moduli on ordinary matter, brings us to the following conclusion: supposing we have a body of length L, this can be modeled with an oscillator made of two masses connected by a spring of the given length L; it can be shown that given eq. 5 the effect of moduli is an external force acting on the oscillator, with an expression similar to that of a tidal force produced by a gravitational wave on a resonator [1]. This behaviour suggests an experimental method to search for such a moduli field, exploiting same apparatus and analysis techniques employed for gravitational wave signals.

2   Auriga detector

We searched for moduli by analyzing the resonant mass gravitational wave detector AURIGA [2] data. Located at INFN National Laboratory of Legnaro (Italy), AURIGA represents the state-of-art in the class of gravitational wave cryogenic resonant-mass detectors. The detector can be modeled by 3 coupled resonators, with nearly the same resonant frequency $f_R \simeq 900\,\mathrm{Hz}$: the core is a cylindrical bar made of an aluminium alloy, which would resonate under the effect of moduli with the right mass range; the mechanical energy of the bar is amplified by a mashroom-shaped resonator, attached to one of the bar's faces, acting also as a transducer, converting the mechanical resonance to an electrical current; the transducer efficiency is further increased by placing the resonance frequency of an electrical LC circuit close to the mechanical resonance frequencies. The electrical signal is detected by a sensitive SQUID amplifier. AURIGA is operated at cryogenic temperatures, with $T = 4.5\,\mathrm{K}$. The system is in thermal equilibrium, thus its fluctuations are described by the Fluctuation-Dissipation theorem. This allows us to model the detector noise with good precision. In particular the detector sensitivity set by the thermal noise is $h = 2 \cdot 10^{-21}\,1/\sqrt{\mathrm{Hz}}$, within a factor of 2, over a bandwidth of $\triangle f \simeq 100\,\mathrm{Hz}$ centered around $f = 900\,\mathrm{Hz}$.

3   Data analysis

The output from the detector is an electrical signal in time digitized with a frequency of $f_s = 4882.8\,\mathrm{Hz}$. A calibration function [3] is applied on these data to convert them into the relative deformation h of the AURIGA resonant bar length. The power spectrum is computed on the calibrated data, obtaining a measure of the noise of the system in thermal equilibrium. The signal we would expect from moduli is a peak within this power spectrum. The peak would have a characteristic frequency around the moduli mass, $f_\Phi = m_\Phi/2\pi$, and a narrow Maxwell-Boltzmann shape [4]. A simulation of this signal has been performed to study the actual signal bandwidth within the detector sensitive region and to fine-tune the analysis workflow. The simulation takes into account that the detector noise around the moduli peak is white, given the narrow bandwidth of the signal.

The estimated signal bandwidth from simulation is $\triangle f \simeq 1\,\mathrm{mHz}$. Therefore, the analyzed dataset has been split into one hour long data streams and power spectrum computation has been performed on each stream to achieve the proper spectrum resolution. Eventually, the
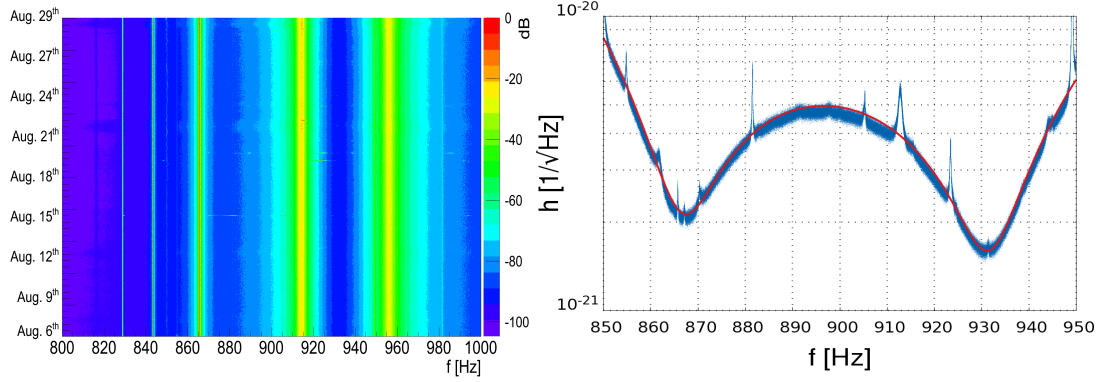
Figure 1: (color online). [left] Evolution of the detector noise spectrum during the data-taking period considered for the analysis. The three main modes of the detector are shown by the yellow-green area. [right] Frequency spectrum of the bar relative deformation computed on AURIGA data (blue curve), compared to the predicted noise power spectrum density by Fluctuation-Dissipation theorem plus noise contribution from the SQUID (red line). Spurious peaks are due to external known sources of background.

one hour long power spectra are averaged to reduce the noise standard deviation and gain sensitivity. Actually, few week of data are enough to reach the sensitivity plateau for this kind of signal, which looses its coherence in about one hour and its standard deviation decreases with the number of averages N as $N^{1/4}$. Using the entire dataset acquired by AURIGA (~ 10 years) would improve the sensitivity just by a factor of ~ 3. So that, for this analysis we focused on a dataset corresponding to about one month of data-taking. AURIGA detector has been running in stable conditions during this period: stability of the detector is inferred by the stable frequencies and shape of the three main detector's modes, checked by studying the evolution of the detector power spectrum on the analyzed dataset, shown in fig. 1-left. Spikes in time due to energetic background events could hide a possible signal from moduli and have been removed by excluding data streams which have a large fluctuation in the time domain. This cut still allows to maintain a 86% duty-cicle of the detector. A check is performed to prove we are not throwing away a possible signal from moduli: a simulated moduli signal has been injected into the real dataset and the analysis workflow successfully reconstructs it. Neither a loss nor an attenuation of the signal strength is observed.

Eventually, the power spectrum of the measured bar relative deformation is shown in fig. 1-right, obtained by averaging N = 400 power spectra from 1 hour long data streams. The comparison to the predicted noise shows a good matching. The thickness of the data curve is due to the noise variance, reduced by averaging the N power spectra. Spurious peaks in data correspond to associated external sources of noise. We stress that these spurious peaks have shape and width not matching the expectation from moduli signal. Data corresponding to spurious peaks have been excluded from the analysis, since we are not able to model the detector response in those regions. Each bin of the power spectrum in fig.1-right has a gaussian distribution: this has been proved by studying the distribution of the bin values and can be understood from statistical reasons, since the power spectrum is the result of averaging a large number ($N = 400$) of single spectra. Consequently, we used a gaussian probability density
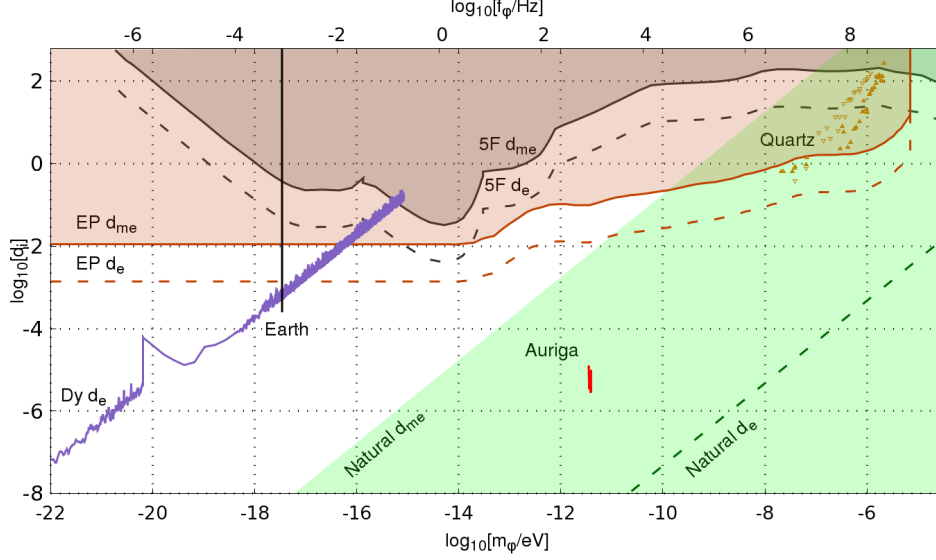
Figure 2: Upper limits on the coupling of both an electron mass modulus ($d_i = d_{m_e}$) and an electromagnetic gauge modulus ($d_i = d_e$) to ordinary matter (red-curve) obtained from AURIGA data and reported in the moduli parameter space: bottom and top horizontal axes represent the moduli mass m_Φ and corresponding frequency $f_\Phi = m_\Phi/2\pi$, vertical axis represents the moduli coupling values. Depicted green area shows the natural parameter space preferred by theory. Other regions and dashed curves represent $95\%\,C.L.$: limits on fifth-force tests (5F, gray), equivalence-principle tests (EP, orange), atomic spectroscopy in dysprosium (Dy, purple-line), low frequency terrestrial seismology (Earth, black vertical line) and piezoelectric quartz resonators (Quartz, yellow-triangles).

function to describe the bin statistics and build a confidence belt by using Feldman and Cousin recipe [5]. The confidence belt provides a confidence interval for the moduli signal strength, given the measured value of h for each bin of the distribution in fig. 1-right. The signal strength is always compatible with zero, thus we set upper limits on the moduli coupling to ordinary matter at 95% confidence level. We improved upper limit calculation by exploiting the noise curve obtained adding thermal noise prediction from Fluctuation-Dissipation theorem and noise contribution from the SQUID (see fig. 1-right). The curve is fitted to data and upper limits are obtained from the χ^2 distribution. This way, a more precise estimation of errors from the fit allows to improve the upper limits. Final upper limits on moduli coupling to ordinary matter are reported in fig. 2. They are better then $d_i \simeq 10^{-5}$ in the sensitive band of AURIGA, $\triangle f = [850, 950]$ Hz, and explore for the first time ever an interesting physical region of the parameter space, within the natural parameter space for moduli [1].

References

[1] A. Arvanitaki, S. Dimopoulos, K. V. Tilburg, Sound of Dark Matter: Searching for Light Scalars with Resonant-Mass Detectors, Phys. Rev. Lett. **116**, 031102 (2016).

[2] M. Cerdonio, M. Bonaldi, D. Carlesso et al, The ultracryogenic gravitational-wave detector AURIGA, Class. Quantum Grav., 14 (1997) 1491;

[3] A. Vinante, Present performance and future upgrades of the AURIGA capacitive readout, Classical Quantum Gravity 23, S103 (2006).

[4] L. Krauss, J. Moody, F. Wilczek, D. E. Morris, Calculations for cosmic axion detection, Phys. Rev. Lett. 55, 1797 (1985).

[5] G. J. Feldman, R. D. Cousin, A Unied Approach to the Classical Statistical Analysis of Small Signals, Phys. Rev. D 57, 3873-38891 (1998).

[6] Proceeding of the Fifth Young Researchers Workshop "Physics Challenges in the LHC Era" 2016, Frascati Physics Series, Volume LXIII.

Latest Results with the KWISP force Sensor at CAST

G. Cantatore[1], on behalf of the CAST Collaboration

[1]University and INFN Trieste, Italy

The KWISP opto-mechanical force sensor has started searching for solar chameleons through their direct coupling to matter. Its sensing element, a 100 nm thick Si_3N_4 membrane, was mounted in the focal plane of the CAST X-ray telescope and several solar trackings were completed using the unique capabilities of the CAST magnet. KWISP is designed to detect, with interferometric techniques, extremely tiny membrane displacements due to the force exerted by chameleons reflecting off it, while a specially devised chameleon beam chopper provides the reference frequency necessary for detection. We will present the initial KWISP setup, discussing its status and results.

1 Introduction

The Cast Solar Axion Telescope has been probing the mysteries of the universe at CERN, in Geneva, since 2003. It has conducted several measurement campaigns searching for axions emitted by the sun, setting the current reference experimental limit on axion-photon coupling over a wide mass range[1]. The solar axion searches ended in 2015 and CAST has launched for 2016-2018 a new physics program, focused on Dark Matter (DM) and Dark Energy (DE) candidates. In particular, the program concentrates on searching for relic axions with several high-Q microwave resonant cavities inserted in the bores of the CAST magnet, and on detecting solar chameleons exploiting both their coupling to photons, and their direct coupling to matter[2]. In the latter search, CAST is pioneering the use of the novel KWISP opto-mechanical force sensor based on a thin and taut Si_3N_4 micro-membrane[3]. Under the influence of an external force, such as that resulting from the pressure exerted by a stream of solar chameleons reflecting, under certain conditions, off it [4], the membrane displaces from its initial equilibrium position in a manner that can be detected with optical interferometric techniques. KWISP also exploits two unique CAST capabilities: solar tracking and the presence of an X-ray telescope which can focus also chameleons, and provide and enhancement in expected flux of about a factor 100. We will briefly report below on the first ever solar tacking run conducted with an opto-mechanical force sensor searching for DE candidate particles, specifically for the direct coupling to matter of chameleons. The sensor was operated in an initial exploratory configuration to obtain a set of live data presently being analysed. A new, upgraded version of the KWISP sensor is now under commissioning at CAST in view of the data taking campaigns foreseen for the last part of 2016 and beyond.

2   The KWISP detector

KWISP is a novel type of particle detector exploiting the exquisite sensitivity to external forces of an opto-mechanical sensor to search for the direct interaction with matter of solar chameleons. Chameleons can be produced within the large magnetic fields present inside the sun, then stream unhindered to the earth. A flux of chameleons coming from the sun can interact directly with the sensing element of KWISP, a 100 nm thick, 5x5 mm^2 Si$_3$N$_4$ micro-membrane. This taut and thin pellicle flexes, much like a sail under a wind, following a force acting on it. Membrane displacements are then detected with interferometric techniques, and the force acting on the membrane can be deduced (see also [3]). More specifically, if the membrane is positioned to intercept the chameleon beam at a grazing incidence angle (5° or less), a sizeable fraction of the impinging particles will reflect off the membrane, thereby exerting on it the equivalent of a radiation pressure (see [4]). In the configuration reported here, the sensing element of the detector (the membrane) is placed at the end of one of the two arms of a Michelson-type interferometer, while the other arm contains a mirror mounted on a piezoelectric linear actuator. A 532 nm, 5 mW CW laser beam is input into the interferometer and interference fringes are then observed at its output by a photodiode: membrane movements will cause a detectable fringe displacement. The piezo-actuated mirror serves for calibration purposes. Figure 1 shows a photograph of the actual interferometer with the laser beam path superimposed. The membrane can be seen at the center (also in the inset at upper right), while the piezo-actuated mirror is visible at center right.
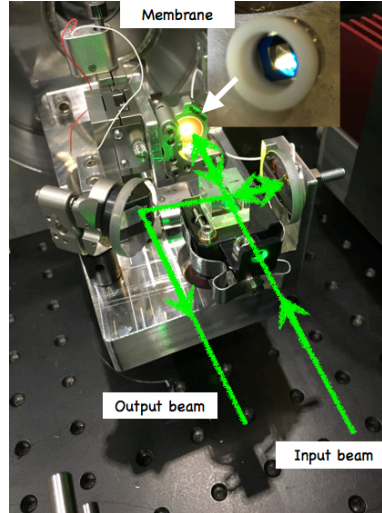
Figure 1: KWISP Michelson-type interferometer setup with the sensing membrane (see also text).

This compact interferometer (about 15 cm by 25 cm) is placed inside a vacuum chamber, mounted on the sunrise side of the CAST magnet and aligned to place the membrane as close as possible to the focal plane of the X-ray telescope available at CAST. This instrument is able to focus chameleons much in the same way as it focuses X-rays, thanks to its cascade of grazing-incidence plates (see [5]). The focusing action increases the expected solar chameleon

flux by a factor ≈ 100. Based on the same principle, the membrane is also tilted with respect to the incoming chameleon beam to provide a 5° grazing incidence angle for maximum chameleon reflectivity. The membrane must be under vacuum in order to ensure that it is not perturbed by the brownian motion of air. In our case, the residual pressure in the chamber was $< 10^{-5}$ mbar. Figure 2 shows the position of the KWISP vacuum chamber on the sunrise side of the CAST magnet, behind the X-ray telescope. The last key element of the setup, not visible in the image of Figure 2, is the chameleon chopper, placed in air at the exit of the X-ray telescope, before the sensing membrane. Its function is to provide an amplitude modulation of the chameleon beam in order to make it, in principle, detectable, as the instrument is not sensitive to static displacements, but rather to time-dependent ones. This modulation is imparted at a chosen frequency, which provides both a reference for data analysis, and a trigger for data acquisition. The chameleon chopper is discussed in better detail in [6].
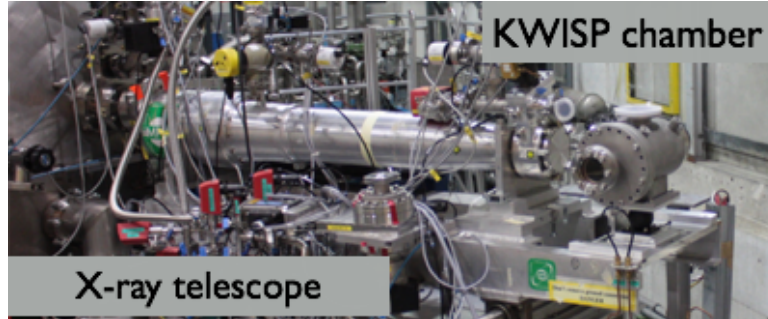
Figure 2: Placement of the KWISP chamber on the sunrise side of the CAST magnet. The chamber is aligned to position the membrane inside it in the focal plane of the X-ray telescope (see also text).

3 Preliminary results from solar tracking runs

The first ever series of measurement runs with a force sensor looking for solar chameleons was conducted at CAST, in April 2016, with the KWISP detector in the preliminary configuration briefly described above. During this campaign, the sun was observed every morning at sunrise for about 1.5 hours, over a period of one week between April 21st and April 28th, 2016. This was possible thanks to the unique sun-tracking capability of the CAST magnet assembly. The current output by the photodiode monitoring the interferometer fringes was amplified, converted to a voltage, digitised and acquired in 100 s long time records. The trigger for data acquisition was provided by the chameleon chopper, allowing for in-phase concatenation of the individual time records. Both the interferometer output and the trigger signal were acquired. At the beginning of each time record a calibration signal was briefly injected into the piezo actuated mirror in order to obtain the instantaneous sensitivity of the instrument. An example of such calibration procedure is shown in Figure 3. Here the photodiode signal (yellow trace) jumps from the dark fringe to the light fringe, corresponding to a fringe shift of $\lambda/2 = 532/2$ nm, when a voltage difference of 1.23 V is applied to the piezo-actuated mirror. This gives a transduction characteristic C = 216 nm/V.
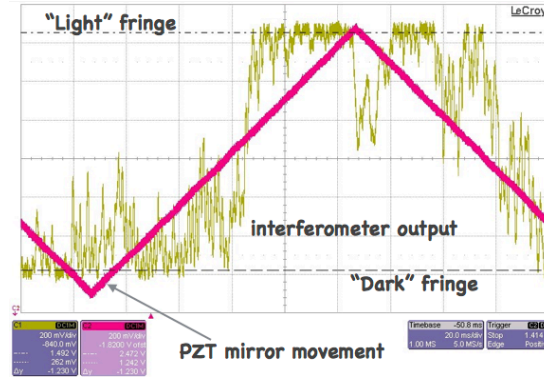
Figure 3: Sample oscilloscope screenshot illustrating interferometer calibration. The yellow trace is the photodiode signal, while the red trace is the voltage ramp applied to the piezo-actuated mirror (see also text).

Data were taken continuously both while tracking the sun, and with the magnet stationary, to provide background levels. In 7 days of running, 9000 s of sun-tracking data (90 time records) and 121400 s of background data (1214 time records) were accumulated. A chameleon signature should appear as a peak at the chopper frequency in the spectrum of the interferometer output photodiode signal. A full data analysis is still in progress, however Figure 4 shows a preliminary example of the type of result that can be expected.
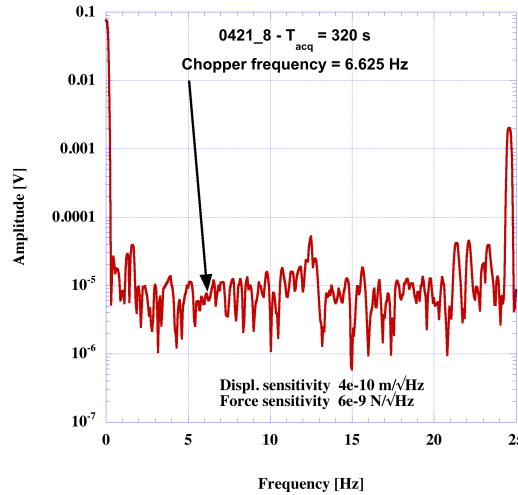
Figure 4: Preliminary sample sun tracking spectrum (see text).

In the case of Figure 4 the chopper frequency was 6.625 Hz, and an arrow indicates the position in the spectrum where a positive chamelon signal should appear. Here the force sensitivity was $6 \cdot 10^{-9}$ N/$\sqrt{\text{Hz}}$.

4 Conclusions

The first ever search for the direct interaction with matter of solar chameleons, with a force sensor, was conducted at CAST in April 2016. The opto-mechanical KWISP sensor, in a preliminary Michelson-type configuration, was placed in the focal plane of the X-ray telescope mounted on the sunrise side of the CAST magnet and used for a week long data taking campaign. The sensor took data stably with a force sensitivity of the order of 10^{-9} N/$\sqrt{\text{Hz}}$. A chameleon chopper, originally invented, was used to provide the necessary reference frequency. Thanks to the dependence of the energy of the reflected chameleon on the chopper angular position, in case of a positive signature there is also the possibility of particle identification. A full data analysis is in progress. Presently, the KWISP sensor is being upgraded to a Fabry-Perot interferometer configuration, where the sensitivity will be amplified proportionally to the Fabry-Perot finesse. With a nominal finesse of $\approx$60000, we project an initial sensitivity of the order of $6 \cdot 10^{-13}$ N/$\sqrt{\text{Hz}}$, or better, at room temperature.

References

[1] M. Arik *et al.* [CAST Collaboration], "New solar axion search in CAST with ^{4}He filling", Phys. Rev. D **92**, 021101 (2015). doi:10.1103/PhysRevD.92.021101

[2] V. Anastassopoulos *et al.*, "Search for chameleons with CAST", Phys. Lett. B **749**, 172-180 (2015). doi:10.1016/j.physletb.2015.07.049

[3] M. Karuza *et al.*, "KWISP: An ultra-sensitive force sensor for the Dark Energy sector", Physics of the Dark Universe **12**, 100-104 (2016). doi:10.1016/j.dark.2016.02.004

[4] S. Baum *et al.*, "Detecting solar chameleons through radiation pressure", Phys. Lett. B **739**, 167-173 (2014). doi:10.1016/j.physletb.2014.10.055

[5] O. K. Baker *et al.*, "Detection of radiation pressure from solar chameleons", (2012) [arXiv:1201.0079 [astro-ph]].

[6] G. Cantatore *et al.*, "Recent Progress with the KWISP Force Sensor", (2015) [arXiv:1510.06312 [physics.ins-det]], Proceedings of the 11th "Patras " Workshop on Axions, WIMPs and WISPs (Patras2015).

Dilatonic Dark Matter: Experimental Detection of Dilaton and Extra Dimension

Young Min Cho

Konkuk University,
Seoul 143-701, Republic of Korea

The Kaluza-Klein dilaton in higher-dimensional unified theory has important implications. First, as the gravitationally interacting massive particle (GIMP) it becomes an ideal candidate of the dark matter of the universe. Second, as the massive scalar graviton (MSG) it generates the fifth force which modifies the Einstein's gravity. Most importantly, it represents the extra space itself, so that detecting the dilaton we can confirm the existence of the extra space. We present a simple way to detect the dilaton experimentally, detecting the two photon decay of the remnant dilaton. We show how the fifth force constraint and the dark matter constraint restrict the dilaton mass and the size of the extra space. Moreover, based on the fact that the dilaton mass comes from the curvature of the extra space, we propose the geometric mass generation mechanism that the curvature creates the mass as an alternative to the Higgs mechanism.

All existing unified theories are based on the higher-dimensional space-time, which makes the experimental confirmation of the extra space an important issue. In this talk we discuss the physical consequence of the higher-dimensional unification, and present a simple way to detect the extra space experimentally.

An unavoidable consequence of higher-dimensional unification is the appearance of gravitationally interacting massive particles (GIMPs) or massive scalar gravitons (MSGs) known as the Kaluza-Klein (KK) dilaton and internal gravitons, in 4-dimensional physics [1, 2]. They come in as the gravitons of the extra space, so that they actually represent the very extra space itself. This means that by detecting them we could confirm the existence of the extra space and justify the higher-dimensional unification.

The dilaton plays very important roles in physics. First, as the GIMP it becomes an ideal candidate of the dark matter. Second, as the MSG it generates the fifth force which could violate the equivalence principle. Third, it realizes the Dirac's large number hypothesis making the cosmological constant space-time dependent. Moreover, it could play the role of the quintessence in cosmology [4, 3]. Finally, it appears in all higher-dimensional unified theories, which strongly implies that the dilaton must exist. This makes the experimental detection of the dilaton very important.

Unfortunately the dilaton (and the internal gravitons) so far have not been received the due attention, because the extra space has traditionally been assumed to be extremely small (of the Planck scale) [1, 5, 6]. A small extra space could make them very heavy and decay quickly, in which case they leave almost no trace in the present universe. And they cannot easily be produced because it will cost too much energy. In this case they become almost irrelevant.

But this is not entirely true. First, even a small extra space can make the dilaton massless [1, 2]. Moreover, there is the possibility that the extra space may not be so small, which could make the dilaton very light [2]. Indeed this is exactly the proposal made by Arkani-Hamed, Dimopoulos, and Dvali (ADD) to resolve the hierarchy problem [7].

The mass of the dilaton is very important for the following reasons. First, it determines the range of the fifth force [8, 9]. Moreover, it determines the energy density of the dark matter [4, 10]. And obviously we have to know the mass to detect the dilaton. So it is crucial for us to understand how the dilaton acquires the mass and to figure out what is the mass range.

We show that the cosmological constraint on the dark matter rules out the dilaton mass between 160 MeV and 276 MeV, and argue that the size of the extra space may not be smaller than 10^{-9} m. Moreover, we suggest to detect the dilaton detecting the two photon decay of the remnant dilatons in the universe. Finally, from the fact that the curvature of the extra space makes the dilaton massive, we propose a geometric mass generation mechanism that mass can be generated by curvatureas an alternative to the Higgs mechanism.

To demonstrate these points, we consider the Kaluza-Klein theory, the protopype of all higher-dimensional unified theories. To obtain the 4-dimensional physics, we have to make the dimensional reduction. There are two contending dimensional reduction schemes, the popular zero mode approximation and the dimensional reduction by isometry. In the zero mode approximation one treats the (4+n)-dimensional space as real and views the 4-dimensional physics as a low energy approximation [5, 6]. In the dimensional reduction by isometry, however, the isometry in the unified space makes the extra space invisible and determines the 4-dimensional physics [1, 11].

A sensitive issue in the zero mode approximation is how one can actually make the approximation. A simple way to do this is to impose a proper isometry as an approximate symmetry. In this case the zero mode approximation becomes very much like the dimensional reduction by isometry. In general, however, the two methods have totally different 4-dimensional physics. This is because the zero mode approximation produces an infinite tower of the KK excited modes in 4-dimension.

To show how the dimensional reduction by isometry works, we suppose that the (4+n)-dimensional unified space has an n-dimensional isometry G and assume the unified space to be a principal fiber bundle P(M,G) made of the 4-dimensional space-time M and the n-dimensional group manifold G. Let $\gamma_{\mu\nu}$ and ϕ_{ab} be the metrics on M and G. In this setting the (4+n)-dimensional Einstein-Hilbert action becomes [1, 2]

$$I_{EH} = -\frac{1}{16\pi G_0} \int \sqrt{\gamma}\sqrt{\phi} \Big[R_M(\gamma_{\mu\nu})$$
$$-\frac{n-1}{4n}\gamma^{\mu\nu}\frac{(\partial_\mu\phi)(\partial_\nu\phi)}{\phi^2} + \frac{e^2\kappa^2}{4}\sqrt[n]{\phi}\,\rho_{ab}\gamma^{\mu\alpha}\gamma^{\nu\beta}F^a_{\mu\nu}F^b_{\alpha\beta}$$
$$+\frac{\gamma^{\mu\nu}}{4}(D_\mu\rho^{ab})(D_\nu\rho_{ab}) + \frac{1}{\kappa^2\sqrt[n]{\phi}}\,\hat{R}_G(\rho_{ab})$$
$$+\Lambda_P + \lambda(|\det\rho_{ab}|-1)\Big]d^4x\,d^n\theta,$$
$$\gamma = |\det\gamma_{\mu\nu}|, \quad \phi = |\det\phi_{ab}|,$$
$$\rho_{ab} = \phi^{-1/n}\phi_{ab}, \quad (|\det\rho_{ab}|=1),$$
$$\hat{R}_G(\rho_{ab}) = \frac{1}{2}f_{ab}{}^d f_{cd}{}^b\rho^{ac} + \frac{1}{4}f_{ab}{}^m f_{cd}{}^n\rho^{ac}\rho^{bd}\rho_{mn}. \tag{1}$$

Here G_0 is the $(4 + n)$-dimensional gravitational constant, R_M is the scalar curvature of M, e is the coupling constant of the KK gauge field $F_{\mu\nu}^a$, κ is the scale of the extra space, Λ_0 is the (4+n)-dimensional cosmological constant, and λ is a Lagrange multiplier. Notice that $\hat{R}_G(\rho_{ab})$ is the normalized curvature of the fiber space G.

To proceed, we introduce the Pauli metric (also called the Einstein metric in string theory) $g_{\mu\nu}$ and the Kaluza-Klein dilaton σ by [1, 4]

$$g_{\mu\nu} = \sqrt{\phi}\, \gamma_{\mu\nu}, \quad \phi = \langle\phi\rangle \exp\left(2\sqrt{\frac{n}{n+2}}\, \sigma\right). \tag{2}$$

But, since κ is left arbitrary, we can always normalize

$$\langle\phi\rangle = 1, \tag{3}$$

without loss of generality. With this understanding we have the following Lagrangian in the Pauli frame [1, 4]

$$\begin{aligned}
\mathcal{L} = -\frac{\hat{V}_G}{16\pi G_0}\sqrt{g}\Big[R + \tfrac{1}{2}(\partial_\mu\sigma)^2 + \frac{1}{4}(D_\mu\rho^{ab})(D^\mu\rho_{ab}) \\
+ \frac{\hat{R}_G}{\kappa^2}\exp\left(-\sqrt{\frac{n+2}{n}}\,\sigma\right) + \Lambda_P \exp\left(-\sqrt{\frac{n}{n+2}}\,\sigma\right) \\
+ \frac{e^2\kappa^2}{4}\,\exp\left(\sqrt{\frac{n+2}{n}}\,\sigma\right)\rho_{ab}F_{\mu\nu}^a F^{b\mu\nu}\Big], \\
\hat{V}_G = \int d^n\theta = \kappa^n. \quad (\langle\phi\rangle = 1)
\end{aligned} \tag{4}$$

This describes the well-known unification of gravitation with the gauge field, *provided that* [1, 2]

$$\frac{\kappa^n}{16\pi G_0} = \frac{1}{16\pi G}, \qquad \frac{e^2\kappa^2}{16\pi G} = 1, \tag{5}$$

where G is Newton's constant.

To understand the meaning of (5), notice that by the first equality κ sets the strength of the higher-dimensional gravity l_0,

$$l_0 = G_0^{\,1/(n+2)} = \left(\frac{\kappa}{l_p}\right)^{n/2(n+2)} l_p, \tag{6}$$

where $l_p = \sqrt{G}$ is the Planck scale. This is precisely what one has in the ADD proposal, which confirms that a large extra space can indeed make the higher-dimensional gravity strong [8, 7]. However, from the second equality κ is determined by the fine structure constant of the KK gauge boson α_{KK} [1, 2],

$$\kappa^2 = \frac{4}{\alpha_{KK}}\, l_p^2. \qquad \left(\alpha_{KK} = \frac{e^2}{4\pi}\right). \tag{7}$$

This means that a large extra space makes α_{KK} extremely small. In fact this tells that, for the ADD proposal which favors $\kappa \simeq 10^{-5}\ nm$, we need $\alpha_{KK} \simeq 10^{-42}$ for $n = 6$. (For $n = \infty$ we have $\alpha_{KK} \simeq 4 \times 10^{-32}$, which sets the upper limit of α_{KK}.)

To find the mass of the KK dilaton, we assume that (4) has the unique vacuum $\langle g_{\mu\nu} \rangle = \eta_{\mu\nu}$, $\langle \sigma \rangle = 0$, $\langle \rho_{ab} \rangle = \delta_{ab}$, $\langle A_\mu{}^a \rangle = 0$, and find the dilaton potential

$$V(\sigma) = \frac{1}{16\pi G}\Big[\frac{\langle \hat{R}_G \rangle}{\kappa^2} \, \exp(-\sqrt{\frac{n+2}{n}}\, \sigma)$$
$$+\Lambda_0 \, \exp(-\sqrt{\frac{n}{n+2}}\, \sigma)\Big] + V_0, \tag{8}$$

where $\langle \hat{R}_G \rangle = \hat{R}_G(\delta_{ab})$ is the (dimensionless) vacuum curvature of the extra space and V_0 is a constant introduced to assure that (8) has no non-vanishing 4-dimensional vacuum energy. Notice that Λ_0 and V_0 are completely fixed by the vacuum condition $dV(0)/d\sigma = 0$ and $V(0) = 0$. From (8) we find the mass of the KK dilaton μ (identifying $\hat{\sigma} = \sigma/\sqrt{16\pi G}$ as the physical dilaton),

$$\mu^2 = \frac{2\langle \hat{R}_G \rangle}{n}\frac{1}{\kappa^2} = \frac{\langle \hat{R}_G \rangle}{2n} \, \alpha_{KK} \, m_p^2, \tag{9}$$

where m_p is the Planck mass. This demonstrates that a large κ (or a small α_{KK}) transforms the Planck mass to a small dilaton mass, which can easily be of the order of the elementary particle mass scale. But notice that here the curvature of the extra space plays the crucial role in making the dilaton massive. In fact when $\langle \hat{R}_G \rangle = 0$ the dilaton becomes massless, independent of κ. Essentially the same conclusion applies to the mass of internal gravitons ρ_{ab}.

The above result shows that we can estimate the size of the extra space from the dilaton mass. There are two important constraints on the dilaton mass, the fifth force constraint and the cosmological constraint. Fifth force experiments can measure the range of the fifth force [9, 4]. Indeed a recent torsion-balance fifth force experiment puts the upper bound of the range to be around 44 μm with 95% confidence level [12]. This implies that the dilaton mass cannot be lighter than 4.5×10^{-3} eV.

Cosmology puts another strong constraint on the dilaton mass, because the dilaton can easily be the dominant matter of the universe. In cosmology one may assume that the dilaton (as a GIMP) starts out at thermal equilibrium, and decouples from other sources very early on. But it is not stable, because it couples to all matter fields. There are two dominant decay processes: two-photon decay and fermion-antifermion decay, which may be approximated by the following Lagrangian [10],

$$\mathcal{L}_{int} \simeq -\sqrt{16\pi G}\Big[\frac{g_1}{4} \, \hat{\sigma} F_{\mu\nu}^2 + g_2 \, m\hat{\sigma}\bar{\psi}\psi \Big], \tag{10}$$

where g_1 and g_2 are dimensionless coupling constants, and m is the mass of the fermion. From this we can estimate the dilaton decay rates [10, 13]

$$\Gamma_{\sigma \to \gamma\gamma} = \frac{g_1^2 \mu^3}{16 \, m_p^2},$$
$$\Gamma_{\sigma \to \bar{\psi}\psi} = \frac{2g_2^2 \, m^2 \, \mu}{m_p^2} \times \Big[1 - \big(\frac{2m}{\mu}\big)^2 \Big]^{3/2}. \tag{11}$$

With this we can estimate the present number density and mass density of the relic dilaton.

Now, for the dilaton to be the dark matter, we must have the following constraints on the dilaton mass. First, the dilaton mass density must be equal to the dark matter density. Second,
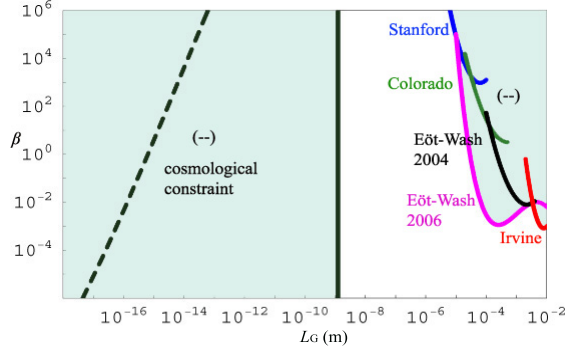
Figure 1: The allowed range of the extra space versus $\beta = \alpha_5/\alpha_g$, where α_g and α_5 are the gravitational and fifth force fine structure constants. The colored region marked by $(-)$ is the excluded region, and the dotted line represents the constraint from the heavy dilaton whose daughter particles overclose the universe.

the energy density of the daughter particles (photons and light fermions) of the dilaton must be negligibly small compared to the dark matter density.

Assuming $g_1 \simeq g_2 \simeq 1$, we find that there are two mass ranges of dilaton in which the relic dilaton could be the dominant matter of the universe; $\mu \simeq 160$ eV with life-time 3.8×10^{35} sec and $\mu \simeq 276$ MeV with life-time 3.3×10^{16} sec [10, 14]. A dilaton lighter than 160 eV survives but fails to be the dominant matter due to its low mass, and a dilaton heavier than 276 MeV does not survive long enough to become the dominant matter of the universe. More importantly we find that, even if the dilaton is not the dark matter, a mass in between these values is unacceptable because it would overclose the universe. Moreover, the second constraint shows that a 276 MeV dilaton is not acceptable as dark matter, because the energy density of the daughter particles must be much bigger than the energy density of dark matter, and thus overclose the universe. This makes the heavy dilaton unacceptable. This means that only the 160 eV dilaton can be a candidate for the dark matter of the universe [10, 14].

We can easily translate these constraints on the dilaton mass to constraints on κ. Putting these constraints together we obtain Fig. 1, which shows the allowed region of the extra space (and the allowed range of the fifth force) in 7-dimensional unification with S^3 compactification of the extra space. Although $\beta = \alpha_5/\alpha_g$ is expected to be of the order one, we leave it arbitrary here.

It has to be emphasized that our estimate of dilaton mass is an order-of-magnitude estimate only, because it is based on crude approximations which also neglect other possible dark matter candidates (for example, the internal gravitons). Nevertheless our result tells that cosmology provides a crucial piece of information on the dilaton mass. In particular, cosmology rules out the 10^{-14} m scale extra space suggested by ADD. Moreover, it implies that the dilatonic fifth force may be too short-range to be detected by the existing fifth force experiments.

A best way to detect such dilaton is to confirm the two photon decay of the remnant dilaton in the universe. Since the above analysis suggests that the dilaton is very light, it could decay mostly to two photons (with a small fraction to three neutrino pairs) which have the unique energy fixed by the dilaton mass. So we can detect the dilaton detecting the two photon decay.

To do that we could think of a dilaton-photon conversion experiment similar to the axion detection experiment. Let $V = L_x L_y L_z$ be the volume of a rectangular resonant cavity and $\vec{B}_{ext} = B_0 \cos(qx)\hat{z}$ be the external magnetic background of the cavity. In this case we can estimate the photon detection power [10, 14]

$$P_d = \Big(\frac{4g_1^2}{\pi m_p^2}\Big)\rho_d B_0^2 L_x V. \tag{12}$$

Notice that the detection power can be enhanced by the strong magnetic background and by the large dilaton density ρ_d in our galaxy (assuming that the gravitational attraction concentrates the dilatons in our galaxy).

This can be compared with the similar axion detection power

$$P_a = 2\Big(\frac{g_\gamma \alpha}{4\pi f_a}\Big)^2 \rho_a B_0^2 L_x V, \tag{13}$$

where g_γ is the axion-photon coupling constant, α is the fine structure constant, and $f_a(\simeq 6 \times 10^{12}$ GeV$)$ is the PQ symmetry breaking scale. From this we have

$$\frac{P_d}{P_a} \simeq 1.9 \times 10^6 \left(\frac{g_1}{g_\gamma}\right)^2 \left(\frac{f_a}{m_p}\right)^2 \simeq 4.7 \times 10^{-7}, \tag{14}$$

when $g_1 \simeq g_\gamma$. If $g_1 >> g_\gamma$, however, P_d can be as big as P_a. Notice that the axion mass is $m_a \simeq 10^{-6}$ eV.

The reason why the dilaton and axion are similar is that both are very weakly interacting light particles which could decay to two photons. But there are differences. First, the weak coupling of dilaton is because it is a GIMP. But the weak axion coupling is due to the small f_a. Second, the dilaton is a scalar, but the axion is a pseudo-scalar. So, the dilaton produces the TE mode (magnetic wave) but the axion produces the TM mode (electric wave). Moreover, for the dilaton the photon polarization is perpendicular, but for the axion the polarization is parallel, to the external magnetic field.

Of course, there are other experiments which could detect the remnant dilaton. For example, the IceCube, Auger, and ANTARES could in principle detect the two photon decay of the dilaton. Moreover, the all-purpose James-Webb telescope could also detect the abnormal two photon cosmic background radiation coming from the dilaton decay.

So far we have concentrated on Kaluza-Klein theory with the dimensinal reduction by isometry, but the generic features our result hold in superstring and supergravity. In string theory, for example, one has the string dilaton which remains massless in all orders of perturbation theory [6]. But it must have the KK dilaton coming from the extra space, and our constraint on the size of the extra space should remain valid.

Moreover, in the zero-mode approximation we must have the KK excited modes which could have similar decay. So, in principle we should be able to check the existence of the excited modes experimentally. If the experiments can't find them, we must discard the zero-mode approximation.

Independent of the details, we emphasize the physical importance of the dilaton. It appears in all higher-dimensional unified theories, so that the it must exist if we believe in the higher-dimensional unification. Moreover, it represents the extra space itself, and we can confirm the existence of the extra space detecting the dilaton. As importantly, it suggests that the mass

could originate from the curvature of space. This allows us to propose the geometric mass generation mechanism which could replace the Higgs mechanism and resolve the hierarchy problem.

This is why the experimental detection of the dilaton is so important, independent of whether it becomes the dark matter or not. A detailed discussion of our r esults and related subjects will be presented separately [15].

References

[1] Y.M. Cho, J. Math. Phys. **16**, 2029 (1975); Y.M. Cho and P.G.O. Freund, Phys. Rev. **D12**, 1711 (1975).

[2] Y.M. Cho, Phys. Rev. **D35**, 2628 (1987); Phys. Lett. **B199**, 358 (1987).

[3] P.A.M. Dirac, Nature (London) **136**, 323 (1937).

[4] Y.M. Cho, Phys. Rev. Lett. **68**, 3133 (1992).

[5] See e.g., M. Duff, B. Nielson, and C. Pope, Phys. Rep. **130**, 1 (1986).

[6] See also M. Green, J. Schwartz, and E. Witten, *Superstring theory*, Vol. 2 (Cambridge University Press) 1987.

[7] N. Arkani-Hamed, S. Dimopoulos, and G. Dvali, Phys. Lett. **B429**, 263 (1998); N. Arkani-Hamed, I. Antoniadis, S. Dimopoulos, and G. Dvali, Phys. Lett. **B436**, 257 (1998).

[8] Y.M. Cho, Phys. Rev. **D41**, 2462 (1990); Y.M. Cho and J.H. Yoon, Phys. Rev. **D47**, 3465 (1993).

[9] Y.M. Cho and D.H. Park, Gen. Rel. Grav. **23**, 741 (1991).

[10] Y.M. Cho and Y.Y. Keum, Class. Quant. Grav. **15**, 907 (1998).

[11] See also R. Penrose, *The Road to Reality : A Complete Guide to The Laws of The Universe* (A.A. Knopf) 2005.

[12] D. Kapner et al., Phys. Rev. Lett. **98**, 021101 (2007); E. Adelberger et al., Phys. Rev. Lett. **98**, 131104 (2007).

[13] E. Kolb, G. Servant, and T. Tait, J. Cos. Astro. Phys. **07**, 008 (2003).

[14] Y.M. Cho and J.H. Kim, Phys. Rev. **D79**, 023504 (2009).

[15] Y.M. Cho, Kyoungtae Kimm, S.H. Oh, and J.H. Yoon, to be published.

Launching Axion Experiment at CAPP/IBS in Korea

Woohyun Chung[1],

[1]Center for Axion and Precision Physics Research, IBS, Korea

The main research focus of the Center for Axion and Precision Physics Research (CAPP) at IBS is to establish a state-of-the-art axion experiment in Korea and to search for relic axion particles converting to microwave photons in a resonant cavity submerged in a strong magnetic field. The initial stage of building our axion experiment, CULTASK (CAPP Ultra Low Temperature Axion Search in Korea) is completed at KAIST (Korea Advanced Institute for Science and Technology) Munji Campus with successful installation of two new dilution refrigerators (one with 8T superconducting magnet) which could lower the temperature of cavities to less than 50 mK. A resonant cavity (10 cm OD) and the support structure were fabricated and installed with the frequency tuning system employing a sapphire rod driven by a piezoelectric actuator. The RF measurements were also performed for evaluating and improving noise figures using cryogenic HEMT amplifiers. I will discuss the status and progress of CULTASK, soon to be complete with a DAQ and monitoring system, and future plans. I will also present the recent results from the development of high Q-factor, ultra pure Cu and Al cavities under high magnetic fields, utilizing the two refrigerators.

1 R&D Projects for Axion research at CAPP
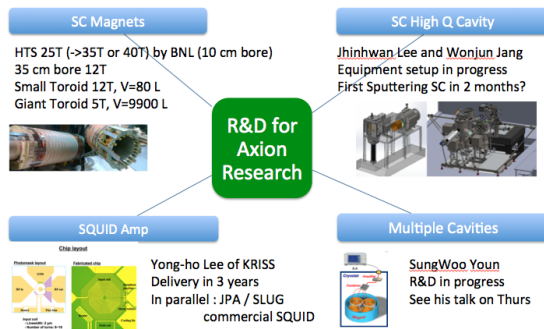
Figure 1: CAPP's R&D projects for axion search

The Center for Axion and Precision Physics Research (CAPP) of the Institute for Basic Science (IBS) is launching a state-of-the-art dark matter axion experiment in Korea. The design of the axion experiment at CAPP is based on P. Sikivie's haloscope scheme[1]. Axions resonantly convert to microwave photons by a reverse Primakoff interaction inside a tunable cavity permeated by a strong magnetic field. The feeble signal from the cavity is amplified through a SQUID amplifier and transmitted to a room temperature RF receiver unit to be processed further.

CAPP is driving a research and development plan to achieve the sensitivity required for the entire range of axion models. The

R&D plan includes high field superconducting magnets with various bore sizes (5, 10 and 35 cm inner diameter), high Q-factor superconducting cavities, high-gain gigahertz superconducting quantum interference device (SQUID) amplifiers and multi-cavity phase locking scheme for higher axion mass (Figure 1).

A powerful 25 T superconducting magnet will be developed and delivered by BNL (Brookhaven National Laboratory) in 2 to 3 years. The ultra high field magnet being developed by BNL has exceptionally big 10 cm bore and is based on a next generation technology called HTS (High Temperature Superconductor). The compact (outer diameter of only 30 cm) design of the magnet is intended to produce even higher field of 35T or 40T by adding another layer of LTS magnet outside in the future. If successful, this magnet will be the highest-field superconducting magnet in the world with HTS technology.

Prof. Jhinhwan Lee of KAIST (Korea Advanced Institute of Science and Technology) is leading the effort of coating superconductors inside resonant cavities. Various configurations and different coating materials are being experimented now to overcome the effect of high magnetic field ($>8T$) that goes through the cavity and to achieve the high Q-factor ($> 10^6$) for the resonant mode of choice (TM_{010}). The first sample of dc SQUID amplifiers (center frequency of 2.5 GHz) developed by Dr. Yong-Ho Lee of KRISS (Korea Research Institute of Standards and Science) will be delivered and tested this year. The physical temperature of the cavity should be maintained extremely low in order to reduce the noise from the black body radiation, and eventually to improve the signal-to-noise ratio and speed up the experiment. The RF receiver unit to amplify and process the radio frequency signal from the resonant cavity is being tested in engineering runs right now.

2 CAPP Ultra Low Temperature Axion Search in Korea (CULTASK)

	BF3	BF4
Model	BlueFors LD400	BlueFors LD400
Magnet	None	8T (AMI), 12cm ID
RF lines	24	8
DC lines	72	72
Cool down to <10 mK	20 ~ 24 hours	40 ~ 48 hours
Base temp at MXC	9 mK	7 mK w/ SC magnet
MXC temp w/ Load	11 mk w/ Al cavity (4cm id) and HEMT amp	30 mk w/ 10 kg OFHC copper support structure and cavity + HEMT amp + Network Analyzer + Piezo Controller

Figure 2: Properties of BlueFors LD400 Dilution Refrigerators at KAIST Munji campus

Figure 3: BlueFors LD400 dilution refrigerator with cavity and frequency tuning system installed

Two dilution refrigerators (BlueFors LD400) were delivered, installed and tested in March this year at CAPP's new laboratory located at KAIST Munji campus. One refrigerator(BF3) is designed for testing RF components (directional couplers, cryogenic circulators, resonant cavities and HEMT or SQUID amplifiers) and the other(BF4) refrigerator equipped with 8T superconducting magnet (12 cm inner bore) is for setting up a small scale axion engineering run. Figure 2 shows the characteristics of two new BlueFors dilution refrigerators. These refrigerators are designed to cool down and warm up relatively quick (20 ∼ 24 hours or 40 ∼ 48 hours when there is a 50 kg magnet attached) and fully automatic with a script so that it could cool down all the way with a touch of a button.

We have designed a pure copper resonant cavity with 9 cm inner diameter (2.5 GHz for TM_{010} mode) and a support structure with frequency tuning system (Figure 3). The physical temperature of the mixing plate which is thermally linked to the cavity and the support structure is around 30 mK now (7mK without cavity) with antenna probe and frequency tuning rod connected to piezoelectric actuators. Sapphire (dielectric) tuning rod is designed to be thermally linked to 100 mK plate. The piezoelectric actuators are used to control frequency tuning rod (rotator) and probing antenna (linear) inside the refrigerator.

2.1 High Q-factor cavity development

Variety of sample cavities (OFHC Cu, 5N Al and 6N Al) were prepared to test the enhancement of Q-factor in a cryogenic temperature. The technique of annealing is crucial for improving a Q-factor and we are at the stage of calibrating annealing furnace for now. The other important factor that has an impact on Q-factor is surface roughness. The high precision diamond-cutting technology is employed and the surface tolerance is less than 50 nm.

2.1.1 Superconducting Al cavity

Al cavity becomes superconducting around 1.2K, which may not be very helpful for axion experiment with powerful magnetic field, because the critical field for Al is around 10 mT. However, it could provide us insights on how to design the cavity when superconducting coating is available. Al cavity of conventional design (cylinder with two lids) gets superconducting and Q-factor rises around 200,000 (TM_{010} mode) when the temperature is about 800 mK. Poor contact between lids and cylinder wall is suspected for not completely superconducting. The examination of TE_{011} mode (no electric field along z direction) shows 2 to 20 million Q-factor

(depending on the temperature). It is clear that the contact problem could be a limiting factor even when we have a superconducting cavity. One important lesson we learn from the simulation of cavity is that the Q-factor of TM_{010} doesn't change when a perfect cavity is sliced vertically, even when split pieces were separated a little. We fabricated Al split cavity by machining two equal whole half pieces (by digging out half cylinder), effectively eliminating a contact problem, and the Q-factor goes up to over 2 million. It is also much easier to coat two half pieces (or many pieces) of cavity and we don't have to worry about the contact problem any more. We are actually applying this technique when coating superconductors to inner surface of cavities now.

2.2 Engineering Run in 2016

We are setting up a small scale, mid-to-low sensitivity axion experiment with BF4 as a starter. This detector includes 8T superconducting magnet, 9 cm inner diameter OFHC Cu cavity, cryogenic RF chain (antenna probe, directional coupler, cryogenic circulators and amplifiers), and a system of room temperature RF receiver. In addition, there should be a DAQ system (CULDAQ) that controls, monitors the whole detector, and collects and stores data for analysis. The frequency tuning system with a sapphire tuning rod controlled by piezoelectric actuator is going through a precision test now and could be added later when we are confident.
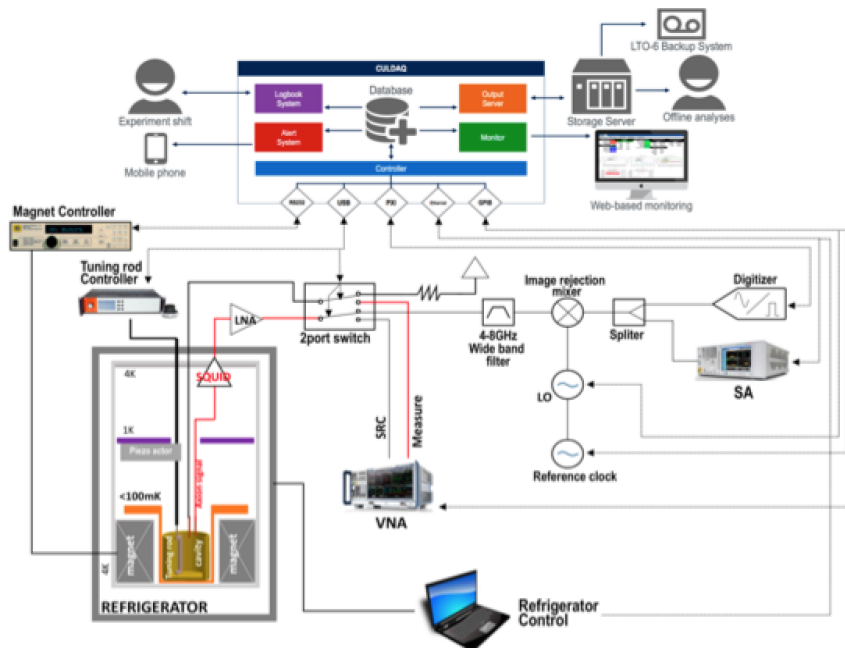
Figure 4: CULTASK DAQ system: CULDAQ

Figure 4 shows a complete axion detector set-up. We won't be able to reach KSVZ[2][3] sensitivity without SQUID amplifiers and superconducting cavity that should be available in a couple of years. However, this engineering run could provide us a great opportunity to prepare ourselves for evaluating and maximizing performance of other RF electronics components.

Cryogenic circulators (isolators) and amplifiers (HEMT) have been received, tested at KRISS by Dr. Yonuk Chong and will be verified at our BF3 refrigerator. The design and fabrication of room temperature RF receiver electronics setup is complete with mixers, filters and a spectrum analyzer. The digitization of signal and the recording of the data has been tested already. The data acquisition system (CULDAQ) that also controls and monitors switches, network analyzer, piezo controller, spectrum analyzer will be ready by September.

3   Plans beyond 2016

The construction of 7 low vibration pads at the axion experimental site in KAIST Munji campus will be compete by the end of September and 4 more dilution refrigerators are to be installed early next year. Two 8T NbTi superconducting magnets (12 cm and 16 cm inner bore) will be used with two BlueFors dilution refrigerators and 18T 5cm bore HTS magnet is scheduled to be delivered in 2017. More superconducting magnets with much bigger bore sizes (35 cm and 50 cm) are also planned in the pipeline. Powerful magnets with different bore sizes along with the efforts on multi-cavity phase locking study would help us to search axions throughout the whole possible mass range. The improvements on booting axion conversion power by developing superconducting high-Q factor cavity and employing quantum limited SQUID amplifiers will pave a way to reach KSVZ QCD axion sensitivity region and beyond.

4   Conclusion

The preparation for the engineering run of CULTASK is complete at this stage and ready to go forward and collect physics data at least for a single frequency this year. The experimental space of 7 low vibration pads at KAIST Munji campus will be ready in a couple of months and more refrigerators are scheduled to be installed early next year (2017). The addition of SQUID amplifiers, ultra high field magnets and high Q-factor cavities with superconducting coating will improve the sensitivity and make a major contribution to axion research in coming years.

5   Acknowledgments

References

[1] P. Sikivie, Phys. Rev. Lett. 41 (1983) 1415

[2] J. E. Kim, Phys. Rev. Lett. 43, 103 (1979).

[3] M. A. Shifman, A. I. Vainshtein and V. I. Zakharov, Nucl. Phys. B 166, 493 (1980).

STAX. An Axion-like Particle Search with Microwave Photons

J. Ferretti[1]

[1]Dipartimento di Fisica and INFN, 'Sapienza' Università di Roma, P.le Aldo Moro 5, 00185 Roma, Italy

We discuss an improved detection scheme for a light-shining-through-wall (LSW) experiment for axion-like particle searches. We propose to use: gyrotrons or klystrons, which can provide extremely intense photon fluxes at frequencies around 30 GHz; transition-edge-sensors (TES) single photon detectors in this frequency domain, with efficiency ≈ 1; high quality factor Fabry-Perot cavities in the microwave domain, both on the photon-axion conversion and photon regeneration sides. We compute that present laboratory exclusion limits on axion-like particles might be improved by at least four orders of magnitude for axion masses $\lesssim 0.02$ meV.

1 Introduction

Axions [1] are between the most serious dark matter candidates. They are light neutral scalar or pseudoscalar bosons, with mass $m_a \approx \mu\text{eV} - m\text{eV}$, coupled to the electromagnetic field via

$$\mathcal{L}_I = \frac{1}{4} G \, a \, F^{\mu\nu} \tilde{F}_{\mu\nu} \tag{1}$$

In QCD axion models (DFSZ [2] and KSVZ [3]), the axion-photon coupling constant G is directly related to m_a; thus, G is the only free parameter of the theory. In axion-like particle (ALP) searches, the parameter space is extended: G and m_a are the free parameters [4].

Axions and ALPs experimental searches can be divided into two main categories: 1) Axions from astrophysical and cosmological sources; 2) Laboratory searches. In the former case, exclusion limits on the axion-photon coupling constant are provided by estimates of stellar-energy losses [4, 5], helioscopes [6, 7, 8] and haloscopes [6, 9]. In the latter case, limits on G are given by photon polarization [10] and Light-Shining-Through-Wall (LSW) [6, 11, 12, 13, 14] experiments.

In this contribution, we will focus on LSW experiments. After a brief description of the standard LSW experimental apparatus, we will discuss how to improve present ALPs laboratory limits on G by at least four orders of magnitude [15]. We are willing to do this by using extremely intense photon fluxes from gyrotron sources at frequencies around 30 GHz, TES single photon detectors with efficiency ≈ 1, and high quality factor Fabry-Perot cavities in the microwave domain ($Q \approx 10^4 - 10^5$), both on the photon-axion conversion and photon regeneration sides.
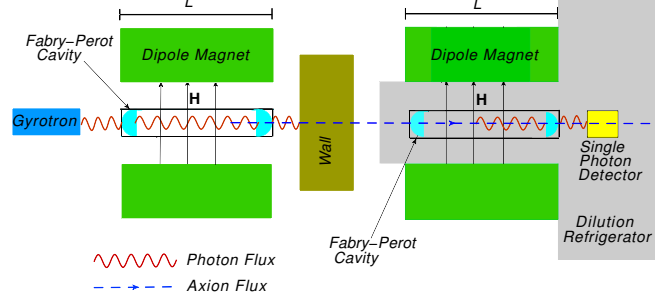
Figure 1: Experimental configuration of the STAX LSW experiment. Fig. from Ref. [15]; Elsevier B.V. copyright.

2 LSW experiments

In a LSW experiment [6, 11, 12, 13, 14], a coherent photon beam traverses an intense magnetic field, $\mathbf{H}$. Here, some photons can convert into axions via the Primakoff effect. Photons exchange 3-momentum $\mathbf{q}$ with $\mathbf{H}$, the energy is conserved. If the $\hat{x}$ axis is chosen in the direction of the propagating photon beam, then the external magnetic is assumed to be uniform in the volume $L_x L_y L_z = L_x S$.

The photons which do not convert into axions are stopped by an optical barrier, "the wall", while axions can cross the wall, due to their negligible cross-section with ordinary matter. On the other side of the wall there is a second magnetic field, which can convert axions back to photons. Reconverted photons may be detected via a single-photon detector.

In the $\epsilon_\gamma \gg m_a$ limit, the photon to axion (axion to photon) conversion probability is given by [6]

$$P_{\gamma \to a} = P_{a \to \gamma} = G^2 H^2 \, \frac{\sin^2(q_x L_x/2)}{q_x^2} \, \frac{\epsilon_\gamma}{\sqrt{\epsilon_\gamma^2 - m_a^2}} \tag{2}$$

where ϵ_γ is the photon (axion) energy and m_a the axion mass. In the limit $\epsilon_\gamma \approx m_a$, which is relevant for the STAX experiment, the previous expression for the conversion probability has to be regulated [15]

$$P_{\gamma \to a} = P_{a \to \gamma} = G^2 H^2 \, \frac{\sin^2(q_x L_x/2)}{q_x^2} \, \frac{\epsilon_\gamma}{\frac{1}{L_x} + \sqrt{\epsilon_\gamma^2 - m_a^2}} \tag{3}$$

The photon-axion-photon rate reads

$$\frac{\mathrm{d}N_\gamma}{\mathrm{d}t} = \Phi_\gamma \eta P_{\gamma \to a}^2 \tag{4}$$

where Φ_γ [s^{-1}] is the initial photon flux and η the single-photon-detector efficiency. The rate can be increased by introducing a Fabry-Perot cavity in the magnetic field area before the wall by a factor of Q, which is the quality factor of the cavity. Moreover, as discussed in Ref. [16], the rate can be further increased with the addition of a second Fabry-Perot cavity in the magnetic field region beyond the wall. See Fig. 1.

3 STAX experimental configuration and calculated exclusion limits

The best laboratory limits for the axion-photon coupling constant have been provided by the ALPS Collaboration [11]. The second stage of ALPS, ALPS-II [13], will improve the previous limits mainly by increasing the magnetic field length as well as introducing a second cavity in the magnetic field region behind the wall. ALPS-II configuration is very similar to that of Fig. 1, but in this case the photon flux is provided by an optical laser.
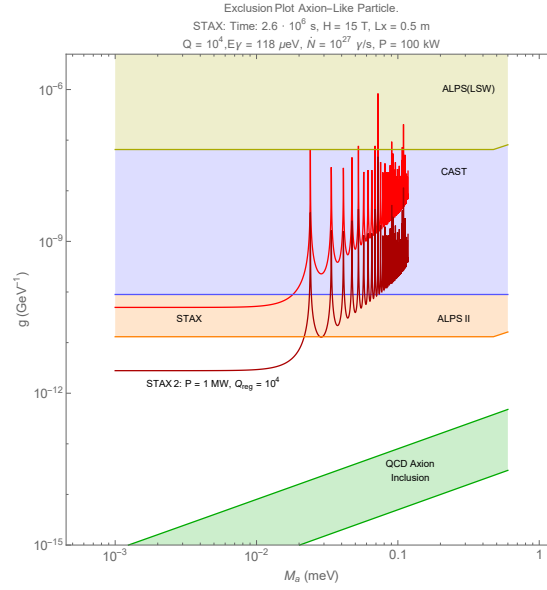
Figure 2: 90% CL exclusion limits that STAX and STAX 2 may achieve in case of a null result for axions with $m_a \lesssim 0.02$ meV. An exposure time of one month and zero dark counts are considered. "STAX" and "STAX 2" configurations correspond to a 100 kW and 1 MW gyrotron sources, respectively. Picture from Ref. [15]; Elsevier B.V. copyright.

Our goal is to develop a new generation LSW experiment and improve the limits on G by using sub-THz photon sources. Sub-THz sources, like gyrotrons and klystrons, can provide very high powers (up to 1 MW) at small photon frequencies, resulting in photon fluxes up to 10^{10} more intense than those from optical lasers, used in previous LSW experiments. We will also use high Q-factor Fabry-Perot cavities for microwave photons and single-photon detectors for light at these frequencies, with almost zero dark count, based on the (Transition-Edge-Sensor) TES technology. The TES detector will be coupled to an antenna and operated at temperatures ≈ 10 mK.

In this way, we computed that present laboratory exclusion limits on axion-like particles might be improved by at least four orders of magnitude for axion masses $\lesssim 0.02$ meV [15]. The limits that STAX experiment may achieve are compared to previous experimental results in Fig. 2.

References

[1] R.D. Peccei and H. Quinn, "CP Conservation in the Presence of Instantons," Phys. Rev. Lett. **38**, 1440 (1977); S. Weinberg, "A New Light Boson?," Phys. Rev. Lett. **40**, 223 (1978); F. Wilczek, "Problem of Strong p and t Invariance in the Presence of Instantons," Phys. Rev. Lett. **40**, 279 (1978).

[2] M. Dine, W. Fischler, and M. Srednicki, "A Simple Solution to the Strong CP Problem with a Harmless Axion," Phys. Lett. B **104**, 199 (1981); A.R. Zhitnitsky, "On Possible Suppression of the Axion Hadron Interactions," Sov. J. Nucl. Phys. **31**, 260 (1980).

[3] J.E. Kim, "Weak Interaction Singlet and Strong CP Invariance," Phys. Rev. Lett. **43**, 103 (1979); M.A. Shifman, A.I. Vainstein, and V.I. Zakharov, "Can Confinement Ensure Natural CP Invariance of Strong Interactions?," Nucl. Phys. B **166**, 493 (1980).

[4] See the review "Axions and Other Similar Particles" on K. A. Olive *et al.* [Particle Data Group Collaboration], "Review of Particle Physics," Chin. Phys. C **38**, 090001 (2014).

[5] M.S. Turner, "Windows on the Axion," Phys. Rep. **197**, 67 (1990); G.G. Raffelt, "Astrophysical methods to constrain axions and other novel particle phenomena," Phys. Rep. **198**, 1 (1990).

[6] P. Sikivie, "Experimental Tests of the 'Invisible' Axion," Phys. Rev. Lett. **51**, 1415 (1983).

[7] M. Arik *et al.* [CAST Collaboration], "New solar axion search using the CERN Axion Solar Telescope with ^{4}He filling," Phys. Rev. D **92** (2015) 2, 021101.

[8] E. Armengaud *et al.* [IAXO Collaboration], "Conceptual Design of the International Axion Observatory (IAXO)," JINST **9**, T05002 (2014); T. Dafni *et al.* [IAXO and CAST Collaborations], "Axion helioscopes update: the status of CAST & IAXO," PoS TIPP **2014**, 130 (2014).

[9] S. J. Asztalos *et al.* [ADMX Collaboration], "A SQUID-based microwave cavity search for dark-matter axions," Phys. Rev. Lett. **104**, 041301 (2010).

[10] L. Maiani *et al.*, "Effects of Nearly Massless, Spin Zero Particles on Light Propagation in a Magnetic Field," Phys. Lett. B **175**, 359 (1986); Y. Semertzidis *et al.*, "Limits on the Production of Light Scalar and Pseudoscalar Particles," Phys. Rev. Lett. **64**, 2988 (1990); E. Zavattini *et al.* [PVLAS Collab.], "Experimental observation of optical rotation generated in vacuum by a magnetic field," Phys. Rev. Lett. **96**, 110406 (2006); E. Zavattini *et al.* [PVLAS Collab.], "New PVLAS results and limits on magnetically induced optical rotation and ellipticity in vacuum," Phys. Rev. D **77**, 032006 (2008).

[11] K. Ehret *et al.* [ALPS Collaboration], "New ALPS Results on Hidden-Sector Lightweights," Phys. Lett. B **689**, 149 (2010).

[12] M. Betz, F. Caspers, M. Gasior, M. Thumm and S. W. Rieger [CROWS Collaboration], "First results of the CERN Resonant Weakly Interacting sub-eV Particle Search (CROWS)," Phys. Rev. D **88**, no. 7, 075014 (2013).

[13] R. Bähre *et al.* [ALPS-II Collaboration], "Any light particle search II. Technical Design Report," JINST **8**, T09001 (2013); B. Döbrich [ALPS-II Collaboration], "What's new in ALPS-II," arXiv:1309.3965.

[14] R. Ballou *et al.* [OSQAR Collaboration], "New Exclusion Limits for the Search of Scalar and Pseudoscalar Axion-Like Particles from "Light Shining Through a Wall", arXiv:1506.08082.

[15] L.M. Capparelli, G. Cavoto, J. Ferretti, F. Giazotto, A.D. Polosa and P. Spagnolo, "Axion-like particle searches with sub-THz photons," Phys. Dark Univ. **12**, 37 (2016).

[16] P. Sikivie, D.B. Tanner, K. van Bibber, "Resonantly enhanced axion-photon regeneration," Phys. Rev. Lett. **98**, 172002 (2007).

A Milli-Charged Particle Detector at LHC P5

Gabriel Magill (on behalf of the milliQan collaboration)

Perimeter Institute for Theoretical Physics, Waterloo, Canada
McMaster University, Hamilton, Canada
gmagill@perimeterinstitute.ca

We propose a dedicated experiment that would detect milli-charged particles produced by pp collisions at LHC Point 5. The experiment would be installed during LS2 in the vestigial drainage gallery above UXC and would not interfere with CMS operations. With 300 fb^{-1} of integrated luminosity, sensitivity to a particle with charge $\mathcal{O}(10^{-3})$ e can be achieved for masses of $\mathcal{O}(1)$ GeV, and charge $\mathcal{O}(10^{-2})$ e for masses of $\mathcal{O}(10)$ GeV, greatly extending the parameter space explored for particles with small charges and masses above 100 MeV.

1 Introduction

We propose a dedicated experiment to search for milli-charged particles (mCP). The proposed experiment is a model-independent probe of mCPs, since it relies only on the masses and charges of such particles. One can view this search as part of a general program to search for additional sectors. A prototypical model of milli-charged particles [14] consists of an abelian gauge field A'_μ that couples to a massive Dirac fermion ψ of mass M_{mCP} and to hypercharge via kinetic mixing. A simple field redefinition removes the kinetic mixing, yielding the Lagrangian

$$\mathcal{L} = \mathcal{L}_{\mathrm{SM}} - \frac{1}{4} A'_{\mu\nu} A'^{\mu\nu} + i\bar{\psi} \left(\slashed{\partial} + ie'\slashed{A}' - i\kappa e'\slashed{B} + iM_{\mathrm{mCP}} \right) \psi.$$

The new matter field ψ therefore has an electric charge of $\epsilon \equiv \kappa e' \cos\theta_w / e \ll 1$, a milli-charge. The parameter space spanned by the mass and charge of the mCPs is constrained by indirect observations [7, 8, 9, 10, 11, 15, 18], although these can often be evaded by adding extra degrees of freedom. Previous experiments have also looked for non-quantized charged particles [5, 6, 8, 16]. However, the parameter space for mCPs with masses $0.1 \lesssim M_{\mathrm{mCP}} \lesssim 100$ GeV and charges at the 10^{-3} $e - 10^{-1}$ e level is largely unexplored by direct searches. In particular, the CMS/ATLAS sensitivity to mCPs in monojet and missing energy searches is precluded by the penalty on the cross-section associated with initial state radiation. In the following, we summarize a recent proposal [4, 12] to construct a dedicated detector at the LHC to target this unexplored part of parameter space.

2 Overview of the Experiment

The experimental apparatus envisaged is 3 scintillator detector layers of roughly 1 m^3 each, positioned near one of the high-luminosity interaction points of the LHC. LHC Point 5 (Cessy)

is host to the Compact Muon Solenoid (CMS) experiment and its supporting infrastructure. As such, the appropriate services - electricity, ethernet, LHC luminosity information - would be available. We propose that the detector be set in the PX56 drainage gallery located above CMS UXC. In Figure 1, a 3D model was combined with a laser scan of the gallery to give a best as-built estimation. An optimal position was found which offered a distance to the IP of 33 m at an angle of 43.1 degrees from the horizontal plane, 17 m of which is through rock. The size of the drainage gallery constrains the length of the detector, but not the sides. Hence there is space to install shielding and forced air cooling.

We are also engineering a system to rotate the detector to a stowed position during access periods. This proposal has already been run through various LHC and CMS operation bodies and no conflicts were identified. The detector itself is a 1 m $\times$ 1 m $\times$ 3 m plastic scintillator array, oriented to point to the CMS interaction point. The array is subdivided into 3 sections each containing 400 5 cm $\times$ 5 cm $\times$ 80 cm scintillator bars optically coupled to high-gain PMTs. A minimum-ionizing particle of charge Q leaves roughly $2Q^2$ MeV/cm in a material of density 1 g/cm^3. We therefore expect an average of $\mathcal{O}(1)$ photoelectron (PE) from each PMT for mCPs of charge $Q = \mathcal{O}(10^{-3})$ e [4]. Requiring a longitudinal triple-incidence within a 15 ns time window amounts to $\mathcal{O}(10)$ events per year with $N_{\mathrm{PE}} \geq 1$.
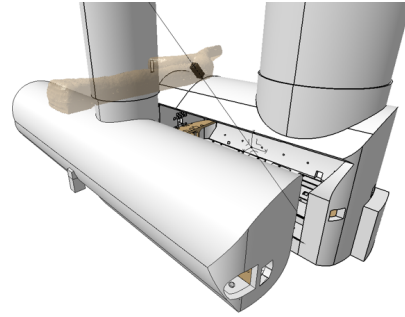
Figure 1: A 3D model with the optimal position of milliQan above CMS UXC.

3 Backgrounds

The dominant background is dark-current in the PMTs. Additional sub-dominant sources of background include activity in the scintillator from background radiation and photo-multiplier after-pulsing. To measure the dark-current, we constructed a test setup using a 3" Bicron-412 scintillator coupled to a 3" Hamamatsu H2431 PMT at 3 kV, readout with a CAEN V1743 digitizer, described in Section 4. Once the board receives a triggering event, the analog buffer is digitized. During this digitization window, which lasts approximately 100 μs, no additional trigger can be accepted. Using this test setup, we measured a dark-current rate of approximately 1 kHz at room temperature. By reducing the high voltage and cooling the PMT we are able to significantly reduce the background rate. With these handles we expect to be able to bring the rate to below 500 Hz. Another source of background are cosmic and LHC muons, which consist of >1000 PEs. We measured the PMT rates in a counting room close to our proposed location. Collecting data with/without the LHC beam, as well as with/without led and polyethylene shielding, we found that the PMT rates with shielding become comparable to the dark-current rates, and hence we don't expect muons to create too much activity and after-pulses in our scintillators. If a muon does hit the detector, it can be easily vetoed offline by its large pulse.

4   Data Acquisition

Analog pulses from the PMTs must be digitized and stored for offline analysis. Furthermore, a trigger will record only those pulses during interesting time windows when significant activity in the detector is observed. This can all be performed for modest cost using the CAEN V1743 digitizer. This digitizer board has 16 channels, each of which is sampled into 7 analog buffers. The digitization is done with 12 bits of precision, and the dynamic range is 2.5 V, allowing good resolution of 0.61 mV. Analog noise is about 0.75 mV per channel, whereas single PE signals can easily be above 3 mV. The only drawback of the analog buffer approach is that the board is dead while digitizing the buffer. This results in a deadtime of $\lesssim 10$ %. However, the time after a trigger is anyways of low quality due to the presence of PMT after-pulses. Thus there is no dead time from readout, up to rates of ~ 1 kHz. For the triggering, we will connect 12 PMTs (2×2/layer, aligned longitudinally) to one board. Two neighbouring PMTs in each layer will form a group. The whole detector will be read out if any two groups in a board are above threshold within a time window of $(\Delta t)_{\text{online}} = 100$ ns. Given PMT dark-current rates of 500 Hz, the trigger rate is expected to be 75 Hz [4]. Offline we will tighten the time window to $(\Delta t)_{\text{offline}} = 15$ ns. The total offline background rate is estimated to be 1.1×10^{-5} Hz. The LHC will have delivered 300 fb^{-1} during Run 3 (3000 fb^{-1} during HL-LHC). We therefore estimate to have 165 (330) background events [4]. We expect to use pulse shapes and expected arrival time of particles produced in the LHC to reduce the total background to ~ 50 (100) events.

5   Simulations and Sensitivity

In order to evaluate the projected sensitivity of the experiment for various mCP electric charges and masses, we performed a full simulation of the experiment, including a GEANT4 [1] model of the detector. In the first stage, MADGRAPH5 and MADONIA were used to simulate the production of mCP particles via Drell-Yan, J/Ψ, Υ(1S), Υ(2S), and Υ(3S) channels at 14 TeV center-of-mass energy [2, 3]. Particles produced at the interaction point were propagated using a map of the CMS magnetic field to the proposed experimental site. The effects of multiple scattering and energy loss were included. The number of expected mCP particles per fb^{-1} of integrated luminosity incident at the detector is shown in Figure 2 as a function of the mass of the milli-charged particle. In the second stage, we calculated the signal efficiency by running the kinematic distributions of mCP particles at the proposed experimental site through a full GEANT4 simulation of the detector based on the specifications provided by the manufacturers for Saint-Gobain BC-408 plastic scintillators and Hamamatsu R329-02 PMTs [17, 13]. This was important to model the reflectivity, the light attenuation length and the dependence on small electric charge. Combining the estimated background rates discussed in Section 3 with the cross-sections, acceptances and efficiencies calculated for all masses and electric charges, the sensitivity projections of the milliQan experiment for LHC and HL-LHC are shown in Figure 2.

6   Summary

We have proposed a dedicated experiment to search for milli-charged particles produced in the LHC. This would greatly extend the parameter space for particles with small charge and masses above 0.1 GeV. We have done sufficient R&D to encourage us to proceed with securing funding. We thank T. Camporesi, J. Butler, and the CMS collaboration for their encouragement.
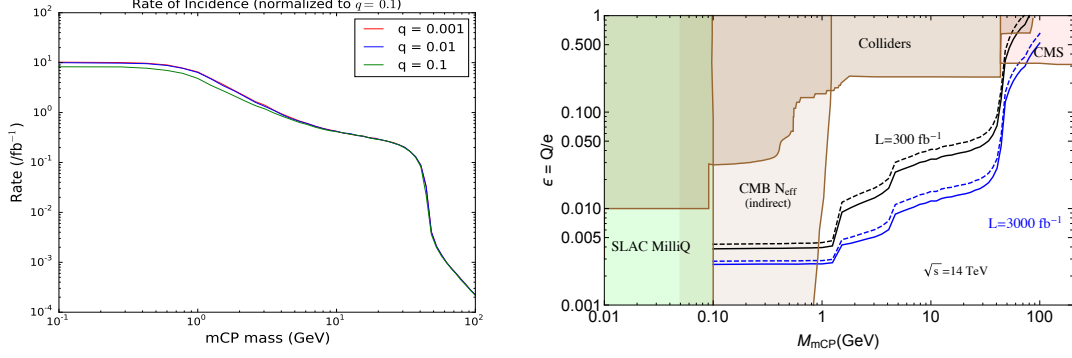
Figure 2: The number of expected mCP particles per fb^{-1} of integrated luminosity incident at the detector, with cross-sections normalized to $Q = 0.1e$ (left). The expected 95% C.L. exclusion (solid lines) and 3σ (dashed lines) sensitivities for benchmark luminosities (right).

References

[1] S. Agostinelli et al. GEANT4: A Simulation toolkit. *Nucl. Instrum. Meth.*, A506:250–303, 2003.

[2] J. Alwall et al. The automated computation of tree-level and next-to-leading order differential cross sections, and their matching to parton shower simulations. *JHEP*, 07:079, 2014.

[3] Pierre Artoisenet, Fabio Maltoni, and Tim Stelzer. Automatic generation of quarkonium amplitudes in nrqcd. *Journal of High Energy Physics*, 2008(02):102, 2008.

[4] Austin Ball et al. A Letter of Intent to Install a milli-charged Particle Detector at LHC P5. 2016, arXiv:1607.04669.

[5] A. Badertscher et al. An Improved Limit on Invisible Decays of Positronium. *Phys.Rev.*, D75:032004, 2007.

[6] Serguei Chatrchyan et al. Search for fractionally charged particles in *pp* collisions at $\sqrt{s} = 7$ TeV. *Phys.Rev.*, D87(9):092008, 2013.

[7] S. Davidson et al. Limits on particles of small electric charge. *Phys.Rev.*, D43:2314–2321, 1991.

[8] Sacha Davidson et al. Updated bounds on millicharged particles. *JHEP*, 0005:003, 2000.

[9] Sacha Davidson and Michael E. Peskin. Astrophysical bounds on millicharged particles in models with a paraphoton. *Phys.Rev.*, D49:2114–2117, 1994.

[10] A.D. Dolgov et al. Constraints on millicharged particles from Planck data. *Phys.Rev.*, D88(11):117701, 2013.

[11] S.L. Dubovsky, D.S. Gorbunov, and G.I. Rubtsov. Narrowing the window for millicharged particles by CMB anisotropy. *JETP Lett.*, 79:1–5, 2004.

[12] Andrew Haas et al. Looking for milli-charged particles with a new experiment at the LHC. *Phys. Lett.*, B746:117–120, 2015.

[13] Hamamatsu. Photomultiplier tube r329-02. `http://www.hamamatsu.com/us/en/product/category/3100/3001/R329-02/index.html`. Accessed: 2016-02-12.

[14] Bob Holdom. Two U(1)'s and Epsilon Charge Shifts. *Phys.Lett.*, B166:196, 1986.

[15] R.N. Mohapatra and I.Z. Rothstein. Astrophysical Constraints on Minicharged Particles. *Phys.Lett.*, B247:593–600, 1990.

[16] A.A. Prinz et al. Search for millicharged particles at SLAC. *Phys.Rev.Lett.*, 81:1175–1178, 1998.

[17] Saint-Gobain. Plastic scintillators. `http://www.crystals.saint-gobain.com/Plastic_Scintillators.aspx`. Accessed: 2016-02-12.

[18] Hendrik Vogel and Javier Redondo. Dark Radiation constraints on minicharged particles in models with a hidden photon. *JCAP*, 1402:029, 2014.

Search for low-mass WIMPs with Spherical Detectors : NEWS-LSM and NEWS-SNO

G. Gerbier[1] for the NEWS collaboration[2],

[1] Queen's University, Physics Department, Kingston, Canada
[2] New Experiments With Spheres : https://www.snolab.ca/news-projects/Collaboration.html

The technique of spherical gaseous detectors has been used for the first time in the Laboratoire Souterrain de Modane to search for WIMP signal. Some details on the used 60 cm diameter detector, operating conditions and preliminary results are given. Thanks to a low energy threshold of 150 eV and the use of Neon target, anticipated sensitivity has been calculated for WIMP masses as low as 0.7 GeV with a Boosted Decision Tree method. Final analysis of this data set is under way. A larger size detector of 140 cm diameter to be installed in SNOLAB is currently under design and planned to be operated end 2017.

1 Introduction

Dark matter is now clearly an essential ingredient of our understanding of the Universe. Its nature is still unknown but -massive- neutral particles, non relativistic at decoupling time, are a generic class of well motivated candidates. Recent -non-findings at LHC [1] and failure from direct detection experiments to find any candidate at masses above 10 GeV [2]suggest that the search should be extended, in particular to low mass. On the other hand, several new theoretical approaches (dark sector, asymmetric dark matter, U-boson, generalized effective theory ...) open the way to candidates with lower mass and/or more complex couplings than the traditional spin (in)dependent ones [3].

The proposed gaseous spherical detector technique, initiated by I Giomataris [4], benefits from two key features: 1) access to extremely low threshold -10's of eV- with sizeable amounts of target mass, few 10's of g to 10's of kg, 2) the so called kinematical match between target (A of nuclei) and projectile (Dark Matter particles) mass by the use of light A targets such as He or H nuclei. Energy transfer is optimized for similar mass of target and projectile, allowing to probe the 0.1 to 1 GeV mass range.

A 60 cm diameter prototype detector has been operated successfully with Ne gas at 3 bars. The next sections describe the used setup, operating conditions and first analysis of data obtained at the Laboratoire Souterrain de Modane (LSM).

2 Experimental set-up at LSM and Operating conditions

The detector consists of a spherical metallic vessel and a small metallic ball located at the center of the vessel. The ball is maintained in the center of the sphere by a rod and is set at high
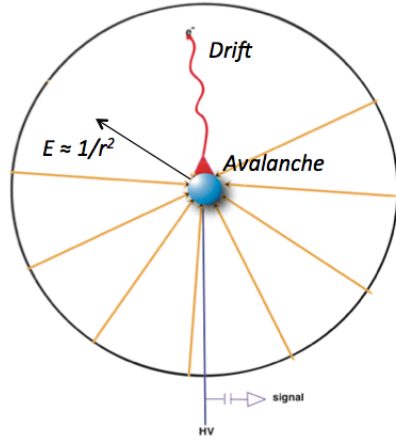
Figure 1: a left) Principle of spherical gas detector - b right) 60cm prototype made of low activity Copper

voltage. The configuration of the electric field, typically varying as $1/r^2$, allows the electrons to drift to the central sensor in low field regions constituting most of the volume, while they trigger an avalanche within few mm around the sensor (Figure 1a). The amplification capability combined with the very low capacitance of the sensor allows to reach single ionization electron sensitivity [5].

At high pressure, nuclear recoils and compton interactions appear both as point like interactions at low energies and cannot be discriminated. However fiducial information can be obtained by measuring the rise time of the pulse, directly linked to the diffusion of primary electrons, thus to the radius at which occurred the interaction.

The present results have been obtained with the SEDINE prototype, a 60 cm spherical detector made of ultra pure copper (Figure 1b). The sphere was installed underground, in the LSM under a rock thickness of 4800 mwe, and protected from external radiations by shields made of, from inside to outside, 8 cm of copper, 10 cm of lead and 30 cm of Polyethylene.

A simple sensor was designed, consisting of a 6.35 mm silicon ball, set to high voltage, to which is welded a 380 micron diameter insulated wire, inside a copper rod at ground.

The sphere was filled with a mixture of Neon and CH_4 in the proportions 99.3/0.7 at a total pressure of 3100 mb. The central ball was set at 2520 V, allowing a sufficient gain to set the acquistion threshold level equivalent to 50 eVee (electron equivalent) energy, that is around a single primary ionisation electron.

The detector was run in sealed mode for 42 days without interruption.

3 Data analysis and expected sensitivity

The acquired pulse shape is a convolution of the arrival time dispersion of the primary ionization electrons, of the current induced by the ions drifting away and of the transfer function of the amplifier.

Numerical unconvolution methods have been applied to the data pulses to obtain the two
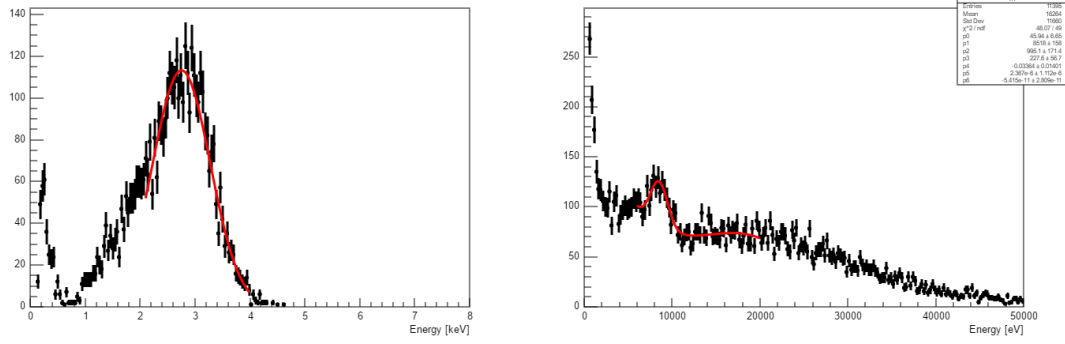
Figure 2: a left) Ar37 calibration b right) Data run with 8 keV induced by copper fluorescence

main parameters used in the analysis described later : the deposited energy and the risetime of the pulse, related to the radius at which occured the interaction.

Simulation of pulses based on physics and electronic described above allowed to validate the pulse uncovolution method. Energy calibration has been performed down to energies of 200 eV thanks to the use of an ^{37}Ar source, which electron capture decay induces X rays at 2.8 and 0.26 keV. The spectrum shown on Figure 2a shows indeed the expected features. The energy spectrum of the dark matter search run exhibits a line at 8 keV induced by copper fluorescence allowing to cross check the calibration with ^{37}Ar (Figure 2b).

The anticipated background interactions occuring in the detector have two main origins, on one hand compton / photoelectric interactions occuring in the volume induced by gamma rays coming from the materials of the detector and outside the detector and on the other hand particles originating from the surface of the detector, expected from Radon daughther deposits, mostly ^{210}Pb decays, beta/X rays, ^{210}Po alphas and associated ^{206}Pb nuclear recoils.

Rise time distribution of these two populations are expected to be very different. Full simulation of the pulses have been performed for volume and surface interactions and their rise time vs energy scatter plots are shown on Figure 3a and 3b.

Futhermore, to calibrate experimentally the response of the detectors to volume events and their risetime distribution, an Am-Be neutron source was used in situ, to produce point like energy deposition all over the volume.

The Figure 4a shows the measured rise time distribution in a typical energy window of 500 to 750 eV together with the simulated distribution of volume point like energy deposition in a simplified spherical symmetry for the electric field. Indeed, there is good agreement between data and model.

For the present analysis, a conservative analysis threshold of 150 eVee has been chosen.

Cuts were applied on the shape of the recorded pulse to remove microdischarges and spurious electronic pulses. The corresponding signal efficiency was measured from nuclear recoil sample.

Events recorded during the WIMP search run are shown in the rise time vs energy plane on Figure 4b. The comparison of Figures 4b 3a and 3b suggests that the data from WIMP search run are mostly a combination of surface and volume events. The shaded region corresponds to our wide preliminary region of interest (ROI) to search for WIMP's. The region highlighted in red is the side band region that is used, together with the probability density functions of the main backgrounds, to determine the expected population inside the ROI. A Boosted Decision
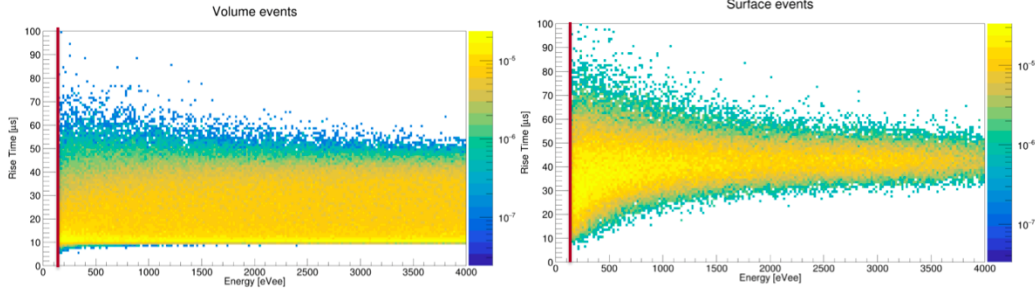
Figure 3: Probability density functions in the risetime vs energy plane of volume events (left) and surface events (right).
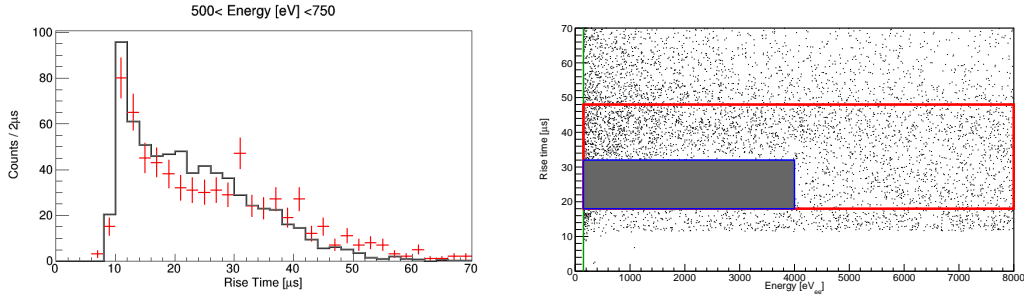
Figure 4: a left) Rise time distribution of events from neutron run calibration (red cross) together with simulated distribution in the 500-750 eV region. b) rise time vs energy distribution from WIMP search data with ROI (shaded) and side band (red rectangle) regions (see text).

Tree was trained in order to define a fine tuned ROI that optimizes the signal/background discrimination for each considered WIMP mass.

To determine the expected sensitivity, hundreds of NEWS-LSM Neon experiments are simulated to account for statistical fluctuations. For each simulated data set, an upper limit was set on the WIMP cross section considering all events in the refined ROI as WIMP candidates, using standard assumptions on WIMP velocities, halo density, and calculated quenching factor of Neon recoils in Neon gas [6]. On Figure 6 are shown the expected 1σ (resp 2σ) sensitivity regions in light green (dark green).

Final analysis of the data is under way.

Quenching factors in Neon and Helium gas are being currently measured in the subkeV region using ion beams provided by a facility of the collaboration.

4 NEWS-SNO

The NEWS-SNO project builds up on the knowledge acquired with the operation of the 60 cm prototype in LSM. It will consist of a 140 cm sphere inserted in a shell of 25 cm archeological and low activity lead shield, itself protected by a 40 cm thick polyethylene shield, to be installed
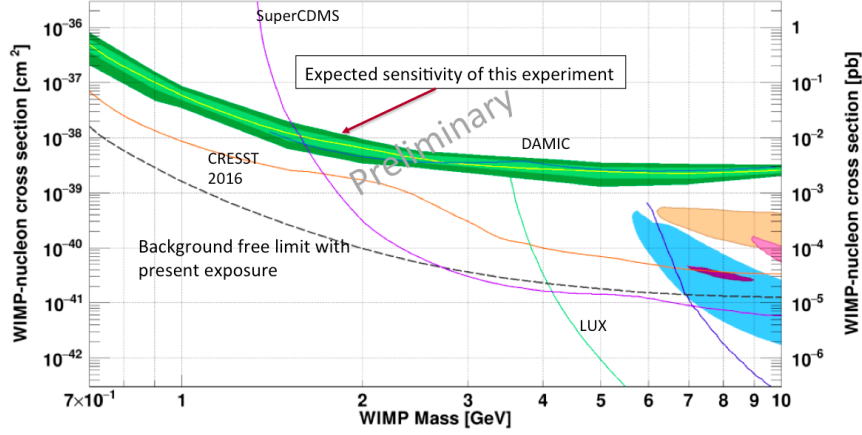
Figure 5: Expected sensitivity of the present search with Neon nucleus

in SNOLAB by end 2017. Space in SNOLAB has been assigned, design of the whole project is completed and TDR phase is ongoing.

Among major improvements, selection of extremely low activity copper (in the range of few μBq/kg of U and Th impurities) and dedicated handling to avoid radon entering the detector at any time will insure significant reductions of the backgrounds levels, both in surface and volume, relative to the above results, and allow sensitivity to Nucleon-WIMP cross section down to 10^{-44} cm^2. Use of H and He targets will allow to reach WIMP mass sensitivity down to 0.1 GeV. Details on set up and expected performances can be found in reference [7].

5 Acknowledgments

References

[1] O. Buchmueller et al, Eur. Phys. J. C72, 2243(2012)

[2] G. Gerbier, M. Drees, Review of Particle Properties, Dark Matter review : http://pdg.lbl.gov/2016/reviews/rpp2016-rev-dark-matter.pdf

[3] Nima Arkani-Hamed et al, Phys. Rev. D 790150142009 ; P Fayet, Phys. Rev. D 751150172007 ; A. Liam Fitzpatrick et al JCAP02 (2013) 004 ; K. M. Zurek, arXiv:1308.0338

[4] I. Giomataris et al, JINST 3:P09007,2008 ; E. Bougamont et al, Journal of Modern Physics, 2012, 3, 57-63,

[5] G. Gerbier et al., arXiv:1401.7902v1

[6] D.-M. Mei, Z.-B. Yin, L.C. Stonehill, A. Hime, Astroparticle Physics 30 (2008) 1217

[7] see https://www.snolab.ca/news-projects

Simulation study on optimization of cavity design for axion search experiments using COMSOL multiphysics

Junu Jeong[1,2], SungWoo Youn[2], Saebyeok Ahn[1,2], and Yannis K. Semertzidis[1,2]

[1]Department of Physics, KAIST, South Korea
[2]Center for Axion and Precision Physics, IBS, South Korea,

A conventional axion search experiment utilizes microwave resonant cavities, where axions are converted into photons under a strong magnetic field. Optimized cavity dimension is essential to enhance signal power from the axion-to-photon coupling, to broaden the frequency range, to minimize mode crossings, etc. An extensive study has been performed to optimize the dimension of a cavity and frequency tuning system using the COMSOL multiphysics simulation software. We introduce a figure of merit for this purpose, and present the results from the simulation study.

1 Introduction

Axions can be detected by the conversion to photons in a strong magnetic field[1]. When we search axion using microwave cavity experiments, the axion's conversion to photon power has proportionality as below.

$$P_{a \to \gamma\gamma} \sim B_0^2 V f C Q \tag{1}$$

where B_0 means external magnetic field, V is volume of cavity, f is resonant frequency of cavity, C is form factor of cavity mode, and Q means quality factor of cavity. Form factor C means how resonant mode of cavity is aligned with external magnetic field[2].

$$C_E = \frac{|\int \vec{E} \cdot \vec{B} dV|^2}{B_0^2 \int \epsilon |E|^2 dV} \tag{2}$$

When one use solenoid magnet and cylindrical cavity to search axions, TM010 mode has the largest value of form factor, C.

Because no one knows exact mass of the axion, we have to sweep the resonant frequency of a microwave cavity. To change the resonant frequency of a cavity, cavity geometry or material inside cavity should be changed. In this simulation, I introduced the long dielectric rod and by changing position of the rod, changed the resonant .

For a given SNR, and $g_{a\gamma\gamma}$, which means axion-photon coupling constant, frequency scanning rate has below proportionality[2].

$$\frac{df}{dt} \sim B_0^4 V^2 f^2 C^2 Q \tag{3}$$

For a cavity with radius = 20mm, and height = 80mm, and a rod with radius = 2mm, and dielectric constant = 9, the resonant frequency dependency of rod position is given as below graph.
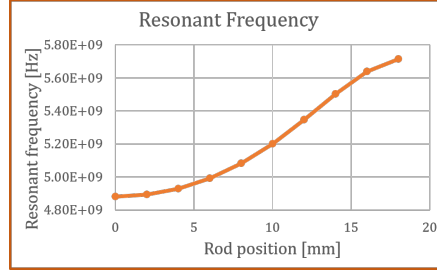
Figure 1: Resonant frequency of TM_{010} vs. rod position where R=20mm, L=80mm, r=2mm, and ϵ_r=9.

Then one can define the totla scan range and total scan time.

$$\Delta F \equiv f_f - f_i \tag{4}$$

$$\Delta T \equiv \int_{t_i}^{t_f} dt = \int_{f_i}^{f_f} \frac{df}{df/dt} \sim \sum_i \frac{\delta f_i}{V^2 C_i^2 f_i^2 Q_i} \tag{5}$$

where f_f and f_i refers that final resonant frequency and initial resonant frequency, respectively. δf_i means the frequency difference between f_i and f_{i+1}, and index i means rod positions. From this, averaged scan rate can be defined as below.

$$\left. \frac{df}{dt} \right|_{averaged} = \frac{\Delta F}{\Delta T} \tag{6}$$

The below graph shows a plot of scan rate of each rod position vs. resonant frequency.
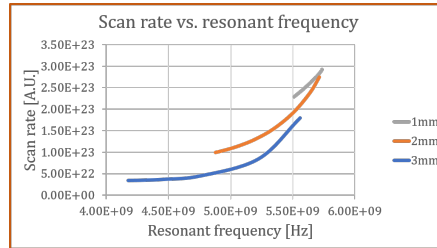
Figure 2: Scan rate vs. resonant frequency for various rod radius.

As you can see in graph, both total scan range and averaged scan rate become important parameters for a given experiment. Scan range maximizes as rod radius becomes larger, but averaged scan rate maximizes as rod radius becomes smaller. By giving equal weight to each parameter, figure of merit can be used as below.

$$F.O.M. = \Delta F \times \frac{\Delta F}{\Delta T} \tag{7}$$

2   Optimization of cavity and rod dimension

Parameters of the tuning system are cavity radius(R), cavity height(L), relative rod radius(r_{rr}), and rod dielectric constant(ϵ_r). We defined relative rod radius as rod radius divide by cavity radius, so it means how rod size is large compared to cavity size. We set rod dielectric constant as 9 for this section.

Simulation procedure was as follows. Firstly, we choose dimension of the tuning system(R, L, r_{rr}). Secondly, we shift the rod positions from cavity center to wall of cavity. And finally, we calculate $F.O.M.$.

The field distribution when rod exists inside cavity is as below.
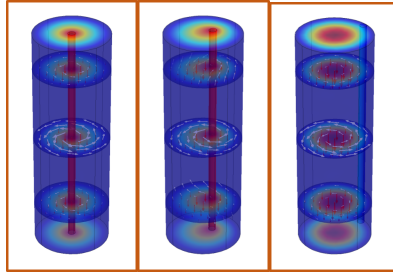
Figure 3: Field distributions of the TM_{010} mode for different dielectric rod positions.

Where the color refers the relative norm of resonant electric field, red arrow means resonant electric field, and white arrow means resonant magnetic field.

The simulation result is as below.
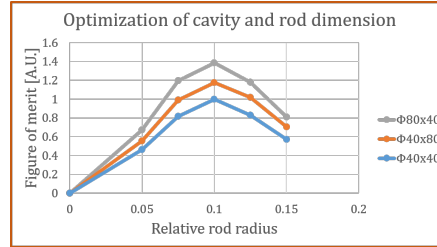
Figure 4: Figure of merit vs. relative rod radius at ϵ_r=9 for various cavity dimensions.

Cavity dimension does not influence the relative optimal size of the tuning rod. So the optimal r_{rr} is independent of cavity dimension. At $\epsilon_r = 9$, the optimal r_{rr} is 0.1

3   Dependence of optimal rod dimension on dielectric constant

We set cavity dimension as R=20mm, and L=80mm, because the cavity dimension was independent with optimal relative rod size. From this, we changed rod dielectric constant(ϵ_r)

from 6 to 11. The simulation procedure was same with previous simulation but from this, we changed not cavity dimension but dielectric constant.

The simulation result is as below.
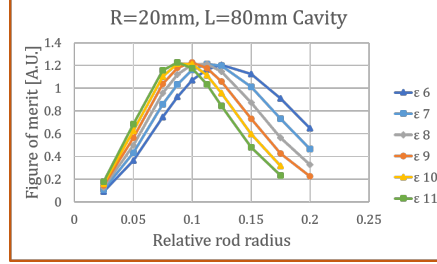
Figure 5: Figure of merit vs. relative rod radius for various rod dielectric constants.

So the optimal relative rod radius is as below.
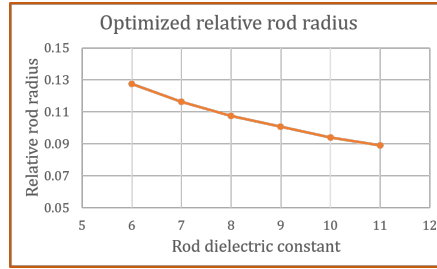
Figure 6: Optimized relative rod radius vs. rod dielectric constant.

As you can see from graph, the optimal r_{rr} is inversely proportional to ϵ_r, and the maximum value of F.O.M. almost independent of ϵ_r.

4   Conclusion

In short, from this simulation study, we can get two important results. First, for a given dielectric constant, the optimal relative size of a tuning system, especially when we use dielectric rod, is constant regardless of cavity dimension. Second, the optimal rod size has a dependence on (inversely proportional to) dielectric constant.

5   Acknowledgments

References

[1] P. Sikivie, "Experimental Tests of the "Invisible" Axion," Phys. Rev. Lett. **52**, 695 (1984). doi:10.1103/PhysRevLett.51.1415

[2] R. Bradley *et al.*, "Microwave cavity searches for dark-matter axions," Rev. Mod. Phys. **75**, 777, (2003). doi:10.1103/RevModPhys.75.777

Status of the XENON Experiments

Junji Naganoma (on behalf of the XENON collaboration)

Rice University, Houston, USA

The XENON experiments search for weakly interacting massive particles (WIMPs) using dual-phase xenon time projection chambers. While the XENON100 experiment completed its science program, the next ton-scale experiment, XENON1T, is fully installed and moving towards science data-taking. The most recent results of the collaboration are presented: from XENON100 latest analysis on low mass WIMPs to XENON1T status and its projected sensitivity, that has been evaluated to reach a minimum cross section of 1.6×10^{-47} cm^2 at a WIMP mass of 50 GeV/c^2 after 2 years exposure with 1 ton of fiducial volume.

1 Introduction

Understanding the nature of the dark matter is one of the most fundamental questions in particle and astrophysics. The XENON dark matter search experiments aim at the direct detection of dark matter in the form of weakly interacting massive particles (WIMPs). In the XENON time projection chambers (TPCs), liquid xenon (LXe) is target and detection medium with the further property of being an excellent self-shielding for background reduction. The WIMP elastic scattering off Xe nuclei would produce low energy nuclear recoils at extremely low interaction rates.

2 The XENON dark matter search experiments

The working principle of the XENON detectors is shown schematically in Fig. 1. Photomultiplier tube (PMT) arrays are placed on top and bottom of the TPC. Cathode, gate, and anode grids define electric fields in the TPC. When a particle interacts with Xe in the LXe volume, the interaction creates the excitation and ionization of Xe. Direct scintillation (S1) from the excitation and electron-ion recombination is detected by the PMTs immediately after the interaction. By the applied electric field, the electrons which escaped from the recombination drift towards the anode. Those electrons are extracted into the gas phase by a high electric field between the gate and the anode, and then accelerated in GXe. This creates proportional scintillation in the GXe, which is recorded as a secondary signal (S2) with a time difference to the S1 depending on the drift velocity of the electrons as well as on the depth of interaction. The three-dimensional interaction position is reconstructed using the drift time and the S2 hit pattern on the top PMT array for the depth and the position in horizontal plane estimations, respectively. From the position reconstruction, it becomes possible to reject background events in outer volume from the detector materials or events with multiple scatterings. The ratio S2/S1 is different for electronic recoils (ERs) and nuclear recoils (NRs), which provides background discrimination in

addition to the position selection. More details of the detector are described in [1]. Since 2006, the XENON detectors have been operating at the Laboratori Nazionali del Gran Sasso (LNGS) in Italy at an average depth of 3600 m water equivalent. It has started with XENON10 [2] and continued with XENON100 [3]. The multi-ton scale next phase of the project, XENON1T, is fully installed and the data-taking is ongoing.
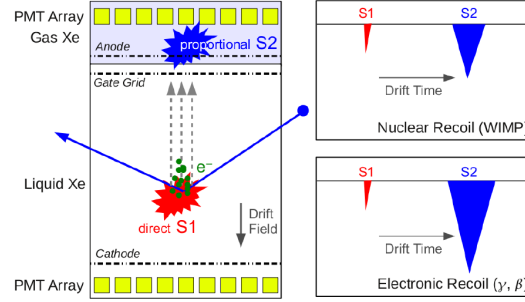
Figure 1: Left: working principle of the XENON dual-phase TPC. Right: sketch of the waveforms of nuclear recoils (WIMPs or neutrons) and electronic recoils (γ or β background), showing the different ratio of the charge (S2) and light (S1) signals for the two types of events.

3 Low mass WIMP search in XENON100

A dedicated analysis has been performed to improve sensitivity on low mass WIMPs [4], using its 225 live days of the XENON100 data. In order to explore the low energy region, the threshold of the detector is lowered by dropping the requirement of an existing S1 and focusing only on single S2 signals. This way a NR threshold of 0.7 keV was achieved, which is significantly lower than the standard analysis of 6.6 keV [3]. Therefore the energy scale was obtained from NR calibration using the S2 signal only, which is also different to the standard analysis, which used only the S1 signal. Because of a difficulty to estimate background without the S1, the analysis assumes every event passing selection criteria could be WIMP signal, which leads to conservative estimation of cross section limit. Figure 2 shows the observed S2 spectrum together with an expected spectrum from WIMP signal of 6 GeV/c^2 at spin-independent (SI) cross section of 1.5×10^{-41} cm^2 (left), and WIMP exclusion limit on the SI WIMP-nucleon scattering cross section at 90% C.L. (right). This analysis improves the result of the previous XENON100 result [3] below $\sim$7.4 GeV/c^2.

4 The XENON1T detector and its expected sensitivity

Following the successful operation of XENON100, XENON1T is the first ton scale liquid xenon detector. XENON1T is expected to have a sensitivity to SI WIMP-nucleon cross section about a factor 100 higher than XENON100. The TPC is 96 cm height and 96 cm diameter, filled with 2 tons of LXe. Total 248 low-radioactive PMTs (Hamamatsu R11410-21 [5]) are distributed at the top and bottom of the TPC. The detector is surrounded by a water tank with a height and diameter of 10 m. This water tank not only acts a shield for external radiation, but also
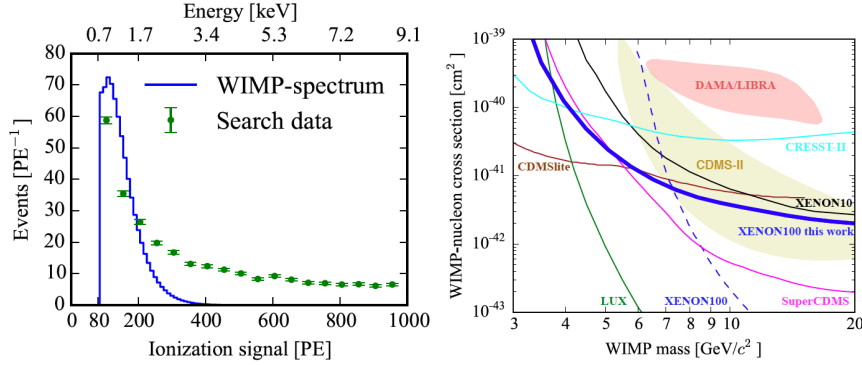
Figure 2: Left: observed S2 spectrum together with an expected S2 spectrum from WIMP signal of 6 GeV/c^2 at a SI WIMP-nucleon scattering cross section of 1.5×10^{-41} cm^2. Right: WIMP exclusion limit on the SI WIMP-nucleon scattering cross section at 90% C.L. Significant improvement from the standard analysis can be seen at WIMP mass below about 7 GeV/c^2.

is operated as an active veto for cosmic muons, since it is equipped with 84 PMTs, which are able to detect Cherenkov light produced by the muons [6].

Figure 3: Left picture shows the water tank and the service building of XENON1T. Right picture shows the installed XENON1T TPC. The copper field shaping rings and the bottom PMT array are visible.

A dedicated Geant4-based Monte Carlo simulation of the XENON1T detector has been developed, including radioactivities of all detector materials, and conversion of energy deposition into S1 and S2 signals. Figure 4 shows an expected S1 spectrum of signals from all contribution background sources as well as a selection of possible WIMP signals (left), and the projected sensitivity to SI WIMP-nucleon interaction (right). The expected XENON1T 90% C.L. SI WIMP-nucleon cross section upper limit reaches 1.6×10^{-47} cm^2 at WIMP mass of 50 GeV/c^2 with 2 ton·year exposure [7].
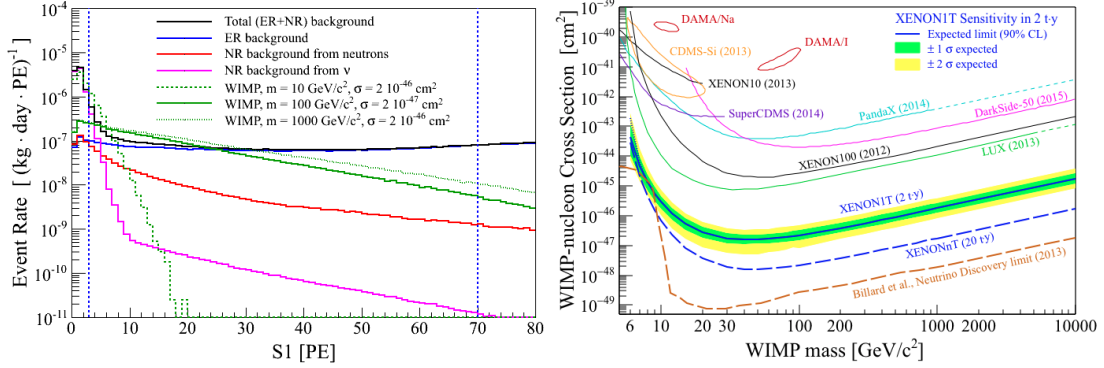
Figure 4: Left: Simulated S1 spectra of backgrounds and WIMP signals. The vertical dashed blue lines delimit the S1 region used in the sensitivity calculation. Only events with S2 > 150 PE are selected, and a 99.75% ER rejection with a flat 40% NR acceptance are assumed. Right: XENON1T sensitivity at 90% C.L. to SI WIMP-nucleon interaction.

5   Summary

The XENON collaboration aims to detect dark matter particle directly with a dual-phase time projection chamber. After the great achievement of XENON100, the next generation XENON1T is the first experiment to use LXe TPC at the ton scale. Its projected sensitivity is two orders of magnitude higher than XENON100. The first science run of XENON1T is expected to start this year.

References

[1] E. Aprile *et al.* [XENON Collaboration], "The XENON100 dark matter experiment", Astropart. Phys. **35** 573 (2012). doi:10.1016/j.astropartphys.2012.01.003 [arXiv:1107.2155]

[2] J. Angle *et al.* [XENON Collaboration], "First Results from the XENON10 Dark Matter Experiment at the Gran Sasso National Laboratory", Phys. Rev. Lett. **100** 021303 (2008). doi:10.1103/PhysRevLett.100.021303 [arXiv:0706.0039]

[3] E. Aprile *et al.* [XENON Collaboration], "Dark Matter Results from 225 Live Days of XENON100 Data", Phys. Rev. Lett. **109** 181301 (2012). doi:10.1103/PhysRevLett.109.181301 [arXiv:1207.5988]

[4] E. Aprile *et al.* [XENON Collaboration], "A low-mass dark matter search using ionization signals in XENON100", [arXiv:1605.06262]

[5] E. Aprile *et al.* [XENON Collaboration], "Lowering the radioactivity of the photomultiplier tubes for the XENON1T dark matter experiment", Eur. Phys. J. C**75** (2015) 546. doi:10.1140/epjc/s10052-015-3657-5 [arXiv:1503.07698]

[6] E. Aprile *et al.* [XENON Collaboration], "Conceptual design and simulation of a water Cherenkov muon veto for the XENON1T experiment", JINST **9**, P11006 (2014). doi:10.1088/1748-0221/9/11/P11006 [arXiv:1406.2374]

[7] E. Aprile *et al.* [XENON Collaboration], "Physics reach of the XENON1T dark matter experiment", JCAP **04** 027 (2016). doi:10.1088/1475-7516/2016/04/027 [arXiv:1512.07501]

Design of a Laser Frequency Stabilization for Cs Atomic Magnetometer

Dongok Kim[1], Younggeun Kim[1], Yunchang Shin[2], and Yannis K. Semertzidis[1,2],

[1]Korea Advanced Institute of Science and Technology(KAIST), Daejeon 34141, South Korea,
[2]Center for Axion and Precision Physics Research(CAPP), Institute for Basic Science(IBS), Daejeon 34141, South Korea

An atomic magnetometer can measure weak magnetic fields with a high sensitivity $\sim fT/\sqrt{Hz}$, which can be reached with a laser stabilization technique. This sensitivity can be used in axion-like field search. When the gradient of an axion domain wall interacts with the spin of a magnetometer, a very weak extraordinary magnetic field is generated and can be measured. We will develop an atomic magnetometer with Cesium vapor for detecting such magnetic fields from the axion like domain walls. The design of the laser frequency (852 nm) stabilization in the magnetometer using the dichroic atomic vapor laser lock (DAVLL) technique is presented.

1 Introduction

The geographically separated, synchronized optical magnetometers with high sensitivities could detect domain walls generated by an axion like field with a coupling to the spins of ordinary Standard Model particles [1][2][3]. The global network of optical magnetometers for exotic physics (GNOME) uses this method that can measure the transient event of encountering between the Earth and gradient of such domain walls interacting with spins of paramagnetic stable alkali metal like 133-Cesium or 87-Rubidium [1][2].

Especially, Cs possesses one stable isotope and it is more affordable relatively than Rb [4]. Also, M_x magnetometer using Cs reached high sensitivity around $fT/\sqrt{Hz}$, which can be realized only with high stabilization of a laser [2][4].

The frequency detuning of the probe light can reduce both the photon shot noise δB_{ph} and the fundamental noise δB_{ba} due to Stark effect by quantum fluctuation of the light [2]. Then the fundamental sensitivity limit δB_f is able to be determined by the atomic shot noise δB_{at} [2]

$$\delta B_f = \sqrt{\delta B_{at}^2 + \delta B_{ph}^2 + \delta B_{ba}^2} \approx \delta B_{at}. \quad (1)$$
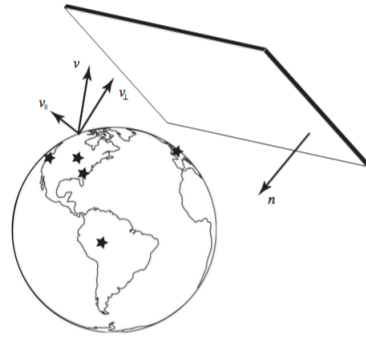
Figure 1: Schematic drawing of the global network of optical magnetometers

2 DAVLL for Cesium

The dichroic atomic vapor laser lock (DAVLL) is a laser frequency feedback system using polarization rotation by dichroic interaction with an atomic vapor [5].

The magnetic field on the Cesium vapor splits degenerated energy levels to distinguished levels have different energy and angular quantum number. Since the circularly polarized light $\sigma^\pm$ carries ± 1 angular momentum, the absorption light from different angular quantum numbered states can be happened by corresponding polarized light to conserve the angular momentum conservation. Such transitions have different energy levels determined by the strength of magnetic field.

The laser beam is linearly polarized initially. It means that it has an equal fraction of left and right circularly polarized lights. The frequency offset of the diode laser makes polarization bias and this causes a rotation of the polarization angle.

The D_2-transition ($6^2S_{1/2}$ to $6^2P_{3/2}$) energy levels of Cesium vapor is used [6].
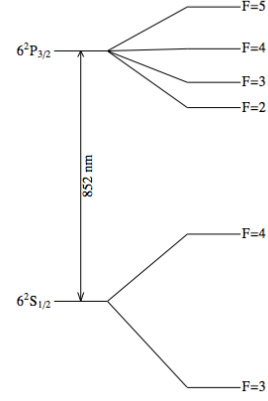
Figure 2: The Cesium D_2-transition energy level and its hyperfine levels.
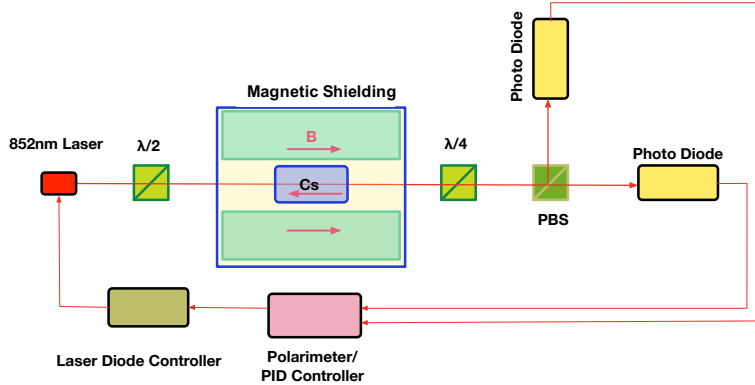
Figure 3: A schematic diagram of DAVLL system.

3 Setup

The experimental setup can be divided into two major parts; the optical and the electronics ones. The optical part generates the DAVLL signal, which is the difference between two polarization intensities. This signal can be used as an error signal for PID controller and the PID controller adjusts laser frequency of the diode laser by modulating laser diode controller. These electronics compose an automatic feedback loop for laser frequency stabilization.

3.1 Optics

The optics setup follows the schematic diagram shown in the Figure 3 and test setup is realized as in the Figure 4.
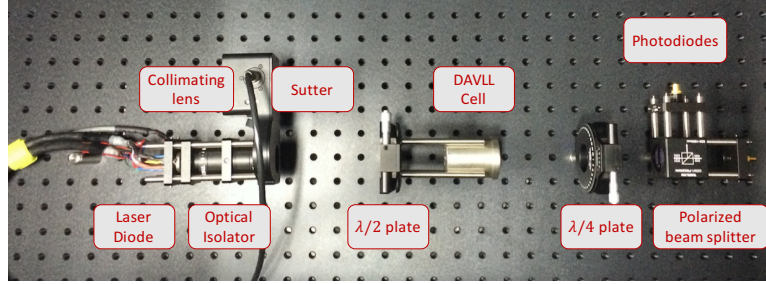
Figure 4: The experimental setup of DAVLL system.

It is used that the 852 nm laser diode (Eagleyard EYP-DFB-0852-00150-1500-TOC03-0005) for Cesium spectroscopy with operation power of $100 \sim 150$ mW. The current flow on the laser diode can be controlled by the laser diode controller (SRS LDC501).

The 10 mm diameter and 30 mm length of Cesium cell (TRIAD Quartz Cell) is used and wound by copper wires for applying the uniform magnetic field to split hyperfine energy levels. The magnetic field generated by the coils had been simulated and measured. The result is shown in the Figure 5. Currently, 28 G of magnetic field map is obtained and the target magnetic field is 200 G [5].
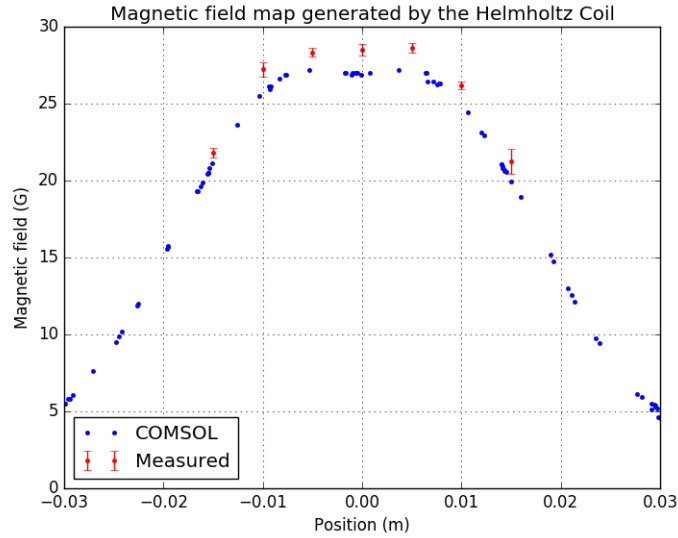
Figure 5: The magnetic field map on the Cesium cell.

3.2   Electronics

The photocurrents from two photodiodes can be converted into the voltage signal with the polarimeter board. The configuration is shown as in the Figure 6. Two photodiode (PD) inputs are copied and subtraction of them (DIFF) is generated. This DIFF signal will be used to modulate the laser diode controller via PID controller.
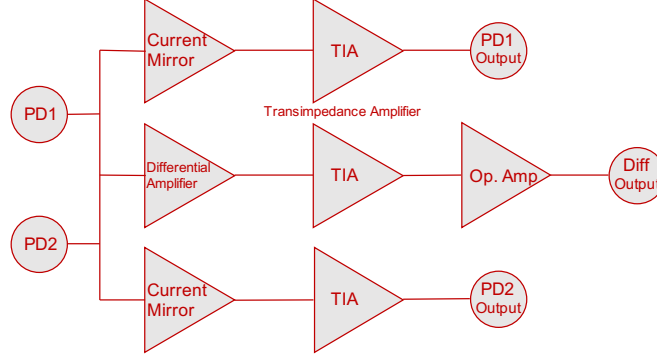
Figure 6: The scheme of the polarimeter board to generate DAVLL signal [4].

On our setup, the PCB board is on the manufacturing stage.

4   Summary

The atomic magnetometry can be used for searching axion-like field with its high sensitivity. One of the key techniques to increase sensitivity is using stabilized laser for the magnetometer. The DAVLL can be applied to stabilization. In this proceeding, the design of DAVLL system is presented and it will be installed to stabilize the laser frequency. We are planning to test laser stabilization and setup whole atomic magnetometer with stabilized laser.

Acknowledgement

References

[1] M. Pospelov et al, Phys. Rev. Lett. **110**, 021803 (2013)

[2] S. Pustelny et al, arXive:1303.5524v2 (2013)

[3] D. Budker and M. Romalis, Nat. Phys. 23, 229 (2007)

[4] M. Sturm, Masters thesis in Physics, TUM (2013)

[5] K. Corwin et al, Applied Optics 37, 15 (1998)

[6] D. Steck, Cesium D Line Data, available online at http://steck.us/alkalidata (revision 2.0.1, 2 May 2008)

[7] V. Yashchuk et al, Rev. Sci. Instrum. 71, 2 (2000)

CP-Conservation in QCD and why
only "invisible" Axions work

Jihn E. Kim

Center for Axion and Precision Physics (IBS), 291 Daehakro, Daejeon 34141, Korea

Among solutions of the strong CP problem, the "invisible" axion in the narrow axion window is argued to be the remaining possibility among natural solutions on the smallness of $\bar{\theta}$. Related to the gravity spoil of global symmetries, some prospective invisible axions from theory point of view are discussed. In all these discussions, including the observational possibility, cosmological constraints must be included.

1   Introduction

From a fundamental theory point of view, presumably the most fundamental parameters are given at a mass-defining scale which is considered to be the Planck mass $M_P \simeq 2.43 \times 10^{18}$ GeV. In this sense, we consider that a natural mass scale is the Planck mass and/or some scale suppressed by a small coupling compared to M_P, i.e. such as the GUT scale.

Then, all smaller mass scales much smaller than M_P are better to come from some symmetry arguments. Such symmetries are chiral symmetry for fermions and global symmetries for scalars. The smallness of electron mass compared to M_P by a factor of 10^{-22} is better come from a chiral symmertry. In the standard model(SM), the chiral symmetry is intrinsically implemented in the fermion representations in the SM. Even though the original Kaluza-Klein model for electromagnetism looked impressive, it fails badly here [1]. A spontaneously broken chiral symmetry leads to a massless Goldstone boson [2]. Among Goldstone bosons, invisible axion a [3] is the most interesting one as this conference witnesses. The invisible axion arises from spontaneously breaking the Peccei-Quinn(PQ) global symmetry [4].

2   The strong CP problem

Because of instanton solutions of QCD, there exists a gauge invariant vacuum parametrized by an angle $\bar{\theta}$ which is the coefficient of the gluon anomaly, $G^a \tilde{G}^a$. It is the flavor singlet and acted as the source for solving the U(1) problem of QCD [5]. Thus, this $\bar{\theta}$ term is physical, but it leads to the so-called "strong CP problem": it comes from the smallness of neutron electric dipole moment(nEDM), "Why is the nEDM so small?" [3]. In this regard, we try to explain why the invisible axion is the remaining solution in natural schemes toward understanding the strong CP problem as presented in the title.

If the CP violating coupling $\overline{g_{\pi NN}}$ is present, nEDM is calculated to be (with the CP
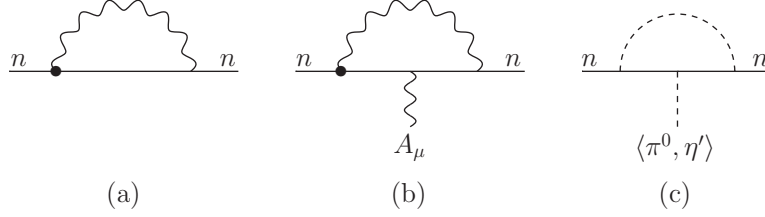
Figure 1: The bullets in (a,b) are the insertions of CP violating interaction shown in (c). VEVs of π^0 and η' break CP. (b) leads to nEDM.

conserving $g_{\pi NN}$ term)

$$\frac{d_n}{e} = \frac{g_{\pi NN}\overline{g_{\pi NN}}}{4\pi^2 m_N} \ln\left(\frac{m_N}{m_\pi}\right). \tag{1}$$

Figure 1 (c) shows $\overline{g_{\pi NN}}$, and Figure 1 (b) shows Eq. (1) [6]. If the $\bar\theta$ term is present in QCD, then π^0 can obtain a VEV and $|\overline{g_{\pi NN}}| = \bar\theta/3$ [3]. The non-observation of nEDM put a limit on $|\bar\theta|$ as less than 10^{-10}.

The most widely discussed solutions in the SM are (i) the "invisible" axion, (ii) massless up-quark, and (iii) calculable $\bar\theta$ models. The massless up-quark possibility is ruled out phenomenologically, $m_u = 2.15(0.15)\,\mathrm{MeV}$ [7]. The calculable models start with CP invariant Lagrangian, and calculate loop effects that the results are safe enough such that the loop generated $\bar\theta$ is less than 10^{-10}. Thus, calculable models within the SM gauge group, $\mathrm{SU}(3)_C \times \mathrm{SU}(2)_W \times \mathrm{U}(1)_Y$, are usually considered: the so-called Nelson-Barr type models [8, 9]. But, it is usually very difficult to remove the $\bar\theta$ term up to two-loop level. Barring the possibility of gauge or global symmetries, one introduces some kind of discrete symmetry toward this objective [10], or some structure on the coupling texture [9]. The texture possibility may rely on discrete symmetries. Spontaneously broken discrete symmetries lead to cosmological domain wall problem. Thus, the calculable possibility is not so attractive compared to introducing just one spontaneously broken global symmetry which we discuss below.

3   The PQ symmetry

Since 1964, there has been always a need for a theory of weak CP violation. The strong CP problem is interwined with the weak CP, $\bar\theta = \theta_{\mathrm{QCD}} + \theta_{\mathrm{weak}}$, where θ_{weak} is the one contributed by the weak CP violation. Now, the Kobayashi-Maskawa(KM) model [11] is accepted for the SM weak CP violation, and there is no need to consider the weak CP in gauge groups beyond $\mathrm{SU}(3)_C \times \mathrm{SU}(2)_W \times \mathrm{U}(1)_Y$. But, in the middle of 1970's, it was not so and many introduced their own models of weak CP violation and even in $\mathrm{SU}(3)_C \times \mathrm{SU}(2)_W \times \mathrm{U}(1)_Y$ there were many [12, 11, 13, 14, 15]. For example, the first gauge theory model was Mohapatra's [12], which appeared as the 2nd example of Ref. [11] but discarded there with the statement 'phenomenologically unacceptable'. One notable one is Weinberg's weak CP violation model [13] which was presented when he used the sabbatical year at SLAC. It was the time when the third quark family was not discovered (even though τ was discovered), and he tried to introduce the weak CP violation in the Higgs potential, without introducing the third family quarks. With two Higgs doublets, he

applied the Glashow-Weinberg method not to have tree-level flavor-changing neutral processes, *i.e.* H_u coupling to up-type quarks and H_d coupling to down-type quarks [16]. Then, the weak CP violation mattered in the potential,

$$V_{\mathrm{W}} = \frac{1}{2} \sum_I m_I^2 \phi_I^\dagger \phi_I + \frac{1}{4} \sum_{IJ} \left\{ a_{IJ} \phi_I^\dagger \phi_I \phi_J^\dagger \phi_J + b_{IJ} \phi_I^\dagger \phi_I \phi_J^\dagger \phi_J + (c_{IJ} \phi_I^\dagger \phi_I \phi_J^\dagger \phi_J + \mathrm{H.c.}) \right\} \quad (2)$$

Weinberg's necessary condition for the existence of CP violation is non-zero c_{IJ} terms. Peccei and Quinn noticed that there emerges a global symmetry by removing the c_{IJ} terms in V_{W}, and has the famous PQ potential

$$V_{\mathrm{PQ}} = \frac{1}{2} \sum_I m_I^2 \phi_I^\dagger \phi_I + \frac{1}{4} \sum_{IJ} \left\{ a_{IJ} \phi_I^\dagger \phi_I \phi_J^\dagger \phi_J + b_{IJ} \phi_I^\dagger \phi_I \phi_J^\dagger \phi_J \right\} \quad (3)$$

which is the basis for the Peccei-Quinn-Weinberg-Wilczek(PQWW) axion [17]. Soon, it was ruled out chiefly by the results on beam dump experiments [18]. Non-observation of the PQWW axion triggered interests in calculable models after whose period the "invisible" axion replaced the PQWW axion in the solutions of the strong CP problem. The PQWW axion is not relevant in this conference which will discuss mostly on the cosmic axion search.

4 The "invisible" axion

After the above tries, finally the "invisible" axions are discovered. These are known as the KSVZ axion [19, 20] and the DFSZ axion [21]. As we witnessed in the previous section, if only a few terms in all possible terms in V are considered, there may appear global symmetries. It has a profound implication in some ultra-violet completed theories. It is known that quantum gravity does not allow global symmetries. However, gauge symmetries are allowed. One possible quantum gravity phenomenon, the wormhole, can connect our Universe to a shadow world. Any method to obtain an effective interaction by cutting off the wormhole will send back to our Universe the flown-out gauge charges due to the existence of flux lines. Figure 2 (a) depicts this phenomenon. But, global charges do not carry flux lines and it is considred that global symmetries are not respected by gravity.

Figure 2 (b) shows all allowed couplings if some discrete symmetry is present. However, if we consider only a few dominant terms shown in the lavender square, then there can appear some global symmetries.

These global symmetries are approximate and broken by the terms in the red parts. The red part adjacent to the lavender symbolizes the terms in the potential V. One such example is heavy axions or axizilla [22], which cannot solve the strong CP problem. The reds not connected to the lavender break the global symmetry by non-Abelian gauge anomalies, and the QCD axion obtains mass basically by this term. In any case, a PQ global symmetry can be obtained at least approximately from an ultra-violet completed theory.

KSVZ: Q_{em}	$c_{a\gamma\gamma}$
0	-2
$\pm\frac{1}{3}$	$-\frac{4}{3}$
$\pm\frac{2}{3}$	$\frac{2}{3}$
± 1	4
(m, m)	$-\frac{1}{3}$

Table 1: KSVZ model with $m_u = 0.5\, m_d$. (m, m) in the last row means m quarks of $Q_{\mathrm{em}} = \frac{2}{3}\, e$ and m quarks of $Q_{\mathrm{em}} = -\frac{1}{3}\, e$.
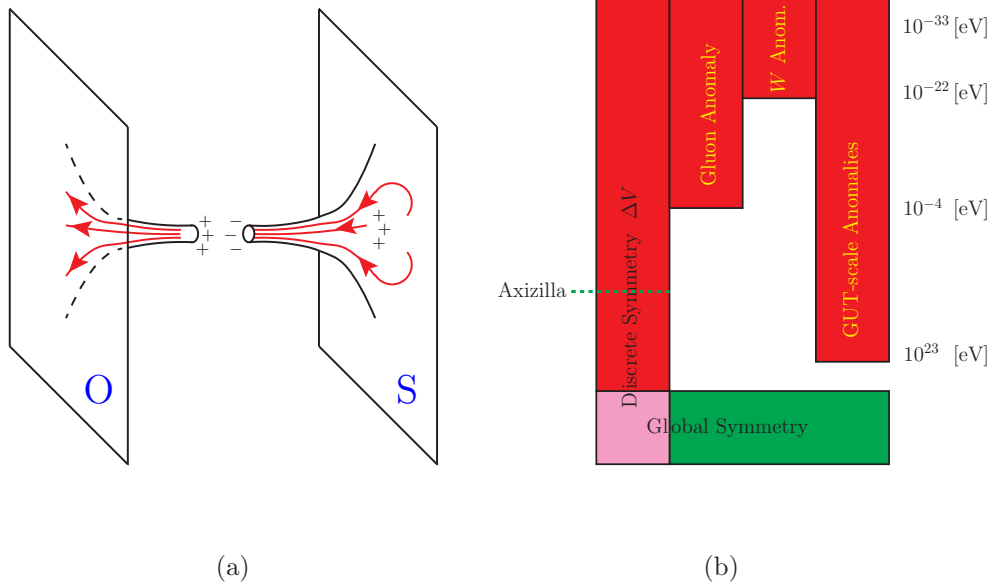
Figure 2: (a) A wormhole connecting our world to a shadow world, and (b) terrms allowed by discrete and global symmetries.

Initially, "invisible" axions were ignored as "invisible", but there surfaced a dim hope of detecting it by cavity detectors [23]. Then, there was a need to calculate the axion-photon-photon coupling, which has been done in Ref. [24, 3] for several invisible axion models. So far, all the existing calculations have been published by the author's group alone [25, 26, 27] with some confirmation by J. Ashfaque, H.P. Nilles and P. Vaudrevange.

Table 1 shows the axion-photon-photon couplings in several KSVZ models. Table 2 shows the axion-photon-photon couplings in several DFSZ models. Here, H_d and H_u^* imply that they give mass to e. GUTs and SUSY choose appropriate Higgs doublets and always give $c_{a\gamma\gamma} = \frac{2}{3}$.

Table 3 shows $c_{a\gamma\gamma}$ for a few string compactifications [28, 29] from heterotic string. In these string compactifications, it is required to start from a model allowing correct SM phenomenologies. This is the reason that there has not appeared any calculation from intersecting brane models.

Therefore, it is a key question how the PQ symmetry is defined. As we witnessed in Eqs. (2) and (3), a small number of terms in V may have a chance to introduce a global symmetry. However, the way Eq. (3) was declared is ad hoc. It

DFSZ: (q^c-e_L) pair	Higgs	$c_{a\gamma\gamma}$
non-SUSY (d^c, e)	H_d	$\frac{2}{3}$
non-SUSY (u^c, e)	H_u^*	$-\frac{4}{3}$
GUTs		$\frac{2}{3}$
SUSY		$\frac{2}{3}$

Table 2: DFSZ model with $m_u = 0.5\, m_d$.

String:	$c_{a\gamma\gamma}$	Comments
Ref. [25]	$-\frac{1}{3}$	Approximate
Ref. [26, 27]	$\frac{2}{3}$	Anom. U(1)

Table 3: String model. Comments are for U(1)$_{\rm PQ}$. In the last line, $c_{a\gamma\gamma} = (1 - 2\sin^2\theta_W)/\sin^2\theta_W$ with $m_u = 0.5\, m_d$.
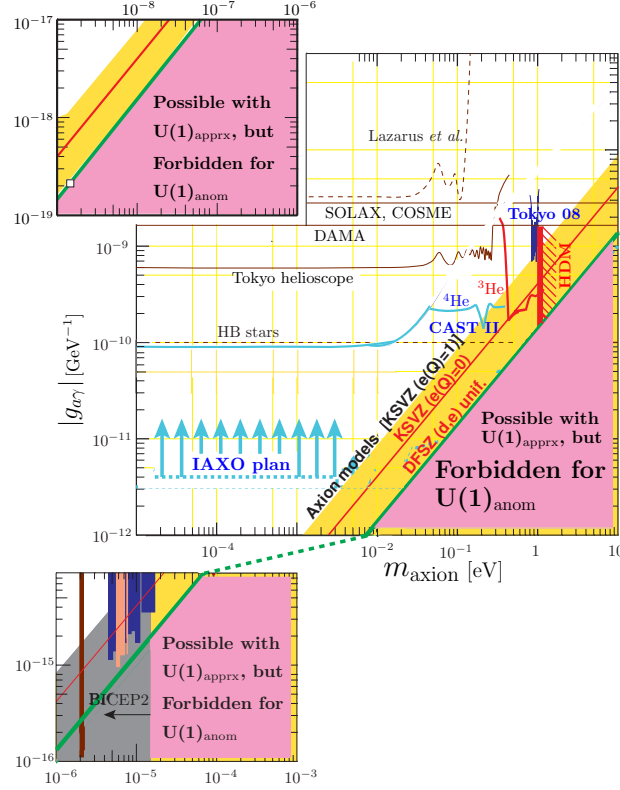
Figure 3: Axion search bounds and some model lines.

amounts to declaring a global symmetry from the outset. It is better if some ultra-violet theory forbids some terms such as c_{IJ} of Eq. (2). The well-known effective interacion example allowed by gauge symmetry is Weinberg's neutrino mass in the SM, $\ell\ell H_u H_u/M$ where M is the scale where a more satisfactory theory is defined. In this vein, suppose the phase of the SM singlet σ is "invisible" axion [19]. Then, the PQ symmetry defining term can be a renormalizable term, $H_u H_d\,\sigma^2$. But, then one must fine-tune the coefficient of this term to have a small ratio $v_{\rm ew}/f_a$, which is the reason that the non-SUSY DFSZ model has a fine-tuning problem [30]. For the KSVZ model, the intermediate scale interaction is

$$\bar{Q}\,Q\,\sigma + {\rm H.c.} \tag{4}$$

where Q is a heavy quark, and the VEV of σ is determined by parameters at the intermediate scale. At the electroweak scale, its effect appears as $(a/f_a)G^a_{\mu\nu}\tilde{G}^{a\,\mu\nu}$ and no fine-tuning is needed even in this non-SUSY SM. In SUSY models, one may consider a renormalizable superpotential term $H_u H_d\,\sigma$ for defining the PQ symmetry. Then, a natural scale for the VEV of σ is $v_{\rm ew}$, which is ruled out phenomenologically. We can use some discrete symmetry to forbid it as depicted in Fig. 2 (b). Then, the most important term in the superpotential defining the PQ symmetry is $H_u H_d\,\sigma^2/M$ as suggested along the way to obtain a reasonable μ [31].

This μ term belongs to the lavender part of Fig. 2 (b). Furthermore, if the U(1) global sym-

metry so defined is exact, then there is no superpotential terms, *i.e.* there is no red part above the lavender box. Then, the situation is as shown in Fig. 4, and the PQ symmetry defined by

$H_u H_d \sigma^2/M$ is exact. However, the red boxes disjoint from the horizontal green are present, *i.e.* the anomaly terms are present, breaking this global symmetry. If this global symmetry arises from anomalous U(1) gauge symmetry from string compactification [32], then the resulting global symmetry is free of gravity spoil and can be a good PQ symmetry for the "invisible" axion U(1)$_\Gamma$. The axion-photon-photon couplings of string axions are listed in [27], and the model-independent axion point is shown in [33], which is reproduced in Fig. 3. The lavender part of Fig. 3 is forbidden if the PQ global symmetry is U(1)$_\Gamma$, derived from the anomalous U(1) gauge symmetry. However, if the PQ global symmetry is approximate, this lavender part is also allowed as shown in Ref. [25].

Figure 4: Global symmetry breaking by anomalies. If an axion is present for a non-Abelian gauge group G_N, then the vacuum angle $\theta_N = 0$ at the minimum of that axion potential.
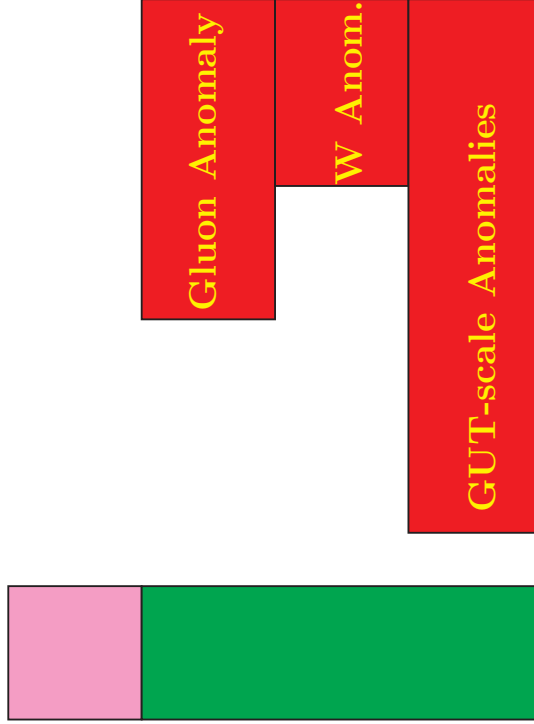
5 The QCD axion in cosmology

The axion solution of the strong CP problem is a cosmological solution. The vacuum of the "invisible" axion potential generated by the gluon anomaly is at $\bar{\theta} = 0$ [34]. If the axion vacuum starts from $a/f_a = \theta_1 \neq 0$, then the vacuum oscillates and this collective motion behaves like cold dark matter(CDM) [35], for which a recent calculation on ρ_a is given in [36].

Topological defects of global U(1)$_\Gamma$ produce an additional axion energy density by the decay of string-wall system, ρ_{st}, for which a recent calculation for $N_{\rm DW} = 1$ models has been given in [37] as $\rho_{st} \sim O(10)\,\rho_a$.

The cosmological axion domain wall number should be 1 [38], which is an important constraint in any axion models. Identifying different vacua has started with Lazarides and Shafi [39], and the most important application obtaining $N_{\rm DW} = 1$ is realized in the Goldstone boson direction [40, 33].

6 Detection of axions

Since most other participants in this conference will discuss on the possibility of detecting "invisible" axions, I will present here just the exclusion plot in the interaction versus axion mass plane, shown in Fig. 3. The detection rate in the cavity experiments are calculated in axio-electrodynamics in Ref. [41].

7 Conclusion

Here, I discussed why we need "invisible" axions for a solution of strong CP problem. One prospective global symmetry toward "invisible" axion is the global symmetry $U(1)_\Gamma$, obtained from anomalous $U(1)$ gauge symmetry. In this case, we argued that there is no obstruction of $U(1)_\Gamma$ by quantum gravity effect. We also commented some cosmological problems, and the "invisible" axion from $U(1)_\Gamma$ has $N_{DW} = 1$ [42, 33].

Acknowledgments

References

[1] E. Witten, "Fermion quantum numbers in Kaluza-Klein theory," SHELTER ISLAND II (Shelter Island, NY, 1-2 June 1983) proceedings, ed. R. Jackiw, N.N. Khuri, S. Weinberg, and E. Witten (MIT Press, Cambridge, MA, 1985). Published in Conf. Proc. C8306011 (1983) 227.

[2] See, for example, T.W.B. Kibble, "The Goldstone theorem," Int. Conf. on Particles and Fields 1967 (Rochester, NY, 28 Aug.-1 Sep. 1967) proceedings, ed. G.S. Guralnik, C.R. Hagen, and V.S. Mathur (Interscience, NY, 1967). Published in Conf.Proc. C670828 (1967) 277-304.

[3] See, for example, J.E. Kim and G. Carosi, "Axions and the strong CP problem," Rev. Mod. Phys. **82** (2010) 557 [arXiv:0807.3125 [hep-ph]].

[4] R.D. Peccei and H.R. Quinn, "CP conservation in the presence of instantons," Phys. Rev. Lett. **38** (1977) 1440 [doi: 10.1103/PhysRevLett.38.1440].

[5] G. 't Hooft, "How instantons solve the U(1) problem," Phys. Rep. **142** (1986) 357 [doi: 10.1016/0370-1573(86)90117-1].

[6] R.J. Crewther, P. Di Vecchia, G. Veneziano, and E. Witten, "Chiral estimate of the electric dipole moment of the neutron in quantum chromodynamics," Phys. Lett. B **88** (1979) 123 [**91** (1980) 487 (E)] [doi: 10.1016/0370-2693(80)91025-4, 10.1016/0370-2693(79)90128-X].

[7] A.V. Manohar and C.T. Sachrajda, "Quark masses," in PDG book [K.A. Olive *et al.* (Particle Data Group), Chin. Phys. **C38** (2014) 090001(URL: http://pdg.lbl.gov)].

[8] A.E. Nelson, "Naturally weak CP violation," Phys. Lett. B **136** (1984) 387 [doi:10.1016/0370-2693(84)92025-2].

[9] S.M. Barr, "Solving the strong CP problem without the Peccei-Quinn symmetry," Phys. Rev. Lett. **53** (1984) 329 [doi:10.1103/PhysRevLett.53.329].

[10] G. Segre and H.A. Weldon, "Natural suppression of strong P and T violations and calculable mixing angles in SU(2)×U(1)," Phys. Rev. Lett. **42** (1979) 1191 [doi:10.1103/PhysRevLett.42.1191].

[11] M. Kobayashi and T. Maskawa, "CP violation in the renormalizable theory of weak interaction," Prog. Theor. Phys. **49** (1973) 652 [doi: 10.1143/PTP.49.652].

[12] R.N. Mohapatra, "Renormalizable model of weak and electromagnetic interactions with CP violation," Phys. Rev. D **6** (1972) 2023 [doi: 10.1103/PhysRevD.6.2023].

[13] S. Weinberg, "Gauge theory of CP violation," Phys. Rev. Lett. **37** (1976) 657 [doi:10.1103/PhysRevLett.37.657].

[14] B.W. Lee, "Gauge theories of microweak CP violation," Phys. Rev. D **15** (1977) 3394 [doi: 10.1103/PhysRevD.15.3394].

[15] H. Georgi, "A model of soft CP violation," Hadronic J. **1** (1978) 155.

[16] S.L. Glashow and S. Weinberg, "Natural conservation laws for neutral currents," Phys. Rev. D **15** (1977) 1958 [doi: 10.1103/PhysRevD.15.1958].

[17] F. Wilczek, "Some problems in gauge field theories," in "Proc. Unification of Elementary Forces and Gauge Theories: Ben Lee Memorial International Conference on Parity Nonconservation Weak Neutral Currents and Gauge Theories," FNAL, Batavia, IL, 20-22 Oct 1977, ed. D.B. Cline and F.E. Mills (Hardwood Academic Press, London, 1978) p.607;
S. Weinberg, "Conference summary," *ibid.* p727-756.

[18] R.D. Peccei, "A short review on axions," in Proc. "19th ICHEP, Tokyo, 23-30 Aug 1978," ed. S. Homma, M. Kawaguchi, and H. Miyazawa (Physical Society of Japan, Tokyo, 1978) p.385-388.

[19] J.E. Kim, *Weak interaction singlet and strong CP invariance*, Phys. Rev. Lett. **43** (1979) 103 [doi: 10.1103/PhysRevLett.43.103].

[20] M.A. Shifman, V.I. Vainshtein, V.I. Zakharov, *Can confinement ensure natural CP invariance of strong interactions?*, Nucl. Phys. B **166** (1980) 493 [doi:10.1016/0550-3213(80)90209-6].

[21] M. Dine, W. Fischler and M. Srednicki, *A simple solution to the strong CP problem with a harmless axion*, Phys. Lett. B **104** (1981) 199 [doi:10.1016/0370-2693(81)90590-6];
A. P. Zhitnitsky, *On possible suppression of the axion hadron interactions (in Russian)*, Sov. J. Nucl. Phys. **31**, 260 (1980), Yad. Fiz. **31** (1980) 497.

[22] J.E. Kim, "Is an axizilla possible for di-photon resonance?," Phys. Lett. B **755** (2016) 190 [arXiv:1512.08467 [hep-ph]].

[23] P. Sikivie, "Experimental tests of the "invisible" axion," Phys. Rev. Lett. **51** (1983) 1415 and *ibid.* **52** (1984) 695 (E) [doi:10.1103/PhysRevLett.51.1415].

[24] J.E. Kim, "Constraints on very light axions from cavity experiments," Phys. Rev. D **58** (1998) 055006 [arXiv:hep-ph/9802220].

[25] K-S. Choi, I-W. Kim, and J.E. Kim, "String compactification, QCD axion and axion-photon-photon coupling," JHEP **0703** (2007) 116 [arXiv:hep-ph/0612107].

[26] J.E. Kim, "Calculation of axion-photon-photon coupling in string theory," Phys. Lett. B **735** (2014) 95 [arXiv:1405.6175 [hep-ph]].

[27] J.E. Kim and S. Nam, "Couplings between QCD axion and photon from string compactification," Phys. Lett. B **759** (2016) 149 [arXiv:1603.02145 [hep-ph]].

[28] J.E. Kim and B. Kyae, "Flipped SU(5) from $\mathbf{Z}_{12-I}$ orbifold with Wilson line," Nucl. Phys. B **770** (2007) 47 [arXiv: hep-th/0608086].

[29] J-H. Huh, J.E. Kim, and B. Kyae, "SU(5)$_{\mathrm{flip}}\times$SU(5)$'$ from $\mathbf{Z}_{12-I}$," Phys. Rev. D **80** (2009) 115012 [arXiv:0904.1108 [hep-ph]].

[30] H.K. Dreiner, F. Staub, and L. Ubaldi, "From the unification scale to the weak scale: A self consistent supersymmetric Dine-Fischler-Srednicki-Zhitnitsky axion model," Phys. Rev. D **90** (2014) 055016 [arXiv:1402.5977 [hep-ph]].

[31] J.E. Kim and H.P. Nilles, "The μ problem and the strong CP problem," Phys. Lett. B **138** (1984) 150 [doi:10.1016/0370-2693(84)91890-2].

[32] J.J. Atick, L. Dixon, and A. Sen, "String calculation of Fayet-Iliopoulos d-terms in arbitrary supersymmetric compactifications," Nucl. Phys. B **292** (1987) 109 [doi:10.1016/0550-3213(87)90639-0];
M. Dine, I. Ichinose, and N. Seiberg, "F terms and dterms in string theory," Nucl. Phys. B **293** (1987) 253 [doi: 10.1016/0550-3213(87)90072-1].

[33] J.E. Kim, "Axionic domain wall number related to U(1)anom global symmetry," Phys. Lett. B **759** (2016) 58 [arXiv:1604.00716 [hep-ph]].

[34] C. Vafa and E. Witten, "Parity conservation in QCD," Phys. Rev. Lett. **53** (1984) 535 [doi:10.1103/PhysRevLett.53.535].

[35] J.E. Kim, Y.K. Semertzidis, and S. Tsujikawa, "Bosonic coherent motions in the Universe," Front. Phys. **2** (2014) 60 [arXiv:1409.2497 [hep-ph]].

[36] K.J. Bae, J-H. Huh, and J.E. Kim, "Update of axion CDM energy," JCAP **0809** (2008) 005 [arXiv:0806.0497 [hep-ph]].

[37] T. Sekiguchi, "Understanding the scaling behavior of axion cosmic strings," talk presented at Sapporo Summer Institute, Sapporo, Hokkaido, Japan, 25 Aug. 2016.

[38] P. Sikivie, "Of axions, domain walls and the early Universe ," Phys. Rev. Lett. **48** (1982) 1156 [doi:10.1103/PhysRevLett.48.1156].

[39] G. Lazarides and Q. Shafi, "Axion models with no domain wall problem," Phys. Lett. B **115** (1982) 21 [doi:10.1016/0370-2693(82)90506-8].

[40] K. Choi and J.E. Kim, "Domain walls in superstring models," Phys. Rev. Lett. **55** (1985) 2637 [doi:10.1103/PhysRevLett.55.2637].

[41] J. Hong, J.E. Kim, S. Nam, and Y. Semertzidis, "Calculations of resonance enhancement factor in axion-search tube-experiments," [arXiv:1403.1576 [hep-ph]].

[42] E. Witten, "Cosmic superstrings," Phys. Lett. B **153** (1985) 243 [doi:10.1016/0370-2693(85)90540-4].

³He gas handling system and RF discharge for optical pumping

Younggeun Kim[1],

[1] Korea Advanced Institute of Science and Technology (KAIST)

Axions are hypothetical pseudo scalar particles that appear in the solution of the strong CP problem. Axions can also be a dark-matter candidate if their mass is in light regime. Many of these haloscope experiments to detect axions are based on this assumption. In addition, Moody and Wilczek postulated an interaction between monopole and dipole masses that can be mediated by axions at macroscopic scale [1]. We propose new experiment that can detect axions by measuring by pseudo-magnetic field induced between monopole and dipole. For this experiment, we have developed ³He polarization system using metastable exchange optical pumping (MEOP) technique.

1 Introduction

Axion Resonant InterAction DetectioN Experiment (ARIADNE) is measuring monopole-dipole interactions to detect axion like particle. In ARIADNE concept is, the axion mediates interaction between monopole-dipole, and this interaction can be expressed as pseudo magnetic field. It is also macroscopic interaction, therefore one can detect pseudo-magnetic field as a function of distance of two objects. We calculated the potential in the case of monopole-dipole interaction case, the unpolarized mass is cylinder shape and polarized ³He, as the function of distance between two objects. ³He is used in this experiment because it has long relaxation time and can be treated as an elementary particle. To make polarized ³He, we used Metastable Exchange Optical Pumping (MEOP). To transport ³He gas to the optics and to do experiment we construct gas handling system and test ³He discharge using RF amplifier.

2 Theory

2.1 Monopole-dipole Interaction

According to monopole-dipole interaction potential,

$$U(r) = (g_s^1 g_p^2) \frac{\hat{\sigma_2} \cdot \hat{r}}{8\pi M_2} [\frac{1}{\lambda r} + \frac{1}{r^2}] e^{-\frac{r}{\lambda}} \ , \tag{1}$$

this interaction is spin dependent, and distance dependent potential. From experiment schematic, polarized ³He is needed rule of spin dependent part, and rotating mass with n-section cylinder will make distance dependent effective B- field. The potential form is $U(r) = -\nabla \cdot \hat{\sigma_2}$, and we detect the effective B- field $\vec{B}_{eff} = \frac{2\nabla V(r)}{\hbar \gamma}$, γ is gyromagnetic ratio.
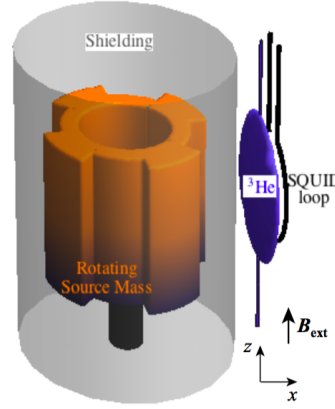
Figure 1: ARIADNE experimental schematic for monopole-dipole interaction [3].

2.1.1 Potential calculation for cylinder model

We calculate the potential generated by monopole dipole interaction with surface approximation, and get analytic solution,

$$U_T(r) = -(g_s^1 g_p^2)\frac{\hat{\sigma}_2 \cdot \hat{z}}{4M_2} n_N \int_{\epsilon}^{\sqrt{C^2+\epsilon^2}} e^{-t/\lambda} dt \simeq -(g_s^1 g_p^2)\frac{\hat{\sigma}_2 \cdot \hat{z}}{4M_2} n_N \lambda e^{-\epsilon/\lambda} \tag{2}$$

however it is 1/2 small than "Resonantly Detecting Axion-Mediated Forces with Nuclear Magnetic Resonance" paper [3]. In this approximation we assume the cylinder as disk with effective radius "C". In Monte-Carlo calculation for this disk model and real cylinder model get similar trend line with our calculation.

(a) Cylinder

(b) Disk
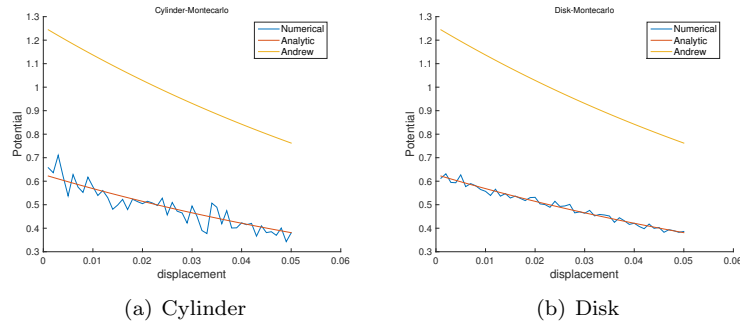
Figure 2: Monte-Carlo Calculation

2.2 MEOP

MEOP is polarizing method of ^{3}He using RF discharge and 1083nm laser. RF discharge excites the atoms into the excited states, and ppm fraction of them will be in the metastable state,

2^3S_1. We apply magnetic field about 50G, spin state of electron and nuclei will couple and make hyperfine structure. Left circularly polarized 1083nm laser will pump the spin state to the $m_F = 1$, and it will decay into sub level of 2^3S_1. By spin exchange collision, the spin state 1^1S_1 in $m_F = -1/2$ will be in the $m_F = 1/2$ states.
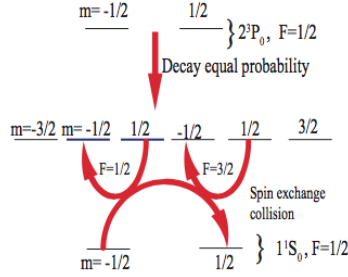
Figure 3: MEOP schematic

3   Experiment setup

3.1 ^{3}He gas handling system

3.1.1   Gas handling system

In ARIADNE experiment, we are going to use ^{3}He as polarized mass object. We need to transport gas from ^{3}He tank with 120atm in 0.46L to non magnetic part which contains polarization and experiment part. After experiment we need to deliver gas to recovery tank denote as R_2. Also we need to transport gas from R_2 to the other gas flow line. In emergency case, this system will separate non magnetic part and magnetic part and recover to the emergency tank. (a) is ^{3}He gas bottle with 120 atm in 0.46L and compressor connected with 6 in gas handling

Figure 4: Gas handling system

system. (b) is emergency tank which is connected to 7. (c) is recovery tank connected with gas

(a)

(b)

(c)

(d)
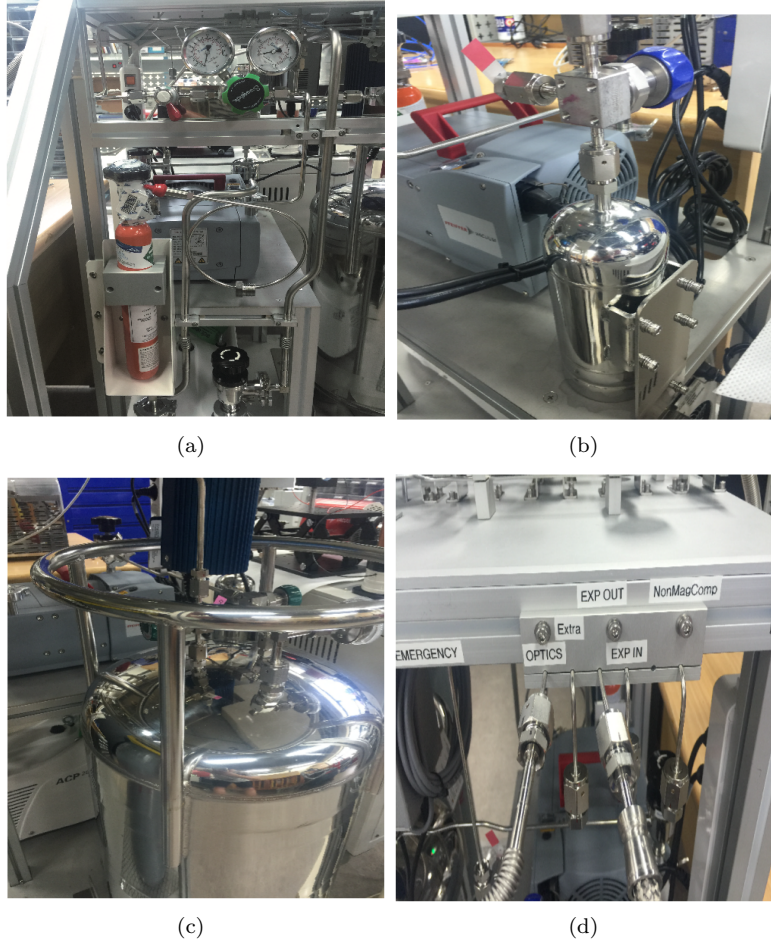
Figure 5: Part of gas handling system

compressor. (d) is the lines which will be connected to non-magnetic part, such as optics system, and non magnetic compressor and experiment part which is 2, 3, 4, 5 part in gas handling system.

3.1.2 Gas compression test

In gas handling system we need to restore almost of ^{3}He used in experiment. We design the restore tank that can contain all of ^{3}He gas which is filled in 120atm in 0.46L bottle. The gas used in experiment will be compressed to the restore tank using compressor. According to our compression test, we can compress gas to the tank over 1atm. That means we can restore the ^{3}He gas which is used in experiment, and recycle it. As a graph, we can increase the restore tank pressure 0.1MPa per 20 minutes in highest flow rate (200sccm).
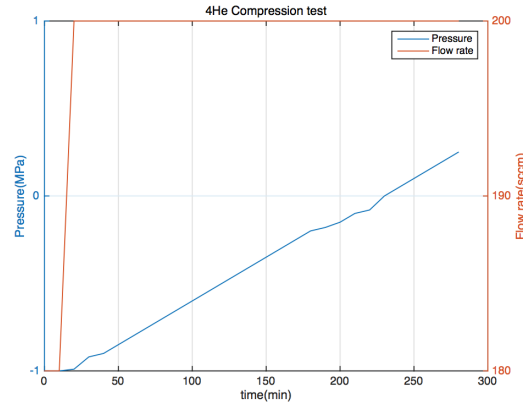
Figure 6: Compression test

3.2 RF discharge study

Our RF amplifier is IFI solid state amplifier, SXXL150 Model, designed to amplifying signal from function generator. This instrument can obtain 1.5 30.0MHz frequency wave and output power is 150W. Using function generator, we make input signal to the amplifier and changing gain of it, we check when ^{3}He cell is discharged. Our ^{3}He has 1mbar pressure and 2 inch diameter and 6cm height. We scan the frequency range from 1.6MHz to 3.0MHz. The amplitude that measured by oscilloscope was over 50V, and approximately about 70V and the frequency was about 400kHz. We measure the discharge maintaining time after ^{3}He is discharged.
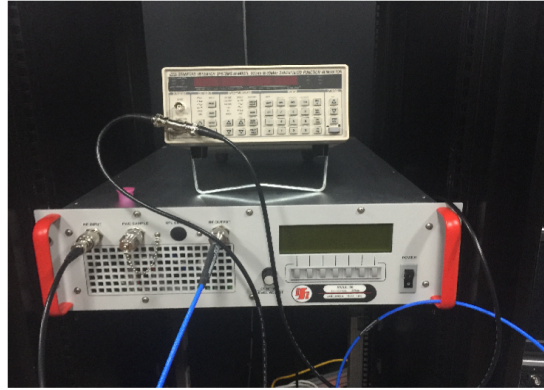
Figure 7: SXXL amplifier and function generator

Figure 8: [3]He discharge

3.2.1 Forward, Reflected power measurement

From this measurement if the gain is over 50W, the [3]He is ignited and for 2.0MHz case and 2.6MHz case the fluctuation of forward and reflected power is stable, however the other cases? fluctuation is huge.
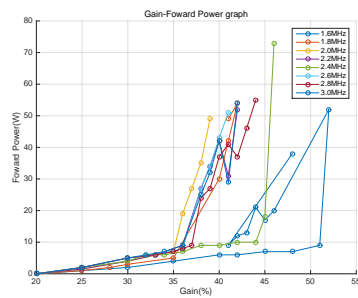
(a)
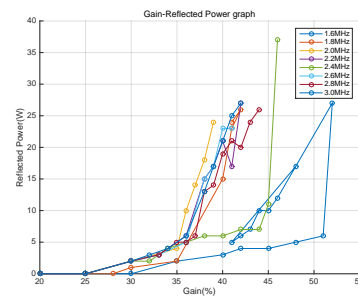
(b)

3.2.2 Discharge maintain time measurement and glow gain-frequency measurement

For 2.0MHz case, the fluctuation is small so we expect it will has long discharge time, however forwarding power decrease slowly, and it turns off at 220 second. For 2.6MHz case forward power is decreased to 40W and maintain over 6 minutes with average forward about 40W. We turn off discharging when 6minutes reached. The first gain when ^{3}He starts discharge is at 43% gain average with standard deviation is 2.8785.
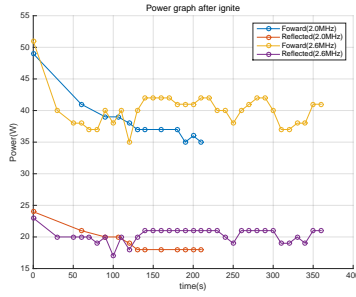
(c)
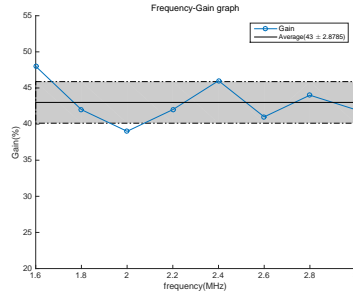
(d)

4   Conclusion

We construct gas handling system for transport ^{3}He gas to the experiment part. We can compress the gas in the flow line to the restore tank which is designed to restore ^{3}He gas in 1atm. According to the compression test using ^{4}He gas, we get compression rate 0.1MPa per 20minutes in 200sccm flow rate. To do MEOP, we need to discharge the ^{3}He cell. In real experiment we will discharge 1m long cell, so we use high power RF amplifier. For test cell with 2 inch diameter and 6cm long cell we can discharge this cell at 43% gain average. For 2.0MHz and 2.6MHz case we can discharge the cell stablely. The glass cell which will be filled with ^{4}He or ^{3}He gas in 1mbar and to increase relaxation time T2, we will construct cleaning system of wall of cell, and we will test polarization of ^{3}He gas using optical polarimeter.

References

[1] J. E. Moody and F. Wilczek. "New macroscopic forces?" Physical Review, 30: 130 − 138, July 1984

[2] F. D. Colegrove, L. D. Schearer, and G. K. Walters. Polarization of He3 Gas by Optical Pumping. Physical Review, 132:2561?2572, Dec. 1963.

[3] A. Arvanitaki and A. A. Geraci. Resonantly Detecting Axion-Mediated Forces with Nuclear Magnetic Resonance. Physical Review Letters, 113(16):161801, Oct. 2014.

Dish Antenna Searches for WISPy Dark Matter: Directional Resolution Small Mass Limitations

Stefan Knirck[1,2,], Joerg Jaeckel[1]*

[1]Institute for Theoretical Physics, Heidelberg University, Germany
[2]Department of Physics, Graduate School of Science, The University of Tokyo, Japan
[*]speaker

Hidden photon and axion-like dark matter may be detected using spherical reflective surfaces such as dish antenna setups converting some of the dark matter particles into photons and concentrating them on a detector. These setups may be used to perform directional searches measuring the dark matter momentum distribution. We briefly review the photon distribution one expects to detect with such an antenna and directional resolution in ray approximation. Furthermore we consider the regime $m_{DM} \lesssim (R_{sp} v_{DM})^{-1}$ where this approximation does not hold anymore due to photon wavelengths exceeding the expected distribution widths. We discuss how this affects the expected distributions and experimental implications.

1 Introduction

Hidden photons and Axion-like-particles (ALPs) turn out to be prime WISPy dark matter candidates, c.f. for example [1, 2]. Hidden photons can be described by the following Lagrangian

$$\mathcal{L} = -\frac{1}{4}F^{\mu\nu}F_{\mu\nu} - \frac{1}{4}X^{\mu\nu}X_{\mu\nu} - \frac{\chi}{2}F^{\mu\nu}X_{\mu\nu} + m_X^2 X^\mu X_\mu + j^\mu A_\nu, \tag{1}$$

where $F^{\mu\nu}$ and $X^{\mu\nu}$ are the ordinary and hidden photon field strength linked to the gauge fields A^μ and X^μ, respectively. m_X is the mass of the hidden photons and j^μ denotes the coupling to matter. Solving the equations of motion one finds for a hidden photon momentum mode $\mathbf{k}_{DM}$

$$\begin{pmatrix} \mathbf{E} \\ \mathbf{E}_{\text{hid}} \end{pmatrix} = \mathbf{E}_{\text{DM}} \begin{pmatrix} -1 \\ 1/\chi \end{pmatrix} \exp(-i(\omega t - \mathbf{k}_{DM}\mathbf{x})) \tag{2}$$

$\mathbf{E}$ describes the ordinary electric field coupled to matter and $\mathbf{E}_{\text{hid}}$ the hidden photon field. Analogous equations are obtained for the Axion in presence of a magnetic field.

Considering a plane conducting surface (or a mirror) the ordinary electromagnetic part in Eq. (2) will cause electron movements on the surface, such that

$$0 = \mathbf{E}_{\text{tot},\parallel}|_{\text{surface}}. \tag{3}$$

We showed in [3] (c.f. also [4]) that for a dark matter incident angle α this causes an emission of a plane electromagnetic wave under the angle

$$\sin(\beta) = \sin(\alpha)\frac{v}{\sqrt{1+v^2}}, \tag{4}$$

with the dark matter velocity $v = \frac{|\mathbf{k}_{DM}|}{m_X}$. Therefore, the emission occurs almost perpendicular to the surface and can therefore be focused by a spherical surface in its center [5].

For a spherical mirror with a curvature radius $R \gg \lambda_{DM} = \frac{2\pi}{k_{DM}} = \frac{2\pi}{vm_X}$ we can calculate the intensity distribution in the center of the sphere in the ray approximation and obtain for a dark matter incident with angle θ rotated around the y-axis of the detector and velocity v

$$I(x,y) = \begin{cases} \frac{1}{2\pi} \frac{|\cos(\theta)v|}{\left([x-R\sin(\theta)v]^2 + y^2 + R^2\cos^2(\theta)v^2\right)^{3/2}} & \text{for} \quad \vartheta_0 \leq \vartheta_{sp,max} \\ 0 & \text{for} \quad \vartheta_0 > \vartheta_{sp,max} \end{cases} \tag{5}$$

where $\vartheta_{sp,max}$ is the aparture angle of the sphere; the result is normalized to the total power flux generated by a full half sphere with $\vartheta_{sp,max} = \pi/2$, and

$$\vartheta_0 = \left| \arctan\left(\frac{\sqrt{(x-R\sin(\theta)v)^2 + y^2}}{R\cos(\theta)v} \right) \right|. \tag{6}$$

Figure 1 illustrates its basic properties.

This may be used to perform a directionally sensitive dark matter search and gives direct implications on the directional resolution, but also on discovery experiments. For more details c.f. [3]. In this note we are going to investigate the validity of this result for long dark matter wavelengths $\lambda_{DM} \gtrsim R$ to infer limitations on the directional sensitivity.

Figure 1: Directional Resolution of dark matter particles with velocity v coming from an angle θ to the detector normal in the ray approximation regime. For a spherical cap the tails are cut off so that the distribution is limited to the dark blue area.

2   Wave Ansatz

For a correct calculation at high wavelengths one has to integrate over elementary waves emitted from the surface of the sphere. Again, this ansatz needs to fulfill Eq. (3). One can show that for a plane surface the far-field part of a classical dipole field is sufficient when integrating over the whole surface. At distance $\mathbf{r}$ from its origin it is given by (except time dependence)

$$\mathbf{E}_d(\mathbf{r}; \mathbf{p}) = k_\gamma{}^2 (\hat{\mathbf{r}} \times \mathbf{p}) \times \hat{\mathbf{r}} \frac{\exp(ik_\gamma r)}{r} \quad ; \quad \mathbf{B}_d(\mathbf{r}; \mathbf{p}) = k_\gamma{}^2 \hat{\mathbf{r}} \times \mathbf{p} \frac{\exp(ik_\gamma r)}{r}, \tag{7}$$

where k_γ is the photon wavenumber and $\mathbf{p}$ the dipole-vector. In order to fulfill (3) one needs to set (up to constant and spatial phase which we discuss below)

$$\mathbf{p} = \frac{1}{2\pi} \frac{\mathbf{E}_{\text{in},||}}{k_\gamma}. \tag{8}$$

Thus, $\mathbf{p}$ is a scaled projection of the dark matter polarization vector[1] on the spherical surface.

The electric field at detector position $\mathbf{x}$ is then given by

$$\mathbf{E}(\mathbf{x}) = \int_{\text{surface}} \mathbf{E}_d(\mathbf{r}'; \mathbf{p}) \, \exp\left(-i\,\mathbf{k}_{DM}\mathbf{r}\right) \, d\mathbf{r} \tag{9}$$

---

[1]We show simulations with circular transversal polarization as this behaves similar to arbitrary averaged polarization. When incoherently averaging over all possible polarizations the limitations for directional resolution are qualitatively the same.

Figure 2: Exemplary numerical results. Left: Stationary Distribution for high photon wavelength, Right: Distribution for wavelength comparable to distribution width.

and the magnetic field analogous, while $\mathbf{p}$ is chosen as above (and thus depends on $\mathbf{r}$), and $\mathbf{r}' = \mathbf{x} - \mathbf{r}$. The factor $\exp\left(-i\,\mathbf{k}_{DM}\mathbf{r}\right)$ accounts for the spatial phase differences between the elementary waves induced by the dark matter wave. The intensity on the detector can be then obtained by evaluating the time-averaged Poynting-vector $\langle \mathbf{S} \rangle \cdot \hat{\mathbf{n}}_{det}$ while

$$\langle \mathbf{S} \rangle = \text{Re}(\mathbf{E} \times \mathbf{B}^*). \tag{10}$$

3 Stationary Case

When the dark matter wavelength exceeds the setup size, i.e. $k_{DM}\ R = m_X v\ R \ll 1$, dark matter oscillations appear stationary in the setup and directional resolution must be lost.

If we further incoherently average over all dark matter polarizations and consider a spherical cap (as typical in most experimental setups), the direction of the field vectors becomes unimportant and we may use a simplified scalar ansatz

$$I(\mathbf{x}) = \left| \int_{\text{surface}} \Psi(\mathbf{r}')\ \exp\left(-i\,\mathbf{k}_{DM}\mathbf{r}\right)\ d^2\mathbf{r} \right|^2 \quad ; \quad \Psi(\mathbf{r}') = \Psi_0\ k_\gamma\ \frac{\exp(ik_\gamma r')}{r'}. \tag{11}$$

We can now easily compute the intensity in the center of the detector $I(0)$, since $\exp\left(-i\,\mathbf{k}_{DM}\mathbf{r}\right)$ is just a constant phase and $r' = R$ constant over the whole sphere. We find

$$I(0) \propto A_{dish}\ (1 - \cos(\vartheta_{max}))\ k_\gamma{}^2 \quad ; \quad \text{FWHM} \propto \frac{\lambda_\gamma}{\sqrt{1 - \cos(\vartheta_{max})}}, \tag{12}$$

while the width dependence is obtained recalling that the total emitted power is $\propto A_{dish}$.

4 Transitional Regime

To infer effects for arbitrary hidden photon mass, we evaluated Eq. (10) numerically. Our results are consistent with ray approximation for small wavelengths and Sec. 3 for large wavelengths.

For intermediate wavelengths smaller than expected distribution widths, the results from ray approximation get reproduced with overlaying interference effects as exemplified on the right side of Fig. 2.

We evaluated major distribution properties for a broad range of wavelengths, such as the distribution full width at half maximum (FWHM) shown in Fig. 3. In the stationary regime the width is consistently proportional to the photon wavelength and converges for smaller wavelengths towards the ray approximated width in an oscillatory manner due to interference effects.

Figure 3: Transition of width between stationary distribution and ray approximation for different incident angles and a full half sphere.

5   Conclusion

All numerical results confirm the stationary and ray approximated widths

$$\text{FWHM}_{\text{sta.}} \sim \frac{\lambda_\gamma}{\sqrt{1 - \cos(\vartheta_{sp,max})}} \quad ; \quad \text{FWHM}_{\text{ray}} \sim \max(\tan(\vartheta_{sp,max}); 1)Rv. \tag{13}$$

Comparing them also determines which of the two is dominant. The transition between stationary case and ray approximation happens from where both quantities are roughly the same to where the stationary width becomes one order smaller than the ray approximated width. Specifying the setup geometry by

$$\hat{R} := \sqrt{1 - \cos(\vartheta_{sp,max})} \max(\tan(\vartheta_{sp,max}); 1)R \tag{14}$$

we find that the expected distributions may be classified as

$$\begin{cases} \hat{R} \lesssim 0.5\lambda_\gamma/v = 1 \times \pi/(v\, m_X) & \text{stationary} \\ \hat{R} \gtrsim 10\lambda_\gamma/v = 20 \times \pi/(v\, m_X) & \text{ray approximated} \end{cases} \tag{15}$$

For experiments aiming for directional sensitivity, v should be set to the smallest velocity one aims to be sensitive for, while for discovery experiments it is sufficient to choose v as roughly the maximum dark matter velocity in order to infer the expected distribution width.

References

[1] A. E. Nelson and J. Scholtz, Phys. Rev. D **84** (2011) 103501 doi:10.1103/PhysRevD.84.103501 [arXiv:1105.2812 [hep-ph]].

[2] P. Arias, D. Cadamuro, M. Goodsell, J. Jaeckel, J. Redondo and A. Ringwald, JCAP **1206** (2012) 013 doi:10.1088/1475-7516/2012/06/013 [arXiv:1201.5902 [hep-ph]].

[3] J. Jaeckel and S. Knirck, JCAP **1601** (2016) 005 doi:10.1088/1475-7516/2016/01/005 [arXiv:1509.00371 [hep-ph]].

[4] J. Jaeckel and J. Redondo, JCAP **1311** (2013) 016 doi:10.1088/1475-7516/2013/11/016 [arXiv:1307.7181 [hep-ph]].

[5] D. Horns, J. Jaeckel, A. Lindner, A. Lobanov, J. Redondo and A. Ringwald, JCAP **1304** (2013) 016 doi:10.1088/1475-7516/2013/04/016 [arXiv:1212.2970 [hep-ph]].

Axion Haloscopes with Toroidal Geometry at CAPP/IBS

Byeong Rok Ko

Center for Axion and Precision Physics Research, Institute for Basic Science (IBS),
Daejeon 34141, Republic of Korea

The present state of the art axion haloscope employs a cylindrical resonant cavity in a solenoidal field. We, the Center for Axion and Precision Physics Research (CAPP) of the Institute for Basic Science (IBS) in Korea, are also pursuing halo axion discovery using this cylindrical geometry. However, the presence of end caps of cavities increases challenges as we explore higher frequency regions for the axion at above 2 GHz. To overcome these challenges we exploit a toroidal design of cavity and magnetic field. A toroidal geometry offers several advantages, two of which are a larger volume for a given space and greatly reduced fringe fields which interfere with our preamps, in particular the planned quantum-based devices. We introduce the concept of toroidal axion haloscopes and present ongoing research activities and plans at CAPP/IBS.

1 Axion haloscopes at CAPP/IBS

One of the primary targets of the Center for Axion and Precision Physics research (CAPP) of the Institute for Basic Science (IBS) in Korea is to search for axion cold dark matter using the method proposed by Sikivie [1], also known as the axion haloscope search. We, CAPP/IBS, are pursuing traditional axion haloscopes with cylindrical geometry, where two significant solenoids are employed. One has 12 T of B field and 32 cm of cold bore and the other has 25 T of B field and 10 cm of cold bore. The former can scan the axion frequency from 0.5 to 1.3 GHz, while the latter can scan from 1.8 to 10 GHz. The details of halo axion searches using these cylindrical geometry will be given in the near future.

In the same pipe line, we are also considering axion haloscopes with toroidal geometry which offer a larger volume and greatly reduced fringe B fields. In view of these advantages, we introduce currently ongoing research activities and plans for toroidal axion haloscopes at CAPP/IBS in this proceedings.

2 Cylindrical geometry vs. toroidal geometry

We compare two axion haloscopes with two different geometry, cylindrical and toroidal, to reveal the advantages of toroidal axion haloscopes mentioned above. Cylindrical cavities have an electromagnetic cavity mode parallel to an external static magnetic field $\vec{B}_{\text{external}}$ provided by the magnet employed in an axion haloscope, which is the TM_{010} mode, and so do toroidal

characteristics	cylindrical geometry	toroidal geometry
$\vec{B}_{\text{external}}$	$\sim B_0 \hat{z}$	$\sim \frac{B_0}{\rho} \hat{\phi}$
$B_{\text{avg}}^2 V$	independent of the cavity location inside a solenoid	depends on the cavity location inside a toroidal magnet
cavity mode $\parallel \vec{B}_{\text{external}}$	TM_{010}	QTM
form factor	$C_E = C_M \propto B_{\text{avg}}^2 V$	$C_E = C_M \propto B_{\text{avg}}^2 V$
B_{fringe}	unavoidable	avoidable with additional coils
mode crossing	Yes	No

Table 1: Comparison of characteristics between cylindrical and toroidal axion haloscopes, where B_0 is a constant, $B_{\text{avg}}^2 V \equiv \int \vec{B}_{\text{external}}^2 dV$, and V is the cavity volume.

cavities, which is to be referred to as Quasi-TM (QTM) mode [2] in this proceedings. As reported in Ref. [3], their electric (C_E) and magnetic (C_M) form factors are also the same regardless of the cavity location inside the magnet.

In the absence of end caps of cavities in a toroidal design, the cavity modes depend only on the minor radius of the toroidal cavity. Therefore, degeneration of the cavity modes is expected to be little and indeed the finite element method [4] demonstrates no degeneracy, or equivalently no mode crossing, in the QTM mode as shown in Fig. 1.

This *no mode crossing* in toroidal geometry enables us to increase the cavity volume very effectively.

The fringe B fields, from toroidal magnets, B_{fringe} are ideally zero and even practically very small compared to those from solenoids. Furthermore, the B_{fringe} from toroidal magnets can be reduced with additional coils. With greatly reduced B_{fringe}, the handling of quantum preamps in toroidal geometry is much easier than that in cylindrical geometry.

Table 1 summarizes the comparison between axion haloscopes with cylindrical and toroidal geometry. Note that z, ρ, and ϕ refer to cylindrical coordinates.
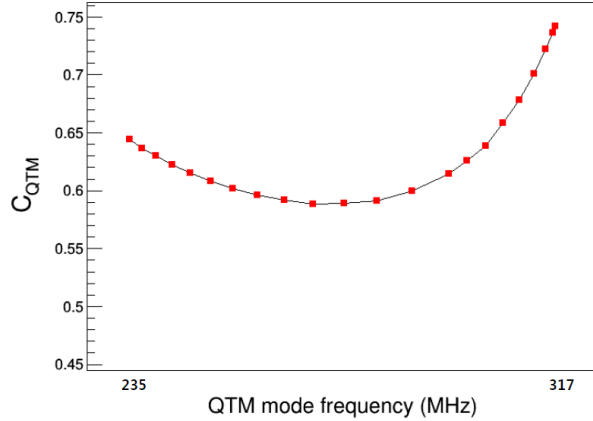
Figure 1: Form factors of the QTM mode of the toroidal cavity as a function of frequency.

3   Axion haloscopes with toroidal geometry at CAPP/IBS

We are considering the two toroidal axion haloscopes whose magnet specifications are shown in Table 2.

The large toroidal magnet illustrated in Fig. 2 can hold a cavity with 200 cm of major radius and 50 cm of minor radius, which enables us to scan the axion parameter space down to 190 MHz with a dielectric ($\epsilon_r = 9.9$) tuning rod. Thanks to 9,870 liters of the cavity volume which is about 50 times larger than the ADMX cavity [5], we can achieve a reasonable scanning rate [6] even with a semiconductor-based preamp and cavity cooling with liquid helium (LHe) which results in the relatively high system noise of ~6 K, with 2 K from the preamp and 4 K from the cavity. The large toroidal magnet also can hold 4 cavities, each of them having 200 cm of major radius and 20 cm of minor radius, which enables us to scan the axion parameter space up to 850 MHz with a conductor tuning rod. With the 4-cavity system, we can achieve a reasonable scanning rate even with a system noise of ~6 K. Figure 3 shows the relevant parameter space and expected sensitivity from the large toroidal axion haloscopes which will be realized in about ten years.

Figure 2: Conceptual design of the large toroidal magnet with 9 coils and the cavity. The color map shows the B field from the magnet.

	small toroid	large toroid
B_{avg}	12 T	5 T
number of coils	36	9
major radius	50 cm	200 cm
minor radius	11 cm	60 cm

Table 2: Specifications of the two toroidal magnets.

The small toroidal magnet can hold a cavity with 50 cm of major radius and 9 cm of minor radius, which enables us to search for axion parameter space from 1.3 to 1.8 GHz with a conductor tuning rod. The cavity can be cool down to 100 mK with a dilution fridge. Then, we can be sensitive to KSVZ [7, 8] axion search using a semiconductor preamp or DFSZ [9, 10] using a quantum version preamp with acceptable scanning rates. Figure 3 also shows the relevant parameter space and expected sensitivity from the small toroidal axion haloscopes which will be realized in a few years.

4 Summary

CAPP/IBS realizes several advantages in axion haloscopes with toroidal geometry, two of which are a larger volume for a given space and greatly reduced fringe fields. Thanks to the very large volume of the cavity in the large toroidal axion haloscopes, we can realize

Figure 3: Axion parameter space where red lines in the lower mass region denote the search region of the large toroidal axion haloscopes and those in the higher mass region denote that of the small toroidal axion haloscopes at CAPP/IBS.

a reasonable scanning rate even with 4 K cavity cooling which can be achieved easily with LHe. The capability of cooling a system using LHe shows how powerful the large toroidal axion haloscopes are. In the near future, we will realize the small toroidal axion haloscopes to demonstrate the feasibility of the large toroidal axion haloscopes.

Acknowledgments

References

[1] P. Sikivie, Phys. Rev. Lett. **51**, 1415 (1983).

[2] Not the same as TM_{010} mode, but similar to it.

[3] B. R. Ko *et al.*, arXiv:1608.00843 [hep-ph].

[4] `www.cst.com`

[5] H. Peng *et al.*, Nucl. Instrum. Methods Phys. Res., Sect. A **444**, 569 (2000).

[6] C. Hagmann, P. Sikivie, N. Sullivan, D. B. Tanner, and S. I. Cho, Rev. Sci. Instrum. **61**, 1076 (1990).

[7] J. E. Kim, Phys. Rev. Lett. **43**, 103 (1979).

[8] M. A. Shifman, A. I. Vainshtein, and V. I. Zakharov, Nucl. Phys. B **166**, 493 (1980).

[9] A. R. Zhitnitskii, Sov. J. Nucl. Phys. **31**, 260 (1980).

[10] M. Dine, W. Fischler, and M. Srednicki, Phys. Lett. B **140**, 199 (1981).

Status of the ADMX-HF Experiment

Samantha M. Lewis,

ADMX-HF Collaboration,
University of California, Berkeley, United States

The axion is a leading dark matter candidate particle. Haloscope-type experiments search for the axion using its resonant conversion to a photon in the presence of a strong magnetic field, enhancing the signal through the use of resonant microwave cavities and quantum-limited amplifiers. The Axion Dark Matter eXperiment – High Frequency (ADMX-HF) is an operating experiment taking a first look at data in the 20–100 μeV ($\sim$ 4–25 GHz) range. This paper discusses the newly completed data run as well as research and development underway that will further the reach of the experiment.

1 Introduction

The axion is a hypothetical pseudoscalar that was originally proposed in the Peccei-Quinn solution to the Strong CP problem. It is also a compelling candidate particle for cold dark matter in the 1–100 μeV range (see Ref. [1]). Like the π^0, the axion can couple to two photons in an inverse Primakoff conversion, one of which can be virtual.

Axion haloscopes attempt to observe this conversion by resonantly enhancing the photon signal using a microwave cavity permeated by a strong magnetic field [2]. The resonant conversion relies on the frequency of the cavity corresponding to the axion mass via the relation $h\nu = m_a c^2 \left(1 + \frac{1}{2} O\left(\beta^2\right)\right)$, where ν is the cavity resonant frequency, m_a is the axion mass, and $\beta \approx 10^{-3}$ is the galactic virial velocity. An overview schematic of the axion haloscope detection mechanism is shown in Fig. 1.

In this process, the power of the axion signal is expected to be very weak (on the order of 10^{-23} W). Thus, various techniques are employed to enhance this signal. The conversion axion-photon conversion power is given by

$$P_{sig} = \eta g_{a\gamma\gamma}^2 \left(\frac{\rho_a}{m_a}\right) B^2 Q_L V C_{nml} \tag{1}$$

where $g_{a\gamma\gamma}$ is the axion-photon coupling constant, ρ_a is the halo axion density, B is the strength of the applied magnetic field, Q_L is the loaded quality factor of the cavity, V is the cavity volume, and C_{nml} is the mode-specific form factor. The η constant specifies the fraction of power coupled out of the cavity. The detectability of the signal depends on the signal to noise ratio, which is governed by the Dicke radiometer equation

$$\frac{S}{N} = \frac{P_{sig}}{kT_{sys}} \sqrt{\frac{t}{\Delta\nu_a}} \tag{2}$$

where k is the Boltzmann constant, t is integration time, and $\Delta\nu_a$ is the width of the axion signal. The system noise temperature T_{sys} is

$$kT_{sys} = h\nu \left(\frac{1}{e^{h\nu/kT} - 1} + \frac{1}{2} \right) + kT_A \tag{3}$$

Here, T is physical temperature of the cavity and T_A is the equivalent temperature of the intrinsic amplifier noise.
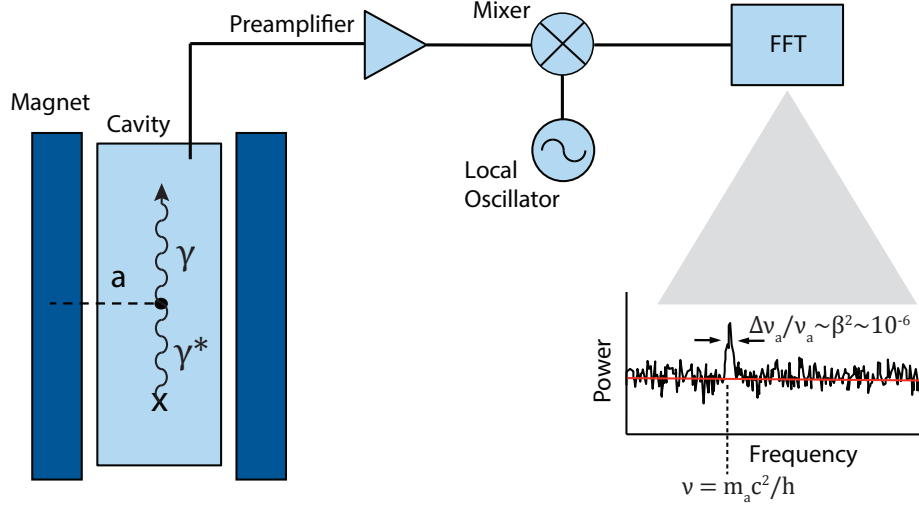
Figure 1: Block diagram of the axion haloscope detection mechanism. A microwave cavity is placed in the bore of a strong superconducting magnet. An axion entering the cavity converts to a real photon when the cavity is tuned to the frequency corresponding to m_a. This photon signal is extracted from the cavity, passing through an RF receiver chain, finally giving a peak.

2 Experiment

ADMX-HF is a collaboration of four institutions: Yale University, the University of California Berkeley, the University of Colorado Boulder, and Lawrence Livermore National Laboratory. The experiment was created to search for QCD axions at higher frequencies than existing haloscope limits and designed as a data pathfinder in the 4–25 GHz range (corresponding to 20–100 μeV in axion mass). These high frequencies can pose challenges that do not exist at lower frequencies. ADMX-HF serves as a small versatile testbed platform for new amplifier and microwave cavity technologies that address these challenges.

To enable the search for QCD axions, ADMX-HF uses state of the art technology. The superconducting magnet (0.40 m × 0.175 m $\oslash$, 9 T) is a dry system and was designed to have a large bore and long straight-field region. A copper cylindrical cavity with a large tuning rod allows for tuning from 3.5 GHz to 5.85 GHz with a loaded, critically coupled quality factor of $Q \sim 2 \times 10^4$. From the outset, the experiment has used Josephson Parametric Amplifiers (JPAs) which allow for amplification with quantum-limited noise. The current JPA has a tuning

range of 4.4–6.5 GHz with ~ 20 dB of gain. Magnetic shielding consisting of a bucking coil, passive coils, μ metal, and superconducting shield layers reduce the magnetic field at the JPA by a factor of 10^8, allowing for proper amplifier performance despite the presence of a strong magnetic field. A dilution refrigerator (base temperature 25 mK) cools the cavity to ~ 100 mK to minimize thermal noise. Altogether, these components enable the experiment's extraordinary sensitivity in the GHz range which has not been achieved by any other experiment. Figure 2 shows a detailed view of these components.
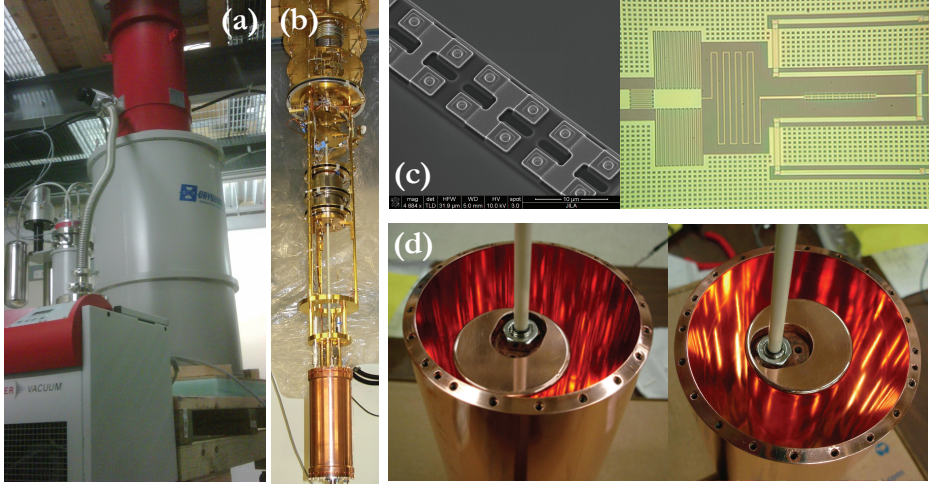
Figure 2: (a) Fully assembled experiment, showing the superconducting magnet. (b) Gantry attached to the dilution refrigerator. (c) Micrographs of a Josephson Parametric Amplifier (JPA) which allows for very low noise amplification. (d) Current microwave cavity, partially assembled, with minimum (left, 3.8 GHz) and maximum (right, 5.85 GHz) tuning positions shown.

ADMX-HF began construction in April of 2012. Integration and commissioning took place from July 2014 to January of 2016. The first data run began in January of 2016 and was recently completed in August of 2016. The next section details the operating characteristics and scope of this first data run.

3   Data run

The first data run of ADMX-HF scanned 100 MHz (~ 0.4 μeV) near the top of the cavity tuning range, 5.8 GHz (24 μeV). In this run, $g_{a\gamma\gamma} \sim 2.3 \times$ KSVZ over the entire range. No exclusion plot appears here as the final exclusion plot with full details will be published soon.

The achieved sensitivity was limited by the physical temperature of the tuning rod. The ceramic axle of the tuning rod limited the thermal link between the rod and the rest of the system. This resulted in a noise temperature on the order of $T_{sys} \sim 1100$ mK, which is roughly 3.5 times the standard quantum limit (SQL) for noise at in this frequency range.

4 Ongoing research and planned upgrades

There are multiple upgrades planned for the near future that will allow the experiment to reach further into the QCD axion model band. A simple solution to improve the thermal linkage of the tuning rod has been identified and will be implemented on all future tuning rods used in the experiment. This will reduce the thermal noise contribution to the originally planned value. Reducing the system noise temperature allows for a shorter integration time, speeding up the possible scan rate for future data runs.

A new dilution refrigerator is ready to be installed on the experiment. It has a lower possible base temperature and should reduce vibrations, which could allow for a lower operating temperature. This switch will likely be made after other upgrades are implemented.

The University of Colorado/JILA group has developed a receiver based on a squeezed state of vacuum that will be implemented on the experiment within the next year. This will allow for amplification with a total system noise temperature below the SQL. As of the time of writing, this would be the first use of a squeezed vacuum device on an operating experiment. Amplification with sub-quantum-limited noise will reduce the system noise temperature and could allow for a large increase in the scan rate.

At the University of California, Berkeley, new cavity designs are being developed to enhance the signal power and move the experiment to new frequency ranges. Efforts are underway to develop cavities with superconducting thin film multilayers that could greatly increase the cavity Q value. The use of Distributed Bragg Reflectors (DBR) is also being studied for use in increasing the Q value as well as the form factor for higher-order TM modes.

Photonic band gap (PBG) devices are being studied for use in creating a resonator at high frequencies that would clear the mode spectrum of TE modes. PBG structures allow for the confinement of modes of interest while other excited modes are allowed to propagate out [3]. In standard cylindrical cavities and the existing ADMX-HF cavity, TE modes undergo avoided crossing with the TM_{010} mode of interest as it is tuned, making the frequency range of the crossing unusable. This is a severe limitation in the operation of existing cavity experiments; eliminating the mode crossing problem would allow for faster scan rates and a larger available tuning range with a single device.

Acknowledgments

References

[1] P. W. Graham *et al.*, "Experimental Searches for the Axion and Axion-Like Particles," Annu. Rev. Nucl. Part. S. **65**, 485–514 (2015). doi:10.1146/annurev-nucl-102014-022120

[2] P. Sikivie, "Experimental Tests of the 'Invisible' Axion," Phys. Rev. Lett. **51**, no. 16, 1415 (1983). doi:10.1103/PhysRevLett.51.1415

[3] E. Yablonovitch, "Photonic Band-Gap Structures," J. Opt. Soc. Am. B **10**, no. 2, 283–295 (1993). doi:10.1364/JOSAB.10.000283

SUSY DM predictions for Direct Detection Experiments, the LHC and the ILC

Miriam Lucio Martínez[1]

[1]Mastercode Collaboration

In this talk, results from the frequentist analysis of the parameter space for the supersymmetric models pMSSM10 [6] and mAMSB, done within the Mastercode collaboration, are reviewed. Among them, special attention is paid to the predictions concerning Direct Detection Experiments, the Large Hadron Collider [1] and the International Linear Collider [2]. Also, the Dark Matter candidate provided in each case is described.

1 Introduction

The Standard Model of Particle Physics (SM) is a very succcessful theory. Nevertheless, it fails to explain important things, such as the origin of dark matter and dark energy or the unification of the forces. Among the alternatives to the SM proposed in order to solve these, supersymmetry plays a major role.

The particle content of the minimal supersymmetrical extension of the SM (MSSM) [3] is made of the SM particles, their supersymmetric partners and 2 Higgs doublets. In this model the Lightest Supersymmetric Particle (LSP) is neutral and stable, which makes it a good Dark Matter candidate. It can be either a gravitino, the lightest neutralino (it can be a Bino, a Higgsino, a Wino or a combination of former), or a sneutrino. Nevertheless, sneutrinos are experimentally ruled out by direct detection experiments.

One of the main drawbacks of the MSSM is the fact that it has more than 100 free parameters, which makes it a very difficult model to confront with experimental data. In order to cope with this a purely phenomenological approach can be taken, like the pMSSM10, that has only 10 parameters. Also, a constrained model can be considered, where an assumption on the scenarios through which spontaneous SUSY breaking is achieved is made. An example of the latter is the mAMSB, with 3 free parameters and 1 sign.

To calculate the observables that go into our likelihood evaluation and perform Global fits of SUSY for these two models, the Mastercode framework is used, that interfaces several public and private code, linked using the SUSY Les Houches Accord (SLHA) [4], [5].

2 pMSSM10 Results

The best-fit point of the sampling provides the mass spectrum shown in Figure 1. It can be seen a clear-prediction for a Bino-like $m_{\tilde{\chi}_1^0}$. Its predicted mass is much lower than other GUT-based models. According to the mass range, the production of SUSY particles in this model would

be possible at ILC, as long as the following condition is fulfilled for the mass of these particles: $m < \sqrt{(s)}/2$, where s∼500 GeV for ILC. Plotting the DM candidate mass against the squark

Figure 1: Mass spectrum for the best-fit point in pMSSM10 sampling

mass (left plot in Figure 2) it is shown that parts of the $\tilde{\chi}_1^\pm$ coannihilation region and the low-$m_{\tilde{\chi}_1^0}$ band are accessible to future LHC searches (especially if the gluino hass a mass of 4.5 TeV). Also, chargino coannihilation is proved to be the main production channel. In the right plot of this figure it is seen that most of the chargino coannihilation region would be accessible to future LZ searches.

Figure 2: Left: $(m_{\tilde{q}}, m_{\tilde{\chi}_0})$ plane. The red and blue solid lines are the $\Delta\chi^2 = 2.30$ and 5.99 contours, and the solid (dashed) purple lines are the current and (projected) 95% exclusion contours for missing E_T searches at the LHC (with 300/fb of data at 14 TeV). The solid lines are almost identical with the contours for 5-σ discovery with 3000/fb. Right: $(m_{\tilde{\chi}_1^0}, \sigma_p^{SI})$ plane. The solid purple lines show the projected 95% exclusion sensitivity of the LUX-Zepelin (LZ) experiment [7]. The green and black lines show the current sensitivities of the XENON100 [8] and LUX [9] experiments, respectively, and the dashed orange line shows the astrophysical neutrino 'floor' [10], below which astrophysical neutrino backgrounds dominate (yellow region)

3   mAMSB Results

As it happened in the previous case, the LSP is a neutralino, almost degenerate with a chargino ($\tilde{\chi}_1^\pm$), as shown in the best-fit point mass spectrum (Figure 3). Because of their high masses, particles in this model are not directly detectable at LHC nor at ILC. The DM candidate can

either be wino-like or higgsino-like. Nevertheless, the wino-like candidate, with mass ~ 3 TeV (common for all the wino DM models), is more favoured than the higgsino-like one. Notice that the preferred LSP mass is much bigger than the pMSSM10 prediction. Again, the main production mechanism of the DM candidate is the chargino coannihilation.

Concerning the $(m_{\tilde{\chi}_0}, \sigma_{SI})$ plane (Figure 4), wino-like candidate contour plots lie below the
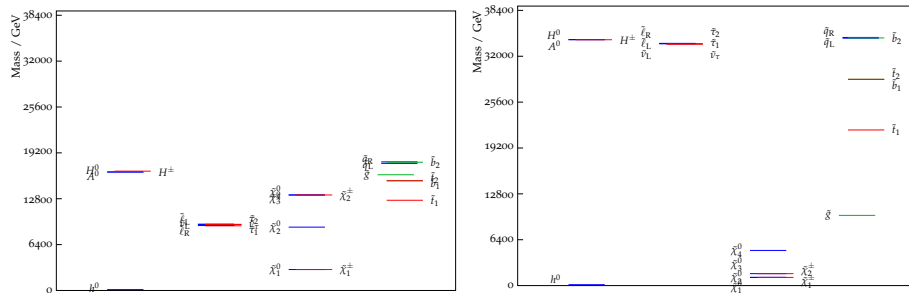
Figure 3: Mass spectrum for the best-fit point in mAMSB sampling, for the wino-like (left) and the higgsino-like (right) candidate

astrophysical neutrino floor, which would make it impossible to detect it with direct detection experiments. However, if the candidate is higgsino-like instead, LZ experiment would have accessibility to its measurement.
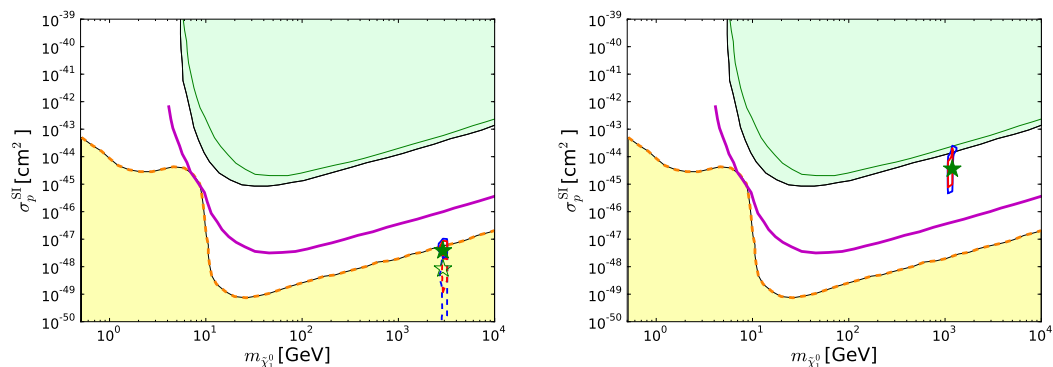
Figure 4: The $(m_{\tilde{\chi}_1^0}, \sigma_p^{SI})$ planes in the mAMSB framework. The plot on the left refers to the wino-like candidate, while the plot on the right corresponds to the higgsino-like one
.

4   Conclusions

Supersymmetry is a good framework for explaining the origin of Dark Matter. Among the different models, both pMSSM10 and mAMSB have shown to provide good candidates. pMSSM10 candidate has much lower mass than other models (such as NUHM2,NUHM1,CMSSM), while mAMSB leads to a heavy wino-like candidate and a lighter higgsino-like candidate.

Acknowledgments

References

[1] L. Evans and P. Bryant, JINST **3** (2008) S08001. doi:10.1088/1748-0221/3/08/S08001

[2] H. Baer *et al.*, arXiv:1306.6352 [hep-ph].

[3] H. P. Nilles, Phys. Rept. **110** (1984) 1. doi:10.1016/0370-1573(84)90008-5

[4] P. Z. Skands *et al.*, JHEP **0407** (2004) 036 doi:10.1088/1126-6708/2004/07/036 [hep-ph/0311123].

[5] B. C. Allanach *et al.*, Comput. Phys. Commun. **180** (2009) 8 doi:10.1016/j.cpc.2008.08.004 [arXiv:0801.0045 [hep-ph]].

[6] K. J. de Vries *et al.*, Eur. Phys. J. C **75** (2015) no.9, 422 doi:10.1140/epjc/s10052-015-3599-y [arXiv:1504.03260 [hep-ph]].

[7] D. C. Malling *et al.*, arXiv:1110.0103 [astro-ph.IM].

[8] E. Aprile *et al.* [XENON100 Collaboration], Phys. Rev. Lett. **109** (2012) 181301 doi:10.1103/PhysRevLett.109.181301 [arXiv:1207.5988 [astro-ph.CO]].

[9] D. S. Akerib *et al.* [LUX Collaboration], Phys. Rev. Lett. **112** (2014) 091303 doi:10.1103/PhysRevLett.112.091303 [arXiv:1310.8214 [astro-ph.CO]].

[10] P. Cushman *et al.*, arXiv:1310.8327 [hep-ex].

MADMAX: A new Dark Matter Axion Search using a dielectric Haloscope

Béla Majorovits[1] and Javier Redondo[2] for the MADMAX working group
(A. Caldwell[1], G. Dvali[1,3], C. Gooch[1], A. Hambarzumjan[1], B. Majorovits[1], A. Millar[1], G. Raffelt[1], J. Redondo[2], O. Reimann[1], F. Simon[1], F. Steffen[1])

[1]Max-Planck-Institut für Physik, München, Germany,
[2]University of Zaragoza, Spain,
[3]Ludwig Maximilians Universität München, Germany,

Axions are an intriguing dark matter candidate, emerging from the Peccei-Quinn solution to the strong CP problem. Current experimental searches for axion dark matter focus on axion masses below 40μeV. However, if the Peccei-Quinn symmetry is restored after inflation the axion mass is predicted to be in the $100\,\mu$eV range. A new project based on axion-photon conversion at the transition between different dielectric media is presented. The axion-photon conversion could be enhanced by a factor $\sim 10^5$ over a single mirror by using ~ 80 layers of dielectrics. Within a 10 T magnetic field this could be enough to detect $\sim 100\,\mu$eV axions with HEMT linear amplifiers. The proposed design for an experiment is discussed. Results from noise, transmissivity and reflectivity measurements in a prototype setup are presented. The expected sensitivity is shown.

1 Introduction

Axions are hypothetical low-mass bosons which emerge as a consequence of the Peccei-Quinn mechanism that explains the absence of CP-violating effects in quantum chromodynamics. They provide an attractive candidate for cold dark matter. There are two general scenarios for dark matter axions: either the Peccei-Quinn symmetry is restored after inflation, or remains unbroken. In the latter scenario, axion dark matter is produced through the misalignment mechanism, which can be arrange to have the correct relic density for a wide range of axions masses by varying the initial conditions with values $\sim 10\ \mu$eV considered most natural. In the first scenario the observable universe contains many casually disconnected patches with different initial conditions which must be averaged over to give the relic abundance. Additionally cold dark matter axions are produced by the decay of axion strings and domain walls leading to a higher favoured mass range $m_a \sim 100\ \mu$eV for dark-matter axions [1].

Most experimental efforts for detecting dark-matter axions, notably the ADMX and ADMX-HF experiments [2, 3], focus on axion masses below $\sim 40\ \mu$eV. These experiments take advantage of the resonant enhancement of a cavity to boost the axion-photon conversion in a magnetic field and so gain sensitivity to axion dark matter. This technique is most effective for $\mathcal{O}(10)\ \mu$eV axions: using cavities to search for axions in the $100\ \mu$eV range is extremely technically challenging. Alternative methods more suited to search for high mass axions are needed.
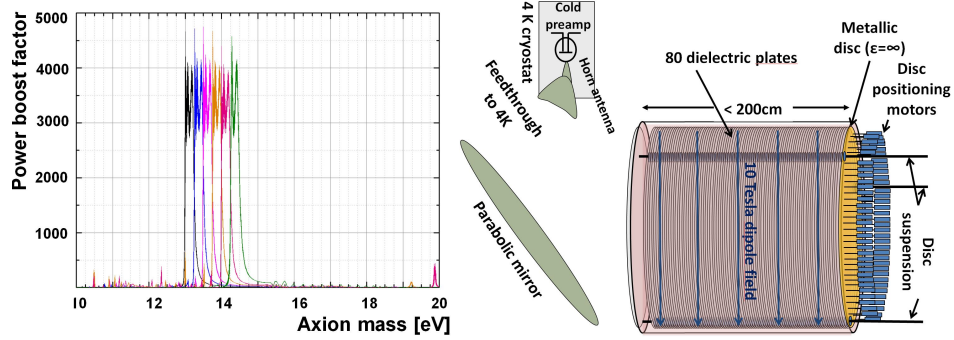
Figure 1: Left: EM simulations of boost factor in dielectric booster with 20 LaAlO$_3$ discs. Right: Conceptual idea for a haloscope that could scan for axions with masses around 100μeV.

2 Dielectric haloscope concept and experimental idea

To scan the axion mass range above 40 μeV, we exploit a novel dielectric haloscope approach derived from the concepts described in [4, 5]. The expected radiation power density from axion-photon conversion at a transition between materials with different dielectric constant ϵ in a magnetic field is

$$P/A = 2 \times 10^{-27} \ \text{W/m}^2 \, (B_{||}/10\,\text{T})^2 \, c_\gamma^2 \, F(\Delta_{\epsilon_1,\epsilon_2}), \tag{1}$$

where A is the surface area, $B_{||}$ the magnetic field parallel to the surfaces, $C_{a\gamma}$ the axion-photon coupling constant normalized to $\alpha/(2\pi f_a)$ [6], and $F(\Delta_{\epsilon_1,\epsilon_2})$ is a function depending on the dielectric constants of the two media. For a metallic mirror in vacuum $F(\Delta_{0,\infty}) = 1$. In order to obtain a detectable power of $P \sim 10^{-23}W$ a mirror magnetized to 10 T field parallel to its surface with $A \sim 5000$ m^2 would be needed, unachievable with current technology.

Instead we propose building a dielectric haloscope: a series of high-ϵ material discs placed in front of a metallic mirror of the same area, contained in a magnetic field. Unlike a resonator, this device is open on one side. By adjusting the spacing between the discs, constructive interference can lead to a boost of the expected axion field induced EM power over a sizeable bandwidth. The power boost factor is defined as the power generated in the booster normalized to the power generated by a single metallic surface with same area. It is a function of the frequency, the number and

Figure 2: Preliminary prototype setup for transmissivity measurements with four adjustable Al$_2$O$_3$ discs.

spacings between the discs, and the dielectric constants of the chosen materials.

The axion field acts as a current in Maxwell's equations, which can be treated classically. The power boost factor as a function of frequency from a first simulation is shown in Fig. 1, left. This used a setup consisting of 20 discs made from LaAlO$_3$ ($\epsilon \sim 24$) and achieves a power boost factor $\gtrsim 3 \cdot 10^3$ within a bandwidth of 250 MHz. The frequency range in which the boost is obtained can be varied by changing the displacement between the discs.

Further investigations using EM modelling have shown that, the area under the power boost factor vs frequency curve scales linearly with the number of discs in the booster. Using this relation it seems feasible that a setup consisting of ∼80 discs made from LaAlO$_3$ can have a boost factor of $\sim 10^5$ in a 40 MHz wide frequency range. Using discs with a diameter of 1 m and a 10 T dipole field, a total power of $\sim 10^{-23}$ W could be generated by high mass dark matter axions. A sketch of the proposed MADMAX setup is shown in Fig. 1, right.

While this is a mechanically challenging setup, it has the advantage of flexibility. One can adopt a significantly broadband search strategy, probing a large frequency range within a reasonable measurement time and, in the event that the broad bandwidth search leads to evidence for a signal, the haloscope can be tuned to higher boost factor across a narrow bandwidth. This would enhance the signal to noise ratio, allowing speedy confirmation of a detection.

One of the big challenges in the experiment will be the availability of a ~ 10 T dipole magnet that allows to house ~ 1 m diameter discs with a length up to 2 m. Presently two design concepts are under discussion, the canted cosine theta [8] and the racetrack [9] designs. Initial investigations indicate that both design concepts are suitable to reach the design criteria. In the near future we will see which of these is better suited for the current experimental proposal.

3   First measurements and sensitivity projection

To determine the required signal strength, a radiometer based on heterodyne detection using a HEMT preamplifier [7] has been built. It was used for a first measurement of a weak signal at 20 GHz with 3×10^{-21} W at room temperature. The fake signal was detected within one week measurement time with $6\,\sigma$ separation from background. According to the data sheet, operating the preamplifier at 4 K temperature reduces its noise by another two orders of magnitude, hence, allowing for the detection of signals with power of the order of 3×10^{-23} W, if the noise contribution of the haloscope itself is low enough.

As transmissivity and reflectivity of the haloscope are correlated with the boost factor curve they can be used to verify the simulated boost factor behaviour. We use this to both test our calculations of the boost factor, and to potentially aid correct disc placement.

This has been done in the prototype setup

Figure 3:   First transmission measurement (gray) taken with five Al$_2$O$_3$ discs between receiver and emitter. The smoothed measurement curve (red) can be compared to the behavior predicted by simulation (blue).

shown in Fig. 2 where five sapphire (Al$_2$O$_3$ with $\epsilon \sim 10$) discs with 200 mm diameter each are used. Discs are positioned by precision motors with a precision of roughly 15 μm. The unceratinty on positioning is due to the mechanical setup. Comparison of transmissivity measurement with simulation is shown in Fig. 3. While details of the transmissivity behaviour slightly differ, encouragingly the general behaviour is similar, especially the position of the peak at highest frequencies. The same has been verified for reflectivity measurements using group delay peaks.

A long term reflectivity measurement using four saphire discs and a metallic mirror was performed to monitor the stability of the group delay peak. The variations of the peak position, attributed to mechanical (vibration) or thermal (contraction or expansion) changes in the setup, are of the order of 1 MHz, and so substantially narrower than the envisioned bandwidth of the boost factor. Even under these experimental conditions without vibrational damping and precise climate control long term measurements can be performed over a sizeable bandwidth.

To estimate the sensitivity of the proposed experiment, we assume a setup consisting of 80 discs with 1 m^2 surface area each, achieving a boost factor of $\gtrsim 10^4$ with a bandwidth of 50 MHz, and cryogenic preamp with a noise level of 8 K. Inside a 10 T dipole magnetic field this would allow for scanning the interesting dark matter QCD axion parameter space, assuming purely axionic dark matter. Each measurement would take approximately one week. The projected sensitivity is depicted in Fig. 4.

4 Outlook and Conclusions

Axions are amongst the best motivated dark matter candidates, with interesting and unique phenomenology. However, the high mass (40–200 μeV) axions predicted for scenarios in which Peccei-Quinn symmetry breaking occurs after inflation are beyond the reach of current experiments. A novel approach to study high mass axions is a dielectric haloscope, using a series of dielectrics contained in a parallel magnetic field to enhance the conversion of axions-to-photons. A comparison of simulations with first measurements indicate that this approach could scan the interesting dark matter QCD axion mass range within a reasonable time span.

Figure 4: Projected MADMAX sensitivity

Acknowledgments: The prototype setup used for first measurements was partly funded as a seed project by the DFG Excellence Cluster Universe.

References

[1] T. Hiramatsu *et al.*, Phys. Rev. D **85**, 105020, (2012), Erratum ibid. **86**, 089902, (2012) ; M. Kawasaki *et al.* Phys. Rev. D **91**, 065014 (2015)

[2] G. Rybka, Proceedings of the 13th Int. Conf. on Topics in Astroparticle and Underground Physics (TAUP 2013) Phys. Dark Univ., **4**, 14 (2014)

[3] B. M. Brubaker *et al.*, arXiv:1610.02580.

[4] D. Horns *et al.*, JCAP **1304**, 016, (2013) [arXiv:1212.2970].

[5] J. Jaeckel and J. Redondo, Phys. Rev. D **88**, 115002 (2013) [arXiv:1308.1103].

[6] A. Ringwald *et al.*, in C. Patrignani et al. (Particle Data Group), Chin. Phys. C **40**, 100001 (2016)

[7] Low Noise Factory, datasheet for LNF-LNC6R_20A, www.lownoisefactory.com, site visited: Oct. 11. 2016

[8] S. Caspi et al., IEEE Trans. Appl. Supercond. **24**, 4000404 (2014)

[9] E. Rochepault, P. Vedrine and F. Bouillault, IEEE Trans. Appl. Supercond. **22**, 4900804 (2012)

Limiting 10 keV - 100 MeV ALPs with supernovae

J. Jaeckel[1], P.C. Malta[2], J. Redondo[3]

[1]Institut für theoretische Physik, University of Heidelberg (Germany),
[2]Institut für theoretische Physik, University of Heidelberg (Germany) and Brazilian Centre for Research in Physics – CBPF (Brazil),
[3]University of Zaragoza (Spain) and Max Planck Institut für Physik (Germany)

We use the gamma-ray signal from SN 1987A to obtain limits on massive (10 keV - 100 MeV) axion-like particles which may decay to two photons on their way to Earth. We also discuss the time and angular distribution of such a signal and estimate the possible improvements if Betelgeuse becomes a supernova. Proceedings for the talk presented by P.C.M. based entirely on Ref. [1], where more details can be found.

1 Introduction

Axion-like particles (ALPs) are an integral part of many beyond the Standard Model scenarios whose typical feature is an interaction with two photons,

$$\mathcal{L}_{\text{int}} \supset \frac{g_{a\gamma\gamma}}{4} a F_{\mu\nu} \tilde{F}^{\mu\nu}, \tag{1}$$

where a denotes the ALP and $g_{a\gamma\gamma}$ is its coupling constant (dimension of inverse energy), which is independent of the mass, m_a. Our aim is to determine the excluded regions in $g_{a\gamma\gamma} - m_a$ space by considering supernova-originated ALPs and their decay to two photons – usually gamma-rays – a process most effective for $m_a \sim$ MeV-GeV. As can be seen from Fig. 2, in this region SNe indeed provide better limits than existing laboratory and astrophysical constraints [2].

For concreteness, we focus on SN 1987A, which has already been used to derive limits on ALPs. For $m_a <$ few $\times 10^{-10}$ eV better limits can be obtained since light ALPs emitted from the supernova (SN) can be reconverted into photons in the magnetic field of the galaxy [3]. For heavier ALPs, however, this process is not effective as the reconversion process is strongly suppressed.

On the other hand, for massive ALPs ($m_a \sim$ 10 keV - 100 MeV), the dominant process is the decay into two photons. This has been considered in Ref. [4], but they assume ALPs coupled to nucleons. Our analysis extends this to the case of pure photon couplings. We highlight that not all photons can reach Earth and we improve the estimate of the number that do so by employing a numerical simulation of the time-delay and angular distributions.

Besides SN 1987A, we also consider the possibility that the red supergiant Betelgeuse explodes in a SN event. This is particularly interesting since its distance to Earth is only $\sim$ 200 pc, much closer than SN 1987A at $\sim$ 50 kpc.

2   Signal events reaching the detector

ALPs are produced in the core of the SN via the Primakoff process with typical energies $\sim 100\,\text{MeV}$. We use the ALP energy spectrum and production rate from Ref. [3] to estimate the ALP-originated photon fluence (photons per unit area on Earth).

We are interested in massive ALPs, thus having a finite life time: $\tau_a = 64\pi/g_{a\gamma\gamma}^2 m_a^3$, i.e., the decay length is $\ell_{\text{ALP}} = \gamma v \tau_a$. For the mass and couplings considered, $\ell_{\text{ALP}} \lesssim d_{\text{SN}}$, most of the ALPs escape the SN and are emitted isotropically, so we may expect a flux of ALP-originated gamma-ray photons. However, the ALP-originated photons from decays inside the SN ($\ell_{\text{ALP}} \lesssim R_* \sim 10^{10}$ m [5]) are absorbed and do not reach the detector.

The ALPs being massive, they will also be appreciably boosted, so the decay angle of the photons, α, is finite and given by

$$\sin\alpha \sim \gamma^{-1}, \tag{2}$$

and this has two important consequences: the ALP-originated photons will not come directly from the line of sight, but rather from an angle – this angular window creates a "halo". Secondly, the non-zero decay angle means that the path from the SN to Earth is not simply d_{SN}, but generally longer, generating a time delay when compared to massless ALPs.

The details of ALP production in the core-collapse SN have been worked out in Ref. [3] for massless ALPs and here we assume their ALP spectrum and apply a correction factor to account for their massiveness. The ALP-originated gamma-ray fluence on Earth for heavy ALPs is given by

$$\mathcal{F}_\gamma = \left(\frac{2}{4\pi d_{\text{SN}}^2}\right)\left[\int_{m_a}^{\infty} dE_a \left(\frac{dN_a}{dE_a}\right)\bigg|_{\text{corr}}\right] \times \mathcal{P}(\delta t), \tag{3}$$

where $\mathcal{P}(\delta t)$ is the probability of observation of the ALP-originated photons within a time frame of δt – for SN 1987A we take $\delta t \simeq 10$ s [6]. The corrected ALP spectrum is given by

$$\left(\frac{dN_a}{dE_a}\right)\bigg|_{\text{corr}} = \left(\frac{dN_a}{dE_a}\right)\bigg|_{m_a=0} \times S(m_a) \tag{4}$$

with the correction factor

$$S(m_a) = \frac{\int \frac{d^3k}{(2\pi)^3}\frac{1}{\exp(\omega/T)-1}\sigma(\omega,m_a)}{\int \frac{d^3k}{(2\pi)^3}\frac{1}{\exp(\omega/T)-1}\sigma_0(\omega)}, \tag{5}$$

where σ_0 and σ are the massless and massive Primakoff cross sections, respectively [7]. Here we use $T \simeq 30$ MeV and $k_s \simeq 16$ MeV coming from the fit of the final spectrum for massless ALPs from Ref. [3].

3   Angular and time-delay distributions

Since the decay angle into two photons is finite, the combined distance travelled by the ALP and the photons is larger than d_{SN}. The distances covered by the ALP and ensuing photon are $L_1 \sim \ell_{\text{ALP}}$ and $L_2 = -L_1 + \sqrt{d_{\text{SN}}^2 - \sin^2\alpha L_1^2}$, respectively. The overall time delay is $\Delta t = \frac{L_1}{\beta} + L_2 - d_{\text{SN}}$, which can be significant: for $E_a \sim 100$ MeV, $m_a = 10$ MeV and $g_{a\gamma\gamma} = 10^{-10}\,\text{GeV}^{-1}$, we find $\Delta t \approx 10^3$ s (cf. Fig. 1).
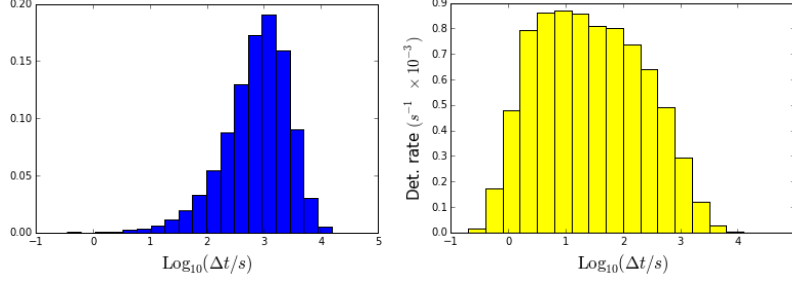
Figure 1: For $m_a = 10$ MeV and $g_{a\gamma\gamma} = 10^{-10}\,\mathrm{GeV}^{-1}$ from SN 1987A: fraction (probability) histogram depicting the distribution of time delays (left) and fractional detection rates (right).

A consequence of the time delay is that the ALP-originated photons arrive on Earth spread over a considerable time period. The probability that a single ALP arrives within a time period δt is given by $P(\delta t, E_a) = \delta t/\delta t_{\mathrm{typ}}$, with $\delta t_{\mathrm{typ}} \sim \ell_{\mathrm{ALP}}\left(1 - \beta\right)/\beta$. This gives $P(\delta t, E_a) \approx \delta t\, E_a\, g_{a\gamma\gamma}^2 m_a^2$ and, convoluting this with the energy distribution and including the extra $g_{a\gamma\gamma}^2$ from the Primakoff cross section, we may expect that the fluence behaves as

$$\mathcal{F}_\gamma \sim g_{a\gamma\gamma}^4 m_a^2 \ \rightarrow \ g_{a\gamma\gamma} \sim m_a^{-1/2}. \tag{6}$$

As for the detection angle, which can be obtained via $\sin\theta = (L_1/d_{\mathrm{SN}})\sin\alpha$, we also find that it can be quite significant: for $m_a = 10$ MeV and $g_{a\gamma\gamma} = 10^{-12}\,\mathrm{GeV}^{-1}$, the opening angle is $\sim 0.03°$, about a tenth of the angular diameter of the Moon.

4   Results

After the $\delta t \simeq 10$ s following the SN 1987A event the gamma-ray detector at the SMM found no unexpected signal, thus setting an upper limit on the fluence $\mathcal{F}_\gamma^{\mathrm{exp}} < 0.6\,\gamma \cdot \mathrm{cm}^{-2}$ for $25 \leq E_\gamma \leq 100$ MeV [6]. Evaluating Eq. (3) numerically and imposing the upper limit of $\mathcal{F}_\gamma^{\mathrm{exp}}$, we obtain the excluded region shown in blue on the left panel of Fig. 2. Two aspects of the bound are important: the turn up caused by the correction factor, as the mass becomes of the same order of magnitude as the temperature of the core, and a recession of the bound for large masses and couplings, which is due to the absorption of the ALP-originated photons inside the region limited by the effective radius $R_* \sim 10^{10}$ m [5].

Looking into the future, Betelgeuse is a red supergiant ($d_{\mathrm{SN}} \sim 200$ pc) and is expected to go SN in the next few hundred thousand years. Its associated ALP-originated gamma-ray flux would be much more intense than that from SN 1987A, so, proceeding similarly, we may calculate the fluence of ALP-originated photons coming from Betelgeuse. Currently, one of the best detection possibilities would be the Fermi-LAT, whose point source sensitivity (PSS) is $3 \times 10^{-9}\,\gamma \cdot \mathrm{cm}^{-2} \cdot \mathrm{s}^{-1}$ for $E_\gamma > 100$ MeV [8]. Restricting ourselves to an observation time of $\delta t \sim 10$ s – comparable to the duration of the neutrino burst during SN 1987A [6] – we obtain an effective upper limit on the fluence of $\mathcal{F}_\gamma^{\mathrm{exp}} \simeq 3 \times 10^{-8}\,\gamma \cdot \mathrm{cm}^{-2}$, which translates into the bound shown on the right panel of Fig. 2.

In conclusion, we have used the non-observation of extra gamma rays from SN 1987A that would be caused by the decay of massive ALPs to exclude regions of parameter space (cf. left
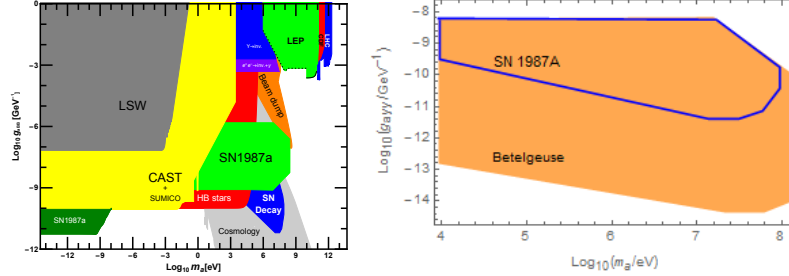
Figure 2: Left: Excluded regions in ALP parameter space (see Ref. [9] and references therein); our bound based on SN 1987A is shown in dark blue ("SN decay"). Right: bound based on Betelgeuse with PSS from Fermi-LAT.

panel of Fig. 2). Extrapolating our analysis to the case of the red supergiant Betelgeuse, we find that the limits can be improved due to the shorter distance to Earth and to the better sensitivity of the instruments for gamma-ray detection (cf. right panel of Fig. 2).

Acknowledgments

References

[1] J. Jaeckel, P.C. Malta, J. Redondo, "New limits on heavy ALPs: an analysis of SN 1987A, again", in preparation for publication.

[2] D. Cadamuro, J. Redondo, "Cosmological bounds on pseudo Nambu-Goldstone bosons", JCAP 02, 032 (2012).

[3] A. Payez, C. Evoli, T. Fischer, M. Giannotti, A. Mirizzi, A. Ringwald, "Reviewing the SN 1987A gamma-ray limit on ultra-light axion-like particles", JCAP 1502, 006 (2015).

[4] M. Giannotti, L.D. Duffy, R. Nita, "New constraints for heavy axion-like particles from supernovae", JCAP 01, 015 (2011).

[5] D. Kazanas, R.N. Mohapatra, S. Nussinov, V.L. Teplitz, Y. Zhang, "Supernova bounds on the dark photon using its electromagnetic decay", Nuc. Phys. B **17**, 890 (2015).

[6] E. Chupp, T. Verstrand, C. Reppin, "Experimental limits on the radiative decay of SN 1987A neutrinos", Phys. Rev. Lett. **62**, 505 (1989).

[7] G.G. Raffelt, "Stars as laboratories for fundamental physics", University of Chicago Press (1996).

[8] Fermi/LAT Collaboration, "The large area telescope on the Fermi gamma-ray space telescope mission", Astrophys. J. **697**, 1071-1102 (2009).

[9] J. Jaeckel, M. Spannowsky, "Probing MeV to 90 GeV axion-like particles with LEP and LHC", Phys. Lett. B **753**, 482 (2016).

Searches for Axionlike Particles Using γ-Ray Observations

Manuel Meyer

Department of Physics, Stockholm University, AlbaNova, SE-106 91 Stockholm, Sweden

Axionlike particles (ALPs) are a common prediction of theories beyond the Standard Model of particle physics that could explain the entirety of the cold dark matter. These particles could be detected through their mixing with photons in external electromagnetic fields. Here, we provide a short review over ALP searches that utilize astrophysical γ-ray observations. We summarize current bounds as well as future sensitivities and discuss the possibility that ALPs alter the γ-ray opacity of the Universe.

1 Introduction

Astrophysical observations with space-borne and ground based γ-ray experiments have proven to be a powerful tool to search for physics beyond the Standard Model. The currently operating *Fermi* Large Area Telescope (LAT), sensitive to γ rays between 20 MeV and above 300 GeV [1], and imaging air Cherenkov telescopes (IACTs), such as H.E.S.S., MAGIC, and VERITAS (sensitive to γ rays above ~ 50 GeV [2, 3, 4]) have provided strong constraints on, e.g., Lorentz invariance violation [5, 6], as well as on the annihilation cross section of weakly interacting massive particles, which are prime cold dark matter candidates [7, 8, 9].

Observations at γ-ray energies can also be used to search for traces of axionlike particles (ALPs). ALPs are closely related to the axion, which plays an essential role in the solution of the strong CP problem in QCD [10, 11, 12, 13]. Just as the axion, ALPs are well motivated cold dark-matter candidates [14, 15, 16, 17, 18] that could be detected through their coupling to photons in external magnetic fields [19, 20]. They arise in several extensions of the Standard Model [21, 22, 23].

Here, we review advancements in astrophysical γ-ray searches for ALPs that have, for certain ALP masses (m_a) below μeV, reached a sensitivity comparable to that of current or future dedicated laboratory experiments. We give a short overview of the relevant astrophysical magnetic fields (Sec. 2),[1] and review the status of evidence found for a reduced γ-ray opacity that might be caused by photon-ALP oscillations (Sec. 2.1). We review searches for ALP-induced spectral irregularities (Sec. 2.2) before closing with an outlook on future observations (Sec. 3).

---

[1]This review focuses on photon-ALP mixing in external magnetic fields, however, searches for γ-ray signals from axion and ALP decays have also been carried out [24, 25].

2 Photon-ALP mixing at γ-ray energies

Solving the full equations of motion for the photon-ALP system, one realizes that the conversion probability becomes maximal and independent of energy above a critical energy $E_{\mathrm{crit}} = |m_a^2 - \omega_{\mathrm{pl}}^2|/2g_{a\gamma}B$, where B denotes the field strength transversal to the photon propagation direction, $g_{a\gamma}$ the photon-ALP coupling, and ω_{pl} the plasma frequency of the medium. This strong mixing regime persists as long as $E < E_{\mathrm{max}} = 90\pi g_{a\gamma}B_{\mathrm{cr}}^2/7\alpha B$, with α the fine structure constant and the critical magnetic field $B_{\mathrm{cr}} \sim 4.4 \times 10^{13}\,\mathrm{G}$. For photons around PeV energies, background photon fields such as the cosmic microwave background cause an additional photon dispersion leading to a modification of E_{max} [26]. Reviews on solving the equations of motion and deriving the photon-ALP mixing matrices in a number of magnetic fields are provided in, e.g., Refs. [27, 28, 29, 30, 31, 32].

One abundantly studied source class to search for traces of ALPs are blazars, active galactic nuclei (AGNs) with their relativistic jets closely aligned to the line of sight [33]. Blazars make up the majority of extragalactic sources detected at γ-ray energies [34]. Their intrinsic brightness, especially during flaring episodes, and the numerous magnetic-field environments traversed by the photon beam along the line of sight make them excellent targets to search for ALP signatures. The photon-ALP oscillations may lead to two observables in the energy spectra of these objects (discussed in the following subsections): a) the γ-ray source flux can be attenuated due to pair production with low energy photons originating from background radiation fields [35, 36, 37]. ALPs produced in the vicinity of the source would circumvent this attenuation, and, if they reconvert to γ rays, could lead to a significant boost of the observed photon flux, and b) oscillations of the flux should be imprinted in the spectra around E_{crit} and E_{max} that depend on the morphology of the traversed B fields.

To accurately model the effect of ALPs on γ-ray spectra, a thorough understanding of the intervening B fields is necessary. Several different B-field environments have been studied in connection to photon-ALP conversions at γ-ray energies. They cover both coherent and turbulent magnetic fields, where the turbulent fields are often modeled with a simplified cell-like structure: each cell has a length equal to the coherence length λ and the magnetic-field orientation changes randomly from one cell to the next. Starting from the blazar, the considered B fields include: the B-field in the AGN jet, [38, 39, 40, 41, 32], the turbulent magnetic fields of the host galaxies (usually found to be elliptical galaxies) that, because of the short coherence legnth of $\lambda \sim 0.1\,\mathrm{kpc}$ should not contribute significantly to photon-ALP mixing [39, 32], the B field of the lobes of AGN jets [41, 42], the turbulent B fields of galaxy clusters that might host the blazar [43, 44, 32], the intergalactic magnetic field (IGMF) [45, 46, 47, 48, 38, 30, 31] (for which only upper limits exist, $B \leqslant 1.7\,\mathrm{nG}$ for λ equal to the Jeans' length [49]), and eventually the Galactic magnetic field (GMF) of the Milky Way [47, 43], which consists of both a turbulent and coherent component. Several models for the GMF have been put forward in the literature [50, 51], with the best-fit values for the model of Ref. [51] recently updated with measurements of the Planck satellite [52].

2.1 Evidence for a reduced γ-ray opacity?

One predominant radiation field responsible for the attenuation of γ rays originating from blazars with energies $10\,\mathrm{GeV} \lesssim E \lesssim 50\,\mathrm{TeV}$ is the extragalactic background light (EBL), which stretches from UV to far infrared wavelengths [53]. The isotropic EBL photon density is difficult to measure directly due to strong foreground contamination with zodiacal light [54]. The EBL

is composed of the emitted starlight integrated over the history of the Universe and the starlight that has been absorbed and re-emitted by dust in galaxies [55, 56]. The exponential attenuation scales with the optical depth $\tau(E, z)$, a monotonically increasing function with γ-ray energy E, source redshift z, and EBL photon density (see Refs. [57, 58, 59, 60, 61, 62] for a selection of EBL models).

Using published IACT spectral data points, several authors have indeed found indications that state-of-the-art EBL models over-predict the observed γ-ray attenuation. Once the observed spectrum has been corrected for the absorption utilizing an EBL model, such an over-prediction would manifest itself by a spectral hardening at energies corresponding to a high optical depth. Accordingly, one way to search for such a feature is to fit power laws, $\phi(E) = dN/dE \sim E^{-\Gamma}$, with spectral indices Γ_{low} and Γ_{high} separately to the low and high energy part of the de-absorbed spectra. If the opacity is over-predicted, the difference between the spectral indices $\Delta\Gamma = \Gamma_{\mathrm{low}} - \Gamma_{\mathrm{high}}$ should increase with redshift as the predicted attenuation increases (this should also holds if the sources get dimmer at higher energies). The above effect has been found and ALPs have been suggested as a possible solution [45, 47, 63, 38, 64, 31, 65, 66, 67]. Alternatively, it is possible to search for the spectral hardening by examining fit residuals $\chi = (\phi_{\mathrm{obs}} - \phi(E)e^{-\tau(E)})/\sigma_\phi$ of fits of smooth concave, i.e. non-hardening, functions $\phi(E)$ multiplied with EBL absorption to the observed spectra ϕ_{obs} with flux uncertainties σ_ϕ. Again, if τ is overestimated, the fit residuals should display a positive correlation with optical depth. A $4\,\sigma$ indication for such an effect was found [68, 69] that could be reduced significantly when photon-ALP oscillations are taken into account [70]. Intrinsic source effects leading to a spectral hardening can fake such a signal (see e.g. Ref. [71] for one possibility), however, it would be highly contrived if such a hardening occurred in several sources at exactly the energy where $\tau > 1$.

So far we have summarized observations of spectral hardening at high optical depths that might hint at photon-ALP oscillations. However, recent analyses could not confirm these results. Using the largest IACT data set to date, the authors of Ref. [72] repeated the analysis of Ref. [68] and found no deviation from EBL-only expectations. Furthermore, when including uncertainties on the IACT energy resolution, and further systematic uncertainties, no spectral upturn can be observed when comparing *Fermi*-LAT and IACT spectra (spectra measured with the *Fermi*-LAT should be less affected by EBL absorption at low redshift due to the lower energy range accessible with the satellite) [73]. Using a sample of *Fermi*-LAT detected blazars above $50\,\mathrm{GeV}$ and up to redshifts of $z \sim 2$, again, no evidence for a spectral hardening was found in *Fermi*-LAT data [74]. It should be noted that the *Fermi*-LAT has only detected γ rays up to $\tau \sim 3$ [75], whereas the ALP effect should become particularly pronounced for $\tau \gtrsim 4$ [42].

Future dedicated analyses that search for spectral hardening carried out by the IACT collaborations (who have access to the full instrumental response functions and raw data) would be extremely valuable. This would enable a full likelihood analysis that could provide important insights not only into ALPs but also into other processes that might alter the γ-ray opacity such as electromagnetic cascades induced by ultra-high energy cosmic rays [76] or the propagation of photons through cosmic voids [77].

2.2 ALP-induced spectral irregularities

In case no spectral hardening is observed, it is difficult to constrain the photon-ALP coupling. The reason is that the non-observation might not be due to the absence of ALPs but due to

a high-energy cutoff of the intrinsic spectrum. This problem is alleviated when searching for spectral irregularities around E_{crit} and E_{max} as these features should be detectable as long as the energy resolution is sufficient to resolve the features and that signal-to-noise ratio is high enough to distinguish the features from Poisson noise.[2]

Such analyses have been carried out at X-ray [79, 80] and γ-ray energies [44, 81] with observations of central AGNs in galaxy clusters and groups. The authors employed more sophisticated B-field models in which the turbulent fields are described with suitable power spectra instead of cell-like morphologies. The non-observation of such features at X-rays leads to the exclusion of ALP masses $m_a < 10^{-11}\,\mathrm{eV}$ [79], and $m_a < 10^{-12}\,\mathrm{eV}$ [80] for $g_{a\gamma} \gtrsim 6 \times 10^{-12}\,\mathrm{GeV}^{-1}$. These bounds also apply for lower masses since $\omega_{\mathrm{pl}} \gg m_a$, leading to irregularities independent of m_a.[3] At γ-ray energies, the strongest bounds on $g_{a\gamma}$ come from *Fermi*-LAT observations of NGC 1275 that are the most constraining limits between $0.5\,\mathrm{neV} \lesssim m_a \lesssim 20\,\mathrm{neV}$ to date [81]. Taken at face value, together with the bounds from the non-observation of irregularities in H.E.S.S. data of PKS 2155-304 [44] and the absence of a γ-ray burst signal from SN 1987A [84], the possibility that ALPs alter the EBL γ-ray opacity is already seriously constrained (see Fig. 1).

3   Conclusion and outlook

Blazar observations at γ-ray energies pose a complementary approach to search for ALPs, that could reveal themselves either through spectral irregularities or a boost of the γ-ray flux that would otherwise be attenuated through pair production. Current limits, future experimental sensitivities, and theoretically preferred regions for low mass ALPs are summarized in Fig. 1.

Future observations with CTA [85], HAWC [86], and HiSCORE [87] with their good point source sensitivities also at energies beyond 1 TeV have the potential to search for ALPs at masses above 10 neV. Especially CTA will be able to probe the entire parameters space where ALPs could explain the hints for a low γ-ray opacity [42]. The planned full-sky extragalactic CTA survey could also be used to search for a spectral hardening correlated with the photon-ALP conversion probability in Galactic magnetic fields [88].

ALPs could also be searched for with γ-ray observations using sources other than blazars. Other possible sources to look for traces of ALPs include spectra of pulsars and observations of pulsar binary systems [89]. Another alternative is to search for a short γ-ray burst from the next Galactic core-collapse supernova. ALPs would be produced in such an event via the Primakoff process and subsequently convert into γ rays in the Galactic magnetic field. These γ rays would arrive simultaneously with the neutrinos produced in the supernova. If such an event occurs during the lifetime of the *Fermi* mission and while the supernova is in the field of view of the satellite (the *Fermi* LAT surveys $\sim 20\,\%$ of the sky at any given moment), it would be possible to probe couplings down to $2 \times 10^{-13}\,\mathrm{GeV}^{-1}$ for masses below 1 neV [90]. Future γ-ray missions such as e-ASTROGAM [91], ComPair [92], or PANGU [93] should even be more sensitive to such a signal given their accessible energy range and improved point spread function in comparison to the *Fermi* LAT.

---

[2]Even for magnetic-field configurations in cell-like models that lead to no mixing in the strong mixing regime, the irregularities would still occur [78].

[3]Interestingly, the conversions of ALPs from a cosmic ALP background could explain excess diffuse X-ray emission observed in several galaxy clusters [82, 83].
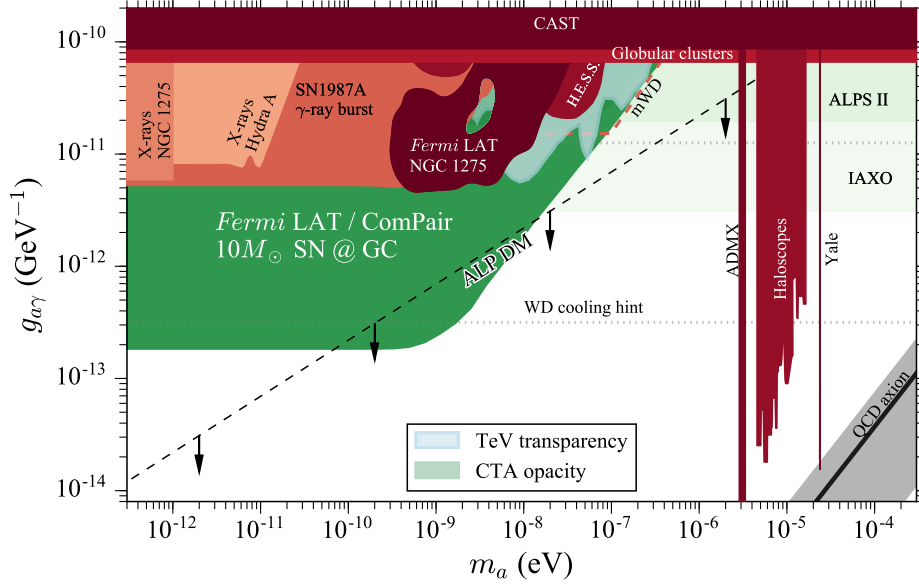
Figure 1: The low-mass ALP parameter space. Current bounds are shown in red and include the non-observations of spectral irregularities at X-ray energies from Hydra A [79] and NGC 1275 [80], at γ-ray energies using the same source with the *Fermi* LAT [81] and PKS 2155-304 with H.E.S.S. [44]. Also shown are bounds from the CAST helioscope [94], and haloscope microwave cavities looking for dark-matter axions and ALPs [95, 96, 97, 98, 99], as well as limits inferred from globular cluster observations [100], and the non-detection of a γ-ray burst from SN 1987A [84]. Limits derived from optical polarization measurements (that could also be interpreted as a preferred region to explain such a polarization) of magnetic white dwarfs (mWD) are shown as a red dashed line [101]. ALP parameters that could explain a low opacity of the Universe to γ rays are shown in blue [70] while those that would cause an additional white dwarf (WD) cooling lie between grey dashed lines [102]. Predicted parameters for one particular QCD axion model (the "KVSZ" axion [103, 104]) are shown together with an order of magnitude uncertainties (grey band). Sensitivities of future experiments such as ALPS II [105], IAXO [106] and future observations with CTA [42] are shown in green along with the parameter space that could be probed with the *Fermi* LAT in case of a core-collapse (10 $M_\odot$) supernova (SN) in the Galactic center (GC) [90]. ALPs with parameters below the black dashed line could account for the entirety of the cold dark matter [18].

Acknowledgments

References

[1] W. B. Atwood, A. A. Abdo, M. Ackermann, *et al.*, "The Large Area Telescope on the Fermi Gamma-Ray Space Telescope Mission," ApJ, vol. 697, pp. 1071–1102, 2009.

[2] F. Aharonian, A. G. Akhperjanian, A. R. Bazer-Bachi, M. Beilicke, W. Benbow, *et al.*, "Observations of the Crab nebula with HESS," A&A, vol. 457, pp. 899–915, Oct. 2006.

[3] J. Aleksi, S. Ansoldi, L. Antonelli, P. Antoranz, A. Babic, P. Bangale, M. Barcel, J. Barrio, *et al.*, "The major upgrade of the magic telescopes, part ii: A performance study using observations of the crab nebula," *Astroparticle Physics*, vol. 72, pp. 76 – 94, 2016.

[4] J. Holder, V. A. Acciari, E. Aliu, T. Arlen, M. Beilicke, W. Benbow, *et al.*, "Status of the VERITAS Observatory," in *American Institute of Physics Conference Series* (F. A. Aharonian, W. Hofmann, and F. Rieger, eds.), vol. 1085 of *American Institute of Physics Conference Series*, pp. 657–660, Dec. 2008.

[5] F. Aharonian *et al.*, "Limits on an Energy Dependence of the Speed of Light from a Flare of the Active Galaxy PKS 2155-304," *Phys. Rev. Lett.*, vol. 101, p. 170402, 2008.

[6] M. Ackermann *et al.*, "A limit on the variation of the speed of light arising from quantum gravity effects," *Nature*, vol. 462, pp. 331–334, 2009.

[7] M. Ackermann *et al.*, "Searching for Dark Matter Annihilation from Milky Way Dwarf Spheroidal Galaxies with Six Years of Fermi Large Area Telescope Data," *Phys. Rev. Lett.*, vol. 115, no. 23, p. 231301, 2015.

[8] H. Abdallah *et al.*, "Search for dark matter annihilations towards the inner Galactic halo from 10 years of observations with H.E.S.S," *Phys. Rev. Lett.*, vol. 117, no. 11, p. 111301, 2016.

[9] B. Zitzer, "A Search for Dark Matter from Dwarf Galaxies using VERITAS," *PoS*, vol. ICRC2015, p. 1225, 2016.

[10] R. D. Peccei and H. R. Quinn, "CP conservation in the presence of pseudoparticles," *Physical Review Letters*, vol. 38, pp. 1440–1443, 1977.

[11] S. Weinberg, "A new light boson?," *Physical Review Letters*, vol. 40, pp. 223–226, 1978.

[12] F. Wilczek, "Problem of strong P and T invariance in the presence of instantons," *Physical Review Letters*, vol. 40, pp. 279–282, 1978.

[13] J. Jaeckel and A. Ringwald, "The Low-Energy Frontier of Particle Physics," *Annual Review of Nuclear and Particle Science*, vol. 60, pp. 405–437, 2010.

[14] J. Preskill, M. B. Wise, and F. Wilczek, "Cosmology of the invisible axion," *Physics Letters B*, vol. 120, pp. 127–132, 1983.

[15] L. F. Abbott and P. Sikivie, "A cosmological bound on the invisible axion," *Physics Letters B*, vol. 120, pp. 133–136, Jan. 1983.

[16] M. Dine and W. Fischler, "The not-so-harmless axion," *Physics Letters B*, vol. 120, pp. 137–141, Jan. 1983.

[17] D. J. E. Marsh, "Axiverse extended: Vacuum destabilization, early dark energy, and cosmological collapse," Phys. Rev. D, vol. 83, p. 123526, June 2011.

[18] P. Arias, D. Cadamuro, M. Goodsell, J. Jaeckel, J. Redondo, and A. Ringwald, "WISPy cold dark matter," *JCAP*, vol. 6, p. 13, 2012.

[19] P. Sikivie, "Experimental tests of the 'invisible' axion," *Physical Review Letters*, vol. 51, pp. 1415–1417, Oct. 1983.

[20] G. Raffelt and L. Stodolsky, "Mixing of the photon with low-mass particles," Phys. Rev. D, vol. 37, pp. 1237–1249, 1988.

[21] E. Witten, "Some properties of O(32) superstrings," *Physics Letters B*, vol. 149, pp. 351–356, 1984.

[22] A. Arvanitaki, S. Dimopoulos, S. Dubovsky, *et al.*, "String axiverse," Phys. Rev. D, vol. 81, p. 123530, June 2010.

[23] A. Ringwald, "Axions and Axion-Like Particles," *ArXiv e-prints*, July 2014.

[24] M. Giannotti, L. D. Duffy, and R. Nita, "New constraints for heavy axion-like particles from supernovae," *JCAP*, vol. 1101, p. 015, 2011.

[25] B. Berenji, J. Gaskins, and M. Meyer, "Constraints on Axions and Axionlike Particles from Fermi Large Area Telescope Observations of Neutron Stars," *Phys. Rev.*, vol. D93, no. 4, p. 045019, 2016.

[26] A. Dobrynina, A. Kartavtsev, and G. Raffelt, "Photon-photon dispersion of TeV gamma rays and its role for photon-ALP conversion," Phys. Rev. D, vol. 91, p. 083003, Apr. 2015.

[27] Y. Grossman, S. Roy, and J. Zupan, "Effects of initial axion production and photon-axion oscillation on type Ia supernova dimming [rapid communication]," *Physics Letters B*, vol. 543, pp. 23–28, 2002.

[28] C. Csáki, N. Kaloper, M. Peloso, and J. Terning, "Super-GZK photons from photon axion mixing," *JCAP*, vol. 5, p. 5, 2003.

[29] A. Mirizzi, G. G. Raffelt, and P. D. Serpico, "Photon-Axion Conversion in Intergalactic Magnetic Fields and Cosmological Consequences," in *Axions* (M. Kuster, G. Raffelt, and B. Beltrán, eds.), vol. 741 of *Lecture Notes in Physics, Berlin Springer Verlag*, p. 115, 2008.

[30] N. Bassan, A. Mirizzi, and M. Roncadelli, "Axion-like particle effects on the polarization of cosmic high-energy gamma sources," *JCAP*, vol. 5, p. 10, 2010.

[31] A. de Angelis, G. Galanti, and M. Roncadelli, "Relevance of axionlike particles for very-high-energy astrophysics," Phys. Rev. D, vol. 84, no. 10, p. 105030, 2011.

[32] M. Meyer, D. Montanino, and J. Conrad, "On detecting oscillations of gamma rays into axion-like particles in turbulent and coherent magnetic fields," *JCAP*, vol. 9, p. 3, 2014.

[33] C. M. Urry and P. Padovani, "Unified Schemes for Radio-Loud Active Galactic Nuclei," PASP, vol. 107, pp. 803–+, 1995.

[34] M. Ackermann *et al.*, "The Third Catalog of Active Galactic Nuclei Detected by the Fermi Large Area Telescope," *Astrophys. J.*, vol. 810, no. 1, p. 14, 2015.

[35] A. I. Nikishov, "Absorption of high-energy photons in the Universe," *Sov. Phys. JETP*, vol. 14, pp. 393–394, 1962.

[36] R. J. Gould and G. P. Schréder, "Pair Production in Photon-Photon Collisions," *Physical Review*, vol. 155, pp. 1404–1407, 1967.

[37] R. J. Gould and G. P. Schréder, "Opacity of the Universe to High-Energy Photons," *Physical Review*, vol. 155, pp. 1408–1411, Mar. 1967.

[38] M. A. Sánchez-Conde, D. Paneque, E. Bloom, *et al.*, "Hints of the existence of axionlike particles from the gamma-ray spectra of cosmological sources," Phys. Rev. D, vol. 79, no. 12, p. 123511, 2009.

[39] F. Tavecchio, M. Roncadelli, G. Galanti, and G. Bonnoli, "Evidence for an axion-like particle from PKS 1222+216?," Phys. Rev. D, vol. 86, no. 8, p. 085036, 2012.

[40] O. Mena and S. Razzaque, "Hints of an axion-like particle mixing in the GeV gamma-ray blazar data?," *JCAP*, vol. 11, p. 23, 2013.

[41] F. Tavecchio, M. Roncadelli, and G. Galanti, "Photons into axion-like particles conversion in Active Galactic Nuclei," *ArXiv e-prints*, 2014.

[42] M. Meyer and J. Conrad, "Sensitivity of the Cherenkov Telescope Array to the detection of axion-like particles at high gamma-ray opacities," *JCAP*, vol. 12, p. 16, 2014.

[43] D. Horns, L. Maccione, M. Meyer, A. Mirizzi, D. Montanino, and M. Roncadelli, "Hardening of TeV gamma spectrum of active galactic nuclei in galaxy clusters by conversions of photons into axionlike particles," Phys. Rev. D, vol. 86, no. 7, p. 075024, 2012.

[44] A. Abramowski, F. Acero, F. Aharonian, *et al.*, "Constraints on axionlike particles with H.E.S.S. from the irregularity of the PKS 2155-304 energy spectrum," Phys. Rev. D, vol. 88, no. 10, p. 102003, 2013.

[45] A. de Angelis, M. Roncadelli, and O. Mansutti, "Evidence for a new light spin-zero boson from cosmological gamma-ray propagation?," Phys. Rev. D, vol. 76, no. 12, p. 121301, 2007.

[46] A. Mirizzi, G. G. Raffelt, and P. D. Serpico, "Signatures of axionlike particles in the spectra of TeV gamma-ray sources," Phys. Rev. D, vol. 76, no. 2, p. 023001, 2007.

[47] M. Simet, D. Hooper, and P. D. Serpico, "Milky Way as a kiloparsec-scale axionscope," Phys. Rev. D, vol. 77, no. 6, p. 063001, 2008.

[48] A. Mirizzi and D. Montanino, "Stochastic conversions of TeV photons into axion-like particles in extragalactic magnetic fields," *JCAP*, vol. 12, p. 4, 2009.

[49] M. S. Pshirkov, P. G. Tinyakov, and F. R. Urban, "New Limits on Extragalactic Magnetic Fields from Rotation Measures," *Physical Review Letters*, vol. 116, p. 191302, May 2016.

[50] M. S. Pshirkov, P. G. Tinyakov, P. P. Kronberg, and K. J. Newton-McGee, "Deriving the Global Structure of the Galactic Magnetic Field from Faraday Rotation Measures of Extragalactic Sources," ApJ, vol. 738, p. 192, 2011.

[51] R. Jansson and G. R. Farrar, "A New Model of the Galactic Magnetic Field," ApJ, vol. 757, p. 14, 2012.

[52] R. Adam *et al.*, "Planck intermediate results. XLII. Large-scale Galactic magnetic fields," 2016.

[53] E. Dwek and F. Krennrich, "The extragalactic background light and the gamma-ray opacity of the universe," *Astroparticle Physics*, vol. 43, pp. 112–133, 2013.

[54] M. G. Hauser, R. G. Arendt, *et al.*, "The COBE Diffuse Infrared Background Experiment Search for the Cosmic Infrared Background. I. Limits and Detections," ApJ, vol. 508, pp. 25–43, 1998.

[55] M. G. Hauser and E. Dwek, "The Cosmic Infrared Background: Measurements and Implications," ARA&A, vol. 39, pp. 249–307, 2001.

[56] A. Kashlinsky, "Cosmic infrared background and early galaxy evolution [review article]," Phys. Rep., vol. 409, pp. 361–438, 2005.

[57] A. Franceschini, G. Rodighiero, and M. Vaccari, "Extragalactic optical-infrared background radiation, its time evolution and the cosmic photon-photon opacity," A&A, vol. 487, pp. 837–852, 2008.

[58] J. D. Finke, S. Razzaque, and C. D. Dermer, "Modeling the Extragalactic Background Light from Stars and Dust," ApJ, vol. 712, pp. 238–249, Mar. 2010.

[59] T. M. Kneiske and H. Dole, "A lower-limit flux for the extragalactic background light," A&A, vol. 515, pp. A19+, 2010.

[60] A. Domínguez, J. R. Primack, D. J. Rosario, *et al.*, "Extragalactic background light inferred from AEGIS galaxy-SED-type fractions," MNRAS, vol. 410, pp. 2556–2578, 2011.

[61] R. C. Gilmore, R. S. Somerville, J. R. Primack, and A. Domínguez, "Semi-analytic modelling of the extragalactic background light and consequences for extragalactic gamma-ray spectra," MNRAS, vol. 422, pp. 3189–3207, 2012.

[62] Y. Inoue, S. Inoue, M. A. R. Kobayashi, R. Makiya, Y. Niino, and T. Totani, "Extragalactic Background Light from Hierarchical Galaxy Formation: Gamma-Ray Attenuation up to the Epoch of Cosmic Reionization and the First Stars," ApJ, vol. 768, p. 197, May 2013.

[63] A. De Angelis, O. Mansutti, M. Persic, and M. Roncadelli, "Photon propagation and the very high energy γ-ray spectra of blazars: how transparent is the Universe?," MNRAS, vol. 394, pp. L21–L25, 2009.

[64] A. Domínguez, M. A. Sánchez-Conde, and F. Prada, "Axion-like particle imprint in cosmological very-high-energy sources," *JCAP*, vol. 11, p. 20, 2011.

[65] W. Essey and A. Kusenko, "On Weak Redshift Dependence of Gamma-Ray Spectra of Distant Blazars," ApJ, vol. 751, p. L11, 2012.

[66] G. Rubtsov and S. Troitsky, "Breaks in gamma-ray spectra of distant blazars and transparency of the Universe," *JETP Lett.*, vol. 100, no. 6, pp. 397–401, 2014.

[67] G. Galanti, M. Roncadelli, A. De Angelis, and G. F. Bignami, "Axion-like particles explain the unphysical redshift-dependence of AGN gamma-ray spectra," *ArXiv e-prints*, 2015.

[68] D. Horns and M. Meyer, "Indications for a pair-production anomaly from the propagation of VHE gamma-rays," *JCAP*, vol. 2, p. 33, 2012.

[69] M. Meyer, D. Horns, and M. Raue, "Revisiting the Indication for a low opacity Universe for very high energy gamma-rays," *ArXiv e-prints*, Nov. 2012.

[70] M. Meyer, D. Horns, and M. Raue, "First lower limits on the photon-axion-like particle coupling from very high energy gamma-ray observations," Phys. Rev. D, vol. 87, no. 3, p. 035027, 2013.

[71] E. Lefa, F. A. Aharonian, and F. M. Rieger, ""Leading Blob" Model in a Stochastic Acceleration Scenario: The Case of the 2009 Flare of Mkn 501," ApJ, vol. 743, p. L19, 2011.

[72] J. Biteau and D. A. Williams, "The Extragalactic Background Light, the Hubble Constant, and Anomalies: Conclusions from 20 Years of TeV Gamma-Ray Observations," ApJ, vol. 812, p. 60, 2015.

[73] D. A. Sanchez, S. Fegan, and B. Giebels, "Evidence for a cosmological effect in gamma-ray spectra of BL Lacs," Astron. Astrophys., vol. 554, p. A75, 2013.

[74] A. Domínguez and M. Ajello, "Spectral Analysis of Fermi-LAT Blazars above 50 GeV," ApJ, vol. 813, p. L34, 2015.

[75] M. Ackermann et al., "2FHL: The Second Catalog of Hard Fermi-LAT Sources," ApJS, vol. 222, p. 5, 2016.

[76] W. Essey, O. E. Kalashev, A. Kusenko, and J. F. Beacom, "Secondary Photons and Neutrinos from Cosmic Rays Produced by Distant Blazars," Physical Review Letters, vol. 104, no. 14, p. 141102, 2010.

[77] A. Furniss, P. M. Sutter, J. R. Primack, and A. Dominguez, "A Correlation Between Hard Gamma-ray Sources and Cosmic Voids Along the Line of Sight," ArXiv e-prints, 2014.

[78] M. Meyer, "Modelling gamma-ray-axion-like particle oscillations in turbulent magnetic fields: relevance for observations with Cherenkov telescopes," in Proceedings, 10th Patras Workshop on Axions, WIMPs and WISPs (AXION-WIMP 2014): Geneva, Switzerland, June 29-July 4, 2014, 2014.

[79] D. Wouters and P. Brun, "Constraints on Axion-like Particles from X-Ray Observations of the Hydra Galaxy Cluster," ApJ, vol. 772, p. 44, July 2013.

[80] M. Berg, J. P. Conlon, F. Day, N. Jennings, S. Krippendorf, A. J. Powell, and M. Rummel, "Searches for Axion-Like Particles with NGC1275: Observation of Spectral Modulations," 2016.

[81] M. Ajello et al., "Search for Spectral Irregularities due to PhotonAxionlike-Particle Oscillations with the Fermi Large Area Telescope," Phys. Rev. Lett., vol. 116, no. 16, p. 161101, 2016.

[82] J. P. Conlon and M. C. D. Marsh, "Excess Astrophysical Photons from a 0.11 keV Cosmic Axion Background," Phys. Rev. Lett., vol. 111, no. 15, p. 151301, 2013.

[83] S. Angus, J. P. Conlon, M. C. D. Marsh, A. J. Powell, and L. T. Witkowski, "Soft X-ray Excess in the Coma Cluster from a Cosmic Axion Background," JCAP, vol. 1409, no. 09, p. 026, 2014.

[84] A. Payez, C. Evoli, T. Fischer, M. Giannotti, A. Mirizzi, and A. Ringwald, "Revisiting the SN1987A gamma-ray limit on ultralight axion-like particles," JCAP, vol. 1502, no. 02, p. 006, 2015.

[85] M. Actis, G. Agnetta, F. Aharonian, et al., "Design concepts for the Cherenkov Telescope Array CTA: an advanced facility for ground-based high-energy gamma-ray astronomy," Experimental Astronomy, vol. 32, pp. 193–316, 2011.

[86] A. U. Abeysekara, R. Alfaro, C. Alvarez, et al., "Sensitivity of the high altitude water Cherenkov detector to sources of multi-TeV gamma rays," Astroparticle Physics, vol. 50, pp. 26–32, 2013.

[87] M. Tluczykont, D. Hampf, D. Horns, et al., "The ground-based large-area wide-angle γ-ray and cosmic-ray experiment HiSCORE," Advances in Space Research, vol. 48, pp. 1935–1941, 2011.

[88] D. Wouters and P. Brun, "Anisotropy test of the axion-like particle Universe opacity effect: a case for the Cherenkov Telescope Array," JCAP, vol. 1, p. 16, 2014.

[89] A. Dupays, C. Rizzo, M. Roncadelli, and G. F. Bignami, "Looking for light pseudoscalar bosons in the binary pulsar system j0737-3039," Phys. Rev. Lett., vol. 95, p. 211302, 2005.

[90] M. Meyer, M. Giannotti, A. Mirizzi, J. Conrad, and M. Sanchez-Conde, "The Fermi Large Area Telescope as a Galactic Supernovae Axionscope," 2016.

[91] V. Tatischeff et al., "The e-ASTROGAM gamma-ray space mission," Proc. SPIE Int. Soc. Opt. Eng., vol. 9905, p. 99052N, 2016.

[92] A. A. Moiseev et al., "Compton-Pair Production Space Telescope (ComPair) for MeV Gamma-ray Astronomy," 2015.

[93] X. Wu, M. Su, A. Bravar, J. Chang, Y. Fan, M. Pohl, and R. Walter, "PANGU: A High Resolution Gamma-ray Space Telescope," Proc. SPIE Int. Soc. Opt. Eng., vol. 9144, p. 91440F, 2014.

[94] S. Andriamonje, S. Aune, D. Autiero, CAST Collaboration, et al., "An improved limit on the axion photon coupling from the CAST experiment," JCAP, vol. 4, p. 10, 2007.

[95] S. De Panfilis, A. C. Melissinos, B. E. Moskowitz, J. T. Rogers, Y. K. Semertzidis, W. Wuensch, H. J. Halama, A. G. Prodell, W. B. Fowler, and F. A. Nezrick, "Limits on the Abundance and Coupling of Cosmic Axions at 4.5-Microev ¡ m(a) ¡ 5.0-Microev," *Phys. Rev. Lett.*, vol. 59, p. 839, 1987.

[96] W. Wuensch, S. De Panfilis-Wuensch, Y. K. Semertzidis, J. T. Rogers, A. C. Melissinos, H. J. Halama, B. E. Moskowitz, A. G. Prodell, W. B. Fowler, and F. A. Nezrick, "Results of a Laboratory Search for Cosmic Axions and Other Weakly Coupled Light Particles," *Phys. Rev.*, vol. D40, p. 3153, 1989.

[97] C. Hagmann, P. Sikivie, N. S. Sullivan, and D. B. Tanner, "Results from a search for cosmic axions," *Phys. Rev.*, vol. D42, pp. 1297–1300, 1990.

[98] S. J. Asztalos, G. Carosi, C. Hagmann, D. Kinion, K. van Bibber, M. Hotz, L. J. Rosenberg, G. Rybka, J. Hoskins, J. Hwang, P. Sikivie, D. B. Tanner, R. Bradley, and J. Clarke, "Squid-based microwave cavity search for dark-matter axions," *Phys. Rev. Lett.*, vol. 104, p. 041301, Jan 2010.

[99] B. M. Brubaker *et al.*, "First results from a microwave cavity axion search at 24 micro-eV," 2016.

[100] A. Ayala, I. Domínguez, M. Giannotti, *et al.*, "Revisiting the bound on axion-photon coupling from Globular Clusters," *Phys. Rev. Lett.*, vol. 113, no. 19, p. 191302, 2014.

[101] R. Gill and J. S. Heyl, "Constraining the photon-axion coupling constant with magnetic white dwarfs," Phys. Rev. D, vol. 84, no. 8, p. 085001, 2011.

[102] J. Isern, E. García-Berro, S. Torres, and S. Catalán, "Axions and the Cooling of White Dwarf Stars," ApJ, vol. 682, pp. L109–L112, 2008.

[103] J. E. Kim, "Weak Interaction Singlet and Strong CP Invariance," *Phys. Rev. Lett.*, vol. 43, p. 103, 1979.

[104] M. A. Shifman, A. I. Vainshtein, and V. I. Zakharov, "Can Confinement Ensure Natural CP Invariance of Strong Interactions?," *Nucl. Phys.*, vol. B166, pp. 493–506, 1980.

[105] R. Bähre, B. Döbrich, J. Dreyling-Eschweiler, *et al.*, "Any light particle search II – Technical Design Report," *Journal of Instrumentation*, vol. 8, p. 9001, 2013.

[106] I. G. Irastorza, F. T. Avignone, G. Cantatore, *et al.*, "Future axion searches with the International Axion Observatory (IAXO)," *Journal of Physics Conference Series*, vol. 460, no. 1, p. 012002, 2013.

Status of CUORE: an observatory for neutrinoless double beta decay and other rare events

Maria Martinez[1], on behalf of the CUORE Collaboration

[1]Dipartimento di Física, Sapienza Università di Roma, Italy
INFN - Sezione di Roma, Italy
Laboratorio de Física Nuclear y Astropartículas, Universidad de Zaragoza, Spain

CUORE is a ton-scale neutrinoless double beta decay ($0\nu\beta\beta$) experiment based on TeO$_2$ cryogenic detectors that is in the last construction stage at the Laboratori Nazionali del Gran Sasso. Its primary goal is to observe $0\nu\beta\beta$ of ^{130}Te, with a projected sensitivity reaching the inverted hierarchy region of the neutrino mass. Thanks to the ultra-low background and large projected exposure, CUORE is suitable to other rare event searches, as solar axions or dark matter direct detection. CUORE-0, a single-tower prototype recently concluded, has served as a proof-of-concept of the CUORE technology. We present the final CUORE-0 results on $0\nu\beta\beta$ and discuss the status and the physics potential of CUORE on different rare event searches.

1   Introduction

CUORE (Cryogenic Underground Observatory for Rare Events) [1, 2] is a ton-scale experiment whose primary goal is to observe neutrinoless double beta decay ($0\nu\beta\beta$) of ^{130}Te using a large array of TeO$_2$ cryogenic detectors. This decay [3] is a second-order lepton number violating process in which a nucleus (A,Z) transforms into (A,Z+2) with the simultaneous emission of two electrons, that can occur only if the neutrino is a Majorana particle. Its observation would not only prove the neutrino nature (Dirac or Majorana) and confirm lepton number violation, but it could also assess the absolute neutrino mass scale. In CUORE, a TeO$_2$ crystal is simultaneously the source of the decay and the detector that measures the energy deposited by the two electrons, which results in a peak centered at the transition energy $Q_{\beta\beta}$ (around 2528 keV for ^{130}Te). The CUORE technology was proven by Cuoricino, that with 40 kg of TeO$_2$ and 19.75 kg×yr of ^{130}Te exposure set a lower limit to the $0\nu\beta\beta$ half-life of 2.8×10^{24} yr (90% C.L.) [4]. It also revealed that the background in the region of interest (RoI) around $Q_{\beta\beta}$ was dominated by surface contaminations in the crystals and near surfaces (mainly the copper structures that hold the crystals). Therefore, for CUORE we implemented very strict protocols for the materials cleaning and assembly. The first tower constructed according to the new standard CUORE procedures was operated in the Cuoricino cryostat as an independent experiment called CUORE-0, and served not only as proof-of-concept of the complete CUORE cleaning and assembling line, but was a $0\nu\beta\beta$ search on its own.
CUORE is currently in the last phase of construction at Laboratori Nazionali del Gran Sasso

(LNGS), in Italy, and is expected to start operations by the end of 2016. With its ultra-low background ton mass, it could also serve as an observatory for other rare searches like solar axions and dark matter (DM).

In the following we report on the CUORE-0 results (Sec. 2), we revise the CUORE physics potential on axions and dark matter searches (Sec. 3) and finally we give an update on CUORE status (Sec. 4).

2 CUORE-0 results

CUORE-0 is an array of 52 TeO$_2$ crystals of 750 g each, for a total mass of 39 kg (11 kg of ^{130}Te). It was operated in the same experimental setup that hosted Cuoricino, at LNGS, from March 2013 to March 2015 for a total exposure of 35.2 kg×yr. A complete description of the detector construction and experimental details can be found in [5].

The success of the new cleaning procedures was soon evidenced in the background spectrum (see it compared with the Cuoricino one in Fig. 1, left). The γ component, that is the major part of the background below 2615 keV, originates in the cryostat and so it is practically the same for both experiments. Above that energy, background is dominated by degraded α decays coming from surfaces near the detector. We measured the rate in the α region (evaluated from 2700 keV to 3900 keV, excluding the ^{190}Pt α line coming from a bulk contamination in the crystals) to be 0.016±0.001 counts/(keV×kg×yr). That means a factor of 6.8 improvement over Cuoricino. The energy resolution, evaluated on the ^{208}Tl line at 2615 keV during calibration runs with ^{232}Th source, was 4.9 keV FWHM.
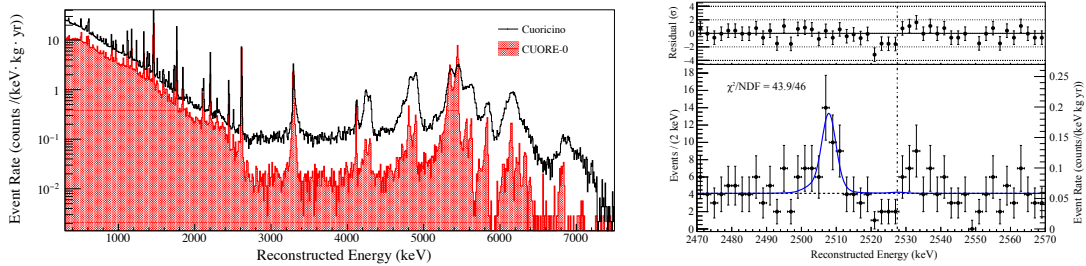
Figure 1: Left: CUORE-0 (red histogram) and Cuoricino (black line) backgrounds. The γ component, below 2615 keV, is originated in the cryostat, the same for both experiments, while there is a strong reduction in the α component above this energy. Right: CUORE-0 data and the best fit model (solid blue line) in the RoI. The normalized residuals are shown above. The peak at 2507 keV is due to ^{60}Co and the dash-dotted line indicates the $Q_{\beta\beta}$.

We kept the CUORE-0 RoI blinded until the sensitivity surpassed the Cuoricino one. Then, after fixing the data selection cuts and the $0\nu\beta\beta$ analysis procedure, we unblinded the RoI and performed an unbinned extended maximum likelihood fit. The final results can be found in [6] and a detailed revision of the analysis procedures in [7]. The result is displayed in the right panel of Fig. 1: There is no excess of events in the RoI, and our best fit limit on the $0\nu\beta\beta$ half-life of ^{130}Te is T$_{1/2}$ >2.7×10^{24} yr at 90% C.L. This is consistent with our median expected 90% C.L. sensitivity of 2.9×10^{24} yr. Combining this result with that of Cuoricino, we obtain

the best limit up to now for ^{130}Te: $T_{1/2} > 4.0 \times 10^{24}$ yr at 90% C.L. Using recent nuclear matrix elements (NME) calculations (see [6] and references therein) this limit is converted onto an upper limit on the effective Majorana mass $m_{\beta\beta} < 270\text{-}760$ meV (see Fig. 2).

3 Other rare event searches with CUORE

Other rare event searches, like solar axions or DM direct detection, demand an energy threshold ≤ 10 keV. In Cuoricino, it was of the order of several tens of keV. Since then, we have done a large effort to reduce the threshold in CUORE-like crystals. In [8], we developed a new trigger based on the continuous application of the optimum filter [9] to the data stream. The filtered data has improved signal-to-noise ratio, so the trigger level can be notably decreased. This procedure was applied to one of the test runs that were performed on the CUORE crystals in order to asses their background and performances [10], carried out in an R&D cryostat not specially design for low background measurements. The result was 3 keV threshold in 3 over 4 crystals and a background at low energy ranging from 25 counts/(keV×kg×day) at 3 keV to 2 counts/(keV×kg×day) at 25 keV, with a peak of unknown origin at 4.7 keV [11].

TeO$_2$ is not a scintillator, so it is not possible to reduce background by electron vs nuclear recoil event-by-event discrimination based on the different light yield, but annual modulation analysis is

Figure 2: Allowed regions for the effective Majorana neutrino mass for the normal and inverted hierarchies, CUORE-0+Cuoricino 90% limit and expected CUORE 90% sensitivity (5 years live time).

possible thanks to the large exposure and projected stable condition over at least 5 years of data-taking. The projection of the measured background and threshold to the exposure of the whole experiment [11] indicates that CUORE could explore the parameter region pointed out by the positive result of the DAMA experiment [12]. CUORE could also look for solar axions through the Primakoff effect in the electric field of the crystal. We envisage two detection strategies: to search for the 14.4 keV peak coming from the iron M1 line [13], and to use the coherent Primakoff conversion that appears when the incident angle of the axion flux with respect to the crystalline plane fulfils the Bragg condition as the Earth rotates, producing a variable counting rate. CUORE prospects for both strategies can be found in [14] and [15] respectively. Currently we are working on the analysis of CUORE-0 data with the optimum trigger. Preliminary results [16] indicate a background in the low energy region of about 1-2 counts/(keV×kg×day) and thresholds of the order of 10-20 keV.

4 CUORE status and prospects

CUORE is currently in the last stage of construction at LNGS. The cryostat commissioning was completed on March 2016. The 19 towers, that were assembled and instrumented by 2014 and
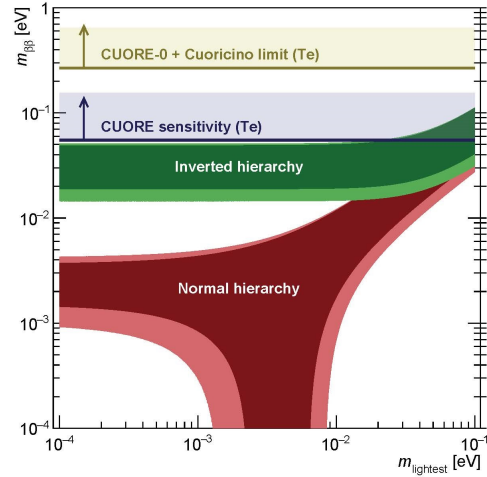
since then stored underground inside nitrogen flushed bags, have been installed in the cryostat in August 2016, so we hope CUORE to start operations by the end 2016. The background reduction measured in CUORE-0 demonstrates the validity of our cleaning procedures. Thanks to the closed-packed structure of CUORE with respect to CUORE-0, our background models predict that the 0.01 counts/(keV×kg×yr) background goal in the RoI is within reach. This corresponds to a sensitivity of 9.5×10^{25} yr at 90% C.L. in 5 years, and a range in $m_{\beta\beta}$ of 50-130 meV (see Fig. 2). CUORE could also look for solar axions and explore the parameter region pointed out by the DAMA positive annual modulation signal.

References

[1] R. Ardito *et al.*, "CUORE: A Cryogenic underground observatory for rare events," hep-ex/0501010.

[2] C. Arnaboldi *et al.* [CUORE Collaboration], "CUORE: A Cryogenic underground observatory for rare events," Nucl. Instrum. Meth. A **518** (2004) 775 doi:10.1016/j.nima.2003.07.067 [hep-ex/0212053].

[3] S. M. Bilenky and C. Giunti, "Neutrinoless double-beta decay: A brief review," Mod. Phys. Lett. A **27** (2012) 1230015 doi:10.1142/S0217732312300157 [arXiv:1203.5250 [hep-ph]].

[4] E. Andreotti *et al.*, "130Te Neutrinoless Double-Beta Decay with CUORICINO," Astropart. Phys. **34** (2011) 822 doi:10.1016/j.astropartphys.2011.02.002 [arXiv:1012.3266 [nucl-ex]].

[5] C. Alduino *et al.* [CUORE Collaboration], "CUORE-0 detector: design, construction and operation," JINST **11** (2016) no.07, P07009 doi:10.1088/1748-0221/11/07/P07009 [arXiv:1604.05465 [physics.ins-det]].

[6] K. Alfonso *et al.* [CUORE Collaboration], "Search for Neutrinoless Double-Beta Decay of ^{130}Te with CUORE-0," Phys. Rev. Lett. **115** (2015) no.10, 102502 doi:10.1103/PhysRevLett.115.102502 [arXiv:1504.02454 [nucl-ex]].

[7] C. Alduino *et al.* [CUORE Collaboration], "Analysis techniques for the evaluation of the neutrinoless double-β decay lifetime in ^{130}Te with the CUORE-0 detector," Phys. Rev. C **93** (2016) no.4, 045503 doi:10.1103/PhysRevC.93.045503 [arXiv:1601.01334 [nucl-ex]].

[8] S. Di Domizio, F. Orio and M. Vignati, "Lowering the energy threshold of large-mass bolometric detectors," JINST **6** (2011) P02007 doi:10.1088/1748-0221/6/02/P02007 [arXiv:1012.1263 [astro-ph.IM]].

[9] E. Gatti and P. F. Manfredi, "Processing the Signals From Solid State Detectors in Elementary Particle Physics," Riv. Nuovo Cim. **9N1** (1986) 1. doi:10.1007/BF02822156

[10] F. Alessandria *et al.*, "CUORE crystal validation runs: results on radioactive contamination and extrapolation to CUORE background," Astropart. Phys. **35** (2012) 839 doi:10.1016/j.astropartphys.2012.02.008 [arXiv:1108.4757 [nucl-ex]].

[11] F. Alessandria *et al.*, "The low energy spectrum of TeO2 bolometers: results and dark matter perspectives for the CUORE-0 and CUORE experiments," JCAP **1301** (2013) 038 doi:10.1088/1475-7516/2013/01/038 [arXiv:1209.2519 [physics.ins-det]].

[12] R. Bernabei *et al.*, "Final model independent result of DAMA/LIBRA-phase1," Eur. Phys. J. C **73** (2013) 2648 doi:10.1140/epjc/s10052-013-2648-7 [arXiv:1308.5109 [astro-ph.GA]].

[13] F. Alessandria *et al.* [CUORE Collaboration], "Search for 14.4 keV solar axions from M1 transition of Fe-57 with CUORE crystals," JCAP **1305** (2013) 007 doi:10.1088/1475-7516/2013/05/007 [arXiv:1209.2800 [hep-ex]].

[14] D. Li, R. J. Creswick, F. T. Avignone and Y. Wang, "Sensitivity of the CUORE detector to 14.4 keV solar axions emitted by the M1 nuclear transition of ^{57}Fe," JCAP **1602** (2016) no.02, 031 doi:10.1088/1475-7516/2016/02/031 [arXiv:1512.01298 [astro-ph.CO]].

[15] D. Li, R. J. Creswick, F. T. Avignone and Y. Wang, "Theoretical Estimate of the Sensitivity of the CUORE Detector to Solar Axions," JCAP **10** (2015) 065 doi:10.1088/1475-7516/2015/10/065 [arXiv:1507.00603 [astro-ph.CO]].

[16] G. Piperno [CUORE Collaboration], "Low energy analysis in CUORE-0," J. Phys. Conf. Ser. **718** (2016) no.4, 042045. doi:10.1088/1742-6596/718/4/042045

High and low mass Axion Haloscopes at UWA

Ben T. McAllister, Stephen R. Parker, Eugene N. Ivanov, and Michael E. Tobar
ARC Centre of Excellence for Engineered Quantum Systems,
School of Physics, University of Western Australia,
35 Stirling Highway, Crawley 6009, WA, Australia.

We consider the design of a haloscope experiment (ORGAN) to probe for axions at 26.6 GHz. The motivation for this search is to perform the first direct test of a result which claims a possible axion signal at this frequency. There are many technical issues and optimisations that must be considered in the design of a high mass axion haloscope. We discuss the current status of the ORGAN experiment, as well as its future. We also discuss low mass axion haloscopes employing lumped 3D LC resonators.

1 Introduction

Axions are a well known solution to the strong CP problem in QCD, proposed by Peccei and Quinn in 1977 [1]. In addition to providing an elegant solution to the strong CP problem, the axion is a compelling dark matter candidate [2]. Many searches for axions are currently underway, employing a variety of detection techniques. One such technique, known as a haloscope, exploits the axion-two photon coupling, in a process known as the inverse Primakoff effect. For an in depth discussion of haloscopes see [3, 4]. The Frequency and Quantum Metrology group at the University of Western Australia is constructing a haloscope to scan for high mass axions, with corresponding photon frequencies around 26 GHz. One motivation for this search is to perform the first direct test of a claimed potential axion signal [5]. This work suggests that axions entering the weak link region of Josephson junctions be responsible for the anomalous Shapiro step-like features seen in a number of experiments. It is claimed that axions with a mass of roughly 110 μeV could create such an effect. This result is surprising, and has been considered potentially spurious, however, as the axion resides in a large and almost unbounded parameter space any candidate signals merit further investigation. Designing a haloscope at high mass presents many difficulties, which can be understood when one considers the expected power in a resonant cavity due to axion conversion (eq. 1) [3].

$$P_a = g_{a\gamma\gamma}^2 \ V \ B^2 \ \frac{\rho_a}{m_a} \ C \ Q \tag{1}$$

Where V is the detecting cavity volume, B is the strength of the magnetic field, ρ_a and m_a are the local axion density and axion mass respectively, Q is the loaded cavity quality factor (provided it is less than the expected axion quality factor of $\sim 10^6$) and C is a mode dependent form factor. Firstly, the resonant frequencies of cavities are inversely proportional to radius, and thus the detector volume decreases with higher frequencies. Furthermore, the quantum noise limit and surface resistivity of metals increase at higher frequencies, thus increasing the level
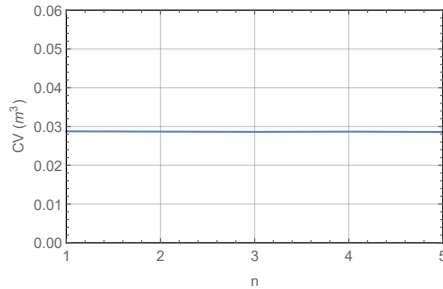
Figure 1: The product of form factor and volume for TM_{0n0} modes at a frequency of 1 GHz, for a cavity length of 1 m.

of background noise from amplifiers, and decreasing the mode quality factor. Our experiment, ORGAN, is nearly ready to commence its initial pathfinder experiment, and we have recently secured ARC funding through the Centre of Excellence for Engineered Quantum Systems, which will enable us to continue this work.

2 ORGAN: status and future

The Cry**O**genic **R**esonant **G**roup **A**xion Co**N**verter is a haloscope experiment with the goal of synchronizing and combining many resonant cavities, in order to achieve sensitive axion searches at high frequencies, 20 GHz and beyond. The pathfinder experiment will explore a narrow region around 26.6 GHz. For this initial run, a single copper resonant cavity will be employed. This cavity has a radius of ~1 cm, and a length of 5 cm. The TM_{020} mode frequency of this cavity is 26.55 GHz at 20 mK. A radially moving metallic rod will provide ~1 GHz of tuning, which is enough to cover the entire range of the Beck result [6]. Commonly the TM_{010} mode is chosen for axion haloscopes, as the form factor, C_{010}, is highest for this mode. Whilst the form factor decreases for higher order TM modes, the corresponding cavity radius at a given frequency increases, which leads to an increase in volume. For a given cavity length and a given desired mode frequency the product of C and V can be shown to be essentially constant, as displayed in fig. 1. The result of this is that there is no overall decrease in sensitivity associated with the form factor decrease in a higher order TM mode. Furthermore we have found, and it has been discussed elsewhere [7], that cavities with lengths greater than ~5 times their radius are disadvantageous to use in haloscope searches, as many length dependent modes crowd around the detector mode, making mode identification and tuning difficult. When this is considered it may be advantageous to employ higher order modes, as the larger radius means a larger allowable length, which means a larger C V product. The limitation to this approach is the space within the magnet. After the pathfinder run, the experiment will undergo several phases. Figure 2 outlines the projected sensitivity, and details the experimental parameters of the different phases. Many proposals for high frequency haloscopes require synchronisation of multiple cavities [8], this provides an engineering challenge in practice. We have been exploring novel techniques to achieve this kind of synchronisation, whilst simultaneously improving the signal to noise ratio of axion signals. Cross-correlation measurements are two channel measurement schemes where the cross-spectrum is computed, rejecting uncorrelated noise sources while
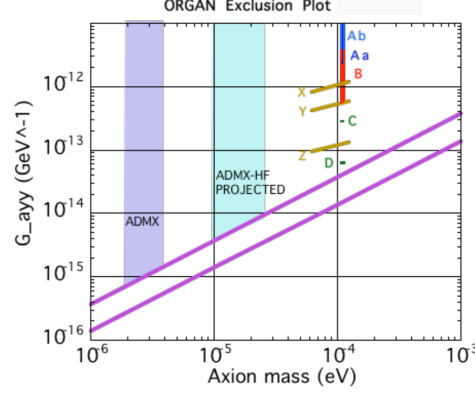
Figure 2: Projected exclusion limits for ORGAN. Aa and Ab represent searches with the current equipment, utilizing 2 cavities. B, C and D represent later phases. Changes include moving from 2 to 8 cavities, implementing a quantum limited JPA in place of the existing amplifier, upgrading the magnet from 7 T to 14 T and improving the quality factor of the cavity using lower loss materials. X, Y and Z represent larger searches at high frequency, with similar experimental scale-ups.

still retaining correlated signals such as those generated in multiple cavities by axion conversion. Cross-correlating signals from multiple cavities, each with their own amplification chain, presents a method of effectively power combining multiple cavities which can be spatially well separated. It is important to note that this technique alone does not provide an improvement over traditional power summation methods. However, for large numbers of resonators we can achieve an improvement. For n cavities there are $\frac{n(n-1)}{2}$ independent cross-spectra. In each of these cross spectra, the mean of the background noise level is lower, the resolution of a candidate signal is higher, and the standard deviation of the background noise is also higher, when compared with a single channel. If we define SNR as the difference between the peak of the signal and the mean of the background noise, divided by the standard deviation of the background noise, a cross-spectrum provides a factor of 2 improvement in SNR, which is the same as a Wilkinson power combiner. However, if we take these $\frac{n(n-1)}{2}$ independent cross-spectra and average them, we can achieve a factor $2\sqrt{\frac{n(n-1)}{2}}$ improvement in SNR, as this averaging process decreases the standard deviation of the background noise. This effect is shown in fig. 3. For a further discussion of this see [9] (update forthcoming). Further research into, and incorporation of this technique is a long term goal of the ORGAN experiment.

3   New experiments: low mass axion detection

Our group is developing proposals for new haloscope experiments. One such recent proposal [10] considers lumped 3D LC resonators. These resonators, commonly known as re-entrant cavities [11] consist of metallic cavities containing a central post or ring, and a small gap between the top of this post or ring and the top of the cavity. Adjusting the size of this gap tunes the resonant frequency of the cavity over a large frequency range, which makes these structure
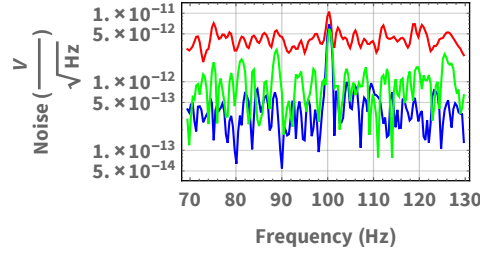
Figure 3: Data from a proof of concept experiment. The PSD is the power spectral density for a single channel with a simulated axion signal injected, the XPSD is the cross-power spectral density for two of the channels, whilst the AXPSD is the averaged cross-power spectral density for the 6 independent cross spectra computed from 4 separate channels.

very appealing for axion searches. These structures are readily implementable inside existing haloscope infrastructure, and can reach promising low mass axion regimes. Our proposal [10] discusses the optimisation of such an experiment, and presents possible axion exclusion limits should such a search be undertaken.

4   Conclusion

The FQM group at UWA is developing high and low mass haloscopes. The ORGAN experiment will soon commence its path-finding run, which consists of a single copper resonant cavity employing a traditional low-noise amplifier and a TM_{020} mode for detection. The early stages of the ORGAN experiment will focus on directly testing the claimed Beck result, followed by a wider scan at high frequency. As a part of the future of this experiment we are developing cross-correlation techniques to increase sensitivity. Furthermore, we are pursuing research into new, novel haloscope designs, with the aim of developing systems to sensitively search for axions over many different regions of the parameter space.

References

[1] R. D. Peccei and H. R. Quinn, Phys. Rev. D **16**, 1791 (1977). doi:10.1103/PhysRevD.16.1791

[2] J. Ipser and P. Sikivie, Phys. Rev. Lett. **50**, 925 (1983). doi:10.1103/PhysRevLett.50.925

[3] P. Sikivie, Phys. Rev. Lett. **51**, 1415 (1983) Erratum: [Phys. Rev. Lett. **52**, 695 (1984)]. doi:10.1103/PhysRevLett.51.1415

[4] P. Sikivie, Phys. Rev. D **32**, 2988 (1983) Erratum: [Phys. Rev. D **36**, 974 (1987)]. doi:10.1103/PhysRevD.32.2988

[5] C. Beck, Phys. Rev. Lett. **111**, 231801 (2013) doi:10.1103/PhysRevLett.111.231801 [arXiv:1309.3790 [hep-ph]].

[6] C. Beck, Phys. Dark Univ. **7-8**, 6 (2015) doi:10.1016/j.dark.2015.03.002 [arXiv:1403.5676 [hep-ph]].

[7] D. Kinion. Seminar given at workshop Vistas in Axion Physics: A Roadmap for Theoretical and Experimental Axion Physics through 2025 (unpublished).

[8] D. S. Kinion, "First results from a multiple microwave cavity search for dark matter axions," UMI-30-19020, PhD Thesis (2001).

[9] S. R. Parker, B. McAllister, E. N. Ivanov and M. E. Tobar, arXiv:1510.05775 [physics.ins-det].

[10] B. T. McAllister, S. R. Parker and M. E. Tobar, Phys. Rev. D **94**, no. 4, 042001 (2016) doi:10.1103/PhysRevD.94.042001 [arXiv:1605.05427 [physics.ins-det]].

[11] J.-M. Le Floch *et al.*, Rev. Sci. Instrum. **84**, 125114 (2013) doi:10.1063/1.4848935 [arXiv:1308.2755 [physics.ins-det]].

Dark Matter Search with DARWIN

Moritz v. Sivers[1] on behalf of the DARWIN consortium

[1]Albert-Einstein-Center for Fundamental Physics,
University of Bern, CH-3012 Bern, Switzerland

DARWIN (DARk matter WImp search with Noble liquids) is a future multi-ton scale detector for the direct detection of Weakly Interacting Massive Particles (WIMPs). The detector will be based on a xenon dual-phase time projection chamber (TPC) with simultaneous charge and light readout. The goal is to build the ultimate detector for WIMP masses $\gtrsim 5 \, \text{GeV}/c^2$, whose sensitivity will only be limited by the irreducible neutrino background. This work focuses on the physics reach and backgrounds related to DARWIN.

1 Setup

The DARWIN detector [1] will employ a dual-phase TPC with a 40 t liquid xenon (LXe) target. The TPC consists of PTFE reflectors, OFHC Cu field shaping rings and is housed in a stainless steel or titanium cryostat. In the baseline design, the LXe scintillation light will be detected by two arrays of photomultiplier tubes ($\sim$1800$\times$ 3 inches or $\sim$1000$\times$ 4 inches). Alternative light detectors like gaseous photomultipliers (GPMs) or silicon photomultipliers (SiPMs) are the subject of ongoing R&D [9]. The cryostat is housed in a water Cherenkov shield with 14 m diameter (see Fig. 1). An additional liquid scintillator shield is under study.
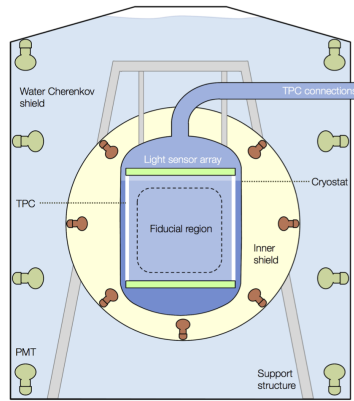

Figure 1: Sketch of the DARWIN detector. The cryostat containing the LXe target is housed inside a water Cherenkov shield. The optional inner shield contains liquid scintillator.

2 WIMP Physics

The primary goal of DARWIN is the detection of galactic WIMPs via scattering off the xenon target nuclei. In Fig. 2 we show the projected sensitivity for spin-independent and spin-dependent WIMP-nucleus scattering. The study assumes a 99.98% electron recoil (ER) rejection at 30% nuclear recoil (NR) acceptance for a 30 t fiducial volume (FV). With an exposure of 200 t y, a spin-independent sensitivity of $2.5 \times 10^{-49}\,\mathrm{cm^2}$ can be reached at a WIMP mass of $40\,\mathrm{GeV/c^2}$. For spin-dependent WIMP-neutron couplings and WIMP masses up to $\sim 1\,\mathrm{TeV/c^2}$, DARWIN will be complementary to the searches conducted by the future high-luminosity LHC, at 14 TeV center-of-mass energy [2].

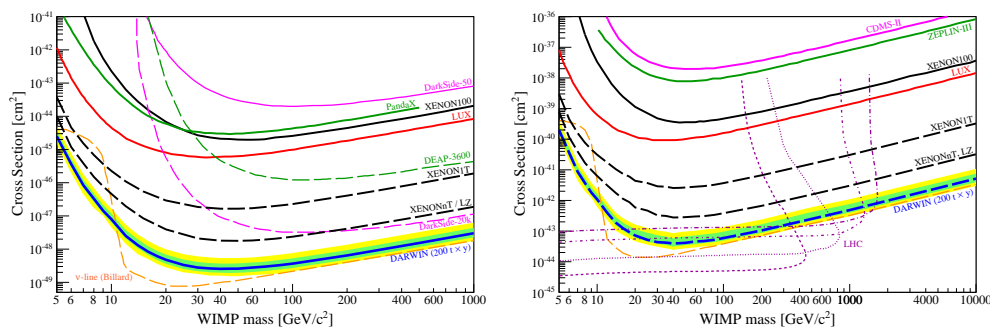
Figure 2: Projected sensitivity of DARWIN for spin-independent (left) and spin-dependent (right) WIMP-nucleus scattering.

3 Backgrounds

The primary backgrounds of DARWIN include ER background from internal contamination and solar neutrinos as well as NR background from radiogenic neutrons and coherent neutrino nucleus scattering (CNNS) of solar and atmospheric neutrinos.

The expected single-scatter nuclear recoil rate from radiogenic neutrons is about $3.8 \times 10^{-5}\,\mathrm{t^{-1}\,y^{-1}\,keV^{-1}}$. To reach this background level, the radioactivity of current detector materials like PTFE and PMTs has to be improved by a factor of 2-5 [3].

CNNS of solar and atmospheric neutrinos poses as an unavoidable background that will ultimately limit the sensitivity of any non-directional WIMP search experiment. For low-mass WIMPs ($\lesssim 8\,\mathrm{GeV/c^2}$) the main background comes from ^{8}B solar neutrinos with a steep exponential spectrum which depends highly on the achievable threshold and energy resolution. At higher energies the background is dominated by atmospheric neutrinos with a fairly flat spectrum and a rate of $\sim 10^{-3}\,\mathrm{t^{-1}\,y^{-1}\,keV^{-1}}$.

The ER background in DARWIN will be dominated by neutrino-electron scattering of solar pp-neutrinos and ^{7}Be neutrinos at the level of $\sim 26\,\mathrm{t^{-1}\,y^{-1}}$ in the low-energy, dark matter signal region of the detector [4]. Other ER backgrounds come from intrinsic contamination with ^{85}Kr and ^{222}Rn. For the sensitivity study shown in Fig. 2 a ^{nat}Kr concentration of 0.1 ppt has been assumed. Even lower concentrations have been already achieved by the Kr removal apparatus of XENON1T [5]. The biggest challenge is the ^{222}Rn contamination which has to be reduced

to 0.1 μBq/kg. This is about a factor of 40 lower than the lowest concentration achieved so far in LXe by the EXO experiment [6].

4 Other Rare Event Searches

As a large scale low-background detector DARWIN will also be suited for other rare event searches in the field of neutrino and axion physics.

Because of its low ER background DARWIN can search for solar axions and galactic axion like particles (ALPs) via the axio-electric effect. For solar axions, the estimated sensitivity for the axion-electron coupling is $g_{Ae} < 10^{-12}$ for axion masses $10^{-5} - 1\,\mathrm{keV/c^2}$. For galactic ALPs a sensitivity of $g_{Ae} < 10^{-14}$ for axion masses $1 - 40\,\mathrm{keV/c^2}$ can be reached.

The first real-time measurement of the solar pp-neutrino flux has recently been achieved by the BOREXINO experiment [7]. A precision measurement of the pp-neutrino flux would test the main energy production mechanism in the sun. DARWIN will be able to measure the solar pp-neutrino flux through elastic neutrino-electron scattering with a precision of 1% after 5 years.

Studying neutrinoless double beta decay can be used to investigate the neutrino mass hierarchy and determine whether neutrinos are Majorana particles. The isotope ^{136}Xe is interesting candidate for neutrinoless double beta decay with a natural abundance of 8.9%. Even without isotopic enrichment DARWIN will be able to reach a half-life limit $T_{1/2} > 8.5 \times 10^{27}$ y with an exposure of 140 t y.

Another interesting physics case would be the detection of neutrinos from a galactic supernova. A possible detection channel is via CNNS which provides sensitivity to all neutrino flavors. Due to the short burst time of a supernova the expected background is negligible. For a $27\mathrm{M}_\odot$ supernova at 10 kpc distance approximately 700 neutrinos can be detected by DARWIN [8].

5 Conclusion

The goal of the DARWIN collaboration is to build the ultimate WIMP detector. After an exposure of 200 t y it will provide a sensitivity for the spin-independent WIMP-nucleon scattering cross section of $2.5 \times 10^{-49}\,\mathrm{cm^2}$ at a WIMP mass of $40\,\mathrm{GeV/c^2}$. DARWIN will also provide important results for many other rare event searches like the neutrinoless double beta decay of ^{136}Xe or solar axions and galactic ALPs. It will also provide a real-time precision measurement of the solar neutrino flux and serve as neutrino detector for a galactic supernova.

References

[1] J. Aalbers, *et al.* [DARWIN Collaboration], "DARWIN: towards the ultimate dark matter detector", [arXiv:1606.07001 [astro-ph.IM]] (2016).

[2] S. A. Malik *et al.*, "Interplay and Characterization of Dark Matter Searches at Colliders and in Direct Detection Experiments", Phys. Dark Univ. **9-10**, 51 (2015).

[3] M. Schumann *et al.*, "Dark matter sensitivity of multi-ton liquid xenon detectors", JCAP **1510**, 016 (2015).

[4] L. Baudis *et al.*, "Neutrino physics with multi-ton scale liquid xenon detectors", JCAP **01**, 044 (2014).

[5] S. Rosendahl, "Gas purification of the XENON dark matter search", PhD thesis, University of Münster (2015).

[6] J. B. Albert *et al.*, "Investigation of radioactivity-induced backgrounds in EXO-200", Phys. Rev. C **92**, 015503 (2015).

[7] G. Bellini *et al.* [BOREXINO Collaboration], "Neutrinos from the primary proton-proton fusion process in the Sun", Nature **512**, 383-386 (2014).

[8] R. F. Lang *et al.*, "Supernova neutrino physics with xenon dark matter detectors: A timely perspective", [arXiv:1606.09243 [astro-ph.HE]] (2016).

[9] E. Erdal *et al.*, "First demonstration of VUV photon detection in liquid xenon with THGEM and GEM-based Liquid Hole Multipliers", [arXiv:1603.07669 [physics.ins-det]] (2016).

Status of the COSINE Experiment

Jungsic Park[1]

[1]Institute for Basic Science (IBS), South Korea
On behalf of the COSINE collaboration

The COSINE collaboration is preparing to test an annual modulation signal of the DAMA/LIBRA experiment unambiguously, with a 4×2 array of low-background NaI(Tl) crystals at the Yangyang Underground Laboratory, South Korea. We have studied more than ten NaI(Tl) crystals as part of an R&D program aiming to reduce internal backgrounds. The first phase of experiment with a ∼106 kg array of NaI(Tl) crystals (COSINE-100) is under preparation to be started by summer, 2016.

1 The COSINE Experiment

COSINE is a joint experiment between KIMS-NaI and DM-ICE to prove or refute an annual modulation of the DAMA/LIBRA [1] experiment using same NaI(Tl) crystals. DAMA/LIBRA shows statistically compelling, 9.3 σ, signals at 2-6 keV energy region with single hit event. However other experiments, such as LUX [2], Super-CDMS [3], KIMS-CsI [4, 5], XMASS [6], did not observe positive signals from WIMP interaction which are conflict with interpretation of the DAMA/LIBRA signal as a WIMP-nucleon interaction. However, it is possible to explain all results due to non-trivial systematic differences in detector responses and possible modifications of halo and dark matter model. Therefore it is necessary to have another experiment using same NaI(Tl) crystals without any dependency on models.

2 Development of NaI(Tl) crystals

In order to achieve better sensitivity than DAMA/LIBRA, it is necessary to achieve low energy threshold as well as to reduce internal background. We have developed low-background NaI(Tl) crystals with less than 2 keV energy threshold [7, 8], especially reduced internal contaminations of ^{238}U, ^{232}Th, ^{210}Pb and ^{40}K.

2.1 Liquid Scintillator Veto

Apart from the effort to reduce internal radioisotope contaminations of crystals, we developed technique to reduce backgrounds from surrounding materials as well as internal backgrounds with multiple gamma and beta decays in which we used liquid scintillator (LS) as an active veto. If we immerse crystals in LS, there are two benefits. First, LS can acts as an additional shield for external background. Second, LS can acts as an active veto to tag internal backgrounds caused by radioactive decays inside NaI(Tl) crystals. Especially internal ^{40}K decay generate

~3keV X-ray and 1460 keV γ-ray. If γ-ray escapes the crystal, 3 keV X-ray can mimic WIMP signals in the region of interest. However, LS can tag escaped γ-ray in which we can effectively reduce the low energy contribution from ^{40}K decay. Before finishing the final design of the full shielding structure, we built a prototype active veto detector to verify its performance. With about 20-cm-think LS, the detector tagged 48 % of the internal ^{40}K background in the 0-10 keV energy region. We also estimated about 60 % tagging efficiency for external background. At the COSINE detector with 40 cm thickness of LS veto system, we expect about ~80 % tagging efficiency for internal ^{40}K as well as external background. With further reduction of ^{210}Pb, it is possible to achieve less than 1 counts/keV/kg/day (dru) background level.

3   Detector

A COSINE detector was constructed from Jan to Jun, 2016 and we started dry run without LS. We installed 8 NaI(Tl) crystals, total amount of ~106 kg, a 4×2 array with acrylic supporting structure at inner most part of the shielding. We attached two, 3-inch Hamamatsu Photomultipliers (PMTs) to individual crystal. Whole crystals will be submerged inside ~2000L of LS [9]. 40-cm-thick LS, which will be filled with acrylic box inside of Cu, acts as an active veto system with total 18, 5-inch PMTs. We installed four, stainless steel calibration rod to across entire acrylic box for energy calibration. We made needle shape calibration sources with specially designed capsule of ^{241}Am, ^{137}Cs, ^{57}Co, and ^{60}Co [10]. Each calibration rod is located between two adjacent crystals, and we can calibrate both two crystals at once. At outermost, we installed total 37 plastic scintillator panels with 42, 2-inch PMTs (muon detector panels), surrounding lead shield with 4π coverage, to tag muon. Top muon detector panels are relatively longer than other muon detector panels, so we installed two, 2-inch PMTs at each side of only top muon detector panels. Figure 1 shows installed COSINE detector with the NaI(Tl) crystals inside.

3.1   Data Acquisition (DAQ) System

We used 500 MHz Flash Analog-To-Digital Converters (FADCs) to acquire data of the NaI(Tl) crystals while charge sensitive ADCs were used for the muon detector panels and LS veto. Root based DAQ program were developed to store data. The FADC has 2.5 V wide dynamic range and 12-bit high resolution. The charge sensitive ADC also has same dynamic range and resolution. Field Programmable Gate Arrays (FPGA) inside the FADC and ADC generated trigger signal for each module. The trigger signal from each module was sent to Trigger Control Board (TCB) in which a global trigger was decided. The global trigger with timing information was sent to all FADCs and/or ADCs at the same time.

4   Sensitivity

With ~106 kg of NaI(Tl) crystals and measured background [7, 8], we calculated expected sensitivity of the COSINE-100 experiment. We assumed 2 dru flat background for ~50 kg of crystals and 4 dru flat background for another ~50 kg of crystals. We calculated both 2-20 keV energy and 1-20 keV energy ranges. Figure 2 shows the expected sensitivity of the COSINE-100 experiment. With 1 keV energy threshold and 2 years operation, we can achieve comparable sensitivity with DAMA/LIBRA allowed region.

5 Summary

We developed the low background NaI(Tl) crystals and constructed COSINE-100 detector. We installed total ∼106 kg of the NaI(Tl) crystals and started dry run. With 2 years of data taking and 1 keV energy threshold, we expect to search DAMA/LIBRA allowed region with same NaI(Tl) crystals.

6 Acknowledgments

References

[1] R. Bernabei *et al.* [DAMA/LIBRA Collaboration], "Final model independent result of DAMA/LIBRA-phasi 1," Eur. Phys. J. C **73**, 2648 (2013). doi:10.1140/epjc/s10052-013-2648-7

[2] D. S. Akerib *et al.* [LUX Collaboration], "Improved Limits on Scattering of Weakly Interaction Massive Particles from Reanalysis of 2013 LUX Data," Phys. Pev. Lett **116**, 161301 (2016). doi:10.1103/PhysRevLett.116.161301

[3] R. Agnese *et al.* [SuperCDMS Collaboration], "New Results from the Search for Low-Mass Weakly Interacting Massive Particles with the CDMS Low Ionization Threshold Experiment," Phys. Pev. Lett **116**, 071301 (2016). doi:10.1103/PhysRevLett.116.071301

[4] H. S. Lee *et al.* [KIMS Collaboration], "Limits on Interactions between Weakly Interacting Massive Particles and Nucleons Obtained with CsI(Tl) Crystal Detectors," Phys. Rev. Lett **99**, 091301 (2007). doi:10.1103/PhysRevLett.99.091301

[5] S. C. Kim *et al.* [KIMS Collaboration], "New Limits on Interactions between Weakly Interacting Massive Particles and Nucleons Obtained with CsI(Tl) Crystal Detectors," Phys. Rev. Lett **108**, 181301 (2012). doi:10.1103/PhysRevLett.108.181301

[6] Abe. K *et al.* [XMASS Collaboration], "Direct dark matter search by annual modulation in XMASS-I," Phys. Lett. B **759**, 272 (2016). doi:10.1016/j.physletb.2016.05.081

[7] K. W. Kim *et al.* [KIMS Collaboration], "Tests on NaI(Tl) crystals for WIMP search at the Yangyang Underground Laboratory," Astropart. Phys. **62**, 249 (2015). doi:10.1016/j.astropartphys.2014.10.004

[8] P. Adhikari *et al.* [KIMS Collaboration], "Understanding internal backgrounds in NaI(Tl) crystals toward a 200 kg array for the KIMS-NaI experiment," Eur. Phys. J. C **76**, 185 (2016). doi:10.1016/j.physletb.2016.05.081

[9] J. S. Park *et al.* [RENO Collaboration], "Production and optical properties of Gd-loaded liquid scintillator for the RENO neutrino detector," Nucl. Instrum. Meth. A **707**, 45 (2013). doi:10.1016/j.nima.2012.12.121

[10] N. Y. Kimi *et al.* [XMASS Collaboration], "Micro-source development for XMASS experiment," Nucl. Instrum. Meth. A **784**, 499 (2015). doi:10.1016/j.nima.2014.11.012

Figure 1: Left : Side view of the COSINE detector. Outermost we installed 37 plastic scintillator panels to tag muon with 4π coverage. Each panel, we attached one (or two for only top panel) 2-inch PMTs. Inside muon detector panels, we have 20-cm-thick lead shielding, and 3-cm-thick copper box. Inside the copper box, we installed LS veto that will contain ∼2000 L of LS inside acrylic box which will be shown with 18, 5-inch PMTs. Right : We installed NaI(Tl) crystals, a 4×2 array, inside acrylic box. Two, 3-inch PMTs were attached at each side of individual crystal. NaI(Tl) crystal is hygroscopic, so each crystal was encapsulated with copper to prevent any contact with air. PMTs also sealed with copper end cap to prevent any leakage when immersed into LS. We attached vikuiti sheet on copper surface and inner surface of acrylic box to increase light collection efficienty of LS veto layer.
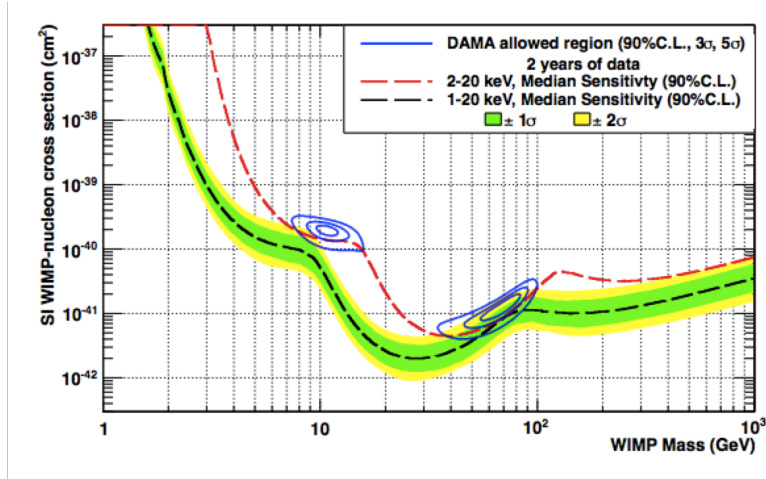
Figure 2: Expected sensitivity of the COSINE-100 experiment with 2 years of data taking. We assumed 2 dru flag background of ∼50 kg of crystals and 4 dru flag background of another ∼50kg of crystals. DAMA/LIBRA allowed regions are depicted with blue contours, corresponding to 90% C.L., 3σ, and 5σ. Red dashed line describes expected sensitivity of COSINE-100 for 2-20 keV energy range and black dashed line shows 1-20 keV energy range, corresponding to both 90% C.L.. Green and yellow bands describes 1σ and 2σ ranges of 1-20 keV case.

Preliminary Study for a New Axion Dark-Matter Haloscope

P. Pugnat[1], R. Ballou[2], Ph. Camus[2], F. Caspers[3,4], B. R. Ko[5], N. Roch[2], and Y. K. Semertzidis[5,6]

[1]Laboratoire National des Champs Magnétiques Intenses (LNCMI), European Magnetic Field Laboratory (EMFL), CNRS & Université Grenoble-Alpes (UGA), France,
[2]Institut Néel (IN), CNRS & Université Grenoble Alpes, France,
[3]European Scientific Institute (ESI), Archamps, France,
[4]CERN, CH-1211 Geneva 23, Switzerland,
[5]Center for Axion and Precision Physics Research (CAPP), Institute for Basic Science (IBS), Daejeon 34141, Republic of Korea,
[6]Department of Physics, Korea Advanced Institute of Science and Technology (KAIST), Daejeon 34141, Republic of Korea

A new haloscope for Axion dark-matter search is under study using in a first step the large bore superconducting magnet in construction at the LNCMI in Grenoble, which will produce 9 T in 812 mm diameter and 1400 mm height. Microwave cavities of high quality factor $Q \sim 10^5 - 10^6$ will be developed at CAPP/IBS in Daejeon. Low-noise microwave amplification of the signal will be ensured by DC superconducting quantum interference devices (SQUID) or/and Josephson parametric amplifiers (JPA) cooled-down to 20 mK by a ^{3}He/^{4}He dilution refrigerator. This new haloscope will be designed to probe QCD dark-matter Axions in the mass range of 1-100 μeV with unprecedented sensitivity.

1 Introduction

A light axion represents one of the most serious cold dark matter candidates and the only non-supersymetric one. It can also solve the strong CP problem [1]. Pierre Sikivie has demonstrated in 1983 that if invisible axions constitute the dark matter of our galactic halo, they can be detected in the laboratory from their conversion to monochromatic photons in a microwave cavity permeated by magnetic field [2]. The signal power to be detected is simply given by:

$$P = g_{A\gamma\gamma}^2 (\rho_{halo}/m_A) B^2 V C Q / 2 \tag{1}$$

with $g_{A\gamma\gamma}$ the unknown axion di-photon coupling constant, $\rho_{halo} \approx 450$ MeV/cm^3 the density of dark matter, $m_A \approx 10^{-6} - 10^{-3}$ eV/c^2 the axion mass range as dark matter candidate, $B^2 V$ the square of the magnetic field B multiplied by the volume V of the cavity, $C \approx 0.5$ the cavity mode form factor and $Q \sim 10^5 - 10^6$ the cavity quality factor. The resonant conversion condition is achieved when the frequency of the cavity is equal to the mass of the axion, *i.e.* $h\nu = m_A c^2 [1 + O(\beta^2)/2]$, where $\beta \approx 10^{-3}$ is the galactic virial velocity and h the Planck constant. The signal is thus monochromatic to 10^{-6} limiting the interest of high Q to 10^6. The

search of axions is performed by tuning the cavity frequency in small overlapping steps and the time integration at each scanned frequency is one of the key limiting factors. The signal to noise ratio (SNR) is of prime importance. In the continuous wave conditions it is given by [3]:

$$SNR = (P/k_B T_{syst})(t/\Delta\nu)^{1/2} \tag{2}$$

with P the detection power in the range of 10^{-23} W, k_B the Boltzmann constant, $T_{syst} = T + T_N$, *i.e.* the sum of the physical temperature T and the intrinsic amplifier noise temperature T_N, t the time integration and $\Delta\nu$ the frequency bandwidth. The haloscope road is being pushed forward by the ADMX collaboration with first study around 1994 [4] and last published results in 2011 [5] following the pioneering work at BNL, FNAL [6] and at Florida University in the late 1980′s [7]. The main figures of merit for haloscope emerging from equations (1) and (2) are B^2V and T_{syst} requiring developments of a high field magnet and working at temperature in the range of a few tens of mK. States of the art cavities with Q reaching 10^6 have also to be developed as well as ultra-low noise amplifier working at the quantum limit and even beyond.

2   The Grenoble hybrid magnet and its large bore superconducting outsert

The Grenoble hybrid magnet under construction in collaboration with CEA Saclay will be a modular experimental platform offering various possibilities of maximum field values and useful warm bore diameters [8]. From the combination of resistive polyhelix and Bitter coils with a large bore superconducting one, a maximum field of at least 43 T will be produced in a 34 mm diameter aperture using 24 MW of electrical power. By combining the Bitter insert alone with the superconducting coil, another hybrid magnet configuration will allow to produce 17.5 T in a 375 mm diameter aperture with 12 MW of electrical power. Finally, the superconducting coil alone will provide a maximum field of 9 T in 812 mm diameter and 1400 mm height bore. The superconducting coil is based on the Nb-Ti and superfluid He technologies. It requires a dedicated He liquefier with a production capacity of 140 l/h [9]. The resistive magnets are cooled with a water flow of 300 l/s.

Compared to other haloscopes such as ADMX [4, 5], the superconducting outsert magnet alone offers an unprecedented value of $B^2V \approx 40$ T^{2}m^3. A further increase of B^2V up to 75 T^{2}m^3 is possible but would imply major changes in the structure of the Grenoble Hybrid Magnet as well as significant investments, which might be considered at a later stage. On another hand, adding the resistive magnets can allow further unique possibilities for this new haloscope to probe axion of larger mass using higher magnetic fields.

3   RF cavity developments at CAPP/IBS

Large magnet bore allows according to equation (1) large cavity volume to enhance the axion signal to be detected. However as the T$_{M010}$ frequency, and thus the axion mass, scales inversely with the cavity radius, probing the whole dark matter axion mass range implies the use of several cavities of different radius. Indeed for a single cavity equipped with conducting rods, its resonant frequency can be typically varied by a factor of about 2. Examples of various RF cavity configurations that can fit within the large bore superconducting magnet are shown in Fig. 1.

The simultaneous use of several cavities implies a coarse tuning of all cavities at the same frequency with phase matching but also individual fine tuning with proper control for each single cavity. In a first step, the optimal selection of five of the cavity configurations shown in Fig. 1, will allow scanning continuously the axion mass in the range from 1.4 to about 15 μeV. RF cavities with high quality factor $Q \approx 10^5 - 10^6$ have to be built to amplify the signal. This requires further developments to improve the Q factor of typical copper cavities or/and developing superconducting ones. This constitutes one of the main ongoing R&D programs at CAPP/IBS [10] with informal collaboration with CERN.
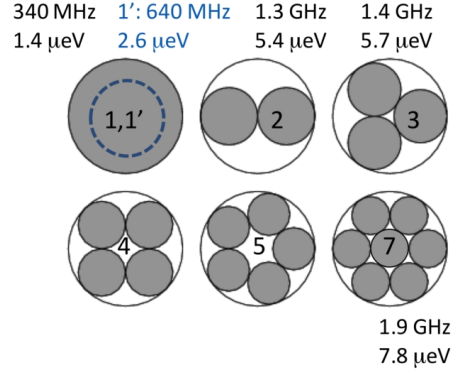

Figure 1: Schematic view of possible RF cavity arrangements within the superconducting magnet aperture with the corresponding resonant frequencies converted in axion mass.

4 Developments of ultra-low noise amplifiers in the range 0.3-10 GHz

One of the main figures of merit of an amplifier is its input noise temperature (T_N). It is defined as the power spectral density at the output of the amplifier divided by its gain, with a matched load at the input of this latter. This parameter is of high relevance, since for $T_{syst} \approx T_N$ inserted in equation (2) the time t required to obtain a given SNR is proportional to T_N^2. In the microwave range, the best performances are obtained using cryogenic devices such as high electron mobility transistor amplifiers [11], SQUID-based amplifiers [12] or parametric devices [13]. To achieve the lowest possible T_N, Josephson parametric amplifiers (JPAs) have become the technology of choice for the supGHz range. Indeed its possible to reach the quantum limit of amplification using such devices [14], as it was demonstrated in various experiments around the world such as [15]. Moreover they can be fabricated using standard lithography techniques and their operating frequency can be adjusted in-situ to follow the one of the resonant cavity.

5 Dilution refrigerators and cryostats

According to equation (2), large SNR requires ultra-low temperature of the overall system at the limit of cryogenic achievements. Not only the quantum amplifier but also the RF cavities have to be cooled typically down to 20 mK. Based on extensive experiences in building ^{3}He/^{4}He dilution refrigerators as well as dedicated cryostats for large underground detectors [16] and space mission such as Planck [17, 18] Néel Institute can provide the required technical expertise and support. The warm magnet aperture needs to be filled with a dilution cryostat optimizing the 20 mK volume for the RF cavity. From a first-cut design of the larger cryostat fitting with the warm superconducting magnet bore, 5 temperature stages from 300 K down to 20 mK with 10 mm space in between are needed, resulting in $\approx$40 mm radius loss over 812 mm for the axion

detection volume. Cryostat with LHe flow and with LHe bath will be both considered with the aim to select the most compact solution. No show stopper has been identified to manufacture the dedicated ^{3}He/^{4}He dilution refrigerator needed to cool down large cavity volumes.

6   Conclusion

The QCD dark-matter Axion is within gunshot range. The sensitivity of the new haloscope under study is expected reaching for the first time the ultimate Dine-Fischler-Srednicki-Zhitnitsky (DFSZ) limit [19]. Important topics have not been addressed in this paper such as for example the coil to compensate the magnetic field at the level of the quantum amplifier, the overall experimental layout but also and mostly the full exploitation of the various maximum field values and bore diameters provided by the Grenoble hybrid magnet under construction. This latter point will be described in a separated paper. The next steps of this project will be the signature of a MoU between participants and the definition of the first haloscope configurations.

References

[1] S. Weinberg, Phys. Rev. Lett. **40**, no. 4, 223 (1978). doi:10.1103/PhysRevLett.40.223 & F. Wilczek, Phys. Rev. Lett. **40**, no. 5, 279 (1978). doi:10.1103/PhysRevLett.40.279

[2] P. Sikivie, Phys. Rev. Lett. **51**, no. 16, 1415 (1983). doi:10.1103/PhysRevLett.51.1415 & P. Sikivie, Phys. Rev. D **32**, no. 11, 2988 (1985). doi:10.1103/PhysRevD.32.2988

[3] R. H. Dicke, Rev. Sci. Inst **17**, 268 (1946). doi:10.1063/1.1770483

[4] K.. van Bibber *et al.* [ADMX Collaboration], Proc. Int. Symp. on Sources of Dark Matter in the Universe, Bel Air, California, 16-18 February 1994; Ed. by David B. Cline (UCLA), World Scientific Publishing 1995; https://cds.cern.ch/record/272035/files/SCAN-9411316.pdf

[5] J. Hoskins *et al.* [ADMX Collaboration], Phys. Rev. D **84**, no. 12, 121302(R) (2011). doi:10.1103/PhysRevD.84.121302

[6] W. U. Wuensch *et al.*, Phys. Rev. D **40**, no. 10, 3153 (1989). doi:10.1103/PhysRevD.40.3153

[7] C. Hagmann *et al.*, Phys. Rev. D **42**, no. 4, 1297(R) (1990). doi:10.1103/PhysRevD.42.1297

[8] P. Pugnat *et al.*, IEEE Trans. Appl. Super. **26**, no. 4, 4302405 (2016). doi:10.1109/TASC.2016.2522975

[9] L. Ronayette *et al.*, Proc. Int. Cryog. Eng. Conf. and Int. Cryog. Mat. Conf., New Delhi, India, 7-11 March 2016; http://icec26-icmc2016.org/March%209,%202016.php; to be published in IOP Conf. Series: MSE.

[10] W. Chung, Proceedings of the 11th Patras Workshop on Axions, WIMPs and WISPs, (Zaragoza, Spain, 2015), p. 116-119 (2015); https://axion-wimp2015.desy.de/sites/sites_conferences/site_axion-wimp2015/content/e13847/e16320/Proc_11thPatras.pdf

[11] S. Weinreb *et al.*, Microwave Symp. Digest, 1988., IEEE MTT-S International, NY, USA, pp. 945-948, vol.2 (1988).

[12] M. Mück *et al.*, App. Phys. Lett. **72**, 2885 (1998). doi:10.1063/1.121490

[13] B. Yurke *et al.*, Phys. Rev. A **39**, no. 5, 2519 (1989). doi:10.1103/PhysRevA.39.2519

[14] C. M.Caves, Phys. Rev. D **26**, no. 8, 1817 (1982). doi:10.1103/PhysRevD.26.1817

[15] N. Roch *et al.*, Phys. Rev. Lett. **108**, no. 14, 147701 (2012). doi:10.1103/PhysRevLett.108.147701

[16] E. Armengaud *et al.* [Edelweiss Collaboration], JCAP **2016**, no. 05, 019 (2016). http://stacks.iop.org/1475-7516/2016/i=05/a=019

[17] L. Sentis, J. Delmas, Ph. Camus, G. Guyot, and Y. Blanc, Cryocoolers 13, pp 533-542, Editor Ronald G. Ross Jr. ISBN: 978-0-387-23901-9 (2005)

[18] P. A. R. Ade *et al.* [Planck Collaboration], Astronomy & Astrophysics **536**, A2, 019 (2016). doi:10.1051/0004-6361/201116486 [arXiv:1101.2023 [astro-ph.IM]].

[19] M. Dine, W. Fischler and M. Srednicki, Phys. Lett. B **104**, no. 3, 199 (1981). doi:10.1016/0370-2693(81)90590-6 & A. R. Zhitnitsky, Sov. J. Nucl. Phys. **31**, 260 (1980).

ALPS II technical overview and status report

Aaron Spector[1] for the ALPS collaboration[†]

[1]Institut für Experimentalphysik, Universität Hamburg, Hamburg, Germany
[†]https://alps.desy.de/e154/

The Any Light Particle Search II (ALPS II) is an experiment that utilizes the concept of resonant enhancement to improve on the sensitivity of traditional light shining through a wall style experiments. These experiments attempt to detect photons passing through an opaque wall by converting to relativistic weakly interacting sub-eV particles and then reconverting back to photons. ALPS II at DESY in Hamburg, Germany will use dually resonant optical cavities before and after the wall to increase the probability of this interaction occurring. This paper gives a technical overview and status report of the experiment.

1 Introduction

The Any Light Particle Search II (ALPS II) is a light shining through a wall experiment that will search for WISPs (Weakly Interacting Sub-eV Particles) in the mass range below 1 meV [1]. Experiments of this type feature a light source shining at an opaque wall or optical barrier and then attempt to observe this light passing through the barrier. A few of the photons from the light source will convert to relativistic WISPs which then traverse the wall and after the wall some of these WISPs will then reconvert back to photons to create a measurable signal. For some classes of particles a magnetic field is necessary for these interactions to take place.

A previous light shining through a wall experiment, ALPS I, featured a Production Cavity (PC) to increase the number of photons circulating in the region before the wall. ALPS II will be the first experiment to use a Regeneration Cavity (RC) to resonantly enhance the probability that WISPs will reconvert back to photons after the wall [2]. This requires that the PC and RC share the same resonant frequency and Eigenmode such that 95% of the light from the PC would couple to the RC if it were directly incident on it. This must be accomplished without allowing any of the photons circulating inside the PC to breach the wall and enter the regeneration side of the experiment as they will be indistinguishable from the signal photons we are attempting to measure. This paper gives a brief overview and technical status report for ALPS II.

2 Experimental design

ALPS II is currently being constructed in two stages. The first stage, ALPS IIa, will feature 10 m cavities with no magnets to test the optical subsystems related to maintaining the dual resonance of the PC and RC as well as single photon detection schemes at the output of the RC. Even though ALPS IIa will not be sensitive to axion-like particles due to the lack of magnets, it will represent the most sensitive search to date for hidden photons in the mass
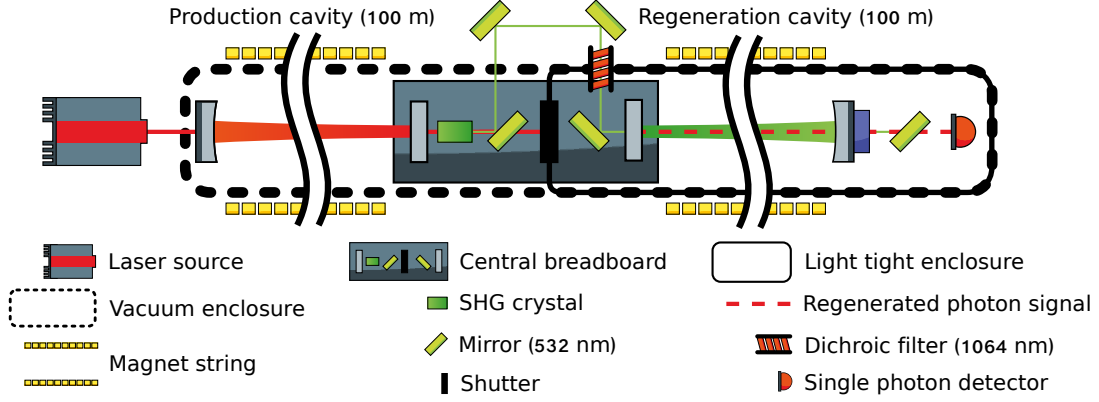
Figure 1: ALPS IIc simplified design.

range $m_{\gamma'} > 5 \times 10^{-5}$ eV [1]. ALPS IIc, the second stage, represents the full scale experiment using 100 m cavities with light propagating through high magnetic fields.

A simplified diagram of the ALPS IIc design is shown in Figure 1. The PC can be injected with up to 35 W of 1064 nm light from a laser system composed of a non-planar ring oscillator with a Nd:YVO$_4$ amplification stage. With a power buildup factor of roughly 5000 there will be 150 kW of power circulating in the PC. A feedback control system will maintain the resonance condition of laser with respect to PC length by actuating on the laser frequency.

The RC will have a power buildup factor of 40,000 for 1064 nm light. Since none of the light circulating in the PC is allowed to couple into the RC a Second Harmonic Generation (SHG) crystal will be used to frequency double the light at the output of the PC. The 1064 nm light is then removed from this beam with a sophisticated system of dichroic filters. This light is coupled into the RC and used in a feedback control scheme that will stabilize its length via a piezo electric device mounted to the out-coupling mirror.

The resonant frequency of the RC must be within 2 Hz of the frequency of the light circulating inside the PC to ensure the resonant enhancement of the reconversion probability of WISPs generated by the PC. This is equivalent to the position of this mirror being actively controlled to better than a picometer.

The PC and RC must also occupy the same spatial Eigenmode. For ALPS IIc both cavities will be operate in a nearly semi-confocal configuration with end mirrors designed to have a radius of curvature of 250 m and flat mirrors located at the waist of the Eigenmode. As shown in Figure 1 both of the flat mirrors will be mounted directly to the Central Breadboard (CBB) to ensure that there are no alignment drifts between these mirrors. ALPS IIa also operates both cavities in a nearly semi-confocal configuration.

The light tight enclosure for ALPS IIc and ALPS IIa will be equipped with a shutter along the optical axis of the cavities. This will allow us to open the shutter and check the spatial overlap between the PC and RC as well as the dual resonance.

ALPS II will need to measure the regenerated photon signal corresponding to single photons over the course of several days. This will be done with two independent techniques. One uses a transition edge sensor (TES) that consists of a superconducting tungsten chip, a constant voltage source and an inductive coil [3]. The chip is linked to a thermal bath that maintains its

temperature at the superconducting transition. Signal photons from the RC are directed to the chip through fiber optics and when a photon is incident on the chip it is absorbed and causes a sudden rise in temperature. This temperature rise in the chip causes a rise in its resistance and thus a drop in the current through the circuit. This negative pulse in the current is read out with a double stage superconducting quantum interference device.

The other method is a heterodyne detection scheme that optically interferes the measurement signal with a local oscillator and then measures the interference beatnote with a photodetector. The phase relation between the local oscillator and the measurement signal will be tracked at a separate point in the experiment and then this information will be used to sum coherently the measurement signal.

ALPS IIc will use 5.3 T superconducting dipole magnets from the decommissioned HERA accelerator to generate the magnetic field. With a string of ten magnets for each cavity, their respective Eigenmodes will each propagate through 466 T·m of magnetic field length.

Equation 1 gives an expression for the sensitivity of ALPS IIc to the coupling constant between axion-like-particles and photons, $S(g_{\alpha\gamma})$. Here BL is the magnetic field length while t is the measurement time. The detector background rate is given by D_n while its detection efficiency is η. P_i is the power incident on the PC while $\mathcal{F}_{PC}$ and $\mathcal{F}_{RC}$ represent the power buildup factors of the PC and RC.

$$S\left(g_{\alpha\gamma}\right) \propto \frac{1}{BL}\left(\frac{D_n}{t}\right)^{\frac{1}{8}}\left(\frac{1}{\eta\,P_i\,\mathcal{F}_{PC}\mathcal{F}_{RC}}\right)^{\frac{1}{4}} \tag{1}$$

With these systems ALPS IIc will have the sensitivity either to detect or rule out axion-like particles with a coupling constant of $g_{a\gamma} \gtrsim 2 \times 10^{-11}\,\mathrm{GeV^{-1}}$ for masses below $10^{-4}\,\mathrm{eV}$ [1].

3   Status

A 20 m cavity was built to characterize several of the input optics control systems for ALPS IIa. The cavity used two of the in-coupling mirrors for the PC in a nearly confocal configuration that would produce the same Eigenmode as the ALPS IIa PC and RC. This allowed us to construct and test the frequency stabilization, automatic alignment control system, and power stabilization scheme. Together these systems were able to reduce the RMS of relative power noise in transmission of the cavity to better than 4.0×10^{-5} [4].

The frequency stabilization scheme suppressed the frequency noise between the input laser and the cavity resonance up to a unity gain frequency of 55 kHz. The control system proved to be very robust and was able to maintain the cavity resonance for up to 48 hours before being manually stopped. An automatic alignment system monitored and controlled the relative pointing between the cavity Eigenmode and the input beam using quadrant photodetectors to do differential wavefront sensing. This ensured that the maximum possible power from the input laser couples to the cavity. In the absence of intra-cavity losses the 20 m cavity was expected to have a power buildup factor of 1,140. We were able to achieve a power build-up factor of 1,010 demonstrating that our systems are capable of maintaining the resonance condition for a long-baseline low-loss optical cavity.

The CBB is currently being built at the Albert Einstein Institute in Hannover, Germany. Tests there have demonstrated that it is possible to align the PC and RC mirrors on the CBB with better than 5 µrad accuracy. Furthermore, long term measurements suggest that

alignment drifts meet our requirements as the angular misalignment between the two mirrors never exceeded the 10 µrad ALPS IIa requirements.

An evaluation of the detection efficiency and energy resolution of the TES is underway and preliminary results suggest a detection efficiency better than 30% and a energy resolution better than 0.1 eV [3]. A similar system at NIST showed a detection efficiency better than 95% as well as an energy resolution of 0.29 eV for photons at a wavelength of 1556 nm [5]. As Equation 1 shows limiting the background event rate is essential to optimizing the sensitivity of ALPS IIc. The primary source of background is expected to be photons generated by blackbody radiation from the optics and fiber system which direct the measurement signal to the TES. An algorithm which fits a theoretical pulse shape to triggered events to help identify signal pulses from pileups has been implemented along with a faster readout system which is expected to improve its precision. Additionally, we plan to install a fiber bandpass filter situated in a cold environment to reduce the rate of blackbody photons incident on the TES. For the heterodyne detection scheme a test-bed is being set up at the University of Florida. Results from this setup are expected in the coming months.

The magnets for ALPS IIc each have a radius of curvature of 600 m and must be unbent before being operated to create a large enough aperture for the light circulating inside of the optical cavities. The full experiment requires 20 magnets. So far two have been unbent and both were successfully operated.

4   ALPS II Timeline

The PC for ALPS IIa is now in the final stages of commissioning and we will begin installing the CBB and input optics for the RC by the end of 2016. We expect to perform a hidden photon search with ALPS IIa within the next year. Work will begin preparing the HERA tunnel and constructing the clean rooms for ALPS IIc by the end of 2017 and the unbending of the magnets is scheduled to be completed in 2018. This will allow for the commissioning of the optical systems for ALPS IIc to take place in 2019 with measurement runs beginning in 2020.

Acknowledgments

References

[1] R. Bähre, B. Döbrich, J. Dreyling-Eschweiler, S. Ghazaryan, R. Hodajerdi, D. Horns, F. Januschek, E. -A. Knabbe, A. Lindner, D. Notz, A. Ringwald, J. E. von Seggern, R. Stromhagen, D. Trines and B. Willke, "Any light particle search II - Technical Design Report," Journal of Instrumentation **8** (9),T09001 (2013).

[2] F. Hoogeveen and T. Ziegenhagen, "Production and detection of light bosons using optical resonators," Nucl.Phys. B 358, 3–26 (1991).

[3] Bastidon, Nomie, Dieter Horns, and Axel Lindner. "Quantum Efficiency Characterization and Optimization of a Tungsten Transition-Edge Sensor for ALPS II." Journal of Low Temperature Physics (2015): 1-3.

[4] Spector, Aaron D., et al. "Characterization of optical systems for the ALPS II experiment." arXiv preprint arXiv:1609.08985 (2016).

[5] Adriana E. Lita, Aaron J. Miller, and Sae Woo Nam, "Counting near-infrared single-photons with 95% efficiency," Opt. Express 16, 3032-3040 (2008)

The $0\nu\beta\beta$ Experiment GERDA
Latest Phase I Results and Phase II Upgrade

Katharina von Sturm for the GERDA *Collaboration*

Università degli Studi di Padova, Italy

Istituto Nazionale di Fisica Nucleare (INFN) Sezione di Padova

GERDA published the best limit on ^{76}Ge $0\nu\beta\beta$ decay's half-life of $T^{0\nu}_{1/2} > 2.1 \cdot 10^{25}$yr (90%C.L.) in 2013. Subsequently, exotic decay modes with Majoron emission were investigated obtaining half-life limits $\sim 10^{23}$yr for spectral indices $n = 1, 2, 3, 7$. The half-life measurement of $2\nu\beta\beta$ from ^{76}Ge to ^{76}Se g.s. was reevaluated with an uncertainty $< 5\%$ and decay modes to three ^{76}Se excited states were analyzed. The lower limits found, $\sim 10^{23}$ yr, rule out a number of nuclear structure model predictions. In a recent major upgrade, amongst other, the detector mass was almost doubled and a new veto system, exploiting liquid argon scintillation light, was installed.

1   Introduction: $0\nu\beta\beta$ decay and the GERDA experiment

In a double-beta ($2\nu\beta\beta$) decay event two neutrons of the same nucleus are transformed to two protons with the emission of two electrons and two anti-electron neutrinos. Theoretically a decay mode without the two neutrinos in the final state — therefore called *neutrinoless* double-beta ($0\nu\beta\beta$) decay — is possible. It violates total lepton number by two units and, thus, if found would indicate new physics beyond the standard model of particle physics (SM). The search for $0\nu\beta\beta$ decay is appealing as its existence would constrain properties of neutrinos like their nature (Dirac or Majorana) and mass. The GERDA (GERmanium Detector Array) experiment, located at Laboratori Nazionali del Gran Sasso (LNGS) in Italy, conducts $0\nu\beta\beta$ decay search using the candidate isotope ^{76}Ge [1, 2]. Its specialty is the operation of High-Purity Germanium (HPGe) detectors submerged bare in a $64\,\text{m}^3$ liquid argon (LAr) cryostat. The HPGe diodes are enriched to about $86\,\%$ of ^{76}Ge and serve thus contemporarily as source and detectors, maximizing the detection efficiency. A water tank surrounding the LAr cryostat, instrumented with photomultiplier tubes (PMTs), is used as a passive shield and active Cerenkov muon veto [3]. In the following, an excerpt of results obtained with GERDA Phase I data will be given. Since December 2015 GERDA is running with an upgraded setup in a second experimental stage [4]. The most important components of the upgrade will be discussed.

2   GERDA Phase I results

Phase I physics data was taken with 8 enriched semi-coaxial (enrCoax) HPGe detectors prior used in the IGEX [5] and Heidelberg-Moscow [6] experiments. Furthermore, 5 custom made enriched Broad Energy Germanium (BEGe) detectors were implemented in the setup [7]. They

add up to a total mass of about $18\,\mathrm{kg}$ enriched material. Pulse shape discrimination (PSD) techniques for enrCoax as well as BEGe detectors were used in the analysis [8]. They are selective for events depositing energy in a small volume inside one detector, which show the desired signal-like event topology. With an exposure of $21.6\,\mathrm{kg\,yr}$ the most stringent limit on $0\nu\beta\beta$ decay in ^{76}Ge to date was placed in 2013 [1]. With a lower limit on the half-life of $T^{0\nu}_{1/2} > 2.1 \cdot 10^{25}$yr at 90%C.L. it strongly disfavors a long pending claim made in 2004 [9].

2.1 Majoron accompanied decay modes ($0\nu\beta\beta\chi(\chi)$) and $2\nu\beta\beta$ decay

$0\nu\beta\beta$ decay is also predicted in exotic models through emission of so called Majorons. These massless Goldstone bosons can have different transformation properties under weak isospin [10]. Newer models suggest non-Goldstone leptonically charged Majorons [11, 12] or the emission of two Majorons in $0\nu\beta\beta$ decay [13]. The spectral shape of all these descriptions depends on the phase space $G \sim (Q_{\beta\beta} - K)^n$ of the emitted particles. With the Q-value of $0\nu\beta\beta$ decay $Q_{\beta\beta}$ and the sum energy of the two electrons K the describing parameter remains the spectral index n. Single Majoron models with spectral index $n = 1, 2, 3$ as well as two Majoron models with spectral index $n = 3, 7$ have been tested using an exposure of $20.3\,\mathrm{kg\,yr}$ of GERDA Phase I data. For non of the spectral indices a signal was found and the limits extracted (90 %C.L.) are $T^{0\nu\chi}_{1/2}\,(n = 1) > 4.2 \cdot 10^{23}$ yr, $T^{0\nu\chi}_{1/2}\,(n = 2) > 1.8 \cdot 10^{23}$ yr, $T^{0\nu\chi}_{1/2}\,(n = 3) > 0.8 \cdot 10^{23}$ yr and $T^{0\nu\chi}_{1/2}\,(n = 7) > 0.3 \cdot 10^{23}$ yr [14]. These values are the most stringent ones for ^{76}Ge published to this date. Furthermore, the half-life of $2\nu\beta\beta$ decay, which has a spectral index of $n = 5$, was reevaluated and the precision of its value has been improved to an unprecedented $< 5\,\%$ uncertainty. The determined half-life is $T^{2\nu}_{1/2} = (1.926 \pm 0.094) \cdot 10^{21}$ yr [14].

2.2 $2\nu\beta\beta$ decay to excited states

The half-life of $0\nu\beta\beta$ decay (and $2\nu\beta\beta$ decay respectively) depends on a nuclear matrix element (NME), $\mathcal{M}^{0\nu}$ ($\mathcal{M}^{2\nu}$), which is calculated based on theoretical nuclear structure models. Uncertainties in the NME directly translate to uncertainties in the effective Majorana mass derived from the half-life [15]. $\mathcal{M}^{2\nu}$ and $\mathcal{M}^{0\nu}$ rely on similar model assumptions, therefore, improving the precision of the $2\nu\beta\beta$ decay half-life can reduce uncertainties in $\mathcal{M}^{0\nu}$ and is used to benchmark nuclear structure models. $2\nu\beta\beta$ decay can occur also into excited states which have a lower rate due to a smaller phase space. Transitions of ^{76}Ge from its $0^+_{\mathrm{g.s.}}$ ground state (g.s.) to ^{76}Se 2^+_1, 0^+_1 and 2^+_2 states have been studied recently with GERDA data [16]. To get a distinct experimental signature from decays to the g.s. de-excitation γs were tracked in coincidence with any energy deposition in a second detector. The detector pair selection and other analysis parameters were optimized for best sensitivity via Monte Carlo simulations. This is supposed to avoid bias as no data blinding was applied in this analysis. The number of signal counts was extracted by means of a profile likelihood fit and no signal was found for any of the transitions. The newly obtained limits are up to two orders of magnitude better than previously found. At 90 %C.L. these are $T^{0\nu\chi}_{1/2}\,(\to 2^+_1) > 1.6 \cdot 10^{23}$ yr, $T^{0\nu\chi}_{1/2}\,(\to 0^+_1) > 3.7 \cdot 10^{23}$ yr and $T^{0\nu\chi}_{1/2}\,(\to 2^+_2) > 2.3 \cdot 10^{23}$ yr. Model predictions for the $0^+_{\mathrm{g.s.}} \to 0^+_1$ decay mode range from 10^{21} to 10^{24} yr. For an exhaustive collection see [16]. This analysis rules out a number of them in the range of $10^{21} - 10^{22}$ yr [16].
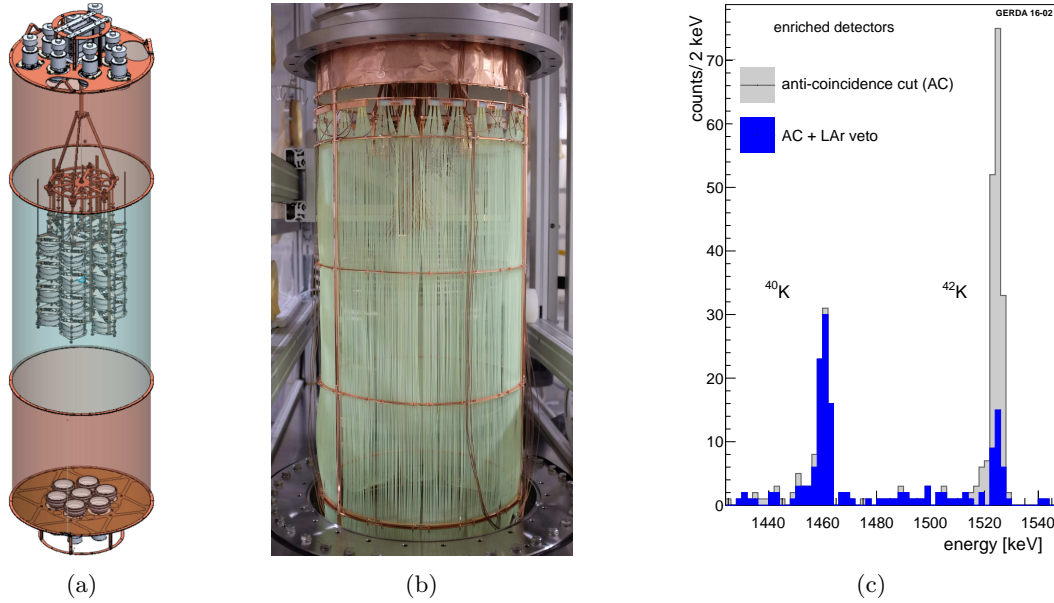
Figure 1: The GERDA Phase II array with seven detector strings surrounded by the LAr veto instrumentation consisting of PMTs and light guiding fibers connected to SiPMs. a) Schematic figure b) picture of the central fiber shroud c) background suppression in the energy region of ^{40}K and ^{42}K γ-lines.

3   The GERDA Phase II upgrade

One goal for rare event searches is the reduction of background to the limit of zero-background for the entire experiment's lifetime. For GERDA this means a design goal of a background index (BI) of 10^{-3} cts/(keV kg yr) in its second experimental stage [4]: that is a factor of 10 lower than the BI achieved in Phase I. In these optimal experimental conditions the median experimental sensitivity improves linearly with the exposure. In GERDA Phase II 40 HPGe detectors, of which 37 are of enriched material, are implemented in a seven-string close-packed array which offers an improved multi-detector-event rejection. The source mass is almost doubled with respect to Phase I. Of the 40 operational detectors 30 are enriched custom made detectors of BEGe type with an improved PSD performance compared to the semi-coaxial detector geometry. The spring-loaded contacts have been replaced by wire bonds, the detector holders manufactured from monocrystalline silicon and front-end electronics of higher radio-purity have been installed in order to reduce close by background sources. The detectors are operated at high voltage of about 4 kV. In order to limit the LAr volume from which potentially radioactive ions can be attracted — in particular the naturally present ^{42}Ar daughter ^{42}K — the detector strings are enclosed in transparent, Tetra-Phenyl Butadiene (TPB) coated Nylon Mini-Shrouds (MS) [17]. The choice for a transparent option is due to a newly installed veto system which utilizes the scintillation light of LAr to veto events depositing energy in the cryo liquid. The LAr veto, a technological novelty, uses light guiding fibers connected to silicon photomultipliers (SiPMs). Equally to the MS, the fibers are TPB coated in order to shift the LAr scintillation light to the sensitive spectral region of the SiPMs [18]. Two PMT arrays, installed at the top and bottom

of the fiber shroud, complete the LAr veto in a hybrid solution. A sketch of the setup and a picture of the fiber shroud are shown in Figure 1a and 1b. A demonstration of the background reduction in the spectral region of ^{40}K and ^{42}K can be seen in Figure 1c. The ^{42}K γ-line at 1525 keV is found to be highly suppressed. Originating from a β decay with an endpoint of 3525 keV, this is a critical background source for GERDA. The emitted electron is highly likely to deposit energy inside the LAr and thus to be detected by the LAr veto. ^{40}K decays via electron capture, no energy deposition is expected in the LAr and hence, its γ-line at 1460 keV results unsuppressed. After half a year of data taking, the first ~ 11 kg yr of GERDA Phase II data have been unblinded in June 2016. Based on the very promising tests background reduction is largely improved. A publication of the obtained results is expected later this year.

References

[1] M. Agostini *et al.* [GERDA Collaboration], "Results on Neutrinoless Double-β Decay of ^{76}Ge from Phase I of the GERDA Experiment," Phys.Rev.Lett. 111 (2013) no.12, 122503. doi:10.1103/PhysRevLett.111.122503

[2] K. H. Ackermann *et al.* [GERDA Collaboration], "The GERDA experiment for the search of $0\nu\beta\beta$ decay in ^{76}Ge," Eur.Phys.J. C73 (2013) no.3, 2330. doi:10.1140/epjc/s10052-013-2330-0

[3] K. Freund *et al.*, 'The performance of the Muon Veto of the GERDA experiment," Eur.Phys.J. C76 (2016) no.5, 298. doi:10.1140/epjc/s10052-016-4140-7

[4] B. Majorovits [for the GERDA Collaboration] "Phase II Upgrade of the GERDA Experiment for the Search of Neutrinoless Double Beta Decay," Phys.Procedia 61 (2015) 254-259. doi:10.1016/j.phpro.2014.12.041

[5] C.E. Aalseth *et al.* [IGEX Collaboration], "Neutrinoless double-beta decay of Ge-76: First results from the International Germanium Experiment (IGEX) with six isotopically enriched detectors," Phys.Rev. C59 (1999) 2108-2113. doi:10.1103/PhysRevC.59.2108

[6] M. Günther *et al.*, "Heidelberg - Moscow beta-beta experiment with Ge-76: Full setup with five detectors," Phys.Rev. D55 (1997) 54-67. doi:10.1103/PhysRevD.55.54

[7] M. Agostini *et al.* [GERDA Collaboration], "Production, characterization and operation of ^{76}Ge enriched BEGe detectors in GERDA," Eur.Phys.J. C75 (2015) no.2, 39. doi:10.1140/epjc/s10052-014-3253-0

[8] M. Agostini *et al.* [GERDA Collaboration], "Pulse shape discrimination for GERDA Phase I data," Eur.Phys.J. C73 (2013) no.10, 2583. doi:10.1140/epjc/s10052-013-2583-7

[9] H.V. Klapdor-Kleingrothaus, I.V. Krivosheina *et al.*, "Search for neutrinoless double beta decay with enriched Ge-76 in Gran Sasso 1990-2003," Phys.Lett. B586 (2004) 198-212. doi:10.1016/j.physletb.2004.02.025

[10] Y. Chikashige *et al.*, "Spontaneously Broken Lepton Number and Cosmological Constraints on the Neutrino Mass Spectrum," Phys.Rev.Lett. 45 (1980) 1926. doi:10.1103/PhysRevLett.45.1926

[11] C.P. Burgess and J.M. Cline, "Majorons without Majorana masses and neutrinoless double beta decay," Phys.Lett. B298 (1993) 141-148. doi:10.1016/0370-2693(93)91720-8

[12] C.P. Burgess and J.M. Cline, "A New class of Majoron emitting double beta decays," Phys.Rev. D49 (1994) 5925-5944. doi:10.1103/PhysRevD.49.5925

[13] P. Bamert *et al.*, "Multi - Majoron modes for neutrinoless double beta decay," Nucl.Phys. B449 (1995) 25-48. doi:10.1016/0550-3213(95)00273-U

[14] M. Agostini *et al.* [GERDA Collaboration], "Results on $\beta\beta$ decay with emission of two neutrinos or Majorons in ^{76}Ge from GERDA Phase I," Eur.Phys.J. C75 (2015) no.9, 416. doi:10.1140/epjc/s10052-015-3627-y

[15] J. Suhonen, O. Civitarese, "Review of the properties of the 0 nu beta- beta- nuclear matrix elements," J.Phys. G39 (2012) 124005. doi:10.1088/0954-3899/39/12/124005

[16] M. Agostini *et al.* [GERDA Collaboration], "$2\nu\beta\beta$ decay of ^{76}Ge into excited states with GERDA Phase I," J.Phys. G42 (2015) no.11, 115201. doi:10.1140/epjc/s10052-013-2330-0

[17] L. Baudis *et al.*, "Enhancement of Light Yield and Stability of Radio-Pure Tetraphenyl-Butadiene Based Coatings for VUV Light Detection in Cryogenic Environments," JINST 10 (2015) no.09, P09009. doi:10.1088/1748-0221/10/09/P09009

[18] M. Agostini *et al.*, "LArGe: active background suppression using argon scintillation for the Gerda $0\nu\beta\beta$-experiment," Eur.Phys.J. C75 (2015) no.10, 506. doi:10.1140/epjc/s10052-015-3681-5

WIMP Search with Underground Argon in DarkSide-50

Masayuki Wada for the DarkSide Collaboration

Princeton University, New Jersey, USA

DarkSide-50 is a direct WIMP detection experiment at Gran Sasso underground laboratory in Italy based on a 50 kg dual-phase argon Time Projection Chamber with liquid argon from underground sources. DarkSide-50 aims to perform background-free WIMP searches with active vetos of a 30-tonne liquid scintillator neutron veto and a 1k-tonne water Cherenkov muon veto. DarkSide-50 has been taking data with underground Ar, which is significantly depleted in radioactive ^{39}Ar, and measured its depletion factor. The result of WIMP searches with 70 live-days of underground argon data will be presented. Also recent study of the liquid scintillator veto's performance and the future plan will be discussed.

1 Introduction

The ultimate goal of the DarkSide program is to detect signals from Weakly Interacting Massive Particles (WIMPs), one of the most popular dark matter candidates, by using liquid argon (LAr) as a target in a dual-phase Time Projection Chamber (TPC) with active background veto systems. In order to achieve the goal, the DarkSide program adopts various technologies to reduce and/or reject background events.

The main motivation to use LAr is its strong pulse shape discrimination (PSD) of electron recoils (ERs) from nuclear recoils (NRs), the expected signals from WIMP scatterings. The results from DarkSide-50 with atmospheric argon (AAr) data show that using PSD, a total of 1.5×10^7 ER events can be completely rejected in the WIMP energy region of interest, leaving no backgrounds (or WIMP signals) in the ROI after an exposure of (1422 ± 67) kg day [1]. Since LAr is relatively dense and easy to purify, it is scalable to large masses. Its high scintillation yield and good transparency to its own UV scintillation light lowers the detection threshold of the WIMP signal low and strengthens the PSD power. The high ionization and high electron mobility in LAr are suitable for TPC applications. It is very useful to remove surface background by fiducializing detection volume according to reconstructed 3D positions from ionization measurements. Furthermore, the ratio of ionization yield over scintillation yield provides additional discrimination power against ER backgrounds. A challenge of employing LAr as a target for WIMP detection comes from the high concentration of the beta-emitting isotope ^{39}Ar in atmospheric argon. Since ^{39}Ar has a decay half-life of 269 years and is mainly generated by cosmic rays in the atmosphere, underground argon sources (UAr) can be free of ^{39}Ar or have only trace amounts activated by radiation from the rock. A pioneering study of the ^{39}Ar activity in UAr was done and placed an upper limit on the ^{39}Ar depletion factor >150 relative to AAr [2]. In Sec. 3, we update this number with a measurement of the depletion factor
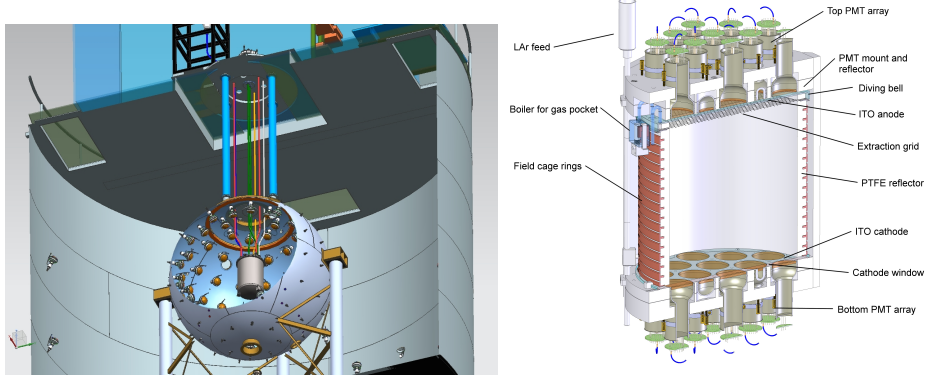
Figure 1: **Left:** The nested detector system of DarkSide-50. The outermost gray cylinder is the WCD, the sphere is the LSV, and the gray cylinder at the center of the sphere is the LAr TPC cryostat. The blue area at top is the radon-free clean room. **Right:** Schematic cross section of the DarkSide-50 Liquid Argon Time Projection Chamber

of ^{39}Ar in the DarkSide-50 detector. The strong PSD and depleted Ar coupled with scalability make LAr a viable target for sensitive WIMP detectors. The plans for a future liquid argon TPC are discussed in Sec. 4.

2 DarkSide-50 Detectors

DarkSide-50 consists of three nested detectors as shown in Fig. 1: the two-phase argon TPC, which is the main detector with a LAr target for WIMP detection; the organic Liquid Scintillator Veto (LSV), providing rejection against neutron and electron recoil backgrounds via anti-coincident signals from radiogenic and cosmogenic neutrons, γ's from the detectors, and cosmic muons; and the Water Cherenkov Detector (WCD), which rejects cosmic muons and suppresses radiogenic background from surrounding rocks and detectors.

Incoming WIMPs recoil from an Ar nucleus and leave excitations and ionizations, which the TPC measures by detecting scintillated photons with 19 PMTs each on top and bottom of the TPC. The excited Ar dimers de-excite and emit the first scintillation light, S1, at the vertex of the recoil. The ionization electrons drift due to an electric field of 200 V/cm, and are extracted into the gas phase at top of the TPC, generating the second scintillation light, S2. The time difference between S1 and S2 gives the depth (z position) of the event, and the transverse (x,y) position is reconstructed from the distribution pattern of S2 light among the top PMTs. The LSV has an array of 100 8" PMTs attached on the inside of a 4 m diameter stainless steel sphere filled with 30 tonne of liquid scintillator. The scintillator is a mixture of pseudocumene (PC) and trimethyl borate (TMB) with a wavelength shifter, Diphenyloxazole (PPO). Neutrons are detected in LSV via thermalization signals and/or capture signals, mainly on ^{10}B in the TMB. The veto efficiency of NRs from only capture signals are studied and estimated to be >99.1 % using an AmBe neutron source and MC simulation [3]. The study of the veto efficiency using thermalization signals is in progress using an AmC source, from which there is no coincident γ-rays produced with the neutrons.The WCD has an array of 80 8" PMTs mounted on the
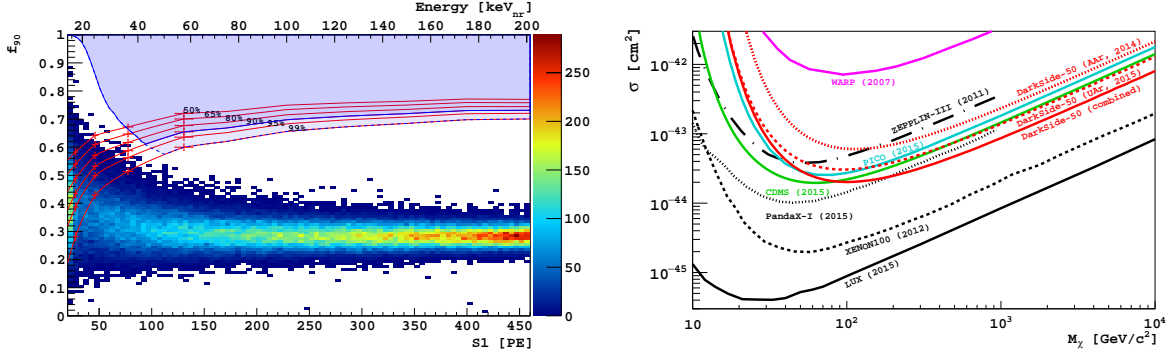
Figure 2: **Left:** Distribution of events in the f90 vs S1 plane surviving all cuts in the energy region of interest. Shaded blue with solid blue outline: WIMP search region. The f90 acceptance contours are drawn by connecting the red points derived from the SCENE measurements [6] and extending the contours using DarkSide-50 AmBe data. **Right:** Spin-independent WIMP-nucleon cross section 90 % C.L. exclusion plots for the DarkSide-50 AAr (dotted red) and UAr campaigns (dashed red), and combination of the UAr and AAr [1] campaigns (solid red).

inside of an 11 m diameter by 10 m high cylindrical tank filled with 1 k tonne of high purity water. Additional important parts of the DarkSide-50 experiment are radon-suppressed rooms with Rn-levels of 5 mBq/m^3, which is significantly less than typical Rn-levels in the air of $\sim$30 Bq/m^3. One of them is located directly on top of the WCD and provides a radon-free way to access the LSV and the TPC.

3   WIMP Search with an Underground Ar Target

The underground argon was extracted from a stream of gas from a CO_2 well in Cortez, Colorado, along with other gases including N_2 and He. This gas mixture was sent to Fermilab for further purification [4]. The purified UAr of (153 ± 1) kg was finally commissioned into the DarkSide-50 TPC at LNGS in Italy on April 1, 2015. In order to determine the ^{39}Ar depletion factor, a GEANT4-based MC simulation is used. The MC is tuned on the high statistic AAr data and validated against several γ calibration sources. The MC includes models of all three detectors and accounts for material properties, the photon propagation, and a model of LAr scintillation and ionization recombination. The ^{39}Ar activity is measured from a simultaneous MC fit to the S1 spectra of the field-off data and field-on (200 V/cm) data and the z-position distribution of events, which provides additional constraints on the rate of γ's from PMTs concentrated on the top and bottom of the TPC. The fit result gives an ^{39}Ar depletion factor of $(1.4\pm0.2)\times10^3$ relative to AAr.

The WIMP search results with UAr [5] were based on the data set acquired from April 8 to July 31 in 2015 (70.9 live-days after data quality cuts) at a drift field of 200 V/cm. The light yield of S1 signals was determined to be (8.1 ± 0.2) PE/keV at zero field from the ^{83m}Kr peak, which is consistent with the light yield in AAr. Due to the purification at Fermilab and getter systems in DarkSide-50, we achieved a long electron lifetime of >5 ms, which is a measure of electronegative impurities, immediately after the UAr commissioning and it remains throughout

the campaign. A set of criteria are used to select only possible WIMP recoils, i.e. single NRs in the fiducial volume, are described in detail in Ref. [5]. The events with coincident signals in the LSV or the WCD are also removed. The PSD parameter used in this analysis is f_{90}, the fraction of S1 light detected in the first 90 ns of the pulse. The WIMP region of interest (ROI) is defined in the f_{90} vs S1 space with a 90 % NR acceptance contour derived from the f_{90} response in SCENE [6], and a leakage curve corresponding to a total predicted leakage of <0.1 events during the exposure. The final event distribution in the f_{90} vs S1 space is presented in Fig. 2, and there are no events in the WIMP ROI. Given the background-free null result, a 90 % C.L. exclusion curve is drawn in Fig. 2. The combined result with AAr [1] puts an upper limit of $2.0 \times 10^{-44} \mathrm{cm}^2$ on the WIMP-nucleon cross section at 100 GeV/c^2 WIMP mass.

4 DarkSide-20k

While DarkSide-50 continues the WIMP search with UAr and further investigates possible backgrounds, the DarkSide collaboration is moving to a next-generation detector. Given the exceptional PSD power of LAr and high depletion factor of UAr, we propose to build DarkSide-20k, a direct WIMP search detector using a LAR TPC with an active (fiducial) mass of 23 tonne (20 tonne) of depleted argon (DAr). In order to suppress both NR and ER backgrounds from conventional PMTs and improve light yield, silicon photomultipliers (SiPMs) are plan to be used and under development. To acquire the required amount of DAr with a sufficient depletion factor, two key projects are planned: Urania is an enlarged argon extraction plant in Cortez, Colorado, with expected capacity of 100 kg/day of UAr and Aria consists of two 350 m tall distillation columns, which are capable of depleting ^{39}Ar in UAr further with additional depletion factor between 10 to 100. DarkSide-20k aims for a 100 t yr exposure to give a projected sensitivity of $1.2 \times 10^{-47} \mathrm{cm}^2$ for WIMP mass of $1 \mathrm{TeV}/c^2$.

5 Conclusion

The DarkSide-50 detector achieved the most sensitive limit on WIMP-nucleon cross section among experiments using LAr. The ^{39}Ar depletion factor in UAr was determined to be $(1.4 \pm 0.2) \times 10^3$ relative to AAr. DarkSide-20k is forthcoming.

References

[1] Agnes, P. *et al.* [DarkSide Collaboration], "First results from the DarkSide-50 dark matter experiment at Laboratori Nazionali del Gran Sasso," Phys. Lett. B **743**, 456 (2015). doi:10.1016/j.physletb.2015.03.012

[2] Xu, J. *et al.*, "A study of the trace 39Ar content in argon from deep underground sources," Astropart. Phys. **66**, 53 (2015). doi:10.1016/j.astropartphys.2015.01.002

[3] Agnes, P. *et al.* [DarkSide Collaboration], "The veto system of the DarkSide-50 experiment," J. Instrum. **11**, P03016 (2016). doi:10.1088/1748-0221/11/03/P03016

[4] Back, H. O. *et al.*, "First Large Scale Production of Low Radioactivity Argon From Underground Sources," arXiv:1204.6024 (2012).

[5] Agnes, P. *et al.* [DarkSide Collaboration], "Results from the first use of low radioactivity argon in a dark matter search," Phys. Rev. D **93**, 081101 (2016). doi:10.1103/PhysRevD.93.081101

[6] Cao, H. *et al.* [SCENE Collaboration], "Measurement of scintillation and ionization yield and scintillation pulse shape from nuclear recoils in liquid argon," Phys. Rev. D **91**, 092007 (2015). doi:10.1103/PhysRevD.91.092007

Search for Dark Particles at Belle

E. Won[1] (on behalf of the Belle Collaboration)

[1]Korea University, South Korea

We search for dark photon A' and the dark Higgs boson h' particles that are suggested in number of recently proposed dark sector models. We present our search results in the production of $e^+e^- \rightarrow A'h'$ with the decay mod of $h' \rightarrow A'A'$. The search was carried out in both inclusive and exclusive modes. We also discuss future prospects of the dark particle search with the Belle II experiment that aims to start in 2018.

1 Introduction

The dark particles were originally considered as a new spin-1 boson for new physics [1] beyond the Standard Model and this proposed the dark sector can be at least a part of dark matter that has not seen yet in hadron collider based searches [2, 3]. The dark boson A' can be produced in a radiative e^+e^- collision via kinetic mixing of a virtual photon with the kinetic mixing parameter ϵ and is illustrated in Fig. 1. This new dark boson requires an extended Higgs sector to break the new $U(1)'$ symmetry and is commonly referred as the dark Higgs h'. In this presentation, we search for the dark boson and the dark Higgs in both exclusive and inclusive modes.
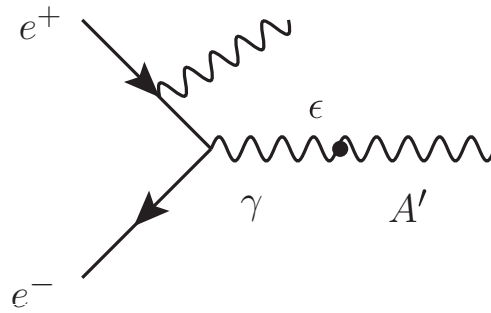

Figure 1: An example Feynman diagram that illustrates production of the dark photon A' in e^+e^- collision.

2 Data Analysis

2.1 Experimental facility and the data set

We use data collected with the Belle detector [4] at the KEKB e^+e collider [5] , amounting to 977 fb^{-1} at center-of-mass energies corresponding to the $\Upsilon(1S)$ to $\Upsilon(5S)$ resonances and in the nearby continuum. We optimize the selection criteria and determine the $e^+e \to A'h'$ signal detection efficiency using a Monte Carlo (MC) simulation where the interaction kinematics and detector response are simulated with the packages MadGraph [6] and GEANT3 [7], respectively. There is no suitable background simulation available, so background samples are taken from data sidebands.

2.2 Main Analysis in Detail

We study the Higgs-strahlung channel, $e^+e^- \to A'h'$. The dark photon A' can decay into lepton pairs, hadrons, or invisible particles while the dark Higgs boson h' can decay into either A', $A'^{(*)}$, leptons pairs, or hadrons, where A'^* is a virtual dark photon [8]. The production
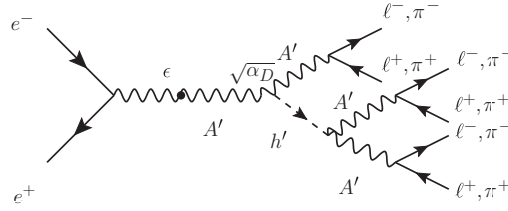

Figure 2: The Feynman diagram that illustrates the Higgs-strahlung channel that we use in this analysis.

and decay modes that we search is indicated in Fig. 2 where α_D is the dark sector coupling constant. In total there are 10 exclusive channels: $3(\ell^+\ell^-)$, $2(\ell^+\ell^-)(\pi^+\pi^-)$, $(\ell^+\ell^-)\,2\,\pi^+\pi^-)$, and $3(\pi^+\pi^-)$. We also look at 3 inclusive modes for $m_{A'} > 1.1$ GeV/c^2: $2(\ell^+\ell^-)X$ where X is the missing mass from the dark photon candidate.

For the background estimation, we use the same esign events from $e^+e^- \to (\ell^+\ell^+)\,(\ell^-\ell^-)$ $(\ell^+\ell^-)$, order masses of lepton (or hadron) pairs as $m_{\ell\ell}^1 > m_{\ell\ell}^2 > m_{\ell\ell}^3$, and plot $m_{\ell\ell}^1 - m_{\ell\ell}^3$ vs. $m_{\ell\ell}^1$. Then select the region in invariant mass distribution and predict the background using the same sign events.The figure 3 shows an example invariant mass distribution difference $m_{A'_{\text{cand}}}^1 - m_{A'_{\text{cand}}}^2$ for the $3(\pi^+\pi^-)$ final state. The normalization is from the side band same sign events and the background in the signal region is counted from the same sign events. The background estimation from MC events and real data agree each other and no significant access of signal events is seen in the data at the signal region defined in Fig. 3.

Figure 4 (a) shows the distribution of $m_{A'_{\text{cand}}}\,m_{A'_{\text{cand}}}$ as a function of $m_{A'_{\text{cand}}}$. Scattered events are largely from inclusive modes or from $3(\pi^+\pi^-)$ states where larger background events are expected. Fig;ure 4 (b) and (c) show the projections on the mass axis of the dark Higgs boson and dark photon, respectively. The of events observed in the signal region, N_{obs}, and the number of predicted background events, N_{bkg}, are in good agreement. Their differences are quantified by the normalized reduals, shown in Fig. 4 (d) and defined as $(N_{\text{obs}} - N_{\text{bkg}})$

$\sqrt{\sigma_{\text{obs}}^2 + \sigma_{\text{bkg}}^2}$, where σ_{obs} and σ_{bkg} are the standard deviations of the distributions. In all cases, the number of events observed is consistent with the background estimate. For exclusive final states, the background is mostly due to processes with ρ and ω resonance paritlces, such as SM 2γ processes. The discontinuity at 1.1 GeV/c^2 in Fig. 4 (c) is an artifact of the selection criteria.

The upper limit on the $\alpha_D \times \epsilon^2$ are computed based on equations described in Ref [8]. Figure 5 shows the 90 % credibility level (CL) upper limits on $\alpha_D \times \epsilon^2$ for Belle, expected and measured, and for BaBar, for five different mass hypotheses for the dark Higs boson (top row) and dark photon (bottom row) masses.

Note that the inclusion of $3(\pi^+\pi^-)$ final state dramatically improves the limit around the ρ and ω resonances. The dominant source of systematic uncertainties are : the integrated luminosity (1%), branching fractions (4%), track identification (6%), particle identification efficiency (5%), detection efficiency (15%), background estimation (10%), and initial-state radiation (15%). All systematic uncertainties added in quadrature aount to 25%.

2.3   Other Ongoing Analyses

We are also working on a long lived dark photon search where $c\tau$ can be as long as 1-10 cm. Since it is low multiplicity final state (two charged tracks and one photon), the efficiencies are low in general in Belle and one analysis is ongoing. Another analysis is a search for invisible decays when the dark photon decays to a pair of dark matter particles [11]. Since this is a final state with a single photon only, the Belle analysis relies on the photon conversion technique. There is also a study going on based on a new possibility of a dark boson coupling to quarks predominantly, based on Ref. [12].

3   Future Prospects

The KEKB e^+e^- collider and the Belle detector are under major upgrade to the superKEKB collider and the Belle II detector in order to acheive the collection of 50 times more data [13]. The Belle II detector will be in fact a brand new detector except the crystal based electromagnetic calorimeter. A two-layer pixel and silicon strip detectors will function as the new vertex detector, and a newly constructed drift chamber provide precision charged particle tracking as well as 3-dimensional online track trigger. Time of propagation counter based particle identification system for barrel and the proximity focusing aerogel ring image Chrenkov detector for the end are now under construction. New resistive plate counter for the barrel and the sciltillator with the multi-pixel photon counter readout is constructed for the endcap muon and K_L particle detection. The full detector operation is expected in 2018.

This upgrades enables us to be dramatically sensitive to the search for new particles in the dark sector. This is not only due to the increase of the data size by 50 times but also due to much improved the online trigger system. The detailed track and energy cluster information is sent to all the way down to the final global trigger logic unit and this will enable us to prepare dedicated trigger lines for the dark particle searches. From this one expect to explore the kinematic mixing parameter values of just above 10^{-4} in the dark photon mass values of 0.01 to 10 GeV/c^2.

4 Bibliography

References

[1] P. Fayet, "Effects of the Spin-1 Partner of the Goldstino (Gravitino) on Neutral Current Pheomenology," Phys. Lett. B **95**, 285 (1980).

[2] G. Aad *et al.*, [ATLAS Collaboration], "Summary of the ATLAS experiments sensitivity to supersymmetry after LHC Run 1 interpreted in the phenomenological MSSM," J. High Energy Phys. **10**, 134 (2015).

[3] S. Chatrchyan *et al.*, [CMS Collaboration], "Interpretation of searches for supersymmetry with simplified models," Phys. Rev. D **88**, 052016 (2013).

[4] A. Abashian *et al.* [Belle Collaboration], Nucl. Instrum. Methods Phys. Res. Sect. A **479**, 117 (2002); also see detector section in J.Brodzicka et al., Prog. Theor. Exp. Phys. **2012**, 04D001 (2012).

[5] S. Kurokawa and E. Kikutani, Nucl. Instrum. Methods Phys. Res. Sect. A **499**, 1 (2003), and other papers included in this Volume; T. Abe *et al.*, Prog. Theor. Exp. Phys. 2013, 03A001 (2013) and following articles up to 03A011.

[6] J. Alwall P *et al.*, "The automated computation of tree-level and next-to-leading order differential cross sections, and their matching to parton shower simulations", J. High Energy Phys. **07**, 079 (2014).

[7] R. Brun *et al.*, GEANT 3.21, Cern/DD/ee/84-1, (1986).

[8] B. Batell, M. Pospelov, and A. Ritz, "Proving a secluded $U(1)$ at B factories", Phys. Rev. D **79**, 115008 (2009).

[9] I. Jaegle *et al.* [Belle Collaboration], "Search for the dark photon and the dark Higgs boson at Belle", Phys. Rev. Lett. **114**, 211801 (2015).

[10] J. P. Lees *et al.* [BaBar Collaboration], "Search for Low-Mass Dark-Sector Higgs Bosons", Phys. Rev. Lett. **108**, 211801 (2012).

[11] R. Essig, J. Mardon, M. Papucci, T. Volansky, and Y. Zhong, "Constraining light dark matter with low-energy e^+e^- colliders", J. High Energy Phys. **11**, 167 (2013).

[12] S. Tulin, "New weakly coupled forces hidden in low-energy QCD", Phys. Rev. D **89**, 114008 (2014).

[13] B. Wang, [for the Belle Collaboration] "The Belle II Experiment and SuperKEKB Upgrade", `arXiv:511.09434`.
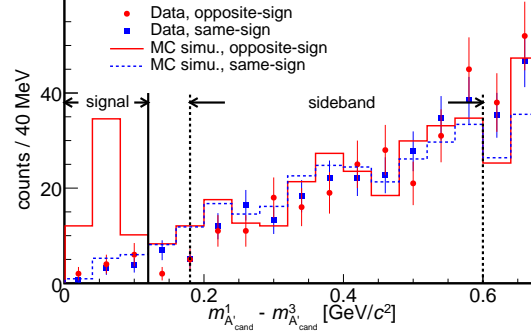
Figure 3: The distribution of $m^1_{A'_{cand}}$ - $m^2_{A'_{cand}}$ for the $3(\pi^+\pi^-)$ final state. The solid and dotted histograms are from opposite-sign and the same-sign MC events. The closed circles (red) and squares (blue) are the data from opposite-sign and the same-sign data events, respectively. The figure is taken from [9].
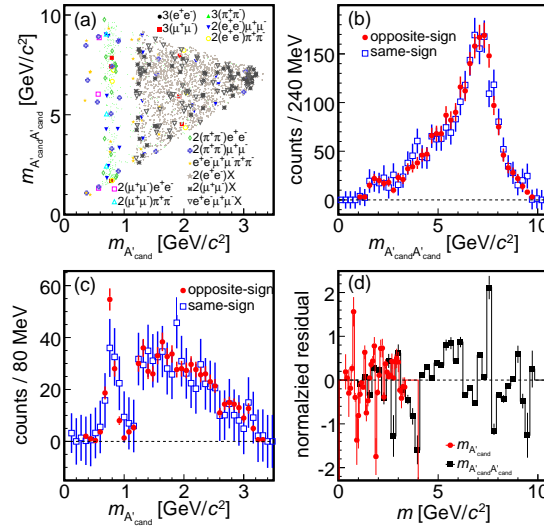

Figure 4: Signal candidates observed versus dark photon candidate mass: $m_{A'_{cand}}$, and dark Higgs boson candidate mass, $m_{A'_{cand}}m_{A'_{cand}}$, for the 13 final states. There are three entries per event. (b) and (c): Projection of signal candidates onto $m_{A'_{cand}}m_{A'_{cand}}$ and $m_{A'_{cand}}$ (red points) with the predicted background (blue squares) from the scaled same-sign distributions for comparison. (d): Normalized reduals between the signal candidate distribution and predicted background, versus dark photon candidate mass (red points) and dark Higgs boson candidate mass (black squares). The figure is taken from [9].
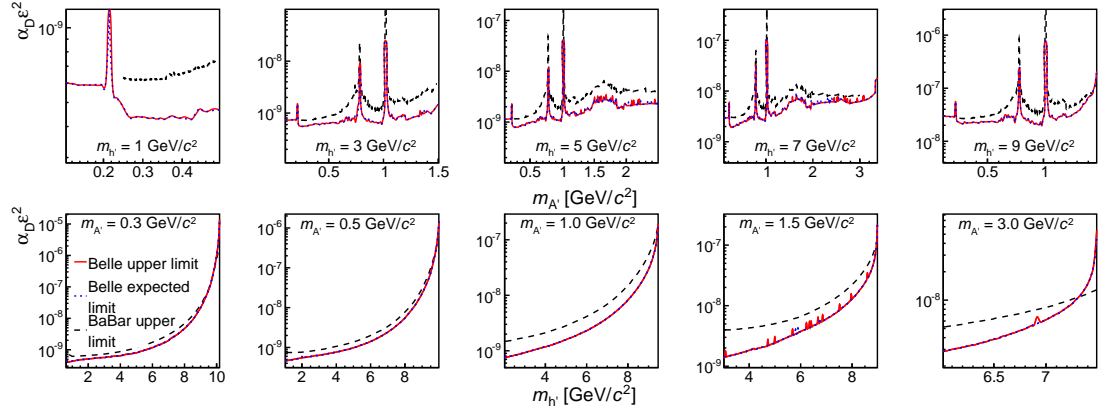
Figure 5: 90 % CL level on the product $\alpha_D \times \epsilon^2$ versus dark photon mass (top row) and dark Higgs boson mass (bottom row) for Belle (solid red curve) and BaBar [10] (dashed black curve). The blue dotted curve, which coincides more or less with the solid red curve, shows the expected Belle limit. The figure is taken from [9].

Status and recent dark matter search results from the PandaX experiment

Mengjiao Xiao[1,2] (On Behalf of PandaX Collaboration)

[1] Department of Physics, University of Maryland, College Park, USA
[2] Institute of Nuclear and Particle Physics (INPAC), Shanghai Jiao Tong University, China

The PandaX project is a staged xenon-based deep underground experiment at the China Jin-Ping Underground Laboratory. The first phase experiment, PandaX-I, a 120 kg dark matter detector using the dual phase xenon time projection chamber (TPC) technology was completed in 2014 with a 54×80.1 kg-day exposure. Recently, the commissioning run of the second phase of the experiment, PandaX-II, was completed with a 306×19.1 kg-day exposure. We report the status of the PandaX experiment, and then present the dark matter search results from both runs.

1 Introduction

PandaX experiment is located in the China Jin-Ping Underground Laboratory (CJPL) in southeast China. The average depth is 2400 m or 6800 m w.e (water equivalent depth) where the muon flux is reduced to around 60 events/m^2/year [1]. The project is developed stagewise. In PandaX-I, the first phase of the project, 120 kg active liquid xenon was contained in the central detector to search for the Weakly Interaction Massive Particles (WIMPs). In the second phase, PandaX-II, the target mass for the WIMP detector was enlarged to a half tone. The PandaX-III, the future phase of the project, will use the high pressure ^{136}Xe gas to search for neutrinoless double beta decay. The collaboration also aim to develop a multi-ton liquid xenon detector for dark matter search. Currently we have completed PandaX-I, and PandaX-II is undergoing.

In PandaX-I and PandaX-II, the dual-phase xenon time projection chamber (TPC) technology, illustrated in Fig. 1, was adopted for WIMP dark matter detection. An incoming particle interaction in the liquid xenon (LXe) produces direct scintillation photons, called S1, as well as the ionization electrons. An electrical field is applied across the liquid xenon volume. The ionization electrons drift to the liquid-gas interface and are extracted into the gaseous xenon by a stronger electrical field, producing secondary proportional scintillation photons, which are called S2. Both signals (S1 and S2) can be detected by the photomultiplier tube (PMT) arrays located at top and bottom of the detector. The time difference of the two signals can be used to calculate the vertical position of the interaction. The S2 signal pattern in the top array allows the reconstruction of the horizontal position. Precise determination of the position of an event enables the fiducialization of a low background target region.

In Fig. 2, the discrimination power of a dual phase xenon TPC is illustrated. Compared to the electron recoil (ER) background, the ionization density of nuclear recoil (NR) signal is much
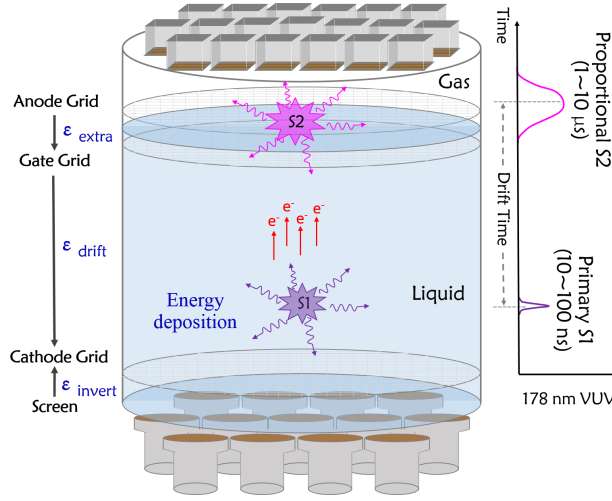
Figure 1: Work principle of a dual phase xenon TPC.

larger, so electrons are more likely to recombine with ions, leading to a relatively smaller S2-to-S1 ratio. Therefore this ratio can be used to discriminate nuclear and electron recoil events. Additionally,dark matter particles can only scatter once in the detector, so the background can be further suppressed by the requirement of single scattering.
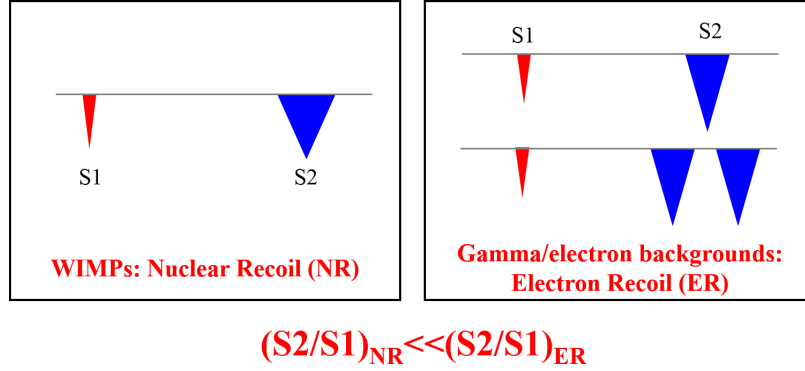

$$(S2/S1)_{NR} << (S2/S1)_{ER}$$

Figure 2: Bacrground discrimination with a dual phase xenon TPC.

2 PandaX-I dark matter search results

The PandaX-I setup is described in detail in Ref. [2]. Fig. 3 shows the TPC design of the PandaX-I experiment. It was a pancake structure, with a drift volume of 60 cm in diameter and 15 cm in height. We had 143 1-inch PMTs (Hamamatsu R8520-406) and 37 3-inch PMTs (Hamamatsu R11410-MOD) with quantum efficiency peaked at 178 nm on the top and bottom,

respectively. To increase the light collection efficiency, PTFE reflectors were installed around the TPC. The electrical field in the TPC was defined by three electrodes, the cathode, gate and anode. During the operation, the anode grid was grounded while separated by 8 mm with the gate grid located 4 mm below the liquid level. High voltage with -15 kV and -5 kV was applied on to the cathode and gate grids respectively. Outside the refelector wall, the shaping rings were used to regularize the drift field. The design goal of the TPC is to achieve good light collection efficiency which is a key to detect low-mass dark matter. The right pictures in Fig. 3 show the real TPC components serving for PandaX-I. From top to bottom, they are the top PMT array, field cage and the bottom PMT array.
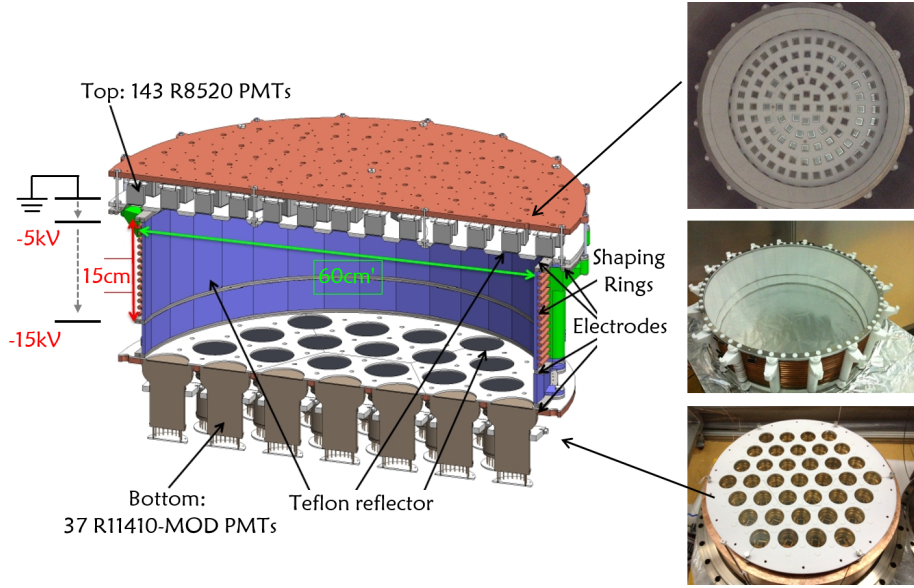

Figure 3: PandaX-I TPC design and pictures.

PandaX-I dark matter search experiment took physical data from May 26, 2014 to Oct. 16, 2014. With a blinded data analysis, we released the dark matter search results with an exposure of 80.1 day $\times$ 54 kg [14]. No positive signal above the background was found. We set the 90% C.L. exclusion limit to the dark matter interaction with nucleon, and the lowest excluded cross section is at about 1×10^{-44} cm^2 for a WIMP mass of 44.7 GeV/c^2. The result strongly disfavors previously reported signals from the DAMA/LIBRA [3], CoGeNT [4], CDMS-II-Si [7] and CRESST-II [5] experiments. Our result offers tighter bound above 7 GeV/c^2 than SuperCDMS. In the xenon experiment community, at that time, we achieved the best reported limit below 5.5 GeV/c^2.

3 Recent updates from the PandaX-II experiment

In parallel with the running of PandaX-I, we started to prepare the PandaX-II detector in 2014. Most of the infrastructures of PandaX-I were reused for PandaX-II: passive shielding, outer Cu vessel, cryogenics, etc. The experiment was located at the same experimental hall in CJPL.
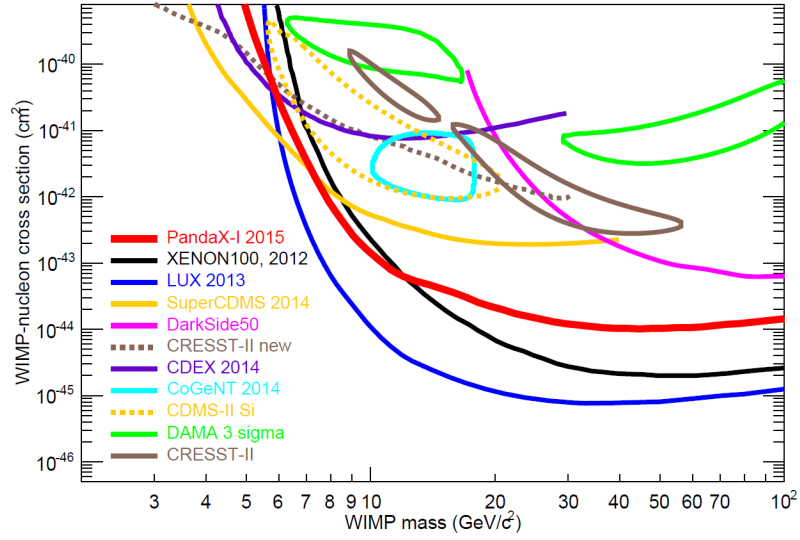
Figure 4: The 90% c.l. upper limit for spin-independent isoscalar WIMP-nucleon cross section for the PandaX-I experiment (red curves). Recent world results are plotted for comparison: XENON100 225 day results [9] (black solid), LUX first results [10] (blue), SuperCDMS results [17] (orange solid), DarkSide results [18] (magenta solid), CRESST-II 2014 limits [5] (brown dashed), and CDEX 2014 limits [6] (solid violet). The claimed WIMP signals are shown as closed contours: CoGeNT 2014 results [4] (cyan solid), CDMS-II-Si results [7] (gold dashed), DAMA/LIBRA 3σ contours [3] (green solid), and CRESST-II 2012 results [5] (brown solid).

The most significant upgrades were the new inner vessel constructed from stainless steel with much lower radioactivity, and a much larger xenon TPC. The cylindrical TPC, as shown in Fig. 5, contains 580 kg LXe in the sensitive volume with an inner diameter of 646 mm and a maximum drift length of 600 mm. In addition, we placed 55 Hamamatsu-R11410-MOD 3-inch PMTs on the top and bottom of the TPC respectively, and added 48 R8520-406 1-inch PMTs outside the target serving as active veto. To further increase the light collection efficiency, the PTFE plates with higher reflectivity were selected to enclose the TPC.
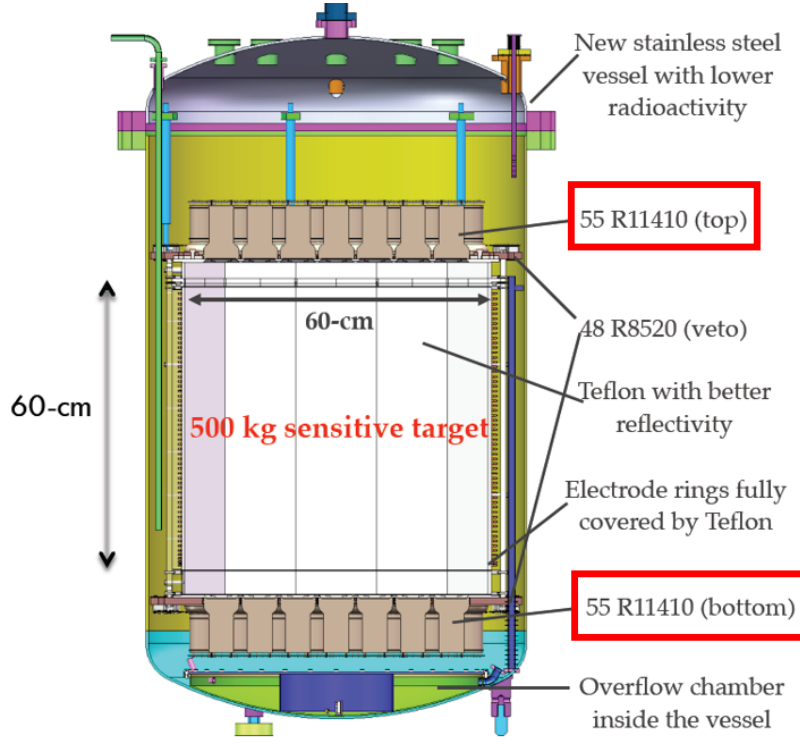

Figure 5: The TPC design of the PandaX-II experiment.

The onsite installation of detector for PandaX-II started in October of 2014. We spent around one year to take series of engineering runs in 2015 to test all the components. A physics commissioning run from Nov.22 to Dec.14 was carried out but ended due to high Krypton background [15]. Here we present the performance of the detector in PandaX-II experiment and the dark matter search results from this commissioning run.

3.1 Detector calibration

During the operation, high voltage of -29 kV and -4.95 kV was applied to the cathode and gate grid, respectively, and the anode was kept at ground. We deployed one neutron source (^{252}Cf) and two gamma sources (^{60}Co and ^{137}Cs) close to the inner detector to calibrate the detector response. Neutrons can excite xenon nuclei or produce metastable nuclear states, leading to de-exciting gamma rays at 40 (^{129}Xe), 80 (^{131}Xe), 164 (^{131m}Xe), and 236 keV (^{129m}Xe). These

energy peaks are used to study the non-uniformity of the detector and extract the detector's parameters. With liquid xenon TPC, any energy deposition in LXe will be released in the form of either S1 or S2. An electron equivalent deposited energy can be reconstructed with Eq. 1 in which $W = 13.7$ eV is the average work function to produce either an electron or photon, PDE is photon detection efficiency, SEG is single electron gain and EEE is electron extraction efficiency.

$$E_{ee} = W \times (\frac{S1}{PDE} + \frac{S2}{SEG \times EEE})$$ (1)

We fitted the photonelectron distribution of the smallest S2 signals with a Gaussian function and obtained SEG = 22.1±0.7 PE/e⁻. Through the anti-correlation between S1 and S2 for various energy peaks, other parameters in Eq. 1 were obtained with a linear fit as shown in Fig. 6. The best fit values are PDE = 11.7%, EEE = 48.1% with the uncertainty of 5.6% and 7.1% respectively.
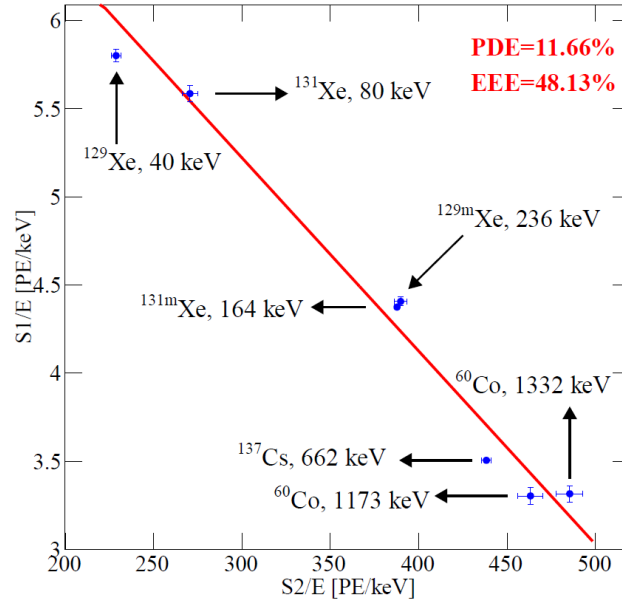

Figure 6: Linear fit in S2/E_{ee} vs. S1/E_{ee} for all energy peaks.

The neutron events in ^{252}Cf calibration data were used to study the detector's response to nuclear recoil signals. In the operation, we obtained 547 events in the target volume for S1 between 3 to 45 PE. The $\log_{10}$(S2/S1) vs. S1 of these events is shown in Fig. 7. Based on the NEST model [12, 13] and the PDE, EEE and SEG obtained above, we peformed a full Monte-Carlo (MC) simulation using Geant4. The MC predication is also overlaid in Fig. 7. A better agreement on the median of the NR distribution can be achieved by tuning the ratio of the initial number of excitation and ionization by a factor of 1.5 in the NEST model. The tunned MC was chosen as the default model. The NR detection efficiency was obtained by the comparison of data and MC predication, parameterized as a function both of S1 and S2 shown

in Eq. 2, where $S2_{raw}$ is the raw S2 before the electron lifetime correction.

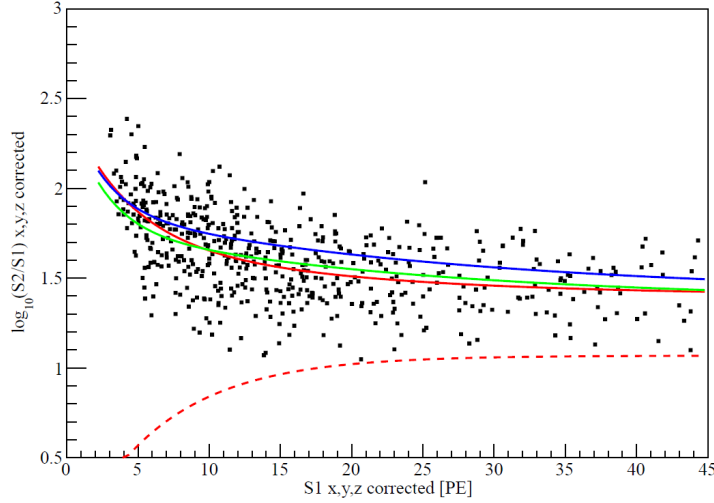$$\epsilon = 0.94[e^{-\frac{S1-6.21}{1.66}} + 1]^{-1}[e^{-\frac{S2_{raw}-79.3}{20.8}} + 1]^{-1} \tag{2}$$

Figure 7: The comparison of ^{252}Cf neutron calibration data with the median from the original NEST model (blue line) and the tuned model (green line). A fit to the median of the data is given by the red line. The dashed red line is the NR 99.99% acceptance line based on the tuned MC model.

3.2   Backgrounds

As in Ref. [14], the background is categorized into three components: the ER, neutron, and accidental background. The ER background consists of external background due to radioactivities in the detector materials, and internal backgrounds due to krypton and radon. Before the detector assembly, the components were assayed with a high purity Germanium counting station at CJPL [16]. These results were used as the inputs of the MC simulation to calculate the external background at low energy, which was estimated to be 0.21 mDRU (1 mDRU=10^{-3} evts/keV/kg/day).

During the commissioning run, serious Kr background was found in data, likely due to an accidental air leak in a previous engineering run. With a β-γ delayed-coincident analysis, the ^{85}Kr was estimated to be 0.082 mBq/kg or 15.04 mDRU with a 3% uncertainty. Similarly, the radon level in LXe can be evaluated by identifying β-α and α-α coincidence events in data. ^{222}Rn was estimated to be 6.57 μBq/kg in the fiducial volume (FV). ^{220}Rn was estimated to be 0.54 (^{212}Bi-^{212}Po) and 0.41 μBq/kg (^{220}Rn-^{216}Po) in the FV, respectively. The ER background components are summarized in Tab. 1.

The neutron background also come from detector components. It was estimated by the MC to be 0.06 events in the final data set after all selection cuts. Same to the analysis in Ref. [14],

Item	Background (mDRU)
^{85}Kr	15.04
^{222}Rn	0.075
^{220}Rn	0.021
PMT array & bases	0.097
PTFE wall	0.021
Inner vessel	0.045
Other Inner components	0.026
Cu outer vessel	0.016
Total	15.33

Table 1: Summary of ER backgrounds from various components.

we studied single S1 and S2 events in the data. The rate of single S1-like events was determined to be 2.8±0.1 Hz within the S1 range cut. In the same data set, 28069 single S2-like events were identified within the final S2 range cut and fiducial radius cut. The accidental background was evaluated by randomly pairing the single S1 and S2 events with all coincidence selection cuts applied. 0.70 qualified accidental events were expected to survive with a 25% uncertainty.

The final expected background budget including the ER, accidental, and neutron background is summarized in Tab. 2. We expect to observe 617±104 events in the fiducal volume after the all cuts while 3.2±0.71 events are expected to below the NR median.

-	ER	Accidental	Neutron	Total Expected	Total observed
All	611	5.9	0.13	617±104	728
Below NR median	2.5	0.7	0.06	3.2±0.71	2

Table 2: The expected background events in 19.1 live-day dark matter search data in the FV, before and after the NR median cut, as well as the final number of candidate events in the data.

3.3 Dark matter search results

We searched for the dark matter signals with a total of 306×19.1 kg-day exposure. The distribution of $\log_{10}$(S2/S1) versus S1 is shown in Fig. 8(a). 728 events in total were selected for the dark matter analysis while two of these events were found below the median of the NR band. Detailed examinations confirmed the high quality of these two events. The vertex distribution of these events is shown in Fig. 8(b). Compared to the expected background, no excess dark matter signal was found. Based on the two observed events and 3.2 expected backgrounds, the final 90% C.L. upper limit for the spin-independent isoscalar WIMP-nucleon cross section was calculated using the CLs method [20, 21]. The final results are shown in Fig. 3.3. The upper limits lie in the ±1σ sensitivity band. The lowest cross section limit obtained is 2.97×10^{-45} cm^2 at a WIMP mass of 44.7 GeV/c^2, which represents an improvement of more than a factor of three from PandaX-I. The cross section limit at WIMP mass of 10, 100, and 300 GeV/c^2 are 8.43×10^{-44}, 4.34×10^{-45}, and 1.13×10^{-44} cm^2, respectively.
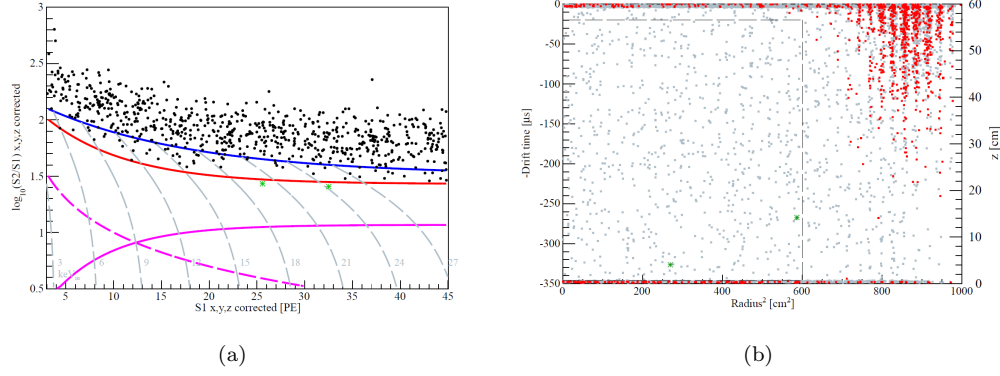
(a)   (b)

Figure 8: (a) The distribution of $\log_{10}$(S2/S1) versus S1 for dark matter search data. The median of the NR calibration band is indicated as the red curve. The dashed magenta curve is the equivalent 100 PE cut on S2. The solid magenta and blue curves are the 99.99% and 33.3% NR acceptance curves, respectively. The grey dashed curves are the equal energ curves with NR energy indicated in the figures. The two data points located below the NR median curve are highlighted in green stars. (b) Position distribution of events that pass all selection cuts (gray points), and those below the NR median (outside FV: red points; inside FV: green stars), with FV cuts indicated as the black dashed box.
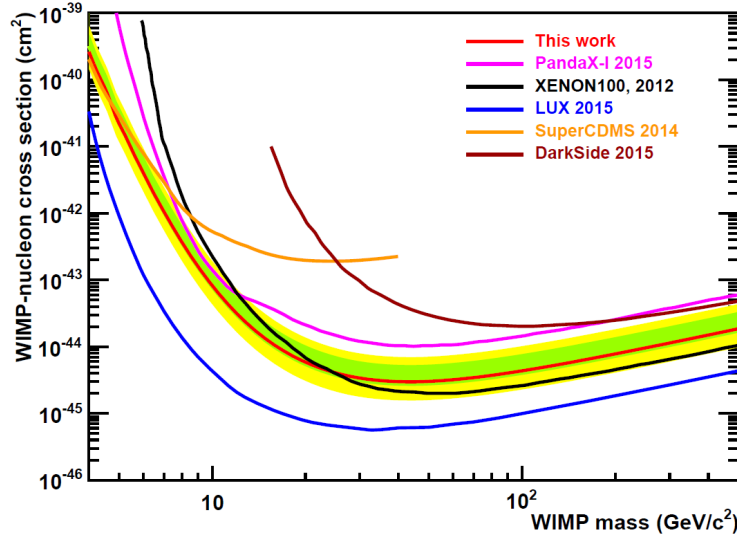
Figure 9: The 90% C.L. upper limit for the spin-independent isoscalar WIMP-nucleon cross section from the PandaX-II commissioning run (red). A selected set of recent world results are plotted for comparison: PandaX-I final results [14] (magenta), XENON100 225 day results [9] (black), LUX 2015 results [11] (blue), SuperCDMS [17] (orange), and Dark-Side 2015 [19] results (brown). The 1σ and 2σ sensitivity bands are shown in green and yellow, respectively.

4 Conclusion and outlook

The PandaX experiment has been producing tight constrains to the WIMP parameter space. The half-ton scale DM experiment of PandaX-II has been commissioned with key components working. No dark matter signal was observed in the commissioning run with an exposure of 306×19.1 kg-day. After the commissioning run, we carried out a distillatation to remove Kr, afterward the ER background was suppressed significantly. The physics data taking was resumed this year. After this conference, PandaX-II released the dark matter results with a total exposure of 3.3×104 kg day [22] and set the world's best reported limit on the spin-independent elastic WIMP-nucleon cross sections.

References

[1] Wu Y C, Hao X Q, Yue Q, *et al.*, "Measurement of cosmic ray flux in China JinPing underground Laboratory", Chin Phys C, 2013, 37 (8): 086001.

[2] Cao X G, Chen X, Chen Y H, *et al.* [PandaX Collaboration]. "PandaX: A liquid xenon dark matter experiment at CJPL", Sci China-Phys Mech Astron, 2014, 57(8): 14761494.

[3] R. Bernabei *et al.* [DAMA Collaboration], Eur. Phys. J. C 56 (2008), Eur. Phys. J. C 67 (2010), Eur. Phys. J. C 73 (2013).

[4] C. E. Aalseth *et al.* [CoGeNT Collaboration], Phys. Rev. Lett. 106, 131301 (2011), Phys. Rev. D88, 012002 (2013), and latest analysis using maximum likelihood method in arXiv:1401.6234 (2014)

[5] G. Angloher et al. [CRESST Collaboration], Eur. Phys. J. C 72 (2012), Eur. Phys. J. C 74 12, 3184 (2014)

[6] Q. Yue *et al.* [CDEX Collaboration], "Limits on light weakly interacting massive particles from the CDEX-1 experiment with a p-type point-contact germanium detector at the China Jinping Underground Laboratory", Phys. Rev. D 90, 091701 (2014)

[7] R. Agnese *et al.* [CDMS Collaboration], "Silicon Detector Dark Matter Results from the Final Exposure of CDMS II", Phys. Rev. Lett. 111, 251301 (2013)

[8] M. Xiao *et al.* [PandaX Collaboration], "First dark matter results from the PandaX-I Experiment", Sci. China Phys. Mech. Astron. 57, 2024 (2014) [arXiv:1408.5114 [hep-ex]].

[9] E. Aprile *et al.* [XENON100 Collaboration], "Dark Matter Results from 225 Live Days of XENON100 Data", Phys. Rev. Lett. 109, 181301 (2012), [arXiv:1207.5988 [astro-ph.CO]].

[10] D. S. Akerib *et al.* [LUX Collaboration], "First Results from the LUX Dark Matter Experiment at the Sanford Underground Research Facility", Phys. Rev. Lett. 112, 091303 (2014), [arXiv:1310.8214 [astro-ph.CO]].

[11] D. S. Akerib *et al.* [LUX Collaboration], "Improved Limits on Scattering of Weakly Interacting Massive Particles from Reanalysis of 2013 LUX Data", Phys. Rev. Lett. 116, 161301 (2016), [arXiv:1512.03506 [astro-ph.CO]].

[12] M. Szydagis, N. Barry, K. Kazkaz, J. Mock, D. Stolp, M. Sweany, M. Tripathi, S. Uvarov, N.Walsh, and M Woods, "NEST: A Comprehensive Model for Scintillation Yield in Liquid Xenon", J. Instrum. 6, P10002 (2011),]arXiv:1106.1613v1 [physics.ins-det]].

[13] M. Szydagis, A. Fyhrie, D. Thorngren, and M. Tripathi, "Enhancement of NEST Capabilities for Simulating Low-Energy Recoils in Liquid Xenon", J. Instrum. 8, C10003 (2013), [arXiv:1307.6601v1 [physics.ins-det]].

[14] X. Xiao *et al.* [PandaX Collaboration], "Low-mass dark matter search results from full exposure of PandaX-I experiment", Phys. Rev. D92, 052004 (2015) [arXiv:1505.00771 [hep-ex]].

[15] A. Tan *et al* [PandaX Collaboration], "Dark Matter Search Results from the Commissioning Run of PandaX-II", Phys. Rev. D93, 122009 (2016) [arXiv:1602.06563 [hep-ex]].

[16] Xuming Wang, Xun Chen, Changbo Fu, Xiangdong Ji, Xiang Liu, Yajun Mao, Hongwei Wang, Siguang Wang, Pengwei Xie, Tao Zhang "Material Screening with HPGe Counting Station for PandaX Experiment", [arXiv:1608.08345 [physics.ins-det]]

[17] R. Agnese *et al.* [SuperCDMS Collaboration], "Search for Low-Mass Weakly Interacting Massive Particles with SuperCDMS", Phys. Rev. Lett. 112, 241302 (2014), [arXiv:1402.7137 [hep-ex]].

[18] P. Agnes *et al.* [DarkSide Collaboration], "Low radioactivity argon dark matter search results from the DarkSide-50 experiment", Phys. Lett. B743, 456 (2015), [arXiv:1510.00702v2 [astro-ph.CO]].

[19] P. Agnes *et al.* [DarkSide Collaboration], "Results from the first use of low radioactivity argon in a dark matter search", Phys. Rev. D 93, 081101 (2016), [arXiv:1510.00702 [astro-ph.CO]].

[20] A. L. Read, "Presentation of search results: the CL_s technique", J. Phys. G28, 2693 (2002).

[21] T. Junk, Nucl. Instrum. Meth. A434, 435 (1999), [arXiv:9902006 [hep-ex]].

[22] A. Tan *et al.* [PandaX-II Collaboration], "Dark Matter Results from First 98.7 Days of Data from the PandaX-II Experiment", Phys. Rev. Lett. 117, 121303 (2016), [arXiv:1607.07400 [hep-ex]].

Multiple-Cavity Detectors for Axion Search

SungWoo YOUN[1]

[1]Center for Axion and Precision Physics Research (CAPP), Institute for Basic Science (IBS), South Korea

Searching higher frequency regions for axion dark matter using microwave cavity detectors requires smaller size cavities as the resonant frequencies scale inversely with their radius. One of the intuitive ways to make an efficient use of a given magnet volume, and thereby to increase the experimental sensitivity, is to bundle multiple cavities together and combine their individual outputs ensuring phase-matching of the coherent axion signal. An extensive study for realistic design of the phase-matching mechanism is performed and an experimental demonstration is undertaken using a double-cavity system.

1 Introduction

Axion is an attractive dark matter candidate originally motivated by the Peccei-Quinn solution to the strong-CP problem [1]. The current technologies utilize the axion-to-photon conversion to detect the axion signal using microwave resonant cavities embedded in a strong magnetic field, suggested by P. Sikivie [2], and conventional experiments employ a single cavity fitting into the given magnet. Exploring higher frequency regions, on the other hand, requires smaller cavity sizes as the resonant frequency of our main interest, TM_{010}, is inversely proportional to their radius R ($f_{\text{TM}_{010}} \sim R^{-1}$). As many experiments rely on a magnet with a fixed bore size, an intuitive way to increase the detection volume for the given magnet, and thereby to improve the experimental sensitivity, is to bundle multiple cavities together and combine their individual outputs in phase, which is referred to as "*phase-matching*".

The idea of multiple-cavity design was introduced in 1990 [3] and the first experimental trial was given in 2000 using a four-cavity detetor [4]. However, it failed to address the methodological advantage mainly because the phase-matching is very a challenging task. The Experiment of Axion Search aT CAPP (EAST-C) is a dedicated project at the Centre of Axion and Precision Physics Research (CAPP) of the Institute for Basic Science (IBS) in Korea to develop the phase-matching mechanism for multiple-cavity systems.

2 Configurations

There are three possible configurations for experimental design of a multiple(N)-cavity system, as summarized in Tab. 1. Configuration 1 is equivalent to N single-cavity experiments, which requires N independent complete readout chains. Configuration 2 represents a N-cavity experiment where the first stage amplification takes place before the signal combination, while configuration 3 represents a similar experiment where the signal combination precedes the first

stage amplification. Assuming the axion signals are correlated while the system noises (from cavities and electronics) are uncorrelated, the former design, characterized by N amplifiers and a combiner, yields the highest sensitivity, while the latter, characterized by a single amplifier and a combiner, provides the simplest design. As a simpler design is significantly beneficial especially N goes large, configuration 3 is chosen as the final design.
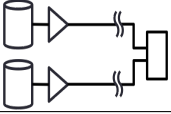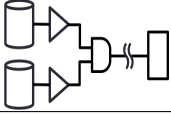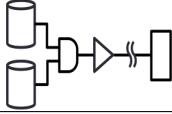
Configuration	1	2	3
Schematic			
Characteristics	N readout chains	N amplifiers 1 combiner	1 amplifier 1 combiner
Sensitivity (SNR)	$\sqrt{N} \cdot \mathrm{SNR_{sngl}}$	$N \cdot \mathrm{SNR_{sngl}}$	$N \cdot \mathrm{SNR_{sngl}}$[1]
Pros	Individual accessibility	Highest sensitivity	Simplest design
Cons	Low sensitivity Complex design	N amplifiers	$\mathrm{SNR_3} < \mathrm{SNR_2}$[2]

Table 1: Possible configurations for the multiple-cavity experiment design. $\mathrm{SNR_{sngl}}$ refers to the signal-to-noise ratio (SNR) of a single-cavity experiment. [1]The combiner is assumed to be perfect, i.e., no power loss and no additional noise. [2]In reality, SNR degrades due to imperfection of the combiner, e.g. a system with a combiner with a noise figure of 0.5 and a amplifier with a gain of 12 and a noise figure of 6 yields a SNR reduction of ∼10%.

3   Phase matching

3.1   Phases

In multiple-cavity axion experiments, three uncorrelated phases are concerned. These are related to 1) coherence of the axion field; 2) resonant frequency matching among cavities; and 3) phase matching in signal combination.

First of all, according to cosmology, axions are entirely virialized in the early universe and thus the axion field is coherent in the present universe. In addition, the de Broglie wavelength of axion ($10^1 \sim 10^3$ m) is much longer than the typical size of axion detectors ($\sim 10^{-1}$ m). Therefore, if axions exist and are detectable, the signals from the cavities in an array are generated almost in phase in a static magnetic field. Secondly, in order to see the coherent axion signal, individual cavities must be tuned at the same resonant frequency. The phase-matching in the frequency domain is an essential and the most challenging part of the phase-matching mechanism. Lastly, the RF signals at the same frequency must interfere each other in a constructive manner at the power combiner to maximize the combined signal. The constructive interference, i.e., phase-matching in the time domain, requires identical cables with the same length.

Since the first and last phase-matchings are theoretically resolved and experimentally archivable in ease, the phase matching in this regards is approximated to the frequency matching.

3.2 Phase (frequency) matching

One of the main sources of frequency mismatch between individual cavities in an array comes from the machining tolerance in cavity fabrication. A typical machining tolerance of ∼50 μm induces a frequency difference of ∼10 MHz for 5 GHz resonant cavities. However, an ideal frequency matching is not possible due to the non-zero position resolution of the turning system, e.g. a resolution of 0.1 m° of a rotator corresponds to a frequency resolution of ∼0.5 kHz for 5 GHz resonant cavities. Instead, a more realistic approach is to allow frequency mismatch up to a certain level where the combined power is not significantly degraded, i.e., the combined power is greater than 95% of that for the ideal case. We refer to the certain level as the frequency matching tolerance (FMT).

3.3 Frequency matching tolerance

In order to determine FMT for multiple-cavity systems, a pseudo-experiment study is performed using a quadruple-cavity detector with an unloaded cavity quality factor $Q_0 = 10^5$ searching for 6 GHz axion signal. Several values of frequency matching tolerance, tolerances under test (TUT), are considered - 0, 10, 20 ,30, 60, 100, 200 kHz, where 0 kHz represents the ideal combination. The cavities are randomly tuned to 6 GHz within the TUT to be concerned and a combined power spectrum is constructed by summing up the power spectra from the individual cavities. Each cavity is assumed to be critically coupled with a RF antenna. The procedure is repeated 1,000 times. The distributions of averaged combined power spectrum for each TUT, and its amplitude and full width at half maximum are shown in Fig. 1. It is drawn that the FMT for a quadruple detector with $Q_0 = 10^5$ for 6 GHz axion signal is 20 kHz. This is generalized for different Q_0 values as FMT $= 2$ GHz$/Q_0$.
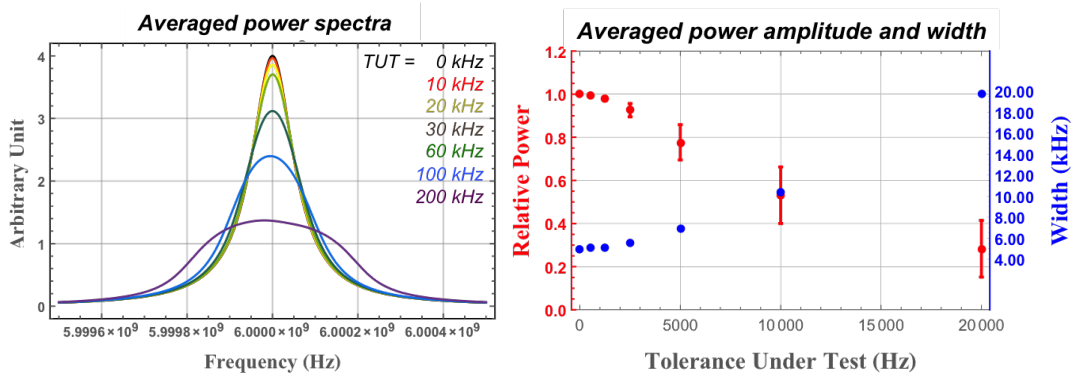

Figure 1: Combined power spectra averaged over 1,000 pseudo-experiments for several TUT values where the power amplitude from each cavity is normalized to the unity (left), and the power amplitude relative to the ideal case and full width at half maximum for the TUT values where the error bars represent the statistical uncertainties (right).

3.4   Tuning mechanism

The basic principle of the tuning mechanism for cavity-based experiments relies on critical coupling of the load with the cavity. The critical coupling is characterized in a network analyzer by a minimized reflection coefficient (Γ) and a circle passing through the center of the Smith Chart. For a single-cavity system, Γ is minimized when the system is critically coupled. For a multiple-cavity system, on the other hand, the combined Γ is minimized when frequency matching is successful as well as the entire system (each cavity) is critically coupled.

The tuning mechanism for a multiple-cavity system consists of three steps: 1) simultaneous operation of the frequency tuners to shift the target frequency; 2) finer operation of the individual tuners to achieve the frequency matching; 3) global adjustment of the load positions to achieve the critical coupling. The global adjustment is chosen at the sacrifice of a sensitivity loss of $<0.5\%$, which is estimated from a machining tolerance of 50 μm and an uncertainty on surface conductivity of 2%.

4   Experimental demonstration

The feasibility of the tuning mechanism for multiple-cavity systems is experimentally demonstrated using a double-cavity detector. It is comprised of two copper cavities with an inner diameter of 3.88 cm whose corresponding resonant frequency is 5.92 GHz and a loaded quality factor of 9,000 at room temperature. A dielectric rod made of 95% of alumina with a diameter of 0.4 mm is introduced to each cavity for frequency tuning and operated by a piezoelectric rotator. With the tuning rod positioned at the center of the cavity, the resonant frequency decreased to 4.54 GHz and Q_L degrades to 2,500. A pair of antennas, each of which is coupled to each cavity, sustained by a holder attached to a linear piezoelectric positioner so that their positions are adjusted in a global manner.

The sequence of the demonstration is shown in Fig. 2. Assembly of a double-cavity system begins with connection of a wilkinson type power combiner to a network analyzer. A calibration is made up to the two couplers using two sets of calibration kits. The critical coupling of a cavity is made while the port of the combiner which is connected to the other cavity is terminated with a 50 Ω impedance, and vice versa. Two cavities are critically coupled at slightly different resonant frequencies. The initial values of Q_L and scattering parameter S_{11} are measured. The system is fully assembled with the two cavities connected to the combiner. Two reflection peaks with S_{11}=6 dB at the above frequencies and two small circles with half radius are observed. At this stage we assume that the slightly different frequencies are the consequence of a global operation of the frequency tuners to shift the target frequency. Now one of the piezoelectric rotators is operated to finely tune its frequency until the combined reflection coefficient becomes minimized, which corresponds to frequency matching. It is also observed that the two small circles become one larger circle. However, it fails to pass the center of the Smith Chart, indicating the critical coupling is not made. The linear positioner is operated to adjust the antenna positions in a global manner to achieve the critical coupling. It is noted that the reflection peak becomes deeper and the circle passes through the center of the Smith Chart. The final Q_L and S_{11} values are measured, and it is seen that they are consistent with the initial values. This confirms that the turning mechanism with phase (frequency) matching for multiple-cavity systems is feasible in real experiments.
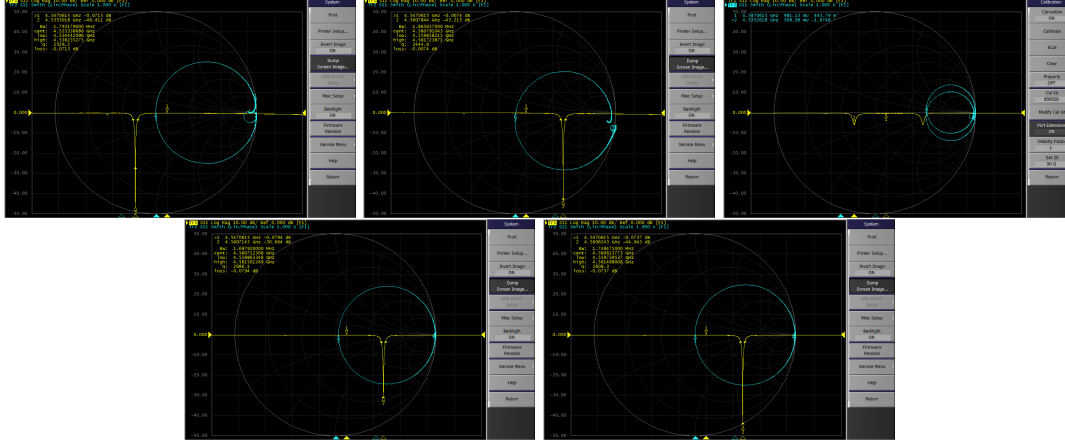
Figure 2: Sequence of the demonstration of the tuning mechanism described in the text using a double-cavity system. Yellow lines are the scattering parameters, S_{11}, in a logarithmic scale and circles in cyan are the representations in the Smith Chart. The first (second) cavity is critically coupled individually, and the initial S_{11} and Q_L read -46.4 (-43.2) dB and 2530 (2440) respectively (Top left and top middle). Two -6 dB peaks and two small circles are observed after the system is fully assembled (Top right). When the frequency matching is achieved, a single deep peak and a single large circle are formed (Bottom left). Once the critical coupling is made in a global manner, the peak becomes deeper and the circle passes through the center of the Smith Chart (Bottom right). The final S_{11} and Q_L read -44.4 dB and 2610.

5 Summary

Multiple-cavity design is an effective way to increase the sensitivity of axion search experiments in higher frequency regions. The frequency matching between individual cavities is a key component of the phase-matching mechanism. A readout chain where signal combination precedes the first stage amplification is beneficial with the simpest setup and minimal signal power degradation. For a realistic approach for phase (frequency) matching, the frequency matching tolerance is introduced and numerically determined for a quadruple-cavity detector for 6 GHz axion signal. An experimental demonstration of the tuning mechanism (phase-matching and critical coupling), successfully made using a double-cavity detector, verifies its feasibility in real experiments.

6 Acknowledgments

References

[1] R. Peccei and H. Quinn, "CP Conservation in the Presence of Pseudoparticles", Phys. Rev. Lett. **38**, 1440 (1977). doi:10.1103/PhysRevLett.38.1440; "Constraints imposed by CP conservation in the presence

of pseudoparticles", Phys. Rev. D **16**, 1791 (1977). doi:10.1103/PhysRevD.16.1791

[2] P. Sikivie, "Experimental Tests of the "Invisible" Axion", Phys. Rev. Lett. **51**, 1415 (1983). doi:10.1103/PhysRevLett.51.1415

[3] C. Hagmann et al., "Cavity design for a cosmic axion detector", Rev. Sci. Instr. **61**, 1076 (1990). doi:10.1063/1.1141427

[4] D. S. Kinion, "First Results From a MultipleMicrowaveCavity Search for DarkMatter Axions, Ph.D. Thesis, UC Davis (2001).

Signals for invisible matter from solar - terrestrial observations

Sergio Bertolucci[1,2], *Konstantin Zioutas*[1,3], *Sebastian Hofmann*[4], *Marios Maroudas*[3]

[1]CERN, Geneva, Switzerland,
[2]INFN, LNF, Italy,
[3]University of Patras, Patras, Greece,
[4]Munich, Germany

Gravitational lensing of invisible streaming matter towards the Sun or the Earth could be the explanation of puzzling solar/terrestrial phenomena. We have analyzed solar flares, EUV emission and also the global ionization content of the Earth atmosphere. Assuming that this invisible matter has some form of interaction with normal matter and that there exist preferred directions in its flow, then one would expect an enhanced activity at certain planetary longitudes, which is also observed. The broad velocity spectrum of the assumed constituents makes it difficult at this stage to identify the origin of the stream(s) or the nature of its constituents.

1   Introduction

The detection of the constituents of dark matter (DM) is one of the central challenges in modern physics. While large scale DM distribution in space is relatively uniform, also local streams have been discussed [1]. The existence of such streams of invisible constituents could be at the origin of the puzzling active Sun or the annual anomaly of the ionization of the Earth atmosphere. We assume here that their triggering is due to planetary lensing of invisible matter stream(s). This scenario is totally different from the models based on tidal forces, which have been attempted with very little success since the discovery of the first large flare some 155 years ago. If this seminal idea holds, there will be ways to explore it further in the future, due to its implications in other ongoing DM searches. A detailed description of the reasoning behind this idea is given in ref. [2]. Here we present also new results.

2   The Observations

2.1   Solar Flares

In this work we provide a statistical analysis of time (=position in the ecliptic) distributions of the inner 3 planets and the Moon, in association with a) the daily occurrence of 6091 M-class and the 491 X-class flares (1976-2015) [3], b) the continuous full disk solar emission in the EUV (1999-2015), and c) the electron content of the Earth ionosphere (1995-2012) [4]. Interestingly, for comparison, this period includes the extreme solar minimum of 2008-2009.

The heliocentric longitudinal distribution for Earth, Venus and Mercury of M- and X-class Flares is shown in Figure 1. For the Earth, the peak around 45° (33°) shows the strongest clustering of such solar energetic bursts, while the peaks at 255° and in particular that at 291° are also of statistically significant. In all the planetary spectra no correction was performed for their orbital eccentricity, which is 6%, 2% and 223% for Earth, Venus and Mercury, respectively. Venus and Mercury show a strong and wide peak around 260°-270° in longitude as well as a second one at ∼ 150°. Interestingly, a strong excess around 250°-290° is happening in all 3 planetary longitudinal distributions, despite the fact that Mercury, Venus and Earth have gone through the same longitudes mostly at different times. In the case of Mercury, a smaller peak appears around 33°. Due to the large orbital eccentricity of Mercury, the expected modulation has been subtracted. The derived residual spectrum makes the aforementioned peaks better visible (Figure 1).

As next, we introduced in the analysis code planetary spatial correlations. A possible combined lensing efficiency might enhance the observed effects on the Sun or the ionosphere. In fact, this has been also observed with statistically significant differences both in intensity and in spectral shape (see Figures 2 and 4). Remarkably, the excess observed with M-Flares and EUV (Figures 2) peaks at exactly at the same values around 241° and 290°. A similar behavior is also shown by the X-Flares, despite the poorer statistics (see [2]).

Figure 3 shows additional results obtained with the flaring Sun and its full disk EUV emission as well as a correlation between both. Surprisingly, the EUV irradiance preceding the onset of 7 huge X-class Flares is suppressed for a period lasting 1-2 months. It is intriguing that this suppression depends on the planetary configuration (not shown), which might be a relevant signature for the trigger of the unpredictable flares.

2.2   The Ionosphere

The total electron content (TEC) of the ionosphere depends primarily on the solar EUV irradiance, but its variations show anomalies, which have not been understood since several decades (see [2]). For example, the measured TEC during December exceeds that around June, which cannot be explained by the annual solar irradiance modulation due to the varying Sun-Earth distance. We investigated the possibility that these anomalies could be connected to planetary lensing, using the same reasoning described above.

Figures 4 shows the results obtained for combined planetary constraints of the global electron content of the ionosphere, derived from an uninterrupted sequence of 6573 daily averaged TEC measurements (1995-2013) [4]. Also this data taken period includes the extremely deep solar minimum between 2008 and 2009, which induced a more quiet behaviour of the electron content of the ionosphere. As before, the time binning of the TEC data is equal to 1 day. Surprisingly, we observed correlations with the position in the ecliptic of Mercury and Venus, including also the orbital positions of the Moon around the Earth. The first two columns in Figure 4 show the longitudinal distribution of Mercury and Venus, requiring a second planet (among the inner 3 planets) to be in a wide heliocentric longitudinal range 20°-140° vs. 200°-320°. Three out of four plots refer to the solar maximum period (1997-2006), while a similar comparison is shown for the extreme solar minimum period. Since the derived rates are normalized to 1 day, longitudinal modulations due to the planetary eccentricity are corrected. Considering long observation time periods of 10 or even 18 years, the derived distributions should be rather isotropic. This is, however, in contrast with observation.

We then addressed the annual TEC anomaly at the solstices, selecting the TEC data in

30° segments around December and June. Figure 4 (*right*, UP) shows the TEC distributions of these data as a function of the Moon phase. Note that during the Earths propagation by 30° in longitude, the Moon has completed one geocentric orbit. Taking into account the 223 orbits the Moon has performed around the Earth during the 18 years described by the dataset, randomly occurring TEC excursions should average out, or at least both distributions in Figure 4 (*right*, UP) should have similar shape. Figure 4 (*right*, DOWN) shows the calculated difference between the two distributions, exhibiting a modulation amplitude by a factor of 6. Remarkably, the position of the maximum coincides with the *New Moon*. This correlation fits well the scenario of this work, assuming a stream of invisible matter, with speed of about 50 km/s, coming from the direction of the Sun gravitationally focused by the interposed Moon onto the Earth.

3 Discussion

By analyzing the occurrence of X- and M-flares during the last 4 solar cycles and the full disk EUV irradiance of the Sun we find a strong evidence that the occurrence of these phenomena is strongly modulated by the position of Earth, Venus and Mercury around their heliocentric longitude. A preferred direction around 270° is common to all three planets, when their lensing effect is studied independently. The effect is further enhanced, as we show for the case of Mercury and Venus, when one takes into account the relative position of the two planets. This observation supports our working hypothesis that the activity of the Sun is triggered by influx of invisible matter and that this matter has some preferred direction or stream, which gets gravitationally lensed by the planets.

In addition, averaged daily GPS TEC measurements of the Earth ionosphere show also a marked planetary correlation, supporting our lensing scenario, which is further reinforced by the observation of the effect of the position of the Moon in modulating the TEC of the ionosphere. We bring to the attention that the anomalously high electron content of the ionosphere in December coincides with the alignment Galactic Center - Sun - Earth, i.e. the same direction around 270° previously described and that this effect becomes even more enhanced when the Moon is aligned around the same direction and interposed between the Sun and the Earth.

The identification of the nature of the predicted slow moving stream is left for future work: of course, one has to suppose that this invisible matter has some form of interaction with normal matter, but at this point we cannot infer any useful indication of its nature. Also, the (re)-analysis of the experiments searching for DM following our approach might give unexpected results.

4 Bibliography

References

[1] C. A. J. O'Hare and A. M. Green, "Directional detection of dark matter streams," Phys. Rev. D 90 (**2014**) no.12, 123511, doi:10.1103/PhysRevD.90.123511 [arXiv:1410.2749 [astro-ph.CO]], and references therein.

[2] S. Bertolucci, K. Zioutas, S. Hofmann, M. Maroudas, "The Sun and its Planets as detectors for invisible matter," *Submitted for publication (***2016**), [arXiv:1602.03666v4], and references therein.

[3] Astrid Veronig, private communication **2014**.

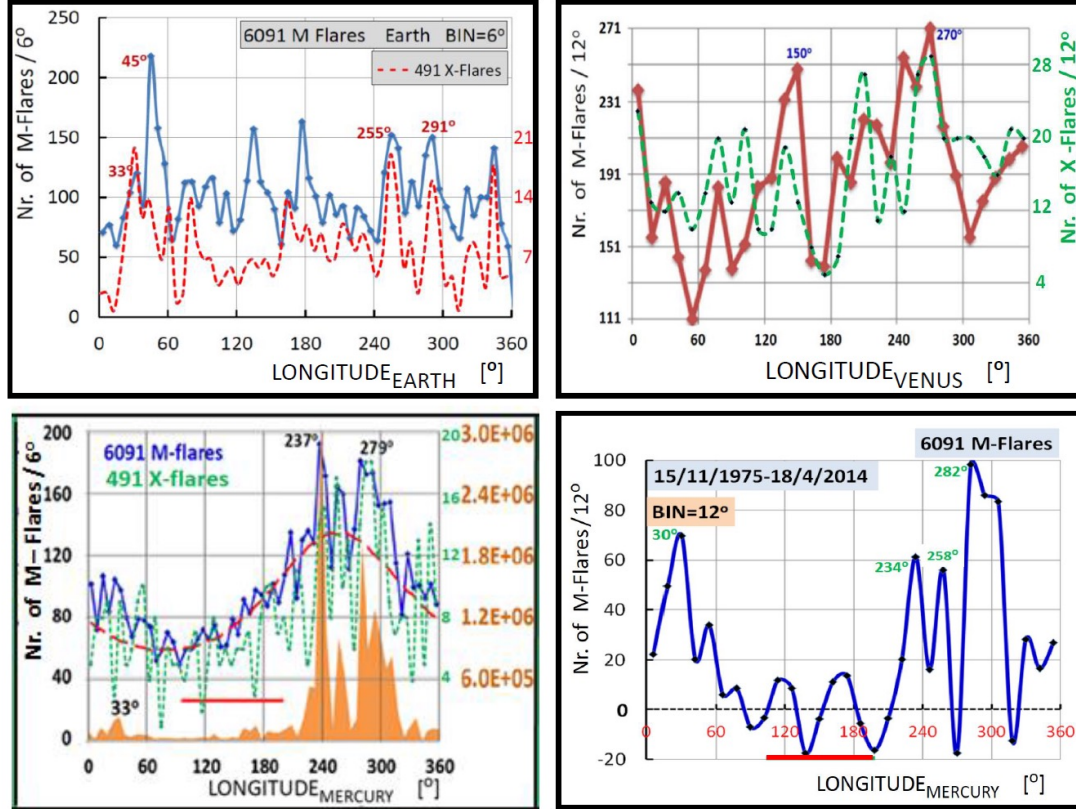[4] Leonid Didkovsky, private communication **2014**.

Figure 1: UP, Earth (*left*), Venus (*right*): Number of M-class Flares and X-class flares (dashed lines) as a function of the heliocentric longitude of the **Earth** ($01/01/1976 - 05/05/2015$) and the **Venus** ($15/11/1975 - 18/04/2014$). DOWN, *left*: Number of M-class flares (blue) and X-class flares (dashed) as a function of **Mercury** heliocentric longitude of the 6091 M-class Flares. The dashed red line is the normalised stay time due to Mercury orbital eccentricity. The horizontal red bar shows the region used for normalization. In orange is shown the "multiplication spectrum" of the 4 solar cycles (M-Flares). On the *right* is shown the residual spectrum (blue - red dashed on the *left*), with the 3 peaks around 30°, 240° and 290° becoming better visible. Note, that we use $BIN = 6°$ (*left column*) and $BIN = 12°$ (*right column*).
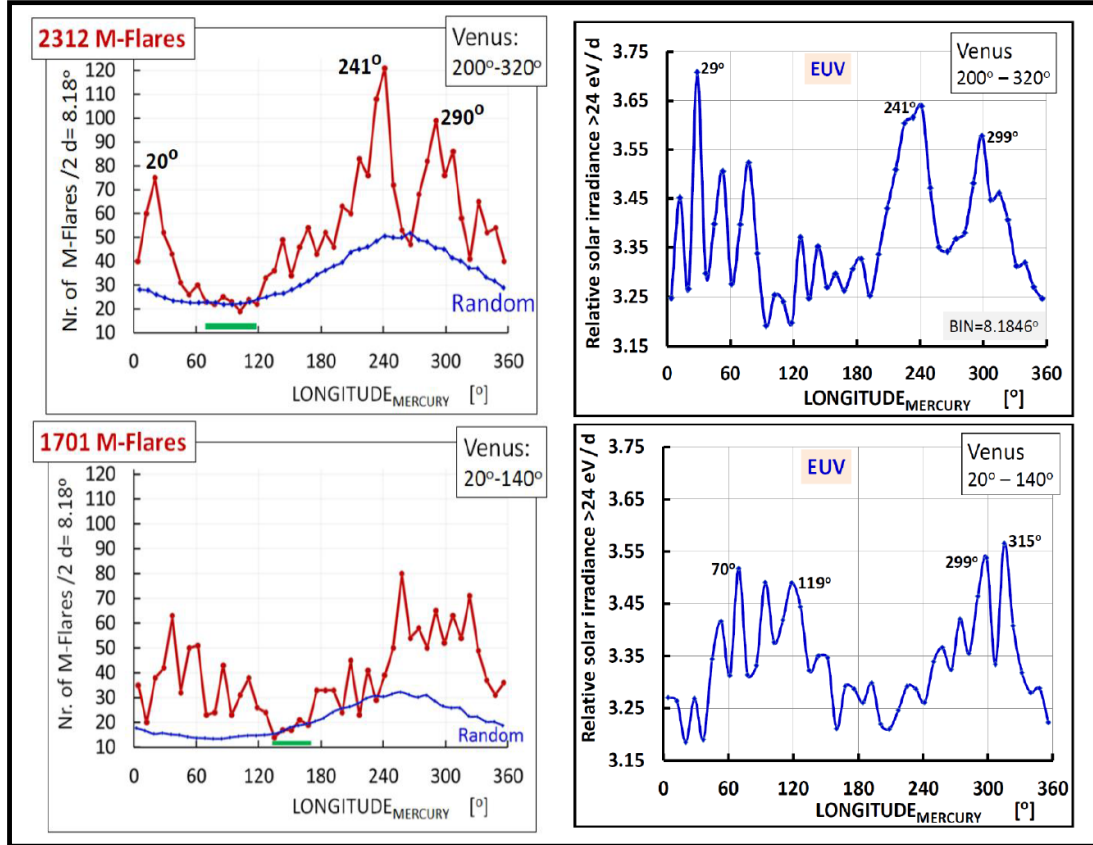
Figure 2: UP: Distributions of M-class Flares (*left*) and full disk EUV irradiance (*right*) as a function of **Mercury** heliocentric longitude with the constraint of Venus being at longitude between 200°-320°. DOWN: The same plots for Venus being between 20° and 140°. The smooth blue lines represent the expected normalized number of flares if equally distributed in time due to the large eccentricity of Mercury. The green bar shows the region used for normalisation. The EUV spectra are time normalised and therefore the eccentricity effect is out.

Figure 3: LEFT, UP: The sum of the daily averaged full disk solar EUV emission in 64 consecutive time intervals of 88 days (1999-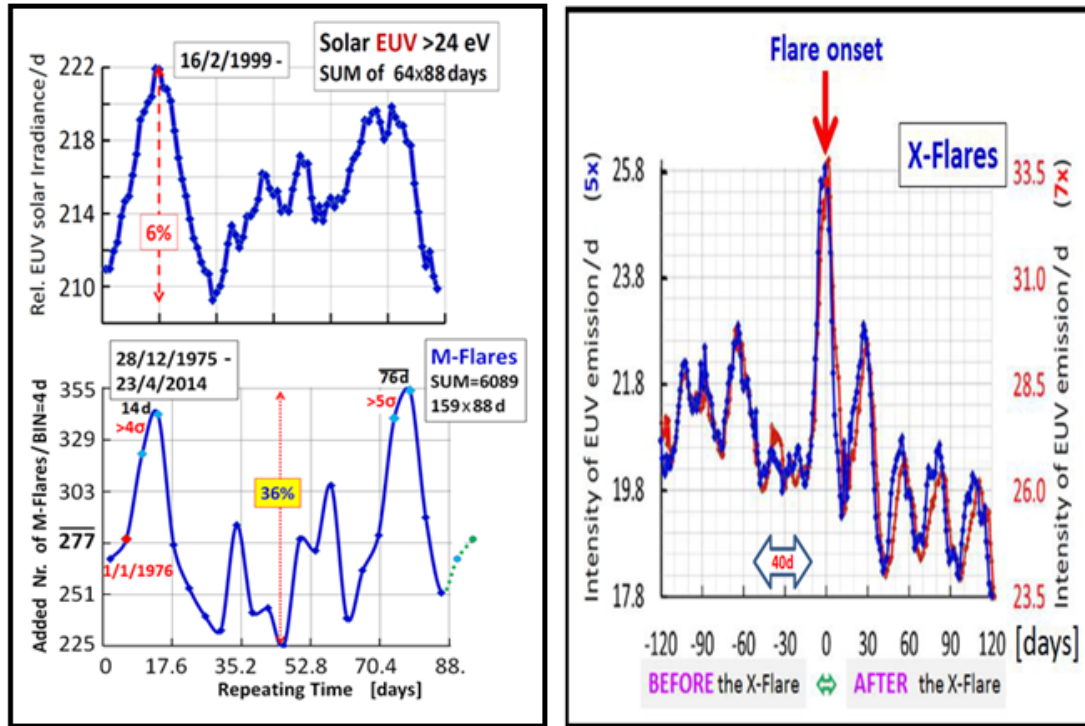2015). LEFT DOWN: The sum of M-class Flares averaged over 4 days in 159 consecutive intervals of 88 days (1976-2014). It is apparent the similar spectral shape of both solar activities. RIGHT: The start time of the biggest 7 X-class Flares during the previous solar cycle (1996-2007) is used as the reference point ($time = 0$) for the emission of full disk solar EUV during 4 months before and after the flare onset, The flares occurred far from each other, excluding double counting effects. The gap of about 40 days before the flare "explosion" is intriguing. Note, for 2 X-flare pairs, being too close to each other, an averaged onset time was used; the initial correlation remains unaffected (blue line)
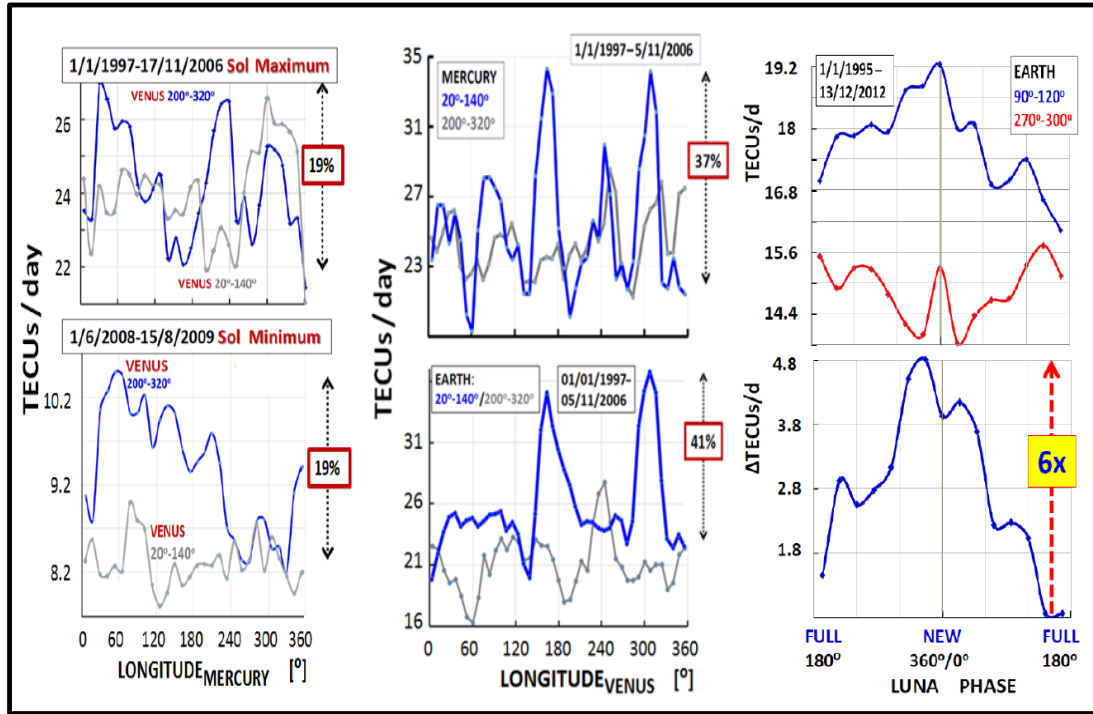
Figure 4: The daily measured longitudinal distributions of Earths atmospheric total electron content [1] for different planetary configurations and time periods of the solar cycle. LEFT: The total electron content [TECUs] as a function of **Mercury** heliocentric longitude during the solar maximum period 1997-2006 (UP) and during the recent extremely deep solar minimum 2008-2009 (DOWN). The thick blue and the thin grey lines are associated with Venus being in one of the two opposite 120° wide orbital arcs. MIDDLE: TECUs as a function of the **Venus** longitude during the same solar maximum requiring Mercury (UP) and Earth (DOWN) to be in one of the 120° segments. RIGHT: TECUs as a function of the **Moon Phase**, while the Earth is in one of the two 30° orbital segments around the solstices (UP) and the difference between the winter-summer solstices (DOWN). Note, the Moon is between the Earth and the Sun at *New Moon*.

Participants

Ahn, Saebyeok	Center for Axion and Precision Physics Research (CAPP/IBS)
Arias, Paola	USACH
Ayala, Adrian	University of Granada
Blanchard, John	Helmholtz-Institut Mainz
Bozorgnia, Nassim	GRAPPA, University of Amsterdam
Braggio, Caterina	University of Padova and INFN
Branca, Antonio	INFN Padova
Camargo, Daniel	UFABC
Cantatore, Giovanni	University and INFN, Trieste, Italy
Caspers, Fritz	CERN
Chang, Seung Pyo	CAPP/IBS and KAIST
Choi, Jihoon	CAPP/IBS
Choi, Kiwoon	CTPU/IBS
Choi, Ki-Young	Chonnam National University
Cho, Kihyeon	KISTI
Chou, Aaron	Fermilab
Cho, Yongmin	Konkuk University
Chung, Woohyun	CAPP/IBS
Cui, Xingzhu	Institute of High Energy Physics,CAS
Deng, Gao-Ming	Beijing University of Technology
Englert, Christoph	Glasgow University
Ferretti, Jacopo	La Sapienza
Fiorucci, Simon	LBNL
Fleury, Leesa	University of British Columbia
Fu, Changbo	Shanghai Jiaotong University
Gerbier, Gilles	Queen's University
Gondolo, Paolo	University of Utah
Heinemeyer, Sven	IFT/IFCA (CSIC)
Hill, Christopher	Fermilab
Hoang, Phuong	CAPP/IBS and KAIST
Hoffmann, Dieter HH	Technical University Darmstadt
In, Seongjin	Sungkyunkwan University
Jaeckel, Joerg	ITP Heidelberg
Jang, Yeaji	CAPP/IBS
Jeong, Hoyong	CAPP/IBS
Jeong, Junu	CAPP/IBS and KAIST
Jiang, Hao	Tsinghua university
Ji, Wei	Tsinghua University
Kang, Haijing	BEIJING UNIVERSITY OF TECHNOLOGY
Keum, Yong-Yeon	Seoul National University
Kim, Chunglee	Seoul National University
Kim, Dongok	CAPP/IBS and KAIST
Kim, Jihn E.	Kyung Hee University
Kim, On	CAPP/IBS and KAIST

Kim, Younggeun	CAPP/IBS and KAIST
Kim, Young-Im	CAPP/IBS
Knirck, Stefan P.N.	Institute for Theoretical Physics, University Heidelberg
Ko, Byeong Rok	CAPP/IBS
Ko, Pyungwon	Korea Inst. for Advanced Study (KIAS)
Krippendorf, Sven	University of Oxford
Kwon, Ohjoon	CAPP/IBS
Lee, Doyu	CAPP/IBS and KAIST
Lee, Hye-Sung	CTPU/IBS
Lee, Hyun Min	Chung-Ang University
Lee, MyeongJae	CAPP/IBS
Lee, Soohyung	CAPP/IBS
Lee, Yujung	CAPP/IBS
Lewis, Samantha	University of California, Berkeley
Lindner, Axel	DESY
Liu, Jianglai	Shanghai Jiao Tong University
Liu, Shukui	Tsinghua university
Lopes, Isabel	LIP-Coimbra, Portugal
Lucio Martinez, Miriam	Universidade de Santiago de Compostela
Luk, Kam-Biu	University of California at Berkeley
Magill, Gabriel	Perimeter Institute for Theoretical Physics
Majorovits, Bela	MPI fur Physik
Malta, Pedro	Institute for theoretical physics - U. Heidelberg
Martinez, Maria	University of Rome - La Sapienza
Martinez Santos, Diego	Universidade de Santiago de Compostela
Martyniuk, Alex	University College London
McAllister, Ben	The University of Western Australia
Meyer, Manuel	Oskar Klein Centre, Stockholm University
Miceli, Lino	CAPP/IBS
Millar, Alexander	Max Planck Institute for Physics
Monroe, Jocelyn	Royal Holloway, University of London and KEK Laboratory
Naganoma, Junji	Rice University
Niemeyer, Jens	Goettingen University
Oh, KaYoung	CAPP/IBS
Oka, Naoya	Kobe University
O'Shaughnessy, Christopher	University of North Carolina at chapel Hill
Park, Jungsic	Institute for Basic Science
Park, Seongtae	CAPP/IBS
Petrakou, Eleni	CAPP/IBS
Pinfold, James	University of Alberta
Prescod-Weinstein	University of Washington
Pugnat, Pierre	CNRS/LNCMI-Grenoble
Rajendran, Surjeet	UC Berkeley
Redonto, Javier M.	Zaragoza U / MPP Munich
Ringwald, Andreas	DESY
Rott, Carsten	Sungkyunkwan University
Rybka, Gray	University of Washington
Semertzidis, Yannis K.	CAPP/IBS and KAIST

Shepherd, William	Niels Bohr International Academy
Solanki, Sami	Max Planck Institute for Solar System Research
Spector, Aaron	University of Hamburg
Sulc, Miroslav	Technical University of Liberec
Torres Machado, Diego	Federal University of Rio de Janeiro
von Sivers, Moritz	University of Bern
von Sturm, Katharina	University degli Studi di Padova
Wada, Masayuki	Princeton University
Wang, Huanyu	Institute of High Energy Physics, CAS
Won, Eunil	Korea University
Wuestrich, Marc	Max-Planck-Institute f. Physics
Xiao, Mengjiao	Shanghai Jiao Tong University
Yang, Byeongsu	ICRR
Yeo, Beomki	CAPP/IBS
Yoon, Chun Sil	GNU
YOUN, SungWoo	CAPP/IBS
ZIOUTAS, Konstantin	University of Patras, Greece